Self-assembly of conjugated (macro)molecules: nanostructures for molecular electronics

DISSERTATION

zur Erlangung des akademischen Grades

doctor rerum naturalium
(Dr. rer. nat.)

im Fach Chemie

eingereicht an der

Mathematisch-Naturwissenschaftlichen Fakultät I

der Humboldt-Universität zu Berlin

von

Paolo Samorí

geb. 3.5.1971 in Imola (Bologna)

Präsident der Humboldt-Universität zu Berlin
Prof. Dr. Dr. h.c. H. Meyer

Dekan der Mathematisch-Naturwissenschaftlichen Fakultät I
Prof. Dr. B. Ronacher

Gutachter/innen	1.	Prof. Dr. Frans C. De Schryver
	2.	Prof. Dr. Jürgen P. Rabe
	3.	Prof. Dr. Klaus Rademann

Eingereicht am: 14.07.2000
Tag der mündlichen Prüfung: 24.10.2000

Table of Contents

TABLE OF CONTENTS....3

ABSTRACT....7

ABSTRAKT....8

LIST OF ABBREVIATIONS....9

1 INTRODUCTION....11

2 SCANNING PROBE MICROSCOPIES....13

2.1 The techniques....13

2.2 Scanning Tunneling Microscopy....16

2.2.1 STM modes....18

2.2.2 Applications of STM....19

2.3 Atomic Force Microscopy....21

2.3.1 Classification of forces....22

2.3.2 Contact mode AFM....25

2.3.3 Vibrating Modes....26

2.3.3.1 Non Contact AFM (NC-AFM)....26

2.3.3.2 Tapping Mode™....27

2.3.4 Applications of AFM....27

3 CONJUGATED MOLECULAR SYSTEMS....29

3.1 Introduction....29

3.2 Application in molecular electronics....31

3.3 Phenyleneethynylenes....32

3.3.1 Kinetics of the polycondensation reaction....35

3.3.2 Molecular weight distribution 35
3.3.2.1 Schulz-Zimm distribution 37
3.3.2.2 Schulz-Flory distribution 38
3.3.2.3 Poisson Distribution 39

3.4 Hexa-*peri*-hexabenzocoronenes 40

4 SELF-ASSEMBLY OF MOLECULES AT SURFACES AND NANOELECTRODE FABRICATION 41

4.1 Physisorption 41
4.1.1 Conductive substrate 42
4.1.2 Insulating substrates 43

4.2 Chemisorption 43

4.3 Metallic nanoelectrodes for a molecular nanowire device 45

5 EXPERIMENTAL PROCEDURES 49

5.1 Preparation of the substrates 49
5.1.1 Layered substrates 49
5.1.2 Amorphous substrates 50
5.1.3 Metallic substrates 50
5.1.3.1 Template Stripped Gold 51

5.2 Scanning Tunneling Microscopy 52
5.2.1 Apparatus 52
5.2.2 Tip preparation 54
5.2.3 Vibration isolation 54
5.2.4 STM on dry films 55
5.2.4.1 SAMs of saturated alk*a*nethiols 56
5.2.4.2 SAMs of unsaturated alk*e*nethiols and mixtures 57
5.2.5 Investigations at the solid-liquid interface 57

5.3 Scanning Force Microscopy 59
5.3.1 Apparatus 59

5.3.2 Investigations on polymeric phenyleneethynylenes 60
5.3.3 Investigations on hexakis-dodecyl-hexabenzocoronene (HBC-C_{12}) 61

5.4 Image Processing 63

5.5 UPS, XPS 64
5.5.1 Photoelectron spectroscopies on phenyleneethynylene derivatives 64
5.5.2 Photoelectron spectroscopies on hexakis-dodecyl-hexabenzocoronene (HBC-C_{12}) ... 65

5.6 Current-voltage (I-V) measurements 65

6 RESULTS AND DISCUSSIONS 69

6.1 Self-assembly of thiols on metallic substrates 69
6.1.1 Introduction 69
6.1.2 Sublimed Au and Ag substrates 70
6.1.3 Template Stripped Gold substrates 74
6.1.3.1 SAMs on Template Stripped Gold substrates 76
6.1.4 Conductivity of SAMs of Alk*e*nes and Alk*a*nes 77

6.2 Role of the substrate in physisorption 85

6.3 Phenyleneethynylene trimers 87
6.3.1 Introduction 87
6.3.2 STM on physisorbed monolayers 88
6.3.3 XRD on single crystals 92
6.3.4 Discussion 97
6.3.5 Dynamics of molecules at the solid-liquid interface 98

6.4 Visualization of single macromolecules in monolayers 104
6.4.1 Macromolecular fractionation 106

6.5 PPE on insulating substrates 112
6.5.1 Introduction 112
6.5.2 Morphology at different concentrations of the solution 113
6.5.3 Morphology at different molecular weight 116
6.5.4 Morphology on different substrates 122

6.5.5 Morphology at different rate of the deposition process 126
6.5.6 Morphology with different side chains 128
6.5.7 Morphology of thiol free end functionalized PPE 129

6.6 Electronic structure of phenyleneethynylene derivatives 130
6.6.1 Introduction 130
6.6.2 Work functions of pristine and doped phenylenethynylene trimer and polymer 133
6.6.2.1 Spin coated PPE trimer 135
6.6.2.2 Spin coated polymer 138
6.6.3 Optical absorption investigation of PPE 141
6.6.4 Density of valence states calculations 141

6.7 Current-Voltage (I-V) Measurements 143
6.7.1 Visualization of the nanoelectrodes 143
6.7.2 Bridging metallic nanogaps with molecules 146

6.8 Growth of dry hexakis-dodecyl-hexabenzocoronene films from solutions 149

7 CONCLUSIONS 157

8 ZUSAMMENFASSUNG 159

9 BIBLIOGRAPHIC REFERENCES 161

10 ACKNOWLEDGMENTS 173

11 LEBENSLAUF 175

12 LIST OF PUBLICATIONS, AWARDS AND CONFERENCES PRESENTATIONS 177

SELBSTÄNDIGKEITSERKLÄRUNG 189

Abstract

In this thesis the self-assembly of π-conjugated (macro)molecular architectures, either through chemisorption or via physisorption, into highly ordered supramolecular nanoscopic and microscopic structures has been studied. On solid substrates structure and dynamics has been investigated on the molecular scale making use primarily of Scanning Probe Microscopies, in particular Scanning Tunneling Microscopy and Scanning Force Microscopy. This allowed to characterize a variety of phenomena occurring both at the solid-liquid interface, such as the dynamics of the single molecular nanorods (known as Ostwald ripening), the fractionation of a solution of rigid-rod polymers upon physisorption on graphite; and in dry films, i.e. the self-assembly of rigid-rod polymers into nanoribbons with molecular cross sections which can be epitaxially oriented at surfaces and the formation ordered layered architectures of disc-like molecules. In addition the electronic properties of the investigated moieties have been studied by means of Photoelectron Spectroscopies. The nanostructures that have been developed are not only of interest for nanoconstructions on solid surfaces, but also exhibit properties that render them candidates for applications in the field of molecular electronics, in particular for building molecular nanowire devices.

Keywords

Conjugated Molecules

Molecular Electronics

Scanning Probe Microscopy

Self-assembly

Abstrakt

In dieser Dissertation wird die Selbstorganisation von π-konjugierten (makro)molekularen Architekturen durch Chemisorption oder Physisorption in hochgeordnete supramolekulare nanoskopische und mikroskopische Strukturen auf festen Trägern untersucht.

Ihre Struktur und Dynamik wurden auf molekularer Skala hauptsächlich mit Rastersondenmikroskopien, insbesondere mit Rastertunnel- und Rasterkraftmikroskopie, untersucht. Dies erlaubte die Charakterisierung einer Reihe von Phänomenen, die sowohl an Fest-Flüssig-Grenzflächen auftreten, wie beispielsweise die Dynamik der einzelnen molekularen Nanostäbchen (Ostwald Reifung) und die Fraktionierung steifer Polymerstäbchen durch Physisorption an der Grafitoberfläche aus der Lösung heraus, als auch in trockenen Filmen vorkommen wie die Selbstorganisation steifer Polymerstäbchen zu Nanobändern mit molekularen Querschnitten, die sich epitaktisch auf Oberflächen orientieren lassen und auch die Ausbildung gestapelter Architekturen von diskförmigen Molekülen. Außerdem wurden die elektronischen Eigenschaften der untersuchten Systeme mit Hilfe von Photoelektronenspektroskopie charakterisiert. Die entwickelten Nanostrukturen sind nicht nur für Nanokonstruktionen auf festen Oberflächen von Interesse, sondern besitzen auch Eigenschaften, die sie für Anwendungen in einer zukünftigen molekularen Elektronik prädestiniert, etwa für den Aufbau molekularer Drähte.

Schlagworte

Konjugierten Molekulen

Molekularen Elektronik

Rastersondenmikroskopien

Selbstorganisation

List of Abbreviations

ϕ	Work function
2D-FFT	Two Dimensional – Fourier Transform
AFM = SFM	Atomic Force Microscopy
DOVS	Density of Valence States
DP	Number Average Degree of Polymerization
E_a	Electron Affinity
E_B	Binding Energy
E_F	Energy of the Fermi Level
E_K	Kinetic Energy
E_{Vac}	Energy of the Vacuum Level
ESCA	see XPS
GPC = SEC	Gel Permeation Chromatography
HBC	Hexa-peri-hexabenzocoronene
HBC-C_{12}	Hexakis-dodecyl-hexabenzocoronene
HOMO	Highest Occupied Molecular Orbital
HOPG	Highly Oriented Pyrolitic Graphite
HV	High Vacuum
I_P	Ionization Potential
I_t	Tunneling Current
I-V	Current – Voltage
LUMO	Lowest Unoccupied Molecular Orbital
MeOH	Methanol
M_n	Number Average Molar Mass
M_w	Weight Average Molar Mass
PES	Photoelectron Spectroscopy
PPE	Poly(para-phenyleneethynylene)
PPP	Poly(para-phenylene)
PS	Poly(styrene)
R_{rms}	Root mean square roughness
R_A	Average roughness
SAM	Self-Assembled Monolayer
SEC	Size Exclusion Chromatography

SEM	Scanning Electron Microscopy
SFM = AFM	Scanning Force Microscopy
SNOM	Scanning Near Field Optical Microscopy
STM	Scanning Tunneling Microscopy
STS	Scanning Tunneling Spectroscopy
THF	Tetrahydrofurane
TEM	Transmission Electron Microscopy
TM-SFM	Tapping Mode – Scanning Force Microscopy
TSG	Template Stripped Gold
T_{sub}	Temperature of the substrate
$U = M_n / M_w$	Polydispersity
UPS	Ultraviolet Photoelectron Spectroscopy
UHV	Ultra-high Vacuum
U_t	Tip bias
VEH	Valence Effective Hamiltonian
XPS = ESCA	X-ray Photoelectron Spectroscopy
XRD	X-ray Diffraction

1 Introduction

In the last two decades there has been a growing interest towards the nanoworld. The scientific community was prying into casting new light on the structure of organic, inorganic and biological materials, probing their chemical and physical properties on a molecular scale and comparing the properties of a single molecule with those of an *ensemble* or *Avogadro* number of molecule. Manipulating single molecules at room temperature [Jun96], visualizing [Sta95a] and stimulating chemical reactions [Hei94] at surfaces are just few examples of how the scientific community has been able to approach to the nanoworld. Particularly interesting in this new scientific approach is what one may call nanochemistry and nanophysics at interfaces.

Until few years ago information on the sub-micrometer scale length was accessible only using indirect techniques such as electron or X-ray diffraction or with electron microscopies that required vacuum environment and conductive materials.

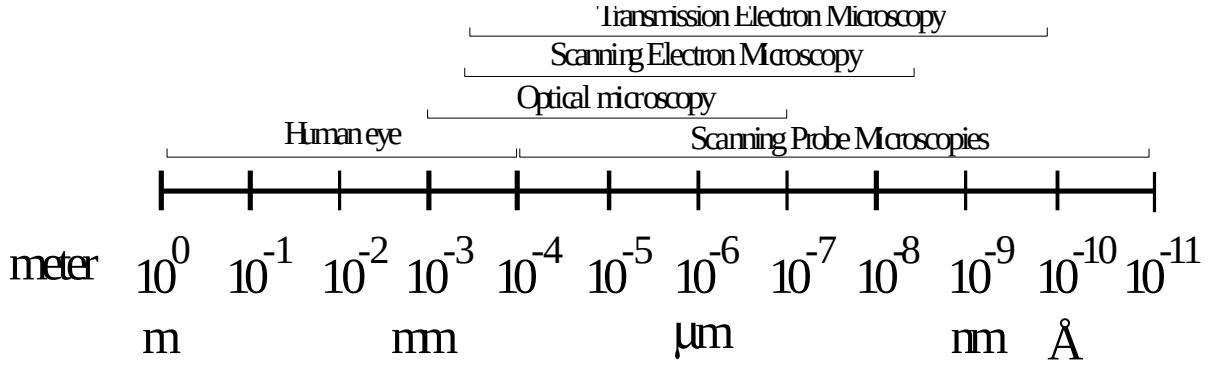

Figure 1.1: Spatial resolution of some microscopical techniques

In 1982 a breakthrough occurred: the Scanning Tunneling Microscope (STM) was invented by Binnig, Rohrer, Gerber and Weibel [Bin82a]. Their project aimed at developing a microscopical technique able to generate real-space images of surfaces with a resolution on the nanometer scale. Four years later they were awarded the Nobel prize in physics for their invention. This discovery represented also a big improvement for the development of miniaturized electronic devices. Even greater importance had the invention of the Atomic Force Microscope (AFM) [Bin86], known also as Scanning Force Microscope (SFM), that

made it possible also to investigate insulating materials such as polymers and biomolecules.

On the other hand in the last two decades conjugated molecular species have received a great deal of attention in the chemical and physics community because they are building blocks of materials with high electronic conductivity and even superconductivity [Chi77].

In view of these two developments, the aim of this thesis is to grow highly ordered molecular nanostructures of conjugated (macro)molecules with well defined chemical functionalities and physical properties that arise from the molecules their selves. These architectures could be useful for building molecular based electronic devices, in particular a molecular nanowire. Scanning Probe Microscopies played a pivotal role in this project because they allowed to investigate self-assembled architectures on flat solid substrates and to monitor dynamic processes at surfaces.

This thesis is divided into seven chapters: after this brief introduction, the second chapter will introduce the different Scanning Probe Microscopies, focusing on the Scanning Tunneling Microscopy and Scanning Force Microscopy. The third chapter introduces to the conjugated molecular systems, their synthesis and their application in the development of molecular based electronic devices. In the fourth chapter the self-assembly of molecular species on flat solid substrates and the development of nanoelectrodes are addressed. The fifth chapter is dedicated to the experimental procedures. The sixth chapter will discuss the results of this research, first chemisorbed monolayers on metallic substrates and then physisorbed layers and multilayers both at the solid-liquid interface and in dry films produced from solution or by sublimation in vacuum. The seventh chapter will summarize and give outlooks of the project. Last but not least, the acknowledgments underline the importance of the collaborative efforts for an interdisciplinary work such as that presented here.

2 Scanning Probe Microscopies

In this chapter Scanning Probe Microscopies are described in detail, focusing particularly on Scanning Tunneling Microscopy and Atomic Force Microscopy.

2.1 The techniques

The Scanning Tunneling Microscope (STM) [Bin82a, Bin82b], developed in the laboratories of IBM in Zürich in 1981, represents just the first of the family of the Scanning Probe Microscopies (SPM)s, which are a class of surface science instruments that introduced a new simple approach in the investigation of conducting, semiconducting and insulating samples [Wie92,Wie98]. They are based on few common principles:

1. A sharp probe (tip) interacts with the sample surface;
2. The tip probes local physical properties of the sample. The tip-sample interaction is very sensitive to small changes in the distance tip-sample;
3. A piezoelectric circuit allows to perform displacements of the tip and/or the sample in the X, Y, and Z directions with a precision of a fraction of an Ångström;
4. A feedback system controls the distance tip-sample.

They exhibit:

1. High vertical resolution (≤ 0.1 nanometer for AFM and STM);
2. High lateral resolution (≤ 1 nanometer for AFM and STM);
3. Possibility to measure at solid-liquid interfaces, i.e. at surfaces in their native environments;
4. Possibility to explore non-crystalline samples;
5. Not or mildly invasive technique.

One of the biggest advantages of SPMs, if compared to Scanning Electron Microscopies (SEM) or Transmission Electron Microscopies (TEM), is the possibility to investigate a

sample outside vacuum, i.e. in air or in a solution. This renders feasible the visualization not only structures, but also dynamic processes that occur on a time scale that spans from few milliseconds to several days.

The STM became the ancestor of all Scanning Probe Microscopies (SPM) that have been developed in the following years. They differ from the type of physical property that governs the interaction tip-sample:

Table 2.1: Main Scanning Probe Microscopies.

	Physical interaction tip-sample	**Type of samples**	**Typical tips**	**Max. lateral resolution**	**Inventors and year**	**Ref.**
STM	Electron tunneling	Conductors, semiconductors	W, Pt/Ir	1 Å	Binnig, Rohrer et al. (1981)	[Bin82a]
AFM or SFM	Forces	Conductors, semiconductors, insulators	W, Si, Si_3N_4	1 Å	Binnig, Gerber, Quate (1986)	[Bin86]
MFM	Magnetic forces	Ferromagnetic materials	Ni AFM coated tips	5 Å	Martin, Wickra-masinghe (1987)	[Mar87]
SNOM	Optical properties under the diffraction limit	Conductors, semiconductors insulating adsorbates and biological films	Optical fiber	10 Å	Pohl et al. (1984)	[Poh84]
STOM	Photon emission from electrons in STM	Conductors, semiconductors	STM tip + photodiode	5 Å	Coombs, Gimzew-ski et al. (1988)	[Coo88]
SNTM	Heat transfer	Conductors, semiconductors insulating adsorbates and biological films	Thermo-couple	30 Å	William, Wickra-masinghe (1986)	[Wil86]
SECM	Ion transfer	Conductors, semiconductors insulating adsorbates and biological films	Electrode in a ionic solution	1000 Å	Liu, Bard et al. (1986)	[Liu86]

where MFM = magnetic force microscopy
SNOM = scanning near-field optical microscopy
STOM = scanning tunneling optical microscopy
SNTM = scanning near-field thermal microscopy
SECM = scanning electrochemical microscopy

The SPM is basically composed of 3 parts:

- the probe;
- the scanning system;
- the system that detects the interaction.

The last two can be controlled by a personal computer or workstation through an analog/ digital converter and a Digital Signal Processing (DSP) card. In all Scanning Probe Microscopes, a piezoelectric scanner behaves as an extremely fine positioning stage able to move the probe over the sample (or the sample under the probe). The SPM electronics drives the scanner in a type of a raster pattern, as shown in Figure 2.1.

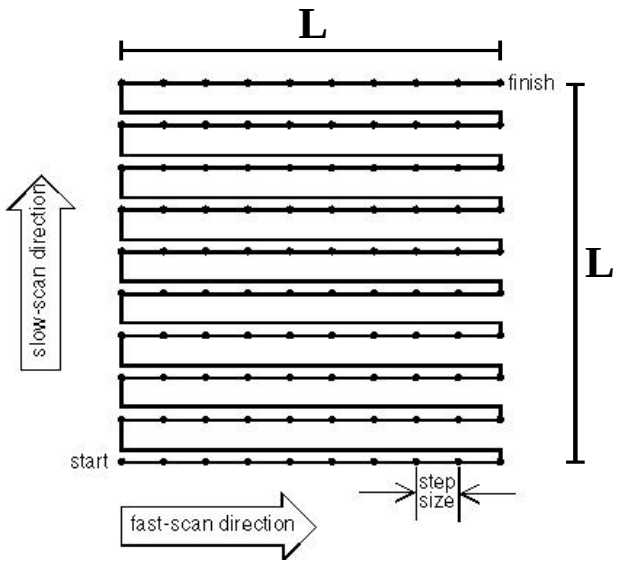

Figure 2.1. Scanner motion during data acquisition

The scanner moves across the first line of the scan, and back. It then steps in the perpendicular direction to the second scan line, moves across it and back, then to the third line, and so forth. While the scanner is moving across a scan line, the image data are sampled

digitally at equally spaced intervals. The data recorded is the tip-sample interaction that varies from SPM to SPM. The scan length of the image (L) spans from tens of Ångström to over 100 microns, and from 128 to 512 data points per line. The image is a square grid of measurements (data points).

2.2 Scanning Tunneling Microscopy

The STM can provide an image of the tunneling current in a plane across a conductive sample which, in a first approximation, corresponds to the topographical map of the sample. More accurately, the tunneling current images give evidence of the electronic density of states (LDOS) at the surface [Lan85, Gim87]. STMs can in fact sense the number of filled or unfilled electron states near the Fermi surface, within an energy range determined by the bias voltage [Han87]. Rather than measuring physical topography, it measures a surface of constant tunneling probability.

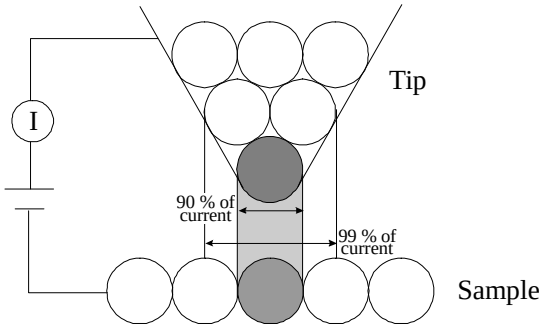

Figure 2.2: Scheme of the STM junction.

The technique is based on the quantum-mechanical effect of electron tunneling. The tunneling occurs between two conductors separated by a gap (or insulating layer), that acts as a potential barrier for the electrons. The tunneling current decays exponentially with the gap width. This causes the current signal to be determined by the tip apex as shown in Fig. 2.2 and it permits a lateral resolution of ~1 Ångström to be achieved [Gim87]. The tunneling current can be estimated by:

$$I \propto f(V) \bullet \exp\left\{-a \bullet s \bullet \sqrt{\Phi}\right\}$$

with:

$a = 10/\left(nm\sqrt{eV}\right)$

V = bias potential between tip and sample;

s = gap width;

Φ = average barrier height between the two electrodes (~4 eV).

Roughly, a variation of the gap of one Ångström gives rise to a variation of the tunneling current of one order of magnitude. Because of this reason a vertical resolution of fractions of an Ångström can be reached.

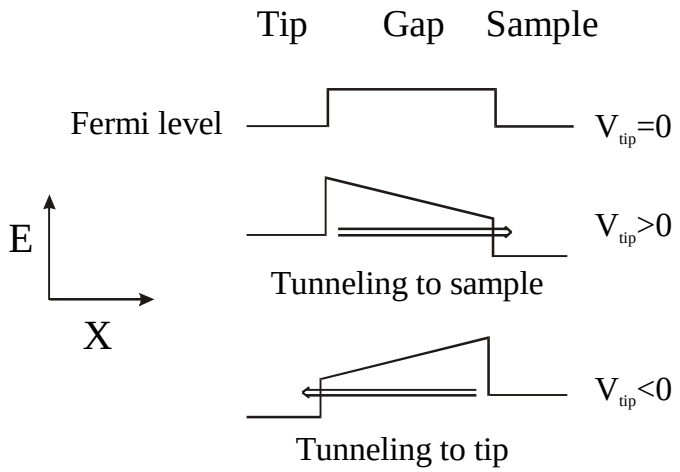

Figure 2.3: Energy diagram explaining tunneling in STM experiments

In the STM apparatus the two electrodes are the sample and an atomically sharpened metallic probe; this latter one is usually produced by cutting or chemical etching of a Pt/Ir or W wire. When the tip is brought into close proximity of the sample surface (few Ångströms), applying a bias voltage (< 1.5 V) between the two electrodes causes the electrons from the sample to tunnel through the gap into the tip or vice versa, depending upon the sign of the bias voltage [Ter83]. (See Fig. 2.3). The resulting tunneling current varies with the tip-to-sample spacing, and it is this signal which is used to create an STM image. A big limitation of STM is that it cannot image thick insulating layers. Having the possibility to probe currents in the picoampere range, the thickness of an insulating layer can be at maximum ~ 15 - 20 Å.

2.2.1 STM modes

The STM can be constructed to scan a sample in either of two modes: *constant-height* or *constant-current mode*, as shown in Fig. 2.4.

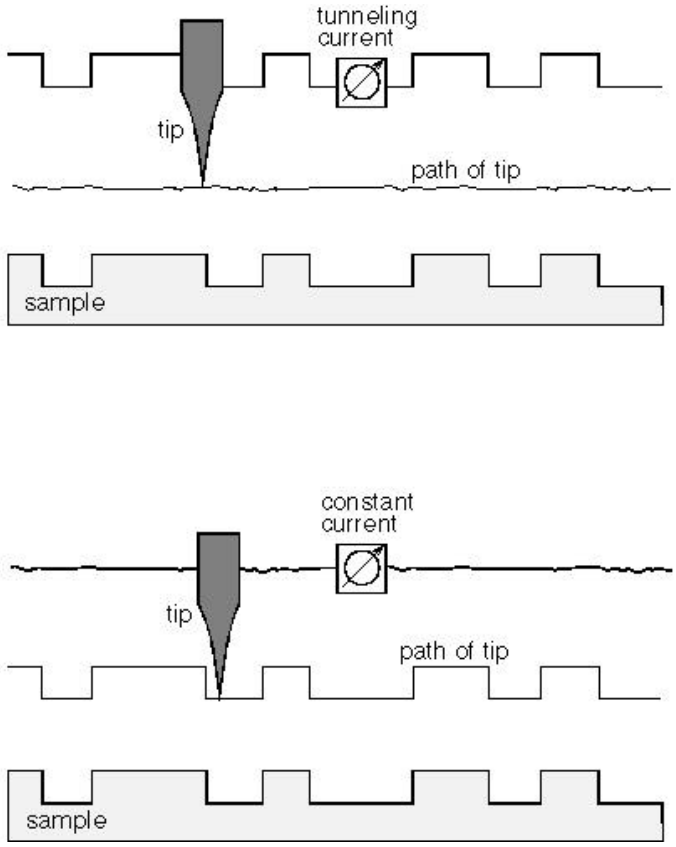

Figure 2.4: Comparison of constant-height and constant-current mode for STM.

In *constant-height mode*, the tip scans in a horizontal plane above the sample and the tunneling current changes depending on the topography and the local surface electronic properties of the sample. The tunneling current measured at each point on the sample surface represents the data set.

In *constant-current mode*, the STM uses a feedback loop that enables the tunneling current to be constant by adjusting the height of the scanner at each measurement location. For example, when the system detects an increase in tunneling current, it adjusts the voltage applied to the piezoelectric scanner in order to enhance the distance between the tip and the sample. In *constant-current mode*, the motion of the scanner constitutes the data set. If the

system keeps the tunneling current constant to within a few percent, the tip-to-sample distance will typically be constant to within a few hundredths of an Ängström.

Each mode has advantages and disadvantages. *Constant-height mode* is faster because the system does not have to move the scanner up and down, but it provides useful information only for relatively smooth surfaces. *Constant-current mode* can measure irregular surfaces with high precision, but the measurement takes more time and the lateral resolution that can be achieved is usually smaller due to the difficulty in setting a proper feedback loop which allows contemporary the tip to follow the surface prosperities and not to introduce a periodic noise in the dataset.

The STM offers the possibility to perform a spectroscopical investigation of the sample down to a sub-nanometer scale using the *Scanning Tunneling Spectroscopy*, (*STS*) mode [Wie98,Fee94,Sta95b]. The tip is "frozen" at a well specific distance to the sample surface (position) and at an increasing voltage (U) (between a selected range within –10 V and 10 V) dI/dU is sampled The resulting curve ((dI/dU)=f(U)) can usually be attributed to structure in the electronic density of states.

2.2.2 Applications of STM

The STM had a big success due to the high resolution imaging that can be achieved.

Metals:

The first samples that have been studied with this technique were metal surfaces. Binnig and co-workers observed the reconstruction of the Au(110) surface [Bin83a]. Later the structure of several other metals have been monitored such as Pt(100) and (110), Pd(100), Ir, Au(100), Ag(111) [Wie92]. These investigations have been carried out either in UHV or air environments.

Inorganic semiconductors:

A breakthrough for the high resolution imaging with STM was the observation of the 7x7

reconstruction of Si (111) according to the model of Takayanagi [Iss91]. Another compound deeply investigated is GaAs [Fee87]. Because of the fast oxidation of this surfaces, these studies have been executed in UHV ambient.

Organic adsorbates:

The STM has been used to monitor the structure of thin organic layers at the solid-liquid interface and in dried films, produced both from solution and from UHV sublimation.

The investigations at the solid-fluid interfaces started from the pioneering work of J.S. Foster and J.E. Frommer on liquid crystals [Fos88, Smi89, Spo89]. It was continued with investigations of small molecular systems at the interface between an almost saturated solution and a crystalline conductive substrate by J. P. Rabe and coworkers on alkanes, alcohols, fatty acids [Rab91a], didodecylbenzene [Rab91b], conjugated oligomers [Bäu95] and a variety of other chemical species. In this environment the resolution in space and in time made it possible to monitor dynamic processes such as coarsening of molecular interfaces [Sta95a], photodecompositions [Hei94] and photopolymerizations [Gri97]. With the same set-up the electronic properties of single molecules have been measured by means of STS [Sta95b].

Studies of UHV sublimed thin films have been performed on naphtalene [Hal91] and azulene derivatives and later porphyrin moieties adsorbed on metal surfaces [Jun97]. Chemisorbed species as Self-Assembled Monolayers of thiol functionalized molecules have been widely investigated on several metallic substrates (Au, Ag, Pt, Pd, Cu) [Ulm91].

Biological samples:

The possibility to observe molecular systems in their native medium was very appealing and has constituted the main reason why biologists have put a big effort into this technique since the early years. The limitations were due to the small electronic conductivity of these kinds of materials. This problem was partly overcomed either by using an STM able to detect currents in the picoampere range [Guc94] or by coating the sample with a conductive layer (e.g. of gold or amorphous carbon).

2.3 Atomic Force Microscopy

The invention of Atomic Force Microscopy (AFM) [Bin86, Rug90] in 1986 also by Binnig and co-workers has solved the problem of imaging samples with a low electrical conductivity. In fact the physical properties that are measured with this apparatus, namely the interaction forces between a sharp conical tip and the sample surface, allow investigations to be performed on electrical conductors as well as on semiconductors, on organic and also on biological materials.

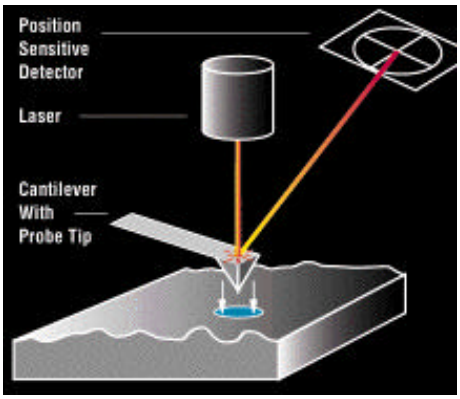

Figure 2.5: The beam-bounce detection scheme.

AFM probes the surface of a sample with a sharp tip, with a terminal radius often less than 100 Å. The tip is located at the free end of a ~ 100µm long cantilever that has got an elastic modulus that can reach tenths of N/m. Forces of a few piconewton between the tip and the sample surface cause deflections of the cantilever in the Ångström spatial scale. A laser beam bounces off the back of the cantilever onto a position-sensitive photodetector (PSD). As the cantilever bends, the position of the laser beam on the detector shifts. The PSD itself can measure displacements of light beams as small as 10 Å. The ratio of the path length between the cantilever and the detector to the length of the cantilever itself produces a mechanical amplification. As a result, the system can detect sub- Ångström vertical movements of the cantilever tip. The measured cantilever deflections enable the computer to generate a map of surface topography. This apparatus can be called also Scanning Force Microscopy, that is its suitable name in particular for studies carried out in a micrometer and sub-nanometer scale.

The interaction forces in the AFM are often quite complex due to several factors:

- Even if the tip apex should be monoatomic, the number of atoms from the tip involved in the interaction is not one, due to the contribution of rather long range forces;

- The forces are dependent on the environment (gas, liquid or vacuum);
- The scan is a dynamic process, which means that velocity dependent forces need to be considered;
- The tip can deform the sample.

2.3.1 Classification of forces

It is important to distinguish the type of forces between the tip and the sample in order to separate the contributions and correctly interpret the experimental results. [Isr92]

Long range forces

van der Waals forces: exist between every types of atoms or molecules; they are proportional to $1/r^6$ where r is the distance between them. The role of these forces in AFM have been discussed by Moiseev [Moi88] and Hartmann [Har90]. They are important in the range from one to tens of nanometers.

1. *Electrostatic forces*: they are due to coulombic interactions; in the present case they can occur between an electrostatically charged tip and a charged area of an insulating surface. They are important in the range from one to thousands of Ångström.
2. *Capillary forces*: the curvature at the contact between the tip and the sample causes the condensation of vapor from the ambient including water from the air. Also surfaces exposed to the air environment are typically coated by a layer of water, whose thickness depends on the relative humidity (RH) of the atmosphere and on the physico-chemical nature of the object. It results in a strong attractive capillary forces (about 10^{-8} N) that hold the tip in contact with the surface. To avoid capillary forces the ambient humidity must be at RH=0%, although Thundat and co-workers demonstrated that below RH=10% they could not detect decays any further of the capillary forces [Tun93]. Two simple experimental procedures can minimize the effect of this kind of forces:

a) flood a sealed chamber for the measurements with a dry inert gas such as N_2 , He or Ar;

b) make use of a fluid cell, that means to perform measurements with both the tip and the sample immersed in a liquid medium [Wei92].

Short range forces

1. *Repulsive forces*: They are proportional to $1/r^n$ with n>8. The interatomic repulsion forces have two origins:

   a) Repulsion between nuclei: the overlap of two electronic clouds gives rise to an incomplete screening of the nuclear charges; this generates coulombic repulsions.

   b) Pauli repulsion: according to the exclusion principles of Pauli, two electrons with the same spin can not occupy the same orbital. Thus the electrons can only overlap when the energy of one electron is increased, which causes a repulsive interaction.

2. *Forces of covalent bonds*: they originate from the overlap of the wave functions of two or more atoms. In this case the density of electric charges is concentrated between the two nuclei. This force decreases abruptly for a separation over a few Ångström. The type of interaction can be also called *chemisorption.*

3. Metallic adhesion: they derive from the interaction between strongly delocalized electronic clouds, which cause strong interactions that decay exponentially with distance. They are important when two metallic surfaces approach to the extent that the electronic wave functions overlap [Ban90]. This case can be called also physisorption.

4. Friction: during the scan, there is a force component parallel to the surface, since the tip is not always oriented exactly perpendicular to the surface. This friction tends to twist the cantilever, and since the torsion angle depends on the composition of the surface, the measurement of the twist provides chemical information [Mat92]. It was also shown that this kind of friction force can be detected on the atomic scale [Mat87].

As a first approximation the forces contributing to the deflection of an AFM cantilever can be considered the *Van der Waals* and the *repulsive forces*. These contributions are on the basis of the Lennard - Jones potential:

$$e(r) = -4e_0\left[\left(\frac{s}{r}\right)^6 - \left(\frac{s}{r}\right)^{12}\right]$$

with:

$\varepsilon_0/4$ = potential energy at the minimum;

σ = effective molecular diameter;

r = interatomic distance.

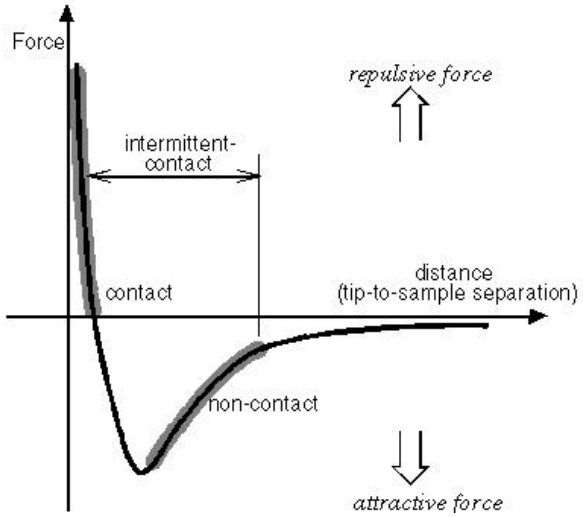

Figure 2.6: Interatomic force vs. distance curve.

The force, which is the negative gradient of the energy, is plotted in Fig. 2.6. Two distance regimes are highlighted: 1) the *contact* regime; and 2) the *non-contact* regime. In the *contact* regime, the cantilever is held less than a few Ångström from the sample surface, and the interatomic force between the cantilever and the sample is repulsive. In the *non-contact* regime, the cantilever is held on the order of tens to hundreds of Ångström from the sample surface, and the interatomic force between the cantilever and sample is attractive (largely a result of the long-range van der Waals interactions). Both *contact* and *non-contact* imaging techniques are described in detail in the following sections.

2.3.2 Contact mode AFM

In contact mode AFM a tip makes soft "physical contact" with the sample. The tip is attached to the end of a cantilever with a spring constant, lower than the effective spring constant holding the atoms of the sample together. As the scanner gently scans the tip across the sample (or the sample under the tip), the contact force causes the cantilever to bend in order to follow the topographic profile. Using very stiff cantilevers it is possible to exert large forces on the sample and the sample surface is likely to get deformed; this may be also used in "nanolithography". The total force that the tip exerts on the sample is the sum of the capillary plus cantilever forces, and must be balanced by the repulsive van der Waals force for contact AFM. The magnitude of the total force exerted on the surface varies from 10^{-8} N (with the cantilever pulling away from the sample almost as hard as the water is pulling down the tip), to the more typical operating range of 10^{-7} to 10^{-6} N.

Similarly to STM, the contact mode AFM can generate the topographic data set by operating in one of two modes – *constant height* or *constant force mode.*

In *constant height mode*, the spatial variation of the cantilever deflection can be used directly to provide the topographic data set because the height of the scanner (consequently also the distance sample surface - tip holder) is fixed as it scans.

In *constant force mode*, the deflection of the cantilever is used as input to a feedback loop that moves the scanner up and down in Z-direction, responding to the topography by keeping the cantilever deflection constant. In this case, the image is generated from the scanner's motion. With the cantilever deflection held constant, the total force applied to the sample is constant. In *constant force mode*, the speed of scanning is limited by the time of response of the feedback loop, but the total force exerted on the sample by the tip can be controlled. This mode is usually preferred for most applications because it gives a real topographic map of the sample surface. *Constant height mode* is often used for recording atomic-scale images of atomically flat surfaces, where the cantilever deflections and thus variations in the applied force are small. This latter mode is also essential for monitoring fast processes in real-time, where high scan rates are essential.

2.3.3 Vibrating Modes

In order to overcome the problem of the friction component during scanning in contact mode, to minimize the forces exerted from the tip on the sample and the effect of the capillary forces, alternative modes have been invented where the AFM cantilever vibrates near (on the order of tens to hundreds of Ångströms) the surface of a sample (Fig. 2.7). Basically, stiff cantilever is forced to oscillate near its resonant frequency (typically from 200 to 400 kHz) with an amplitude of a few hundreds of Ängströms. While the tip scans over the sample the system detects the shift in the phase and the gradient in the amplitude of the swing of the cantilever and keeps it constant with the aid of a feedback system that moves the scanner up and down. By keeping the amplitude constant, the system is expected to also keep the average tip-to-sample distance constant. The sensitivity of this detection scheme provides sub-Ängström vertical resolution in the image, as in contact AFM. Due to the elimination of the shear forces that are applied from the tip to the sample, these modes are particularly useful for studying soft materials such as biological and organic films. As a consequence of the reduction of the overall interaction forces between the tip and the sample surface, these modes do not suffer from tip or sample degradation effects that are sometimes observed after taking numerous scans with contact AFM. Unfortunately, the lateral resolution that can be reached is a few nanometers, which is lower than in the contact mode.

2.3.3.1 Non Contact AFM (NC-AFM)

In this mode the tip-sample interaction is indicated on the force-distance curve of Fig. 2.6 as the non-contact regime. Because the force between the tip and the sample in this regime is low (generally about 10^{-12} N), the force measurement is more difficult than in the contact regime, where it can be several orders of magnitude larger. Furthermore, cantilevers used for NC-AFM must be stiffer than those used for contact AFM because soft cantilevers can be pulled into contact with the sample surface. The small force values in the non-contact regime and the greater stiffness of the cantilevers used for NC-AFM are therefore both factors that limit the force resolution, and consequently the lateral resolution, that can be achieved.

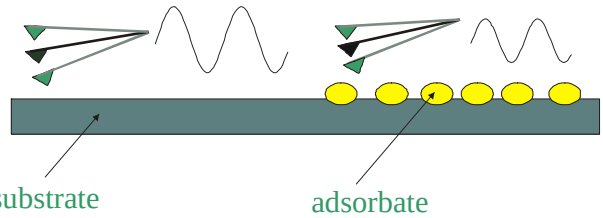

Figure 2.7: Vibrating modes: the tip-sample interaction affects the amplitude and phase of the swing.

2.3.3.2 Tapping Mode™

Tapping Mode™ (TM-AFM) or intermittent-contact atomic force microscopy (IC-AFM) is similar to NC-AFM, except that for TM-AFM the vibrating cantilever-tip is brought closer to the sample so that at the bottom of its travel it just barely hits, or "taps" the sample [Zho93, Tam96,Bus95]. The intermittent-contact operating region is indicated in the force-distance curve in Figure 2.6. Some samples are best handled using TM-AFM instead of contact or non-contact AFM. In general, it has been found that TM-AFM is more effective than NC-AFM both for imaging larger scan sizes, that may include greater variations in sample topography, and for the slightly higher resolution that can be achieved, due to the stronger tip-sample interaction forces that are sampled. The latest development of the Phase Imaging, where the gradient in phase of the vibrations is detected, made it possible to increase further the spatial resolution [Lec96,Fin97,Sto98a]. This imaging mode provides contrast caused by differences in surface adhesion and viscoelasticity; it is therefore very helpful for detecting different phases coating the sample surface.

2.3.4 Applications of AFM

Layered materials:

They represent a family of substrates which are atomically flat on a micrometer scale, and which are easy to prepare freshly by cleaving the surface with an adhesive tape.

Graphite: Highly Oriented Pyrolitic Graphite (HOPG) was the first material to be resolved with lattice resolution [Bin87]. It is commonly used as standard for the calibration of the scanner in all the 3 dimensions.

Mica: is widely used for deposition of organic and biological samples [Sha93], it is also ordinarily utilized, in place of HOPG, to calibrate scanners on a sub-nanometer scale.

Dichalcogenides are also extremely flat and suitable for studies also with STM (due to their metallic or semiconducting properties that vary with the chemical composition). Well-known examples are MoS_2 [Lie91], $NbSe_2$ [Kim91] and ReS_2 [Kel94].

Ionic Crystals:

LiF, NaCl, PbS and AgBr are some of the inorganic crystals that have been investigated achieving atomic resolution imaging [Hei92].

Organic molecules:

The structure of films prepared by the "Langmuir Blodgett" technique have been monitored for the case of barium arachidate [Bou93] and stearic acid [Chi93]. Only few studies have been carried out on single crystals, as for example tetracene [Ove91]; one reason being that this type of investigation does not give more information than a typical X-Ray analysis.

The use of SFM is more suitable for the investigation on the self-assembly of (macro)molecules adsorbed at surfaces either by vacuum sublimation [Bis95] or from solution [Sam99a]. The SFM can be also used to probe interactions between functional groups (CH_3-CH_3, COOH-CH_3, COOH-COOH) by functionalizing the SFM tip and measuring the interaction forces between the tip and the substrate [Fri94] or by breaking chemical bonds and gaining insights into the strength of different chemical interactions [Gra99].

Biological samples:

The possibility to visualize the surface of insulating biologic materials in their native physiologic environment renders this technique interesting for biophysical and biomolecular investigations. Research includes investigations on tissues, microorganisms, cells down to nucleic acid molecules and their super-hierarchical organization. An example of dynamic process that has been visualized is the Escherichia coli RNA polymerase (RNAP) transcribing two different linear double-stranded (ds) DNA templates [Kas97]. It was also possible to monitor the modification of the quaternary structure induced by bonding with an enzyme [Eri94].

3 Conjugated molecular systems

3.1 Introduction

While macromolecules and organic materials have been known for many decades [Flo53], their intrinsic conductive properties as semiconductors and metals have only be recently discovered. The report in 1977 about the high electrical conductivity of *trans*-poly(acetylene) [Chi77] that can be achieved upon *p* and *n* doping opened new avenues of exploration for chemistry and physics, and for technology. The key finding by Mac Diarmid and Heeger [Chi77] was a chemical species characterized by a delocalized π -electron system along the polymer backbone. The semiconductor properties of the materials arise from the overlap of p_z orbitals that originates from the double bonds. If the overlap is over several sites, delocalised π valence and π conduction bands occur, with a relatively small energy gap. The limitation in the firsts experiments was the chemical stability of the poly(acetylene) in air and the difficult material processing.

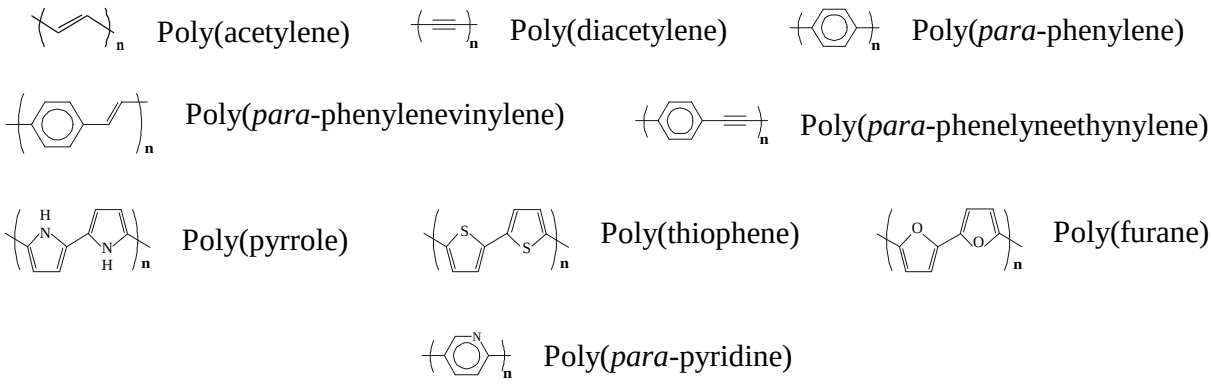

Figure 3.1: Chemical formulae of several conjugated polymers.

The synthesis of different conjugated derivatives [Bäu93, Tou96, Kra98, Mar99] allowed later to design new materials with different band gaps and electron affinities and in addition made it possible processing to be carried out under different conditions, i.e. in organic solvents, inorganic solvents and aqueous media. A step forward in the processability of conjugated

macromolecules has been made by attaching long flexible aliphatic side-chains to the conjugated skeletons, which give rise to the entropic stabilization of the polymer chain in solution [Reh89]. The polymeric species obtained have been called “hairy-rods”. They exhibit a remarkable increase in the solubility of the molecules in organic solvents, while the molecular packing in the solid state is tremendously affected. The most well-known conjugated polymers are shown in Figure 3.1.

During the last years a great deal of effort has been devoted to oligomers of conjugated macromolecules because they are good model compounds of their related polymers with respect to their electronic properties and moreover they can much more easily be handled [Mül98a]. In fact their reduced size enables them to be processed in thin films using typical techniques that until few years ago were just used for inorganic materials, like sublimation in ultra-high vacuum (UHV), known also as Molecular Beam Epitaxy (MBE). Furthermore their monodispersity makes it possible for them to self-assemble into 2D and 3D mono-crystalline structures. Typical examples of this synthetic effort are oligothiophenes [Hot93]. Other types of monodisperse systems, which are very interesting because of their high charge carrier mobilities (0.13 cm^2/Vs), are hexa-*peri*-benzocoronenes (HBC)s [Sta95b, Vdc98, Mül98b].

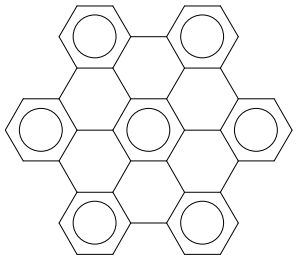

Figure 3.2: Chemical formula of hexa-*peri*-benzocoronenes (HBC).

They are nanoscale versions of an infinite 2D graphene sheet that, upon functionalization with side chains, can exhibit a good solubility in several organic solvents. HBC is just the first representative of a large family of poly-aromatic hydrocarbons that have been designed by Müllen and co-workers. Recently they have been able to extend this 2D moieties to more than 200 carbon atoms in the aromatic core [Mül98c].

3.2 Application in molecular electronics

Research on conjugated (macro)molecules is particularly appealing because of several reasons: a remarkable versatility of the materials, the possibility to build large area electro-optical devices, which have not necessarily a flat shape, their easy processability in different environments and also their low cost of production. In particular, materials based on conjugated polymers have great potential for electronic and photo-physical applications such as flat-screen displays [Wed98], light emitting electrochemical cells [Pei95], light emission devices [Bur90], organic transistors [Gar90], and solar cells [Hal95]. A breakthrough was the work of Friend and co-workers who built the first Light Emitting Diode (LED) based on a polydisperse poly(*para*-phenylenevinylene) (PPV) active layer assembled on an indium tin oxide (ITO) surface by spin coating [Bur90]; this first device exhibits quite moderate quantum efficiencies (photons emitted per electron injected), namely up to 0.05%. The work-up of these devices is strongly dependent on the interplay between electronic structure and molecular arrangement [Bäu95,Bis95]. This latter feature, as reported later in the thesis, arises from the interplay of intra-molecular as well as inter-molecular and interfacial interactions, making it possible to design very precise and reproducible 2D and 3D architectures.

A key question that has not been answered so far, is whether the charge carrier transport does occur also in the case of a single (macro)molecular chain or a well defined assembly of parallel chains. The latter would be necessary in order to insight into the role played by charge carrier hopping, which is required to transfer the charge carrier from one chain end to another. Indeed the long-term goal of the research described here is the fabrication of a molecular nanowire. A novel set-up used for probing the electronic properties of single molecules have been presented recently by Reed and co-workers [Ree97]. Their approach was based on the "Mechanically controllable break junctions" which offers a way to obtain metallic nanoelectrodes with a gap of 1-2 nm. A critical analysis of this method casts some doubts on the real molecular packing between the two metallic contacts since uncontrolled aggregations of the molecules can be expected; this affects the reproducibility of the measurements. This lack can be overcome by constructing a highly ordered molecular architecture with dimensions in the tens of nanometer scale, and to interface this well-defined assembly with Au nanoelectrodes that exhibit a gap in the same spatial range. The choice to work on these scales enables the structure of both the organic and metallic component to be

observed using Scanning Force Microscopy in every step of the device preparation.

The ideal organic moiety for producing this device should posses a good solubility in organic solvents, functional groups that can attach covalently to the Au nanoelectrodes, a high stiffness and a good conductivity along the unsaturated backbone. Good candidates that belong to the family of conjugated macromolecules are poly(*para*-phenyleneethynylene)s [Tou96, Gie96, Bun00]. They exhibit a rigid-rod structure along the conjugated backbone [Mor94, Wau96], strongly anisotropic electronic properties, an electroluminescence in the blue green-region [Tad96], and a high and stable photoluminescence quantum yield [Wed96] that made it possible to use them for the development of a liquid-crystal based photoluminescent display [Wed98]. A direct measurement of their molecular conductivity for the case of short oligomers has be carried out using Scanning Tunneling Microscope (STM) probing the average resistance of the self-assembled organic monolayers [Bum96, Dhi97].

3.3 Phenyleneethynylenes

For the project that will be discussed in detail in chapter 6, oligomeric and polymeric derivatives of *para*-phenyleneethynylenes have been synthesized with a polycondensation route by Dr. Viola Francke in the group of Prof. Dr. Klaus Müllen in the MPI for Polymer Research in Mainz within a collaborative project.

Two different types of PPE (**2**) α-iodo-ω -[(2,5-dihexyl-4-ethynyl)phenyl]-poly[(2,5-dihexylphenylene-1,4)ethynylene)] and (**6**) α-[[4-[(N,N-dimethylcarbamoyl)thio]phenyl] ethynyl]-ω-[4-[(N,N-dimethylcarbamoyl)thio]phenyl]-poly[(2,5-dihexylphenylene-1,4) ethynylene)] were synthesized by efficient Pd-catalysed coupling of the AB-monomer 4-ethynyl-2,5-dihexyliodobenzene (**1**) [Dra 98] (see Fig. 3.3). The procedure involves the coupling of the AB-monomer under $Pd(PPh_3)_4$/CuI catalysis according to Hagihara [Son75, Die75], followed by the addition of an excess of 4-[(N,N-dimethylcarbamoyl)thio]iodobenzene (**3**) as end-capping reagent. After the work-up procedure, which is necessary to remove the remaining end-capping reagent, the iodine function of the resulting α-iodo-ω-[4-[N,N-dimethylcarbamoyl)thio]phenyl]-poly[(2,5-dihexylphenylene-1,4)ethynylene] (**4**) was coupled with 4-ethynyl-[(N,N-dimethylcarbamoyl)thio]benzene (**5**) under the same conditions described above to yield (**6**).

The average contour length of the macromolecules are between 8 and 30 nanometer according to ^{1}HNMR analysis on the end groups. Furthermore, α-phenylethynyl-ω-phenyl-ter[(2,5-dihexylphenylene-1,4)ethynylene)] (**9**), has been synthesized also by efficient Pd-catalyzed coupling of 1,4-diethynyl-2,5-dihexylbenzene (**7**) with 2,5-dihexyl-4-[(trimethysilyl)ethynyl]iodobenzene (**8**) under Hagihara conditions (see Fig. 3.4).

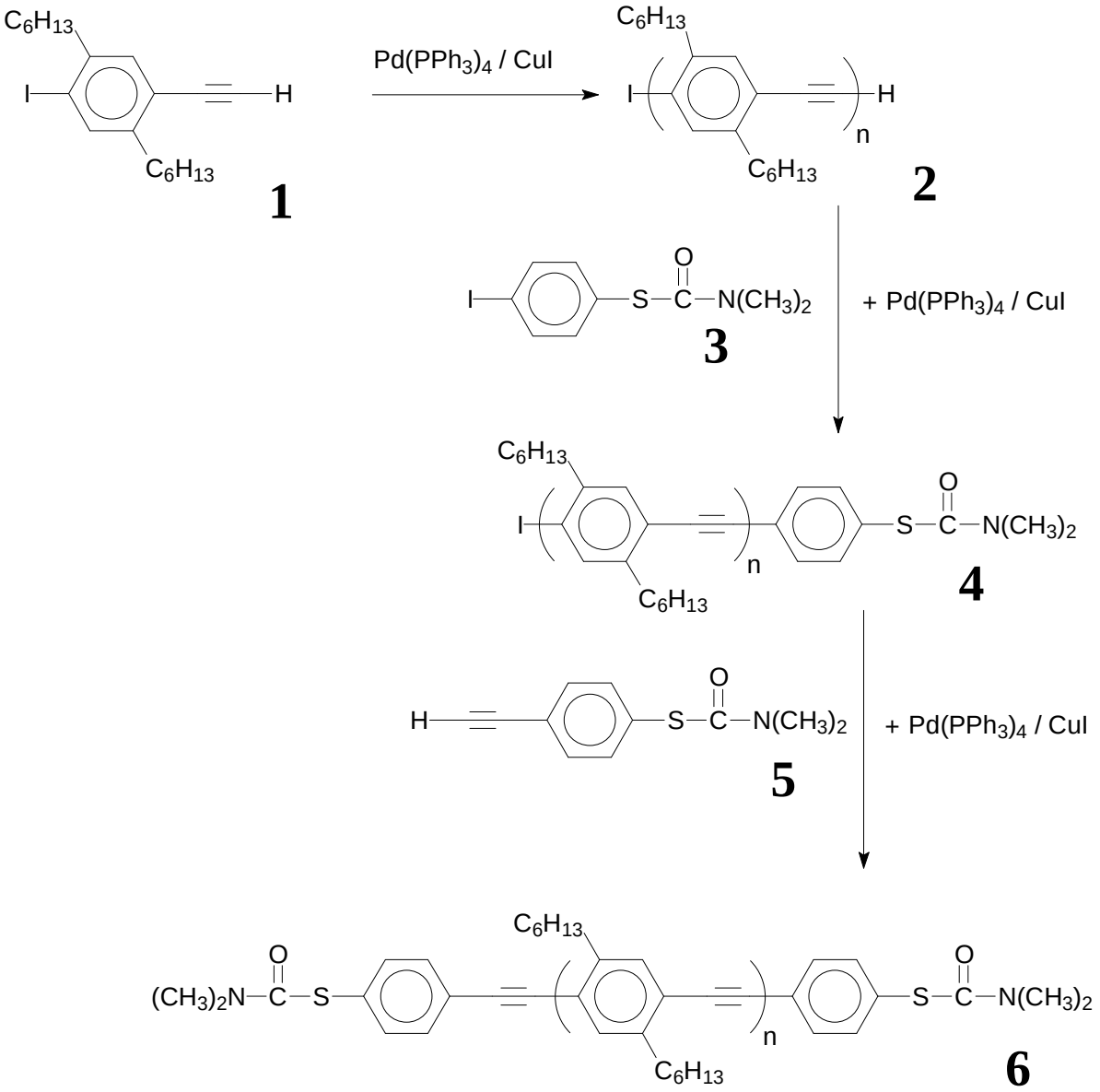

Figure 3.3: Synthesis of poly(*para*-phenyleneethynylene).

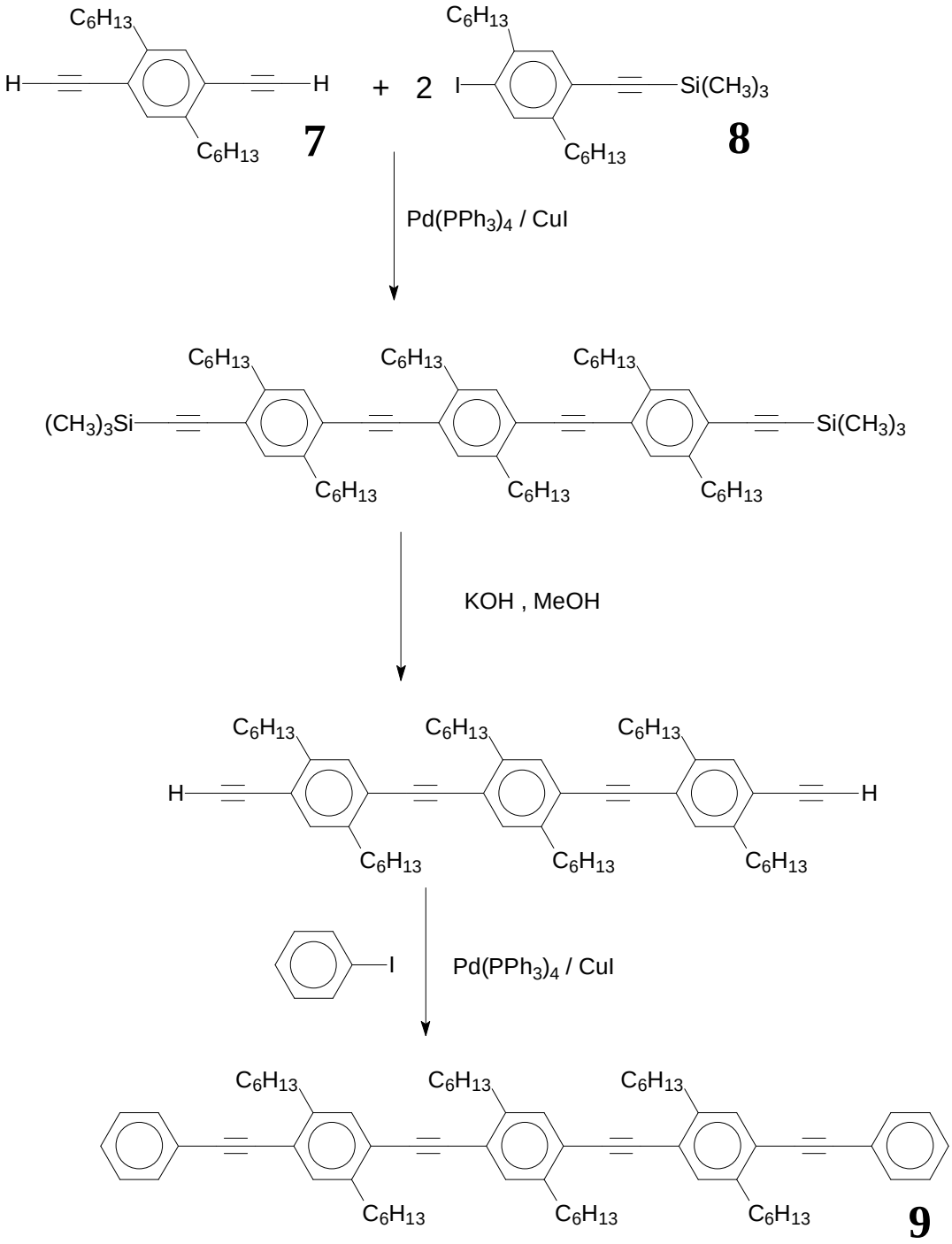

Figure 3.4: Synthesis of *para*-phenyleneethynylene trimer.

3.3.1 Kinetics of the polycondensation reaction

The synthetic route followed for producing the PPE was a polycondensation reaction. Consider the case of a general polycondensation reaction A+B→ C+D [Bra89], which is characterized by a kinetic of the second order $-\frac{d[A]}{dt} = \frac{d[C]}{dt} = k[A][B]$. In the present case

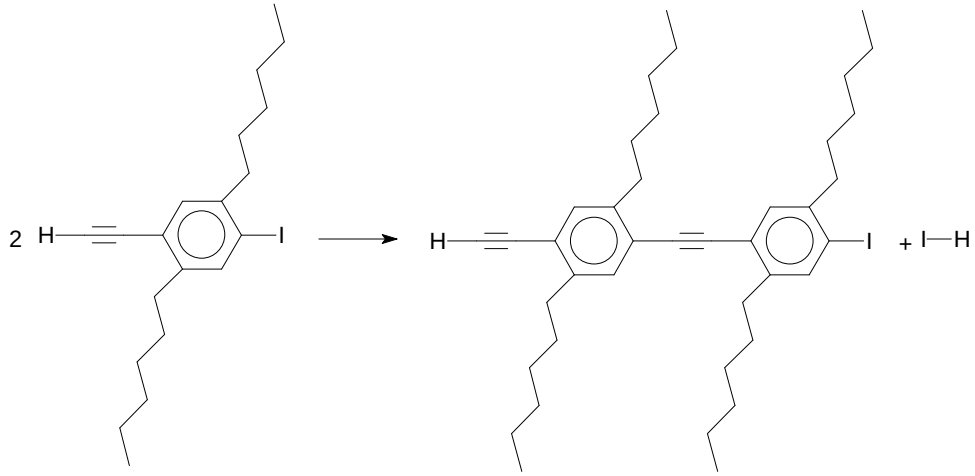

A=B and the reaction is:

Since [A]=[B], then $-\frac{d[A]}{[A]^2} = kdt$, which means that $-\int_{c_0}^{c}\frac{d[A]}{[A]^2} = \int_{0}^{t} kdt \Rightarrow \frac{1}{[A]} - \frac{1}{[A]_0} = kt$

where: k = reaction constant;

t = time;

$[A]_0$ = initial concentration;

[A] = concentration at time t;

p = fraction of functional groups initially present that reacted at time t.

It is known that: $[A]=(1-p)[A]_0$ and so we have $\frac{1}{[A]_0}\left(\frac{1}{1-p} - 1\right) = kt$

3.3.2 Molecular weight distribution

Macromolecules can be classified into 2 different classes:

Monodisperse: Single definite molar mass (used also as an approximation for polymers when $U \leq 0.1$, see below).

Polydisperse: Sample is a mixture of molecules with various chain lengths (typical of polymers that usually have $U \approx 2$).

The distribution of molecular masses can be described by means of several parameters:

1) The arithmetic average: the *Number Average Molar Mass*:

$$\overline{M_n} = \frac{1}{N}\sum_i N_i M_i \qquad (3.1)$$

where N= total number of molecules

N_i = number of molecules with molar mass M_i

2) The weight average: the *Mass Average Molar Mass*:

$$\overline{M_w} = \frac{1}{m}\sum_i m_i M_i \qquad (3.2)$$

where m = total mass of the sample

m_i = total mass of molecules of molar mass M_i

3) The width of the distribution can be expressed in terms of the *Polydispersity*:

$$U = \frac{\overline{M_w}}{\overline{M_n}} - 1 \qquad (3.3)$$

The full distribution functions can be expressed as normalized *mole fraction distribution* F(r), that is the fraction of molecules of size *r:*

$$\sum_1^\infty F(r) = \int_0^\infty F(r)dr = 1 \qquad (3.4)$$

Alternatively one may use the *weight fraction distribution*:

$$W(r) = \frac{rF(r)}{\sum_{1}^{\infty} rF(r)} = \frac{rF(r)}{\int_{0}^{\infty} rF(r)dr} \qquad (3.5)$$

The average number of structural units or repeat units in the molecule is the *Number average degree of polymerization*:

$$\overline{r_n} = \frac{\sum_{1}^{\infty} rF(r)}{\sum_{1}^{\infty} F(r)} = \frac{\sum_{1}^{\infty} W(r)}{\sum_{1}^{\infty} \left[W(r)/r\right]} \qquad (3.6)$$

therefore: $W(r) = rF(r)/\overline{r_n}$

The is related to the number average molar mass by: $\overline{r_n} = \overline{M_n}/M_{r.u.}$

Where $M_{r.u.}$ is the molar mass of a repeat unit

In the case of the polycondensation synthesis, the distribution of molecular weights is according to one of the following theoretical functions that describe particular cases:

3.3.2.1 Schulz-Zimm distribution

Mole fraction distribution:

$$F(r) = y^k r^{k-1} \frac{e^{-yr}}{\Gamma(k)} \qquad (3.7)$$

where:

k is the degree of coupling (i.e. the number of independently growing chains required to form one dead chain) and gives the curve shape. Moreover $k = \frac{1}{U}$

In the present case *k* =2 as for a standard linear polymerization reaction. Therefore the expected polydispersity, assumed in the Schulz-Zimm function, is $U = \frac{1}{k} = 0.5$.

$y = \frac{k}{\overline{r_n}}$ where $\overline{r_n}$ is the number average degree of polymerization.

G(k) is the gamma function: $\Gamma(x) = (x-1)\cdot\Gamma(x-1)$: for k=2 $\Rightarrow \Gamma(k) = 1$

Weight fraction distribution:

$$W(r) = y^{k+1} r^k \left[\exp(-yr)\right] / \Gamma(k+1) \qquad (3.8)$$

Number average degree of polymerization:

$$\overline{r_n} = \frac{\Gamma(k+1)}{y\Gamma(k)} \qquad (3.9)$$

(this parameter could be measured by means of Gel Permeation Chromatography investigations or elemental analysis (C,H)).

For *k*=1: this distribution reduces to the Schulz-Flory distribution (see below).

k = large values: this distribution approximates the Poisson distribution (see below).

3.3.2.2 Schulz-Flory distribution

Known also as "Most Probable Distribution".

Number Average Molar Mass:

$$\overline{M_n} = \frac{M_0}{1-p} \qquad (3.10)$$

where M_0 = mean molecular weight for a structural unit

Mole fraction distribution:

$$F(r) = p^{r-1}(1-p) \qquad (3.11)$$

where *p* = a real number less than 1, indicating the extent to which the reaction goes to, or as the probability that A reacts with B;

r = number of reacted monomers = number of repeating units in the polymer.

Weight fraction distribution:

$$W = r(1-p)^2 p^{r-1} \qquad (3.12)$$

Number average degree of polymerization:

$$\overline{r_n} = \frac{1}{1-p} \qquad (3.13)$$

3.3.2.3 Poisson Distribution

Mole fraction distribution:

$$F(r) = e^{-n} \frac{n^{r-1}}{(r-1)!} \qquad (3.14)$$

where n = mean main chain length

r = number of reacted monomers = number of repeating units in the polymer

Weight fraction distribution:

$$W(r) = \left[\frac{n}{n+1}\right] r e^{-n} \cdot \frac{n^{r-2}}{(r-1)!} \qquad (3.15)$$

Number average degree of polymerization:

$$\overline{r_n} = 1 + n \qquad (3.16)$$

The Schulz-Flory distribution is commonly used for low degrees of polymerization and Schulz-Zimm for high ones.

3.4 Hexa-*peri*-hexabenzocoronenes

Hexa-*peri*-benzocoronenes (HBC)s are a good candidate to build-up columnar aggregates on Highly Oriented Pyrolytic Graphite (HOPG) where the disc like molecules are packed with a high degree of order thanks to π–π interactions as displayed in Fig.3.5 [Vdc98]. In this case the tip of the STM could be used to gain insight into the conductivity along one column.

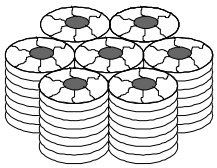

Figure 3.5: Columnar stacking of HBC-C_{12}.

Previous explorations at the solid-liquid interface on the soluble HBC-C_{12} with STM have shown that the molecules tend to lie flat on the basal plane of a conductive HOPG substrate. In addition with Scanning Tunneling Spectroscopy (STS) is was possible to detect a diode-like electrical behavior of the aromatic cores while the aliphatic part of the molecules has exhibited a symmetric current vs. voltage (I-V) curve [Sta95b].

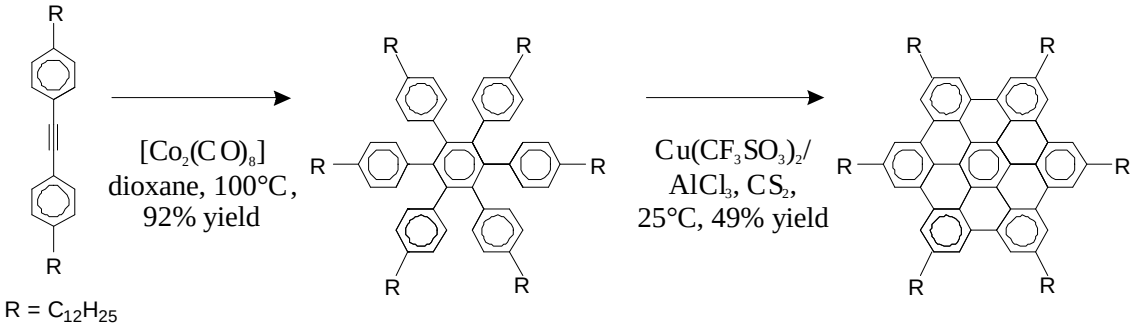

Figure 3.6: Synthesis of HBC-C_{12}.

The synthesis of HBC-C_{12} has been performed by Dr. Johan D. Brand in the group of Prof. Dr. Klaus Müllen (MPI-Mainz) (Fig. 3.6).

4 Self-assembly of molecules at surfaces and nanoelectrode fabrication

Making use of intramolecular, intermolecular and interfacial forces it is possible to design highly ordered 2D and 3D polymolecular architectures. A precise control of the molecular self-assembly both from solutions and from vacuum depositions can be obtained on such substrates that posses well defined chemical functionalities and physical properties [Ulm91]. A first requirement for a highly reproducible modification of a surface is a good flatness of the support. Because of this reasons it is worthwhile to put effort on the selection and careful preparation of the substrate. Then, atoms and molecules can attach to surfaces in two different ways: by means of *physisorption* (physical adsorption) or *chemisorption* (chemical adsorption).

4.1 Physisorption

The physisorption is the adsorption of molecules at surfaces which is characterized by the absence of a formation of a chemical bond both between molecule-molecule and molecule-substrate. It arises from the interplay of weak attraction forces (predominantly van der Waals and electrostatic which exist over long ranges) and hard core repulsions. Physisorption is an exothermic process; its enthalpy can be measured by monitoring the rise in temperature of a sample of known heat capacity during the adsorption or by investigating the thermal programmed desorption of the adsorbate. A typical enthalpy of physisorption is about 20 kJ/mol [Atk94]. This small enthalpy change is insufficient to lead to bond breaking, so a physisorbed molecule retains its identity, although it could be distorted by the surface.

Molecular organization in the case of physisorption is governed by intra-molecular, intermolecular and interfacial interactions, which may be described by the following potential:

$$V = \sum_{bonds} f_r \left(r - r_{eq}\right)^2 + \sum_{angles} f_d \left(d - d_{eq}\right)^2 + \sum_{dihedral} f_n \{1 + \cos(n f - g)\}$$
$$+ \sum_{i<j} \sqrt{\in_i \in_j} \left\{ \left(\frac{s_i + s_j}{r_{ij}} \right)^{12} - 2 \left(\frac{s_i + s_j}{r_{ij}} \right)^{6} \right\} + \sum_{i<j} \frac{q_i q_j}{r_{ij}} + \sum_i V_{surf}(r_i)$$

Formulae 4.1: Physisorption of a molecule at surface [Hen93].

The first three terms in formula 4.1 describe the intramolecular forces, while the next two are intermolecular contributions to the overall interactions, and the last one describes the interfacial forces. The terms are respectively related to bond stretching, valence angle vibrations, torsional vibration, Lennard-Jones, Coulombic interactions and external static potential due to the surface acting on the adsorbate.

Besides, several experimental studies carried out in the recent past on the molecular physisorption at surfaces revealed distinctly different adsorbate arrangements on the molecular level when using *conductive* and *insulating substrates*.

4.1.1 Conductive substrate

Conjugated molecules tend to self-assemble into layers lying flat on the basal plane of conductive substrates, such as HOPG, dichalcogenides, Au or Ag surfaces. This is behavior, which is true mainly for molecular films with a nominal thickness of maximum a few monolayers, is due to a rehybridization of orbitals of the adsorbate with those of the substrate that exhibit metallic or semiconducting properties [Bis00]. Examples include several adsorbates at the interface between a liquid and the basal plane of on HOPG, namely oligomeric liquid crystals [Fos88, Smi89, Spo89], alkanes, alcohols [Rab91a], oligothiophenes [Bäu95], hexakis-dodecyl-hexabenzocoronene [Sta95b], diacetylenes [Rab93], isophthalic acids [Eic96], anthrone derivatives [Sta95c]; this tendency have been also detected on dried films prepared both by solution casting (dendronized poly(*para*-phenylene)s [Sto98a] and poly(styrene)s [Sto98b]) and by UHV sublimation (perylene derivatives [Lud94]). A similar arrangement have been detected also on dichalcogenides (alkanes [Cin93] and perylene derivatives [Lud94]), on Au (oligothiophenes [Buo96] and porphyrins [Jun97]), on Ag (oligothiophenes [Sou96] and porphyrins [Jun97]), on Cu

(phthalocyanines [Lip89] and porphyrins [Jun97]) and on Pt (naphtalenes [Hal91]).

4.1.2 Insulating substrates

Chain molecules usually do not lie flat on the insulating substrates. The main chain tends to stand on the basal plane of the non conductive support being sometimes oriented perpendicular to it. This has been observed for mica substrates (oligothiophenes [Bis95]) and for SiO_2 (polymeric liquid crystals [Vix98] and oligothiophenes [Ser93]). This molecular arrangement is therefore characterized by a weak coupling with the substrate.

4.2 Chemisorption

The chemisorption is the adsorption of molecules at surfaces which is characterized by the formation of a chemical bond between molecule and surface; in this type of adsorption the molecules tend to find sites that maximize their coordination number with the substrate. The enthalpy of chemisorption is bigger than that for physisorption, and amounts typically to ca. 200 kJ/mol [Atk94]. Chemisorption is commonly used to generate a well defined, tightly packed molecular structure that coats a surface uniformly. The film resulting is a so called Self-Assembled Monolayer (SAM). It can be formed spontaneously by the immersion of an appropriate substrate into a dilute solution of an active surfactant in an organic solvent or by sublimation of the molecular adlayer in vacuum. There are several types of SAMs that have been created. These include organosilicon on oxidized surfaces (SiO_2, Al_2O_3), alkanethiols on Au, Ag, Cu, Pt; dialkyl sulfides and disulfides on Au; alcohols and amines on Pt; carboxylic acids on Al_2O_3 and Ag [Ulm91].

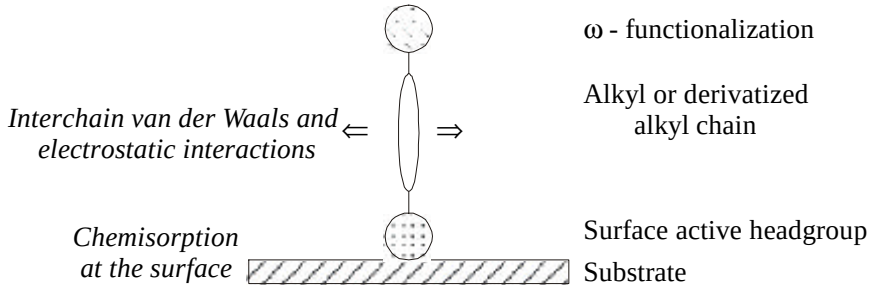

Figure 4.1: Chemisorption reaction of a surfactant on a substrate.

A self-assembling surfactant molecule is typically composed of 3 parts (Fig. 4.1):

1) head group: it provides the chemisorption to the substrate (exothermic process). The very strong molecule-substrate interactions result in a pinning of the head group to a specific site on the surface through a chemical bond. This can be:

- covalent (e.g. in Si-O-Si for alkyltrichlorosilanes on oxidized surfaces);
- covalent and slightly polar (e.g. in Au-S for alkanethiols on gold;)
- ionic (e.g. in $-CO_2^-Ag^+$ in the case of carboxylic acids on AgO/Ag).

As a result of the exothermic head group - substrate interaction, molecules try to occupy every available binding site on the surface, and in this process molecules that have been already adsorbed tend to pack one beside the other. Therefore, often a crystalline assembly is formed upon annealing.

2) alkyl chain: it plays an important role in the packing at surfaces because when the distance between adjacent molecules is so small that short-range, dispersive, London-type, van der Waals forces become effective molecules tend to reorganize due to these interactions between the alkyl chains. When the alkyl chain is substituted with a polar bulky function there are also long-range interactions that sometimes are energetically predominant.

3) ω–functionalization: the ω function can be such that it opens the possibility of successive adsorptions (anchoring) or chemical reactions (like the photopolymerization of diacetylenes [Kim96]).

The most studied case, as previously mentioned, is the one of thiol functionalized molecules self-assembled on a Au(111) surface [Del96, Poi97]. The rate of the chemisorption from solution is such that it can occur on a 20 hours time scale. A faster adsorption can be obtained on an Ag substrate, which, however, has the disadvantage of getting oxidized easily in air environment. Nevertheless reproducible SAMs on Ag(111) have been developed and compared to Au(111): they exhibit the advantage that the aliphatic chains pack perpendicular to the substrate whereas for Au(111) they prefer to assemble at 30° from the normal [Hei95]. This causes the packing of alkanethiols to be more tight for silver than for gold.

4.3 Metallic nanoelectrodes for a molecular nanowire device

The electronic properties or the conductivity of single molecules or of a small *ensemble* of molecules can be elucidated by making use of 2 different types of contacts (Fig 4.2).

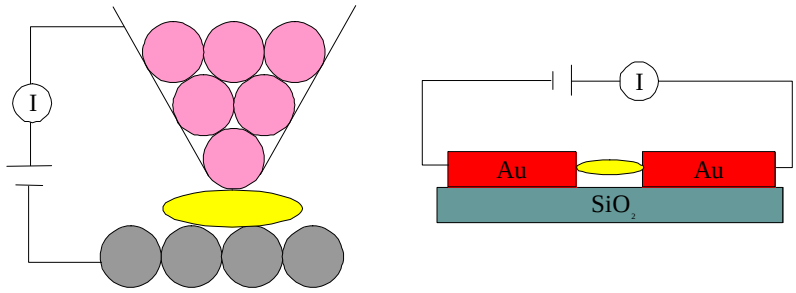

A) **STM junction** B) **Nanoelectrodes**

Figure 4.2: Junctions for probing electronic properties of a single molecule or molecular object.

In the first case (A) the STM set-up is used to measure the conductivity of a molecule or a molecular aggregate. The measurement can be performed by imaging the current at constant height and voltage if the adsorbate exhibits a high degree of order, like in the case of a SAM [Hei95]. Alternatively one my perform a spectroscopical study on single molecules (STS) [Sta95b]. In the latter case (B), one requires a particular test sample: one molecule or a well defined array of molecules assembled between two Au nanoelectrodes.

One method that can be used to produce gold nanoelectrodes is Electron Beam Lithography (EBL). It utilizes the fact that certain chemicals change their properties when irradiated with electrons just as a photographic film does when irradiated with light. The electron beam is generated in a Scanning Electron Microscope which normally is set up to provide an image of an object by rastering with a well focused beam of electrons over it.

Collecting electrons that are scattered or emanated from that object for each raster point provides an image. With computer control of the position of the electron beam it is possible to write arbitrary structures onto a surface. The steps to produce a structure by EBL are shown below: the sample is covered with a thin layer of poly(methylmetacrylate) (PMMA), then the desired structure is exposed with a certain dose of electrons. The exposed PMMA changes its solubility towards certain chemicals. This can be used to produce a trench in the thin layer. If one wants to produce a metallic structure, a metallic film is evaporated onto the sample and after dissolving the unexposed PMMA with its cover (lift-off) the desired metallic nanostructure remains on the substrate. This method, shown in Fig. 4.3, allows gaps to be

engineered down to the 10 nanometer regime [Bez97a, Bez97b, Her98]. This gap might be bridged by the molecular aggregate. This would enable to relate the electronic properties of the object to its order on a molecular scale. The resulting 10-20 nm gap can be visualized with SFM.

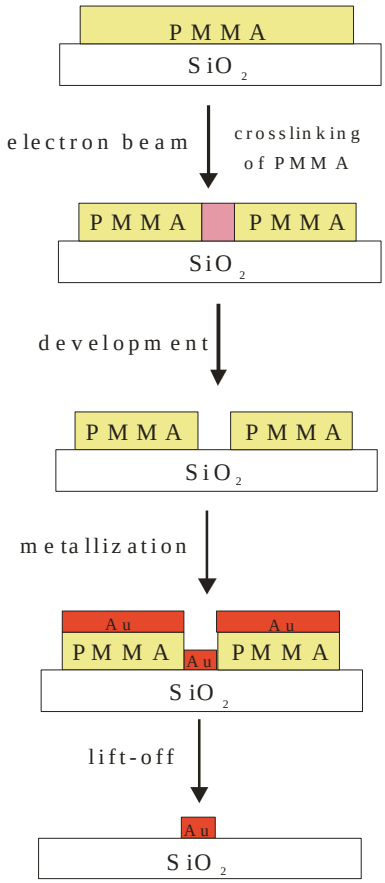

Figure. 4.3: Scheme of the e-beam lithography procedure used for producing Au nanogaps.

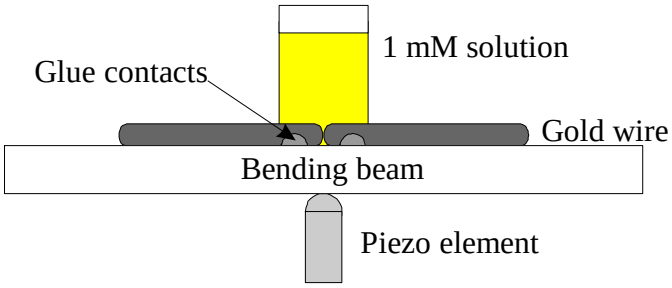

Figure 4.4: Method for developing " Mechanically controllable break junctions".

Another procedure for developing metallic nano-contacts, the so called "Mechanically

controllable break junctions" [Ree97] (see also chapter 3) provides metallic nanoprobes with a gap of 1-2 nm. The production is based on a fracture of a Au wire that takes place upon applying pressure on it with a piezoelectric crystal (Fig. 4.4). Unfortunately, in my opinion, the reproducibility of these type of gaps is rather poor. The procedure includes molecular self-assembly that is carried out bathing the filament during the breakage with a solution of benzene-1,4 dithiol. A successive relaxation of the pressure induced by the piezo cause the two probes to approach each other again. The authors claim that the nanoprobes are separated by an organic monolayer of self-assembled molecules and current vs. voltage characterization of the system gives insight into the conductivity of the monolayer, thus of the single molecules.

5 Experimental procedures

In this chapter the experimental methodologies which are used for the work presented below are discussed. The chapter is divided into 5 paragraphs:

- Preparation of the substrates
- Scanning Tunneling Microscopy (STM);
- Scanning Force Microscopy (SFM);
- Ultra-violet Photoelectron Spectroscopy (UPS), X-ray Photoelectron Spectroscopy (XPS);
- Current vs. Voltage (IV) measurements.

5.1 Preparation of the substrates

The preparation of the substrate plays a key role for the self-assembly of molecules at surfaces. In order to obtain highly reproducible results, very flat substrates with precisely controlled chemical functionalities, freshly prepared just before the chemical deposition, have been used.

5.1.1 Layered substrates

Layered substrates are widely utilized for the adsorption of the organic materials and SPM studies.

For the present investigations two different commercially available supports were chosen:

- Muscovite mica (Plano GmbH);
- Highly Oriented Pyrolitic Graphite (HOPG) (grade ZYB, Advanced Ceramics, Cleveland, Ohio, U.S.A.).

Both of them can be easily cleaved with adhesive tape. The ease and reproducibility of the sample preparation as well as the chemical inertness and the atomical flatness on the

micrometer scale that can be achieved, render this type of preparation commonly used for Scanning Probe Microscopy investigations of physisorbed samples.

Muscovite mica has been used widely as support for both self-assembly of molecules from solutions and sublimation of a metallic layer in high-vacuum (HV). Slices, 120 μm thick, were cut into discs of variable sizes with a punch and die set (Precision Brand, Downers Grove, Illinois U.S.A.) to maintain nicely cleavable edges.

HOPG was used for STM studied at the solid-liquid interface and also as conductive support for producing dry layers of HBC-C_{12} from solution.

5.1.2 Amorphous substrates

Non-crystalline insulating substrates have been also utilized for understanding the role of the crystallinity of the support (mica) in the growth of PPE from solution. Thin glass discs (120 μm thick and with a diameter of 1 cm) have been first cleaned at 60°C for twice 5 minutes in trichloroethylene, acetone and ethanol respectively. Then they have been rinsed with deionized H_2O (Milli-Q) and dried with a gentle blow of N_2.

In addition for the TEM investigations of PPE thin films 400-mesh carbon coated copper grids have been utilized as amorphous substrates.

5.1.3 Metallic substrates

Metallic substrates are useful supports for self-assembly and in particular for chemisorptions. They can be produced by sublimation in HV with a chamber pressure of ~ 10^{-6} mbar or in ultra high-vacuum (UHV) with a pressure of < 10^{-9} mbar. The goal of this kind of preparation is to obtain an epitaxial or pseudo-epitaxial substrate that exhibits a very high flatness. In collaboration with Dr. P. Thiele (Department of Physics, Humboldt University Berlin) thin films of Ag and Au have been sublimed onto freshly cleaved mica discs in HV at a chamber pressure of ~ 10^{-5} - 10^{-7} mbar [Chi88]. The temperature of the substrate during the sublimation and the nominal thickness of the metallic adlayer (between 50 and 200 nm) were varied systematically in order to find conditions yielding a pseudo epitaxial film. The

nominal thickness of the sublimed film was detected with a quartz oscillator that was calibrated according to the Au or Ag parameters. The temperature of the substrate during the sublimation was measured with a thermocouple that was placed on the edge of the surface that was got coated. Inside the vacuum chamber the crucible and the substrate holder have got two separate heating systems. For the case of silver, since its surface gets oxidized very rapidly, some precautions have been taken too minimize its contact with air: after the sublimation, the vacuum chamber was vented to room pressure with an argon flow and as soon as the chamber was open, the films were immersed in organic solutions that were also under Ar reflux. On the other hand, in order to increase the epitaxiality of the Au surfaces prepared by sublimation, post annealing (followed by quenching in EtOH or millipore H_2O saturated with N_2) has been applied to the 200 nm thick metallic films. This post treatment has been carried out both by flame annealing and shock annealing with an halogen lamp from the front and from the rear side of the sample. The temperatures during all these processes cannot be easily determined but are more likely within a range of 500-600 °C; the duration of the process is about one second. STM imaging has been used to characterize the film structures, in particular their roughnesses, on a micrometer scale.

5.1.3.1 Template Stripped Gold

Alternatively, in collaboration with Dr. J. Diebel (from the group of Dr. H. Löwe, Institute of Microtechnology Mainz) we have designed a method to grow Template Stripped Gold (TSG) substrates. The sample preparation scheme is shown in Fig. 5.1. [Sam99b]

A 200 nm thick gold film has been evaporated in high-vacuum (~ 10^{-6} mbar) onto freshly cleaved muscovite mica kept at a T=300 °C. Subsequently a layer of Ni of about 200 μm was electroplated on the free Au surface. A rubber ring was then attached to the upper Ni surface. At this point the mica can be easily stripped off mechanically by pulling the rubber ring with tweezers. The Au/Ni film was immersed with the gold face up into a 3.5 mM solution of undecanthiol ($CH_3(CH_2)_{10}SH$) (Lancaster) or nonanthiol ($CH_3(CH_2)_8SH$) (Aldrich) in methanol or benzene and left for 20 hours. The chemisorbed adlayer after immersion was rinsed several times with the same solvent and blown dry under a gentle flow of Ar or N_2.

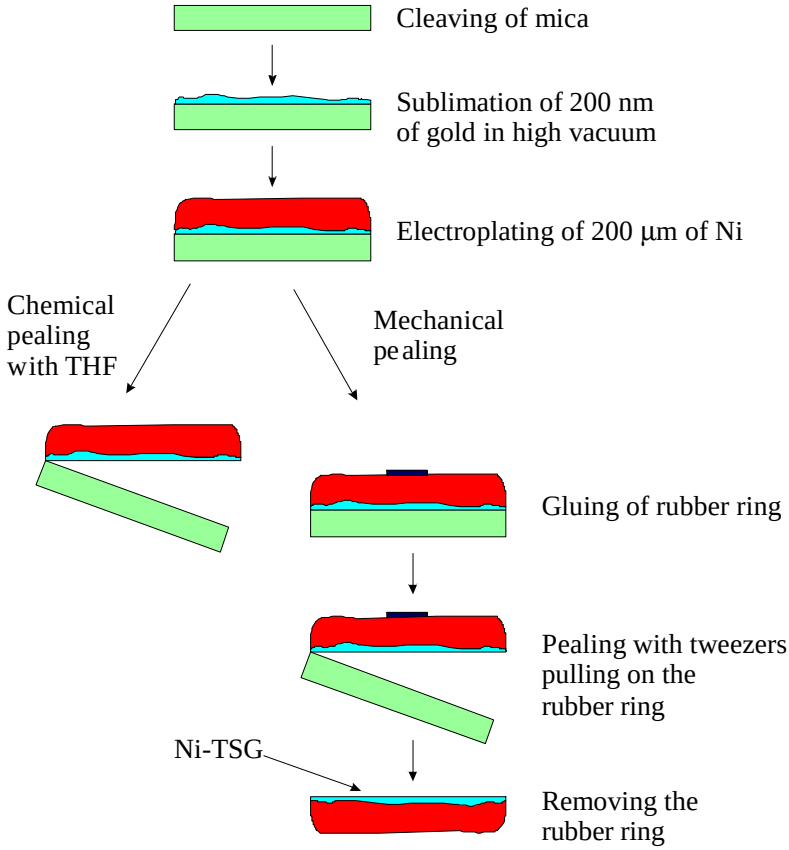

Figure 5.1: Schematic representation of the Ni-TSG preparation

5.2 Scanning Tunneling Microscopy

5.2.1 Apparatus

STM investigations have been carried out using a home-made STM interfaced to Omicron Electronics (Omicron Vakuumphysik GmbH,Taunusstein,Germany). This apparatus, was built by Dr. P. E. Hillner (group of Prof. Dr. J. P. Rabe, Department of Physics, Humboldt University Berlin) according to the Besocke beetle-type design (Fig. 5.2) [Bes87, Bes88, Fro89]. Four identical piezoelectric legs expand and contract with temperature at the same rate. Three of these legs are placed at the edges of an equilateral triangle and behave as the "feet" of the STM head and the fourth leg in the middle ends with the STM tip. The sample holder (Fig 5.3) is a equilateral triangle of either glass or quartz at whose 3 edges steel discs have been glued. The sample is also glued at the center of the triangle and silver paint was used to make the contact with the back foot.

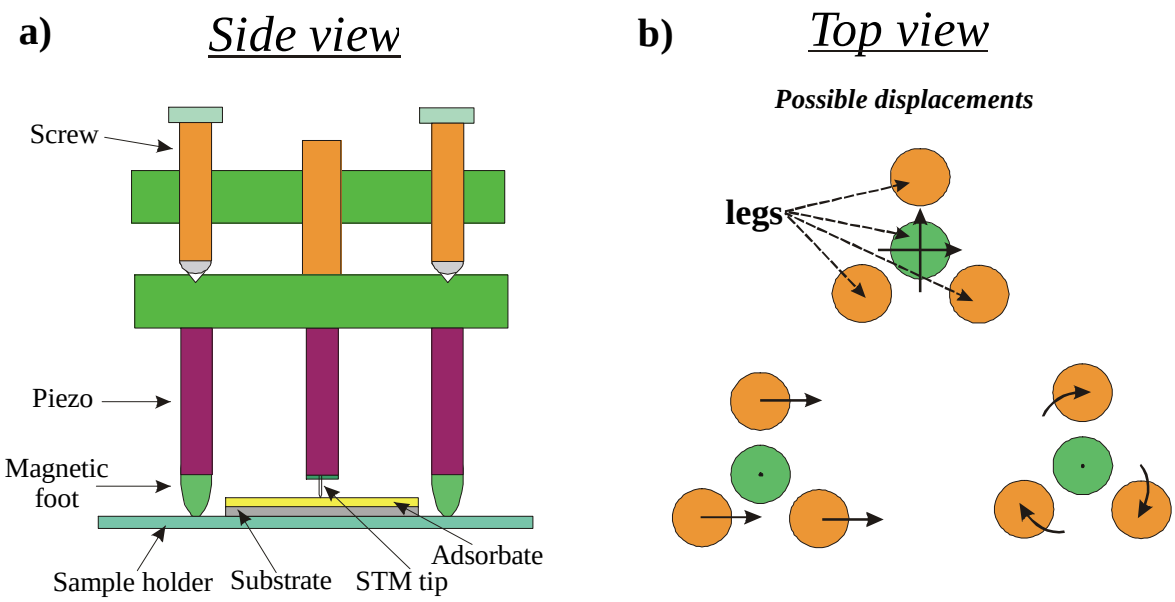

Figure 5.2: Scheme of the STM set-up: a) Side view of the apparatus; b) Top view of the piezo system: possible displacements in which the drift minimized.

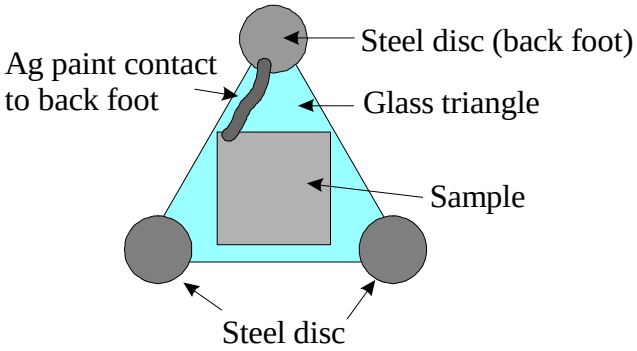

Figure 5.3: Scheme of the sample holder.

Two additional features make of this home made apparatus ideal for the investigation of organic adsorbates:

1. the possibility to detect currents down to 8 pA; this is very important for imaging materials with a large resistivity, such as organic films;
2. the possibility to achieve rather high scan rates (200 Hz/line); this is essential since the mobility of molecules and molecular clusters at surfaces can be quite high.

The microscope is supplied with a piezo system that allowed to do investigations that span from a 5 μm scan length to the nm scale.

5.2.2 Tip preparation

Pt/Ir (80:20) wire has been selected as material because it is chemically stable in air and sufficiently stiff.

A 0.25 mm wire has been electrochemically etched in a solution of 2N KOH + 6N NaCN. Keeping the voltage constant at 6-10 V (50 Hz, alternate current) the etching takes place as long as the current through the wire is bigger than 40 mA. At this threshold the voltage gets interrupted automatically. The tip is then rinsed with Millipore water and dried with a gentle flux of Ar or N_2. This recipe leads to reproducible atomically sharp stable metallic needles ready to be used [Mel91, Wei95].

5.2.3 Vibration isolation

The STM is placed on a "bungy" cord set-up, which consists of a large mass, M, attached to bungy cords (four total, one in each corner in our configuration), firmly anchored to the building ceiling (Fig. 5.4) [Par87].

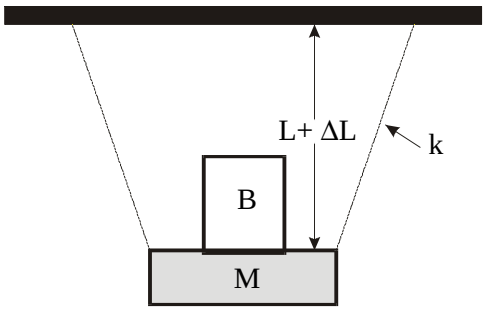

Figure 5.4: Scheme of the bungy set-up.

The equation of motion governing the movement of the AFM in a box, B, if the one of a damped harmonic oscillator, with the solution

$$z = z_0 \cos(w_0 t) \cdot e^{-t/t}$$

where:

z is the vertical deflection away from equilibrium;

z_o is the maximum deviation from equilibrium;

ω_o is the angular resonance frequency of the mass;

τ is the damping time constant of the bungy cord.

For our system, the bungy cords have a length of L = 0.7 m and a diameter of 6 mm. They are attached to a granite slab with a mass of about M = 50 kg. The mass extends the length of the bungy by about ΔL=0.8 m. From this extension of the bungy cord we can determine its spring constant, k=Mg/ΔL ~ 600 N/m and the resonance frequency $n_0 = \frac{1}{2p}\sqrt{\frac{k}{m}} = \frac{1}{2p}\sqrt{\frac{g}{\Delta L}}$ ~ 0.5 Hz $\Rightarrow$ k=100 N/m

Noteworthy, the resonance frequency can be independent of the mass M, depending only on the stretch of the bungy [2]. The damping of the oscillation can be attributed to rubbing of the rubber fibers inside of the bungy cord against the outside lining material. Ideally one seeks a high damping situation, that is, where τ~1 second. This can be optimized (damping can be enhanced) by greater weight on the bungy cords up to a point before plastic deformation of the bungy material, after which it is no longer useful for vibration isolation. Since, this will also lead to a shortened life of the cords, care must be taken to support the mass when the system is not in operation.

Box B (Fig. 5.4) is an environmental control chamber that completely engulfs the microscope. Such a box enables the user to remove all moisture from the microscope by fluxing inert gases through the chamber. Between the low resonance frequency of the bungy cord system and the high resonance frequency of the microscope head (> 10 kHz), the SPM effectively comprises a band pass filter. This allowed us to safely image samples in the intermediate range of about 1-100 Hz and achieve atomic resolution.

5.2.4 STM on dry films

The STM set-up can be used to investigate the morphology and the structure of a thin dry organic film. The essential requirement is a sufficiently low thickness of the non-conductive organic layer. Using the apparatus described above, the morphology and structure of metallic films (Au, Ag, TSG) has been studied before and after chemisorption. In the latter case the tunneling parameters have to be selected in order not to damage the adsorbate (Fig 5.5).

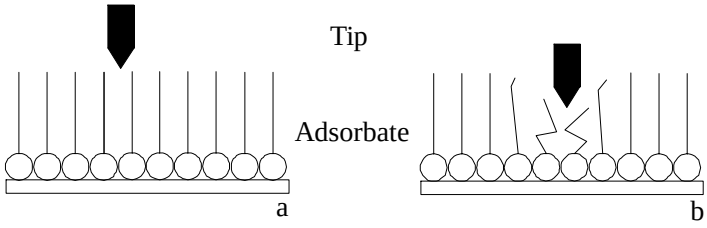

Figure 5.5: STM measurement of a dry film. a) suitable tunneling parameters; b) invasive mode due to inappropriate parameters (too low resistance set-point).

The SAMs grown on TSG have been imaged first on a large (micrometer) scale in order to select a flat crystallite; then zooming in on a terrace, it was tried to resolve the molecular packing on a sub-nanometer scale. Typical scan rates were 1-3 Hz per line for topographical images (constant current mode) on the micrometer scale and 50-200 Hz for molecular imaging on a sub-nanometer scale (constant height mode).

5.2.4.1 SAMs of saturated alk*a*nethiols

SAMs of fully saturated commercial alk*a*nethiols have been produced on several surfaces of Ag(111) and Au (111), which were prepared as previously presented in this chapter. 1 mM solutions in ethanol (EtOH) or benzene have been prepared and the fresh surfaces of the metallic supports have been immersed face up in the organic solution for ~1-3 hours for the case of Ag and ~18-24 hours for the case of Au. After this, the coated surface was rinsed several times with the pure solvent and dried using a gentle flux of N_2 or Ar. Subsequently the samples have been investigated with STM.

5.2.4.2 SAMs of unsaturated alk*e*nethiols and mixtures

In collaboration with Dr A. Wei (group of Prof. Dr. J. -M. Lehn, Univ. Strasbourg) alk*e*nethiols and mixtures of alk*a*nethiols and alk*e*nethiols have self-assembled on metallic surfaces.

In all cases concentrated organic solutions were received frozen and have been defrozen just before use. Although they did not show any insoluble particles floating in the solutions, they have been passed through a disposable membrane filter and diluted. Both the solutions and the assembled films have been stored in the dark.

Four types of experiments have been carried out:

1) Ag (111) films (substrate temperature (T_{sub})=275 °C and nominal thickness of the metallic film (Z=50 nm)) have been immersed for 6 hours in different ratios of saturated/unsaturated C_9 , C_{11} , C_{12} chains in 5mM solutions in benzene, where in C_n *n* is the number of carbons on the main chain.

2) Ag (111) films (T_{sub}=275 °C and Z=50 nm) have been immersed for 1 hour and 6 hours in different ratios of saturated/unsaturated C_9 , C_{11} , C_{12} chains in 1mM solutions in benzene;

3) TSG and sublimed Au have been immersed for 22 hours in different ratios of saturated/unsaturated C_{11} chains in 0.66 mM or 2 mM solutions in benzene;

4) sublimed Au surfaces have been immersed for 22 hours in different ratios of saturated/unsaturated C_{11} chains in 0.66 mM or 2 mM solutions in benzene.

5.2.5 Investigations at the solid-liquid interface

The STM set-up can be used to perform investigations at the interface between a solid conductive substrate, like HOPG, and an almost saturated organic solution (Fig. 5.6) [Rab91a].

The proper selection of the tunneling parameters, tunneling current, I_t (~1 nA), and voltage between tip-sample, U_t (~1V), allows to control the distance tip-sample and therefore to

choose to image only the first layer physisorbed on HOPG. By varying the tunneling parameters, in order to decrease the distance tip-sample, it has been possible to visualize the HOPG lattice underneath and therefore to calibrate the piezo *in situ*. Molecular resolution at the solid-liquid interface have been achieved using high scan rates (~ 60-200 Hz/line) in the *constant-current mode*.

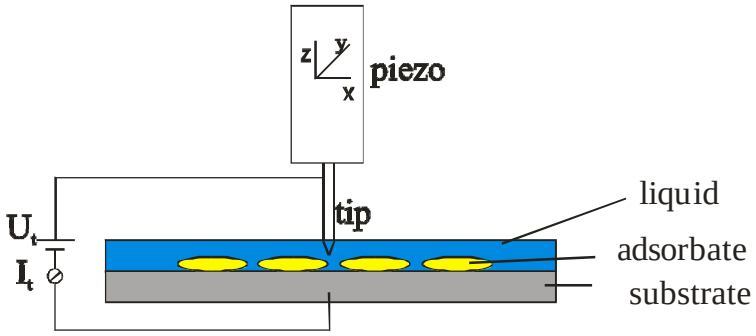

Figure 5.6: Scheme of the solid-liquid interface STM studies.

These kinds of measurements require the use of a solvent with a low volatility:

- 1-phenyloctane (boling point(b.p.) = 261-263 °C)
- 1,2,4 trichlorobenzene (b.p. = 215-220 °C)

Both solvents are available from Aldrich Chemicals and both are suitable for this kind of measurements; in addition the second one is also rather aggressive and more toxic. When it has been possible it was preferred to use the first one. The solvents allowed to measure for several hours having the tunneling tip immersed in the solution.

During the experiments, first the HOPG lattice is resolved for 2-4 hours until the images exhibit a good stability due to an absence of drift. Only at this point a drop of the organic solution is applied to the basal plane of the substrate.

Crystalline powder of α-iodo-ω -[(2,5-dihexyl-4-ethynyl)phenyl]-poly[(2,5-dihexylphenylene-1,4)ethynylene)] , α-[[4-[(N,N-dimethylcarbamoyl)thio]phenyl] ethynyl]-ω-[4-[(N,N-dimethylcarbamoyl)thio]phenyl]-poly[(2,5-dihexylphenylene-1,4)ethynylene)] (PPE) or α-phenylethynyl-ω-phenyl-ter[(2,5-dihexylphenylene-1,4)ethynylene)] was solubilized in 1-phenyloctane and a drop of the almost saturated solution was applied to the freshly cleaved highly oriented pyrolitic graphite (HOPG) substrate.

5.3 Scanning Force Microscopy

5.3.1 Apparatus

Scanning Force Microscopy investigations have been executed on a commercial Nanoscope IIIa set-up (Fig. 5.7) produced by Digital Instruments, Santa Barbara, CA that can run both in contact and in Tapping mode. We have used different commercial microfabricated cantilevers available either from Digital Instruments, Santa Barbara, CA or from Olympus Opt. Co. LTD.

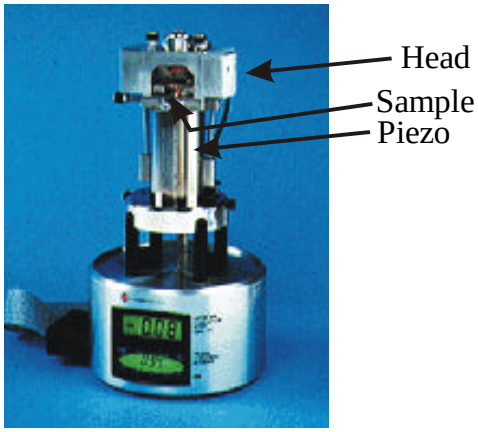

Figure 5.7: Nanoscope Multimode IIIa (Digital Instruments).

k (N/m)	Cantilever length (μm)	Mode	Brand	Material/shape
17 – 64	125	Tapping mode	DI	Si/rectangular
0.06	200	Contact mode	DI	Si_3N_4/triangular
0.12	200	Contact mode	DI	Si_3N_4/triangular
0.38	100	Contact mode	DI	Si_3N_4/triangular
0.58	100	Contact mode	DI	Si_3N_4/triangular
0.02	200	Contact mode	Olympus	Si_3N_4/triangular

k= Force constant

Three different scanners have been used to explore different ranges of scan lengths:

Scanner	Maximum Scan length (μm)
A	1
E	13
J	130

Most of the studies have been performed with scanner E. On the other hand scanner A is useful to explore samples on a molecular scale, while the J scanner allows to get an overview of the surface on a hundred micrometers scale. For distance calibration of the piezo controller, images of mica and gold calibration gratings were employed routinely. The samples have been attached with a double sided tape or with epoxy glue to a steel disc that is held magnetically on the piezo.

It was possible to obtain an overview of the cantilever and of the sample surface on a hundreds of micrometers scale by using an optical microscope (Nikon-Japan) that is interfaced with a CCD camera and is therefore able to produce images on a monitor. This set-up renders possible the selection of the investigated area with a good precision in the tens of μm range.

An analogous bungy set-up described for the STM has been used with the SFM, alternatively to a heavy table made from a 1m*2m granite slab, which stands on a pneumatic system that keeps it floating with N_2 pressure.

5.3.2 Investigations on polymeric phenyleneethynylenes

PPE solutions have been applied to different non conductive substrates, which were either amorphous (glass, carbon copper grids) or crystalline (mica). Mica was freshly cleaved before use while the other two substrates have been cleaned chemically. The concentration of

the solutions (from 3.0 g/l to 0.01 g/l of PPE), the type of solvent and size of the macromolecular system (molecular weight) have been varied systematically. The solvent has been chosen in order to vary the rate of evaporation and of crystallization of the organic adsorbate. Pure tetrahydrofurane (THF , boiling temperature 69 °C), methanol (MeOH , b.p. 65 °C), a mixture of THF and 1-phenyloctane and pure 1-phenyloctane have been used.

Molecular self-assembly was achieved in two different ways:

1. *spin coating*: a drop of solution is placed on the substrate that is rotated very fast for 30 sec (Fig. 5.8a). The adsorption therefore occurs very rapidly.
2. *solution casting*: applying a drop of solution onto a freshly cleaved mica surface and letting the solvent evaporate (Fig. 5.8b). Making use of different solvents the self-assembly can take place in a few hours (2-3 for THF) or in a few days (2-3) for the mixture. The evaporation of the solvent for the case of pure 1-phenyloctane required more than one month time and therefore is considered impractical.

The thin dried films have been observed by SFM in air environment both in contact and in Tapping Mode using mainly the E-scanner in a range of scan lengths from 10 μm to 0.3 μm.

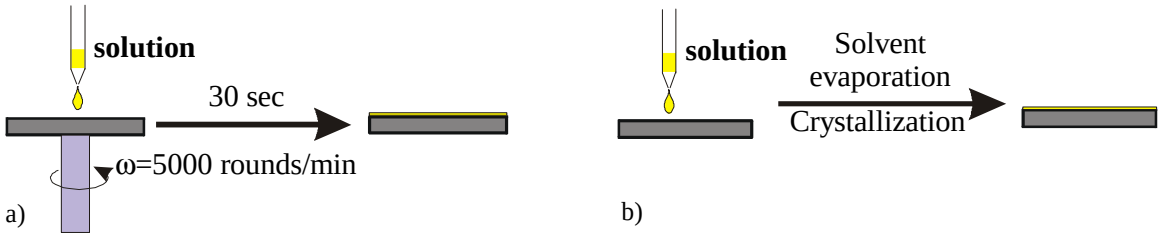

Figure 5.8: a) Spin coating deposition; b) Solution casting.

5.3.3 Investigations on hexakis-dodecyl-hexabenzocoronene (HBC-C_{12})

The exact quantity of HBC-C_{12} dissolved in 1,2,4 trichlorobenzene for covering homogeneously the HOPG substrate with 1 layer (solution I) and 1000 layers (solution II) have been deposited, using different procedures discussed here below, following the hypothesis that HBC-C_{12} molecules pack on HOPG with the disc oriented flat on the basal plane of the substrate, as observed in previous studies at the solid-liquid interface [Sta95b].

The according quantity can be calculated as follows:

Molecular Weight of HBC-C_{12}: 1540 g/mol

3.8 mg of HBC-C_{12} in 1.5 ml of TCB → concentration = 2.53 g/l

Avogadro Number: $6.022*10^{23}$ mol^{-1}

Surface covered by a single molecule: 1.94nm*2.64nm*sin80°=5.044 nm^2 (area unit cell calculated according to [Sta95b])

Surface of the HOPG substrate: 10^{14} nm^2 = 1 cm^2

Number of molecules required to make a single layer on the substrate: $10^{14}nm^2/5.044$ $nm^2=1{,}983*10^{13}$ molecules

Concentration=3.8 mg/1.5 ml=2.533 g/l à 2.533g/l / 1540 g/mol= $1.645*10^{-3}$ mol/l

Volume of solution cast on the substrate = 20 µl

Solution I: using 20 µl of a $1.645*10^{-3}$ mol/l solution, one nominally creates 10^3 layers on the HOPG basal plane.

Solution II: using 20 µl of a $1.645*10^{-6}$ mol/l solution, one nominally creates a single layer on the HOPG basal plane.

The self-assembly was carried out in the two ways described for PPE in chapter 5.3.2. An alternative route of solution casting was applied with an almost sealed environment of the vapors of the organic solvent. The substrate freshly coated with a drop of solution and a beaker of solvent are placed under a big beaker (Fig. 5.9). This procedure leads to a further decrease of the rate of adsorption.

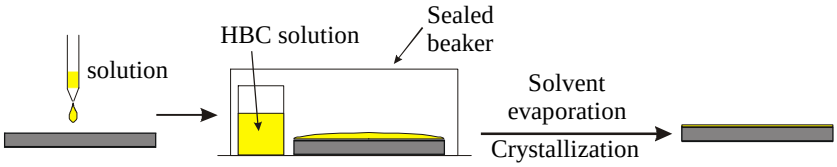

Figure 5.9: Solution casting in an ambient saturated with the solution vapors.

The rate of the adsorption processes are :

Method	Process	Rate
A	Spin coating	~ 30 sec
B	Solution casting	~ 3-5 hours
C	Solution casting in sealed ambient	~ 12 hours

The films, prepared according to the different routes, have been investigated with SFM in Tapping Mode (detecting the amplitude signal and the phase lag) and in contact mode, using the E scanner in air ambient. Also STM investigations have been carried out in order to estimate the thickness of the adsorbate by measuring the average film resistance.

Nominal contour sizes of the molecules have been computed by means of molecular mechanics calculations using a commercial software, DISCOVER VERSION 4.0.0, Biosym Technologies Inc., San Diego, CA.

5.4 Image Processing

SPMs are local probe techniques that reveal local features, which are not necessarily representative for the whole sample surface. Because of this reason it is appropriate to record and process several images. This allows to minimize the influence of a particular sample area and to determine an average behavior. All the evaluations that are described in the following paragraph have been carried out quantitatively and averaged over a large number of samples making use of different image processing software.

STM: Making use of the HOPG micrographs as reference, STM images of the adlayer have been corrected one by one for the piezo drift with the software of the STM instrument. The dimensions of the unit cells have been determined utilizing a public domain software, Scanning Probe Image Processor (SPIP), vers. 3.0, developed by J.F. Jorgensen. On the other hand the software package Image Tools 1.27 produced by University of Texas - Health Science Center in Saint Antonio has been used as an electronic ruler to measure the spacing between parallel backbones from STM micrographs. The surface roughnesses have been

evaluated with the SPIP software on raw data constant current images.

For the Ostwald ripening studies, measurements of the area of the molecular crystallites have been computed by drawing manually the contours of the molecular domains from several images [Bis95] using NIH-Image software (National Institutes of Health, Bethesda, Maryland). An analysis of the evolution of the crystallite areas as a function of time on the minute time scale has been executed on several individual domains from different images. A linear fitting of the area of the crystals vs. time has been computed for the last 2-4 minutes of each island life time, and was averaged.

SFM: The height of features like the ribbons of PPE or the layer thicknesses for HBC-C_{12} have been evaluated from singular profiles using the software of the Nanoscope IIIa instrument. Besides, the ribbon widths have been surveyed with Image Tools 1.27 software.

5.5 UPS, XPS

Photoelectron spectroscopies studies have been carried out in Linköping together with Dr. Matthias Keil within the group of Prof. W.R. Salaneck. The X-ray (XPS) and ultraviolet (UPS) photoelectron spectroscopy investigations have accomplished using an ultra-high vacuum (UHV) apparatus with a base pressure of better than 10^{-9} mbar. The X-ray source was a 1254.6 eV Mg(K_α) radiation while UPS was performed using monochromatized HeI (21.2 eV) or HeII (40.8 eV) photons from an He discharge source. The beam was usually oriented at 45° from the normal to the substrate except for the case of angle resolved measurements of C_{12}-HBC where also spectra at 0° have been recorded. The thermal annealing of the films was performed inside the vacuum chamber.

5.5.1 Photoelectron spectroscopies on phenyleneethynylene derivatives

Films of the trimer and the polymer of phenyleneethynylene have been grown on 200 nm thick Au(111) films sublimed on silicon wafers. The trimer, namely (α-phenylethynyl-ω-phenyl-ter[(2,5-dihexylphenylene-1,4)ethynylene)]), possesses 74 carbon atoms (20 carbon atoms per "monomer"). It has been processed in thin films both by sublimation in UHV and by spin-coating using THF as solvent. The UHV-sublimation of the organic compound has

been executed at 250 °C for 11 minutes at a pressure that ranged between 1.6 and $2.0*10^{-9}$ mbar, while spin-coating of a trimer solution (2.4 g/liter) in THF has been carried out at 2000 round/minutes for 2 minutes.

The polymer, (α-phenylethynyl-ω-phenyl-poly[(2,5-dihexylphenylene-1,4)ethynylene)]), exhibits a number averaged molecular weight of M_n= 3542 g/mol (from GPC investigation poly(*para*-phenylene), PPP, calibrated) which indicates an average degree of polymerization (number average of repeating units) of ~13 repeat units, and a polydispersity ($U=M_w/M_n$)=2.12. The average number of carbon atoms for each macromolecule is ~ 274 (20 carbon atoms per "monomer"). Films of this macromolecular system have been prepared by spin-coating on Au films using THF as a solvent.

Before the deposition of the organic layer, the Au substrates have been cleaned by acetone and iso-propyl alcohol (known also as 2-propanol) successive baths in a sonicator apparatus for 5 minutes each step. The samples have been dried after each step with a gentle flow of N_2.

Evaporation of Na on the bare Au surfaces have been carried out in order to calibrate the Na source, and the intensity and the shape of the peaks in XPS. This has been executed both on a Au surface cleaned by Ne sputtering and with a Au surface cleaned by acetone and 2-propanol. The sodium was evaporated from a getter source which was heated with a current of 7 A. The Na doping of the interface have been performed with successive increasing evaporation time of the same sample. After each step (one or two minutes of evaporation) XPS (survey scan, C 1s and Na 1s) and UPS (HeI, HeII) spectra have been recorded.

5.5.2 Photoelectron spectroscopies on hexakis-dodecyl-hexabenzocoronene (HBC-C_{12})

Thin films of hexakis-dodecyl-hexabenzocoronene prepared from solution (as described in paragraph 5.3.3) have been investigated complementary by means of XPS and angle resolved UPS.

5.6 Current-voltage (I-V) measurements

The deprotection of α-[[4-[(N,N-dimethylcarbamoyl)thio]phenyl]ethynyl]-ω-[4-[(N,N-dimethylcarbamoyl)thio]phenyl]-poly[(2,5-dihexylphenylene-1,4)ethynylene)] has been accomplished following the route described in Fig. 5.10. The polymeric polycrystalline powder was dissolved in a solution of THF or in a mix of phenyloctane/THF (volume ratio 1:10). The pH of the solution was increased by adding KOH pellets dissolved in MeOH. The solution was stored in a well controlled environment inside a glass balloon. Successive cycles of vacuum and Argon venting were executed in order to obtain an oxygen free ambient; after this, the balloon was kept under a gentle flow of Ar. All solvents have been degased before the use. Following to this first step HCl was added in order to protonize the end groups leading to thiols (-SH).

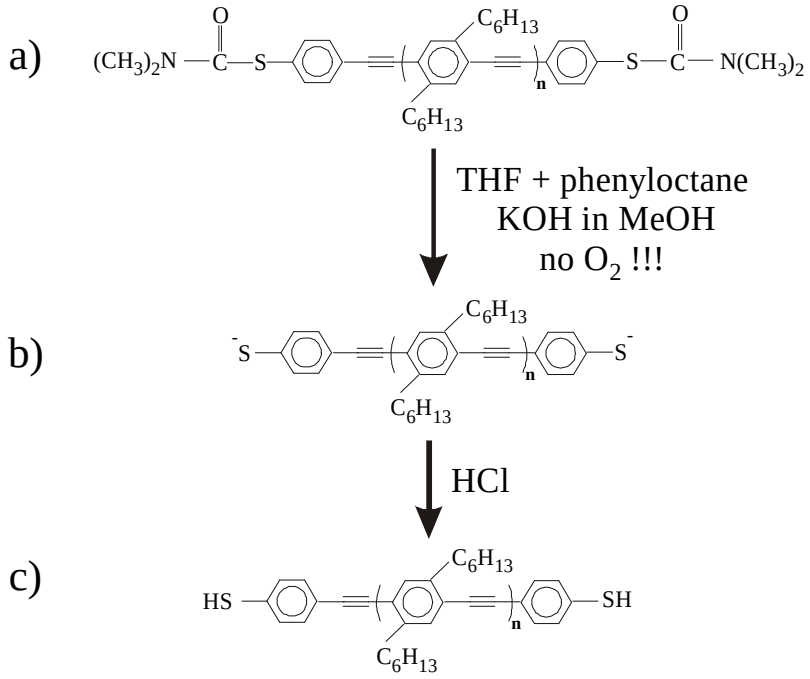

Figure 5.10: Deprotection reaction of α-[[4-[(N,N-dimethylcarbamoyl)thio]phenyl] ethynyl]-ω-[4-[(N,N-dimethylcarbamoyl)thio]phenyl]-poly[(2,5-dihexylphenylene-1,4)ethynylene)].

The Au nanoelectrodes, after testing their I-V behaviour one by one, were immersed for 18-22 hours in the solution either when the polymer exhibited ionic sulphide groups at their edges (Fig. 5.10b) or after acidification (Fig. 5.10c). In both cases the self-assembly was performed in two different modes:

1) applying a voltage between the two electrodes

2) without voltage between the two electrodes.

The first approach was executed in order to help the dielectric matter (PPE) to get pulled into the position where the electric field is most intense, that is in the center of the gap. The drawback could be that if the intensity of the electric field is too high, a random and strong molecular precipitation between the electrodes can take place. To avoid this risk a small voltage (1 Volt) was applied between the electrodes. In the latter case the molecular self-assembly is expected to be governed by the chemisorption of the functionalized molecules on Au.

The I-V characteristics of the electrodes and of the molecular aggregate adsorbed between them have been probed using a Keithley 487 picoammeter - voltage source commercial set-up interfaced to a personal Computer. This allowed to detect currents down to the 10^{-14} A range.

6 Results and discussions

In this chapter are presented the main experimental results with relative discussions.

6.1 Self-assembly of thiols on metallic substrates

6.1.1 Introduction

The electronic properties of single molecules or of a small *ensemble* of molecules can be probed following two different strategies as introduced in paragraph 4.3. The first of them is using the STM set-up to measure the conductivity of a highly ordered adsorbate. In this context, self-assembly of thiol functionalized molecules on metallic substrates [Ulm91] has been studied intensively as a model for controlled solid-liquid interface reactions. Gold has been widely used as a substrate because it is a rather inert metal for many gases and liquids [Ham95] and in addition alkanethiols pack on it in a simple stable commensurate $\sqrt{3}\times\sqrt{3}R30°$ overlayer with a lattice parameter of a=5.00 Å [Del96]. Such self-assembled monolayers (SAM)s have been characterized both in Ultra-High Vacuum (UHV) and in ambient conditions by Fourier Transform Infra-Red spectroscopy [Por87, Nuz90], Second Harmonic Generation [Buc91], X-ray Photoelectron Spectroscopy [Bai89a,Nuz87, Bai89b], ellipsometry [Por87, Chi90], Grazing Incidence X-ray Diffraction [Cam93a], Transmission Electron Diffraction [Str88], Near Edge X-ray Absorption Fine Structure Spectroscopy [Häh93], He scattering [Cam93b, Chi89], Atomic Force Microscopy [Alv92] and Scanning Tunneling Microscopy (STM) [Wid91,Kim92,Del96,Poi97]. The mechanism of alkanethiol self-assembly has been recently studied by Poirer and Pylant by means of UHV-STM measurements [Poi96]. On the other hand, a very little work has been performed on SAMs of thiols on Ag(111) so far. By FTIR spectroscopy and Raman spectroscopy significantly smaller tilt angles than on Au(111) were reported. In UHV, dosing of dimethyl disulfide on annealed Ag(111) results in a LEED pattern, which can be indexed as two domains of a (v7Xv7)R10.9° coincidence structure. It is explained by the cleavage of the S-S bond to form a methanethiolate film. The same structure was found previously for adsorption of H_2S and sulfur on Ag(111). It was assigned to two dimensional crystals of γ-Ag_2S. For octadecanethiolate, however, Eisenberger and coworkers proved a larger adsorbate lattice using LEHD and GIXD. Recently Heinz and Rabe provided insight into alkanethiols SAMs

on Ag(111) by studying the packing and conductivity of the adlayer at increasing lengths of the aliphatic chain from CH_3SH to $C_{11}H_{23}SH$ [Hei95]. In the first part of this chapter, varying the metallic substrate and the chemisorbed type of thiol-functionalized molecule, the structure and the electrical conductivity of the formed SAM are investigated using STM.

6.1.2 Sublimed Au and Ag substrates

Key issues for a reproducible SAM formation are the flatness and the crystallinity of the metallic substrate. Therefore metallic supports have been developed using different procedures.

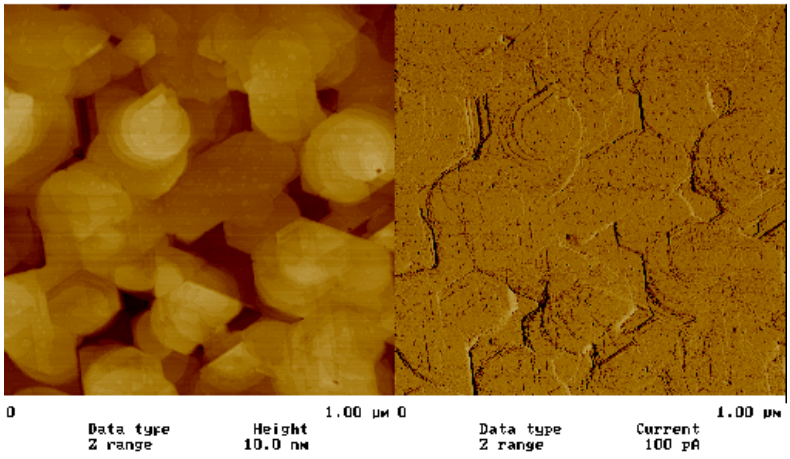

Figure 6.1: STM images of Ag(111). Flat crystallites with sharp angles of 120°.
Tip bias (U_t)= 1.5 V; Average tunneling current (I_t) =0.03 nA.

First, Ag and Au surfaces were sublimed on freshly cleaved muscovite mica discs in high vacuum (HV) varying systematically the parameters of the deposition, i.e. the temperature of the substrate during sublimation (T_{sub}) and the nominal thickness of the metallic adlayer (Z), in order to find conditions leading to a pseudo epitaxial film. In the case of silver, the best surfaces have been obtained at T_{sub}=275 °C and Z=50 nm. The Ag films, on a micrometer scale, exhibit atomically flat terraces with hexagonal domains (Fig. 6.1) with 120° angles that indicate macroscopic evidence for epitaxial growth.

Unfortunately, the surface of Ag in contact with air gets oxidized very rapidly. Indeed films that have been exposed to air for 30 minutes show a crystalline lattice with a spacing of 5 Å (Fig. 6.2) that can be assigned to Ag_2O. This oxidation is confirmed by the presence of clusters on micrometer scale images. Because of this reason, a series of precautions have

been taken, including venting the UHV chamber with argon, and bathing Ag films in organic solutions under Ar reflux. In addition, the STM set-up was put in a box (box B in Fig. 5.4) which could be filled with an inert gas (Ar, He, N_2).

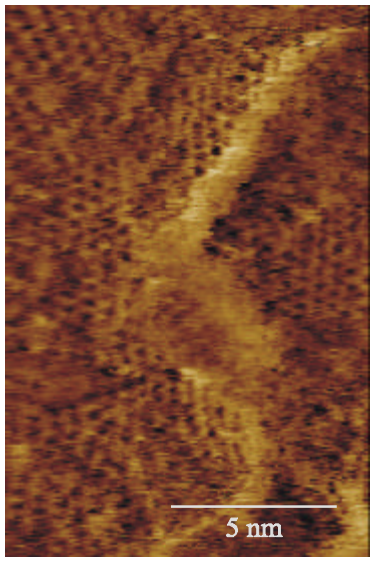

Figure 6.2: STM constant current image of uncoated Ag surface after 30 min.exposure to air.

Also gold surfaces have been prepared by sublimation in HV. Film sublimed at T_{sub}=350 °C and Z= 50 nm have exhibited a polycrystalline morphology with crystallites extending on a scale of several tens of nanometers (Fig. 6.3).

Subliming Au films at T_{sub}=400 °C and Z= 200 nm lead to films that exhibit a morphology made of flat crystallites extending on an area of some μm^2 (Fig. 6.4). The surface flatness was characterized by its root mean square roughness:

$$R_{rms}=\sqrt{\frac{1}{N^2-1}\sum_{mn=1}^{N\times N}(h_{mn}-\bar{h})^2} \qquad (6.1)$$

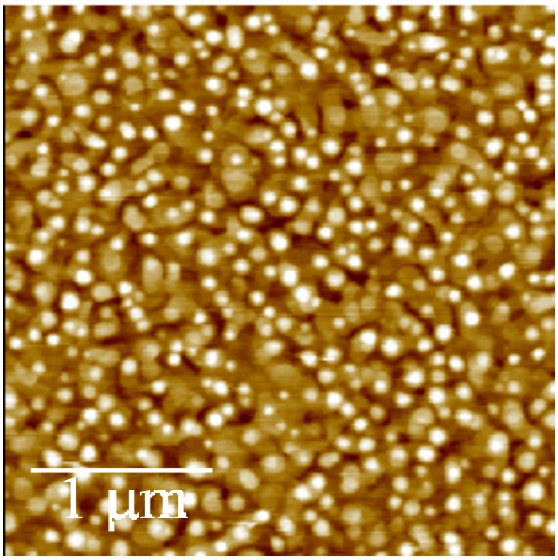

Figure 6.3: STM Constant current image of uncoated Au surface (T_{sub}=350 °C, Z= 50nm), exhibiting a polycrystalline structure. The gray scale height is (h)=20 nm.

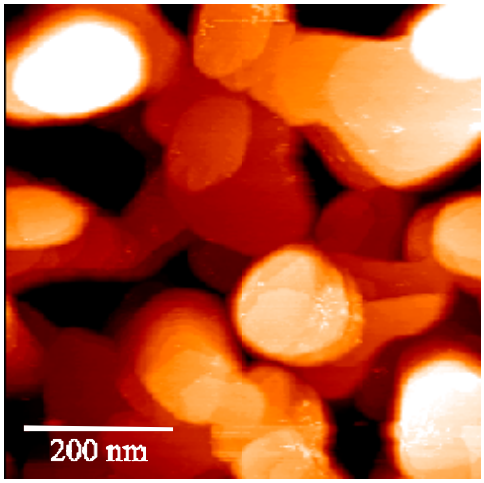

Figure 6.4: STM constant current image of uncoated Au surface (T_{sub}=400 °C, Z= 200nm), exhibiting epitaxial terraces. The gray scale height is (h)=1.78 nm.

where N×N is the number of pixels (512*512), h_{mn} is the height value of the pixel *mn* and $\bar{h}$ is the mean height of the pixel calculated from the N×N values. It was also characterized by its average roughness: $R_A = \frac{1}{N} \sum_{mn=1}^{N \times N} \left| h_{mn} - \bar{h} \right|$ (6.2)

On an area of 1µm^2 these parameters amount to R_{rms}=19 Å and R_A= 15 Å, respectively.

With the aim of increasing the flatness and epitaxial character of the Au surface, different types of thermal annealing post treatments have been carried out. All of them were very fast processes where the temperature could hardly be controlled.

I. Flame-annealing (Fig. 6.5);

II. Annealing with a halogen lamp from the front side (Fig. 6.6);

III. Annealing with a halogen lamp from the rear side (Fig. 6.7).

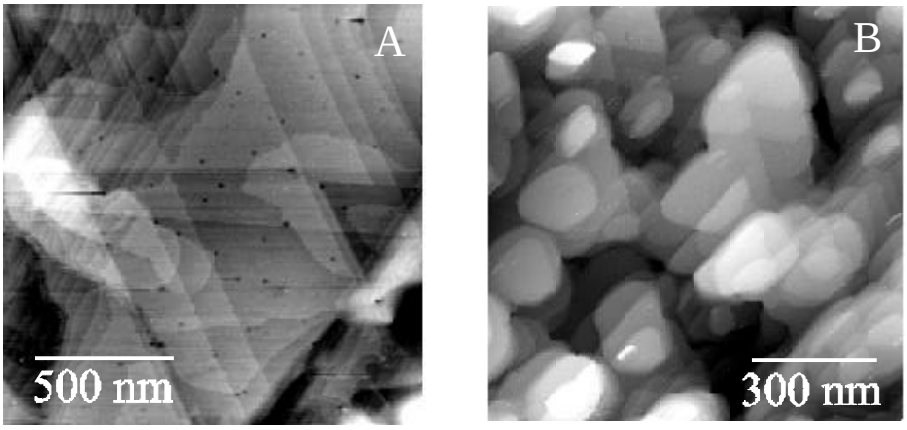

Figure 6.5: STM constant current images of Au flame-annealed sample recorded in different areas of the surface. A) U_t = 0.1 V; I_t =0.3 nA; scan rate = 7.4 Hz; scan length (L) = 1.5 μm, R_{rms}=4.94 Å resolution 250X250 px; B) 0.13 V; 0.2 nA; 10.8 Hz; L = 1 μm, R_{rms}=6.14 Å; 512X512 px.

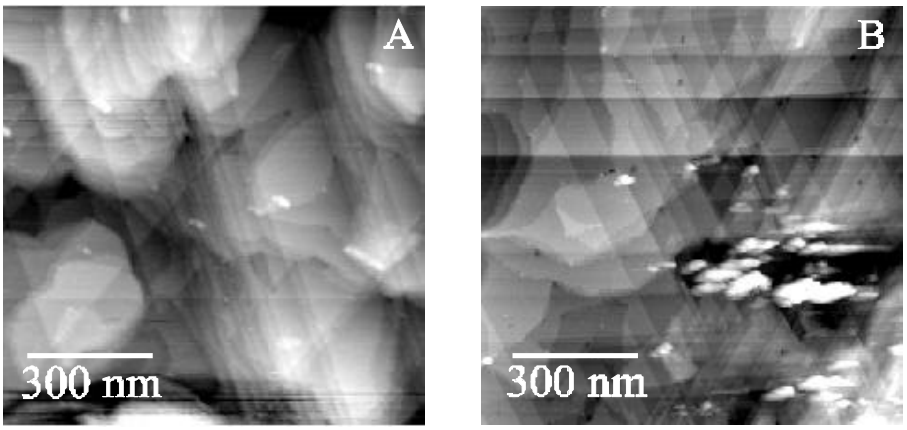

Figure 6.6: STM constant current image of Au shock-annealed sample (from the front) recorded in different areas of the surface. A) U_t = 0.12 V ; I_t = 0.2 nA; scan rate = 11.1 Hz; L = 1 μm, R_{rms}=5.52 Å; 250X250 px; B) 0.13 V ; 0.2 nA ; 10.3 Hz; L = 1 μm, R_{rms}=4.56 Å; 512X512 px.

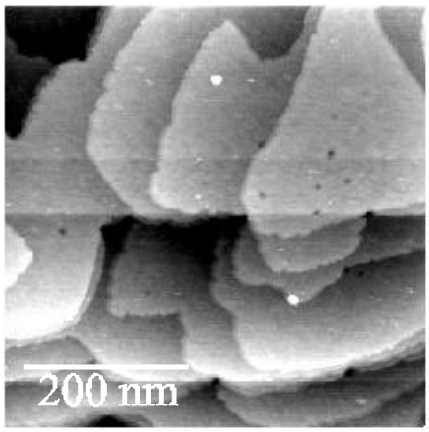

Figure 6.7: STM constant current image of Au shock-annealed sample (from the back).
U_t = 0.13 V ; I_t = 0.348 nA ; scan rate = 9.8Hz; L = 0.5 μm, R_{rms}=1.88 Å; 512X512 px.

An increase of the epitaxial character with all the thermal annealings can be recognized from the STM images by the existence of several crystallites with sharp boundaries separated by angles of 60°, forming triangular domains. Between these 3 types of samples the flame annealed ones (Fig. 6.5) seem to exhibit an higher epitaxiality, although also samples II and III are extremely flat with existence of big crystallites.

6.1.3 Template Stripped Gold substrates

For enhancing further the quality of the gold substrate, a method to produce ultra large, atomically flat gold films glued onto Si wafers was reported by Hegner et al. [Heg93, Wag95]. This method, known as Template Stripped Gold (TSG), is based on a) deposition of Au onto mica sheets, b) supporting the free Au surface by gluing it to a Si wafer (using epoxy or ceramic glues), and c) stripping the Au film from the mica. The limitation of this procedure, for the case of epoxy glues, is the instability of the multilayer against commonly used organic solvents. Ceramic glues, that do not suffer the same type of limitation, oblige to a rather complicated procedure for the TSG preparation [Wag95]. Similarly Stamou and coworkers have recently prepared TSG by evaporating a Au film on a smooth silicon wafer and supporting the Au free surface by gluing it to a glass slide [Sta97]. A novel simple method based on a different way of supporting the Au film have been developed. These surfaces have been produced by first sublimating a thin epitaxial gold film on mica, then

electroplating a thick nickel layer (~200 μm) and finally stripping the metal from the mica that in the following case is done mechanically, although it can be performed also chemically (see Fig. 5.1) . [Sam99b]

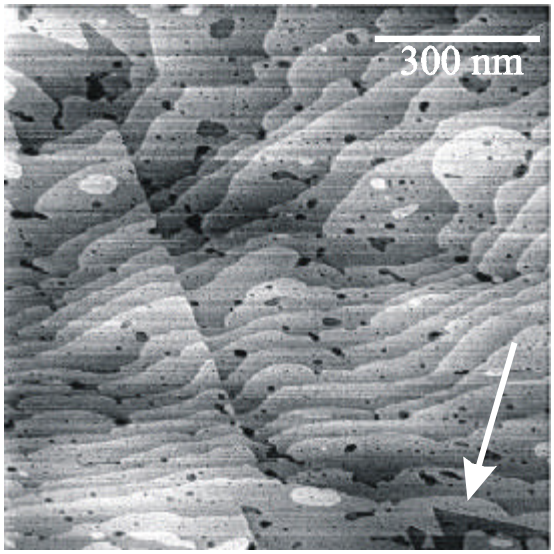

Figure 6.8: Unfiltered topographical STM image of a coated Ni supported-TSG surface (U_t=20 mV, average I_t= 800 pA). Height range= 11.4 Å; R_{rms}=2.3 Å.

Fig. 6.8 shows an STM image of the Ni supported TSG surface coated with an undecanthiol monolayer recorded on the micrometer scale in the constant current mode. The image reveals three typical topographical features of a Au surface where alk*a*nethiols had chemisorbed, as recently reviewed by Delamarche et al. [Del96]. First, the gold surface exhibits atomically flat terraces extending over up to several hundreds of nanometers. Second, triangular areas with 60° angles, typical of epitaxial Au(111) grown in UHV, can be recognized (indicated with white arrow in Fig 6.8). Third, randomly distributed depressions, either one or two gold steps deep (2.4 Å and 4.8 Å), due to the etching of the Au surface during the alkanethiols chemisorption, are also present.

The values for R_{rms}=(2.2±0.2) Å and R_A=(1.7±0.2) Å, measured on an area of 1μm^2, are remarkably about one order of magnitude lower than those obtained on the free Au surface evaporated on mica in high-vacuum (HV) at 400°C substrate temperature (Fig. 6.4), and half or one third of the ones annealed (Fig. 6.5 – Fig. 6.7). It is also smaller than values found for TSG films prepared by evaporating Au both onto mica [Wag95] an onto a Si wafer [Sta97],

most likely because the supporting procedure with glue introduces in the system more mechanical stress than the electroplating. Obviously, the atomical flatness of our TSG substrates extends at least over the micrometer scale. Ni supported TSGs produced at T_{sub}= 35°C during the Au evaporation exhibit a R_{rms} which is approximately only twice as large as the one obtained at T_{sub}= 300°C, even though they do not exhibit atomically flat terraces extended over several hundred nanometers with typical 60° angles. The reproducibility and easiness of the mechanical pealing for all samples have been proven by the absence of an insulating tunneling barrier, which would be expected for mica leftovers [Wag95]. In addition, the intertness of our multilayer makes it possible that pealing is carried out also chemically with THF. This allows to avoid any mechanical stress that could be induced in the film during the pealing process carried out with tweezers.

It is worth to note that this alternative route to produce TSGs leads to a Au surface with an increased flatness, which is ascribed to the minimized mechanical stress introduced in the system during each step of the substrate preparation. Moreover, since the procedure described here does not require any gluing between the Au film and the support, the application of this TSG does not suffer from any limitation due the physical and chemical stability of epoxy glues. This is important both for the choice of the solvent to be used for molecular assembly on the substrate and for any chemical in-situ modification of the SAM to be carried out. This method described for TSG preparation is very simple and easily transferable to large scale production. The thick film of Ni grown on the upper Au surface can be replaced with any other thick (and preferably inexpensive) metallic layer, which is stiff, chemically inert and stable in time. The metal supported TSG may become the golden support of choice for SAMs formation and scanning probe microscopy imaging both in biology and in material science. [Sam99b]

6.1.3.1 SAMs on Template Stripped Gold substrates

Figure 6.9 shows STM images of 1-undecanthiol chemisorbed on TSG recorded in constant height mode on the nanometer scale (unfiltered and filtered). A hexagonal pattern of undecanthiol molecules was visualized at a high gap impedance, resulting from rather high voltages (~800 mV) and low tunneling currents (30-60 pA). The minimal tunneling resistance to maintain molecularly resolved imaging on undecanthiol and nonanthiol films were 27-10 GΩ and 1 GΩ, respectively. This strong dependence on the alkyl chain length is an indication

for the non-destructive imaging of the SAM [Hei95]. The average spacing was (5.2±0.3) Å, consistent with the √3×√3R30° adsorbate layer on Au(111) surfaces (α-phase).

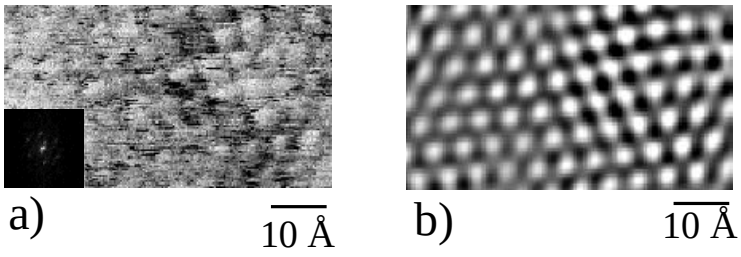

Figure 6.9: STM constant current image of undecanthiol on Ni supported-TSG surface. U_t = 800 mV; I = 40 pA. a) Unfiltered image with the 2D-Fourier Transform showing the periodicity of the hexagonal lattice (α–phase); b) band pass filtered image. Although a high frequency noise blurs the raw image (as evident also from the FFT), the lattice of the adlayer can be seen in both images.

6.1.4 Conductivity of SAMs of Alk*e*nes and Alk*a*nes

Alk*a*nethiols are linear, flexible saturated hydrocarbons, which form insulating materials. When they are crystallized in a SAM their structure is tightly packed and stable. On the other hand alk*e*nethiols are non-saturated oligomeric model systems for poly(acetylene), which is a stiff polymer, forming a semiconductive material. The aim of this work is to design a prototype system of a molecular wire by preparing SAMs of unsaturated alk*e*nethiols on Ag(111) and Au (111) and to study the average conductivity of their self-assembled monolayers with STM. Alk*a*nethiols on Ag(111) form a √7*√7 R10.9° adlayer with the alkyl chains oriented nearly perpendicular to the basal plane of the substrate [Hei95]. In fact the tilt angle with respect to the surface normal is 12° while on Au(111) it is 27°, thus the molecules are more tightly packed on Ag than on Au. This suggests Ag(111) as an ideal substrate for SAM preparation of alkyl chains assembled perpendicular to the substrate.

The experiments can be divided into four separate sets I to IV:

I) Three different types of alk*e*nethiols varying the number of carbon atoms and consequently of double bonds in the main chain have been investigated:

C9A 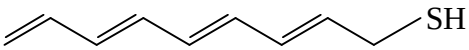

C11A 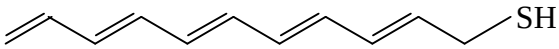

C12A 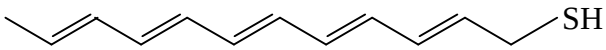

Ag(111) surfaces have been immersed for 6 hours in 5 mM mixtures of unsaturated and saturated alk*a*nethiols solutions in benzene.

Unsaturated	0 %	5 %	20 %	80 %	100 %
Saturated	100 %	95 %	80 %	20 %	0 %

With the naked eye the films with a bigger amount of unsaturated alk*e*nethiols appear less shiny. The light reflectivity of the sample increases with the percentage of saturated alk*a*nethiols. The poor shine of the film by naked eye indicates that the surface of the film possesses a roughness on the order of micrometers. This feature makes STM and AFM studies difficult. In fact the maximum excursion of a piezo in the Z axis is usually just a few micrometers (less than 5). Such a "macroscopic" rearrangement of the surface can be explained only with a drastic process. An oxidation of the Ag or of the double bound is not enough to give rise to this rough morphology. It seems more likely to explain the phenomenon with a rearranging of the Ag (111) surface, as suggested by Seidel [Sei93]. Indeed it is well known that strong chemisorption forces can override the substrate-substrate bonding, which in turn can cause a reconstruction of the surface followed by a decrease of the surface atom coordination number [Ulm91].

II) Three different types of alk*e*nethiols with 9 carbon atoms in the main chain have been used:

C9A 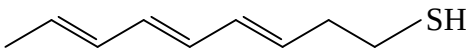

C9B 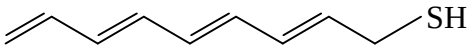

C9C 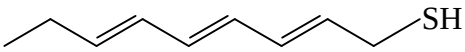

The samples produced by bathing the Ag for 1 hour either in a 1 mM or in 5 mM solution of C9A reveal a similar morphology on the micrometer scale, suggesting that the large roughness seen in the previous experiments was probably due mainly to an excessive immersion time, and to a much lesser degree to the concentration of the solution.

Based on previous experiments, it was decided to decrease the concentrations to 1 mM and to reduce the time of immersion of the Ag film in the solution to 1 hour. Comparing these experiments with the previous ones, the films appear more shiny. Indeed the surface roughness is smaller allowing these samples to be studied with STM.

Nevertheless, the film roughness existing on a micrometer scale does not permit to achieve molecular resolution imaging on either fully and partially unsaturated alk*e*nethiol films.

III) Thiol end functionalized - C_{11} pentaene, both in a solution: a) with > 90% all-trans and; b) with >85% all-trans has been diluted with benzene and the following solutions have been used for chemisorption onto the metallic surfaces:

C11A 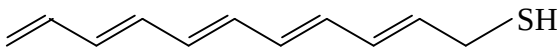

Table 6.1: Sample of unsaturated C11A mixed with fully saturated $C_{11}H_{23}SH$

Unsaturated	Saturated	Stock solution	Total concentration of alkanethiols	Type of Au substrate	Sample Name
100 %	0 %	1	0.66 mM	TSG	C11A1
95 %	5 %	1	2 mM	Sublimed	C11A2
80 %	20 %	2	2 mM	TSG	C11A3
20 %	80 %	2	2 mM	Sublimed	C11A4
0 %	100 %		2 mM	TSG	C11A5

Note: stock solution 1 is > 90% all-trans conformation and solution 2 > 85% all trans.

TSG surfaces coated with saturated alk*a*nethiols (C11A5) have been imaged at ambient conditions in the constant current mode and described in paragraph 6.1.3.1. They exhibit crystallites extending over several hundreds of nanometers with steps at 60° angles typical for Au (111) surfaces as in Fig. 6.8. Also for the case of alk*e*nethiols (C11A1) the morphology is made of small holes on a sub-micrometer scale. This feature, which is due to the etching of the Au surface (Fig. 6.10, 6.11) confirms the occurrence of the reaction of thiol functionalized molecules with gold. Noteworthy, this feature has been visualized on all the samples.

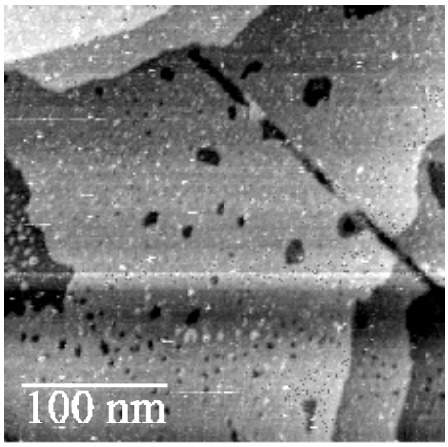

Figure 6.10: STM constant current image of TSG coated surface (U_t = 800 mV; I =30 pA) (sample C11A1). Typical holes proving the reaction of the thiols with gold. Height range= 7.2 Å; R_{rms}=1.4 Å.

An STM investigation of sample C11A1 on the molecular scale did not reveal any periodic lattice, although some periodical features with spacings in the range of 5 Å have been

observed. After being stored for 4 days adsorbed on Au in the dark, sample C11A1 exhibits a roughness increased of almost one order of magnitude on the several nm scale (Fig. 6.12 to be compared to Fig. 6.10). This suggests a notable instability of the organic interface.

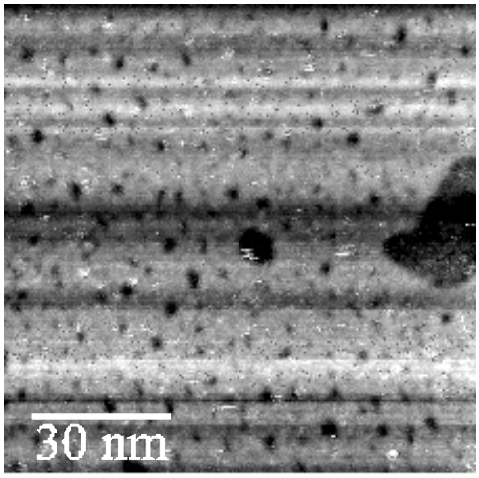

Figure 6.11: STM constant current image of TSG coated surface (U_t = 800 mV; I = 20 pA) (sample C11A1). Typical holes proving the reaction of the thiols with gold. Height range= 7.2 Å; R_{rms}=1.5 Å.

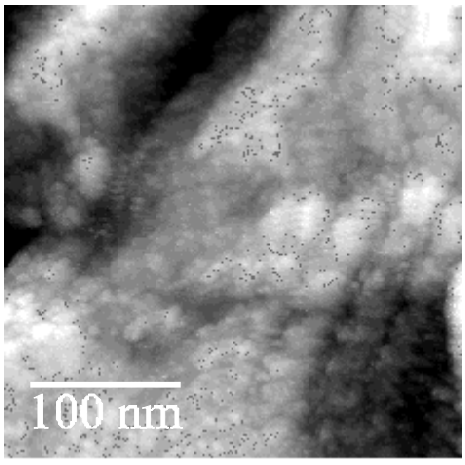

Figure 6.12: STM constant current image of C11A1 on TSG (U_t = 800 mV; I = 50 pA). Typical holes proving the reaction of the thiols with gold. Height range = 49.6 Å; R_{rms}=12.0 Å .

On the other hand, sample C11A3 exhibits on a 200 nm scan length micrograph a defined structure with different alignments on two different crystallites of Au (Fig. 6.13).

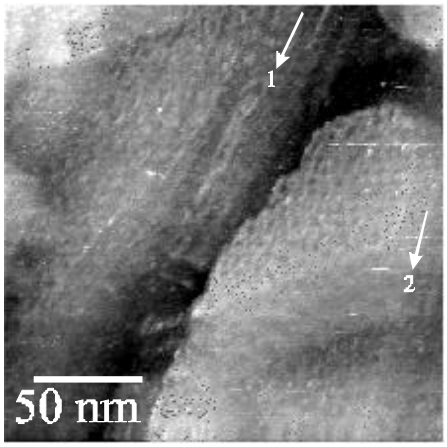

Figure 6.13: STM constant current image of C11A3 on TSG (U_t = 500 mV; I = 50 pA). Different Au crystallites with different alignments of adsorbed molecules indicated with black arrows.

On a sub-nanometer scale a periodic pattern has been recorded in Fig. 6.14.

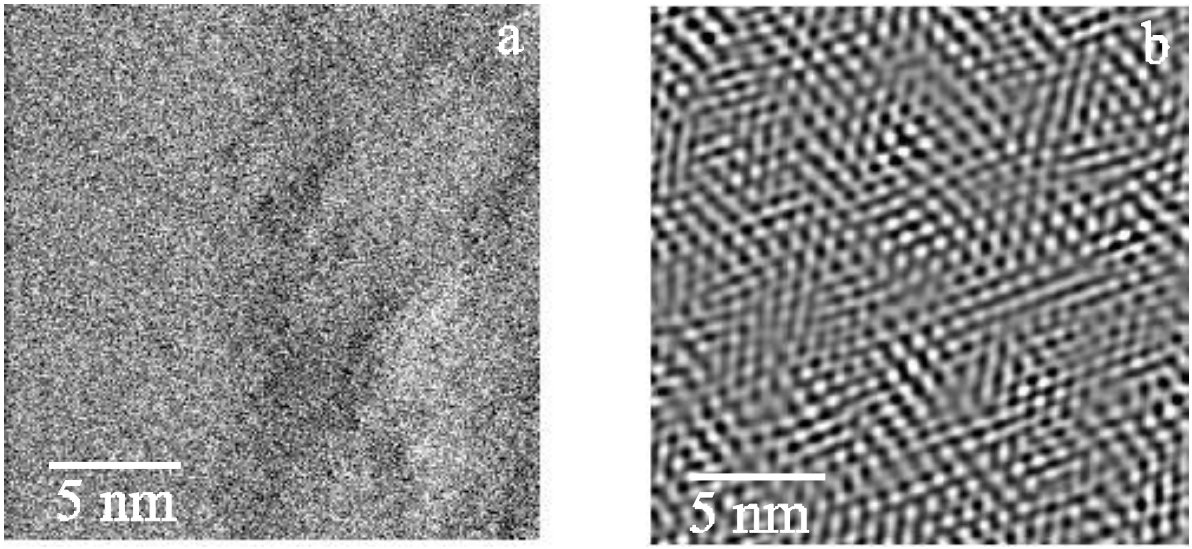

Figure 6.14: STM image of sample C11A3 on Ni supported-TSG surface. U_t = 500 mV; I = 50 pA. a) Unfiltered image; b) band pass filtered image. Although a high frequency noise blurs the raw image, the lattice of the adlayer can be recognized in both images.

It appears clear that the chemical stability of the system, both in solution and as a thin film on Au, is decreasing with an increasing quantity of conjugated molecules. Since a well defined hexagonal lattice has been visualized completely only on fully saturated alk*a*nethiols (sample C11E in Fig. 6.9), it is hazardous to conclude something about the different electrical

resistivity measured on the different samples, i.e. to estimate the effective resistance of the different molecules investigated. Nevertheless we can note that contrasts due to single ends of alk*a*nethiol molecules have been imaged using the following tunneling parameters:

Sample C11A1: 400 mV and 3.5 nA (corresponding to R= 114 MΩ);

Sample C11A3: 800 mV and 200 pA ; 500 mV and 50 pA (corresponding to R= 4-10 GΩ);

Sample C11A5: 700 mV and 65 pA ; 800 mV and 40 pA (corresponding to R= 10.7 - 20 GΩ).

This indicates that the electrical resistivity increases with the increasing quantity of fully saturated alk*a*nethiols in the layer.

Sample C11A2 and C11A4, due to the lower quality of the Au surface, did not exhibit any extremely flat area and, because of this reason molecular resolution images have not been achieved.

IV) Thiol end-functionalized C_{11} pentaene have been self-assembled on Au sublimed films:

C11A

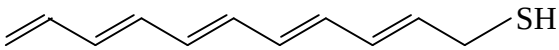

Deposition of the organic solutions onto Au discs have been performed both in Strasbourg with ultrafresh polyenes (for samples C11A10-C11A17, see table 6.2) and in Berlin with some of them stored frozen for 9 days (samples C11A18- C11A24).

In table 6.2 the 2mM solutions in benzene, are listed which have been used for the chemisorption.

As previously observed:

- The gold etching confirms that alkanethiol molecules have chemisorbed on the Au surface;
- The stability of the system, both in solution and in the thin film on Au, is decreasing with

the increasing quantity of conjugated molecules. Moreover the roughness of the surface increases tremendously with the enhancing storage time of the organic films in a dark air environment;

- An estimation of the average electrical resistivity of the layer calculated for images with molecular resolution is listed in table 6.3.

Table 6.2: Sample of C11A mixed with saturated ones

Sample	**Unsaturated**	**Saturated**	**Bath time**
C11A10	100 %	0 %	18 hours
C11A11	95 %	5 %	18 hours
C11A12	80 %	20 %	18 hours
C11A13	20 %	80 %	18 hours
C11A14	5 %	95 %	18 hours
C11A15	100 % 50 %	0 % 50 %	for 1 hour for 17 hours
C11A16	100 % 50 %	0 % 50 %	for 6 hour for 12 hours
C11A17	100 % 0 %	0 % 100 %	for 2 hour for 16 hours
C11A18	100 %	0 %	24 hours
C11A19	95 %	5 %	24 hours
C11A20	80 %	20 %	24 hours
C11A21	20 %	80 %	24 hours
C11A22	5 %	95 %	24 hours
C11A23	0 %	100 %	24 hours
C11A24	100 % 0 %	0 % 100 %	for 4 hour for 20 hours

Table 6.3: Sample of C11A mixed with the fully saturated analogue: electric properties

Unsaturated	**Saturated**	**U_t**	**I_t**	**Mean Resistance**
100%	0%	400 mV	3.5 nA	114 MΩ
80%	20 %	800 mV	200 pA	4-10 GΩ
0%	100%	700 mV	65 pA	10.7 - 20 GΩ

These results clearly indicate an increasing resistance with the increasing quantity of fully saturated alk*a*nethiols.

In contrast with the previous experiments a periodic lattice has been visualized also on 100% unsaturated alk*e*nethiols (image not shown), although the quality of the imaging was poorly reproducible in terms of lattice spacing. In the present case samples C11A15, C11A16, C11A17, C11A24, which were prepared according to different procedures, did not exhibit a different morphology and stability, also if compared to the related pure unsaturated samples C11A10 and C11A18.

Thus, it is concluded that the stability of the synthesized polyenes is rather poor on both Au and Ag substrates. This did not allow to achieve reproducibly molecular resolution STM imaging and quantitative evaluation of the resistance of the adsorbed monolayer, even though the results are qualitatively in line with an increased conductivity with the unsaturation of the alkyl chains.

6.2 Role of the substrate in physisorption

The requirement for a well controlled and reproducible physisorption of organic layers on solid substrates is an extreme flatness of the support, a well defined chemical composition and cleanliness of the surface to be coated.

As introduced in chapter 4, molecules tend to adsorb on the surfaces in different ways, with one parameter being the conductivity of the support.

A typical conductive substrate used for STM investigations is highly oriented pyrolitic

graphite (HOPG) [Bin87] (Fig. 6.15) which is a layered substrate that can be freshly prepared by cleaving its surface with an adhesive tape. An atomically flat surface on a micrometer scale is in this way made to appear. This flat interface is neutral and inert to organic solvents. Therefore it should be ideal for the self-assembly of either neutral or ionic adsorbates, since electrostatic interactions can be neglected.

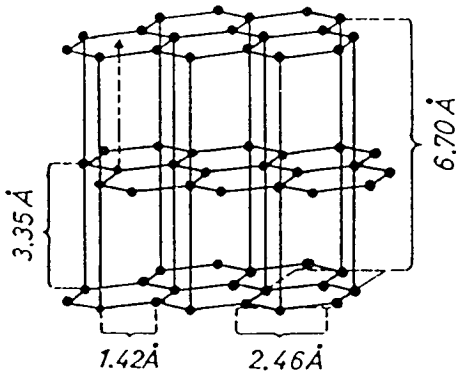

Figure 6.15: HOPG crystallographic structure.

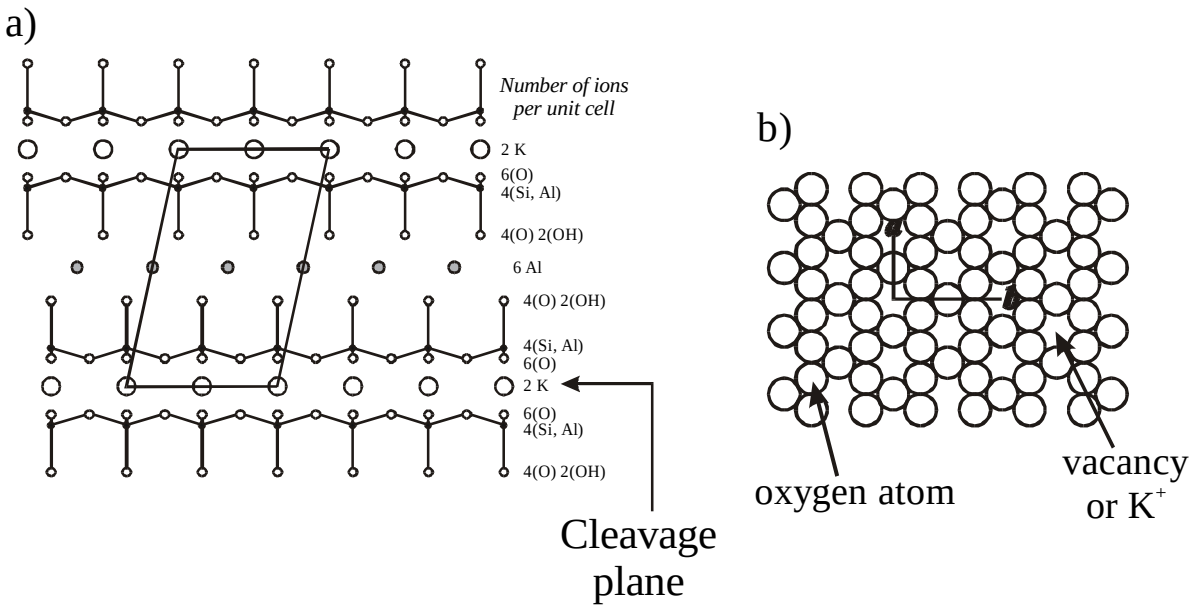

Figure 6.16: Layer structure of muscovite mica structure: A) Side view; B) Top view: the cleaved plane is the basal plane, composed of hexagonal array of oxygen ions with regular vacancies which are randomly filled with potassium. Unit cell: a= 5.2Å , b=9.0 Å.

Other typically flat layered conductive substrates used for STM studies are dichalcogenides [Wil69]. They posses various chemical compositions and structures, which makes it possible to select the ideal support for a given study. Unfortunately they are only rarely commercially available, and therefore they are not so wide spread as HOPG. Moreover they are chemically less stable.

On the other hand, the most used insulating support for SFM investigations is ruby mica (muscovite) which is a composite of sheets, belonging to the phyllosilicates. In this crystal a layer of octahedrally coordinated aluminum cations is sandwiched between two identical layers of linked $(Si,Al)O_4$ tetrahedra (Fig. 3a). Two of these tetrahedrally coordinated sheets are linked by an interlayer of potassium cations. The lamellar cleavage takes place between these tetrahedral layers exposing a basal plane of oxygens (Fig. 3b) with a structural imbalance of charge and a partial potassium coverage. The charge imbalance is due to the isomorphous substitution of the cations coordinated in the tetrahedral sheet or in the octahedral layer that is located underneath. In the case that Al(III) replaces Si(IV), the overall charge gets negative by one elementary charge. This charge imbalance is neutralized in the solid state by interlayer potassium cations [Dee65]. The maximum theoretical lattice imbalance is taken as the number of surface sites per square meter $N_S = 2 \times 10^{18}$ sites/m^2 of surface, or one charge site per 46.8 $Å^2$ [Nis94,Nis95]; this leads to a surface charge density σ = 0.34 C/m^2. According to this, a very high limiting "local" concentration (estimated to be up to 33.5 M) of cations on the mica surface is reached [Sam96]. When mica is cleaved the plane indicated by the arrow in Fig. 3a is split, and potassium cations left on the two split surfaces only partially screen their negative charges.

6.3 Phenyleneethynylene trimers

6.3.1 Introduction

A fine tuning of the performance of molecular based electronic devices depends on the spatial arrangement of the molecules. Therefore a crucial issue is to drive the molecular self-assembly onto flat solid substrates towards highly ordered, reproducible and thermodynamically stable supramolecular structures [Leh93]. In this context oligomers are widely investigated as model compounds of their related macromolecules for their electronic

properties [Mül98a]. Among conjugated species, *para*-phenyleneethynylene derivatives have received a reduced attention [Tou96, Gie96, Bun00]; besides their optoelectronic properties [Tad96, Wed96], they possess a remarkable stiffness and linearity along the conjugated backbone [Mor94, Wau96] which are features that can play a pivotal role in the 2D and 3D self-assembly into well-defined nanostructures. The capability of Scanning Probe Microscopies to achieve true atomic resolution imaging renders them the only techniques that up to now can give evidence of structural defects at the atomic level [Bin83b, Ohn93].

6.3.2 STM on physisorbed monolayers

A monodisperse molecular system physisorbing at the interface between its almost saturated solution and an Highly Oriented Pyrolitic Graphite (HOPG) substrate can assemble in an epitaxial monolayer following the three-fold symmetry of the support [Rab91a]. The monocrystalline structure of α-phenylethynyl-ω-phenyl-ter[1,4-(2,5-dihexylphenylene) ethynylene)] (**2**) (Fig 6.17) is displayed in Fig. 6.18.

Both the aliphatic side chains and the conjugated skeletons lie flat on the (0001) plane of graphite. Since the contrast in STM imaging is mainly ruled by the energy difference between the electronic states of the substrate and the ones of the adsorbate, darker parts can be assigned to the aliphatic groups, characterized by a larger energy difference, and bright rods can be recognized as the conjugated backbones, with a smaller energy difference [Laz97].

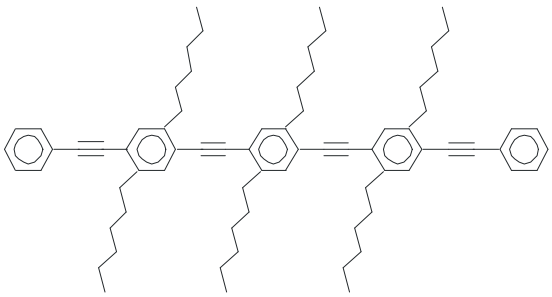

Figure 6.17: α-phenylethynyl-ω-phenyl-ter[1,4-(2,5-dihexylphenylene)ethynylene)] (**2**).

Unlike most of the organic compounds investigated at the solid-fluid interface with STM

[Rab91b], there is no evidence that in the system described here the alkyl chains are aligned along one of the crystallographic axis of the HOPG substrate.

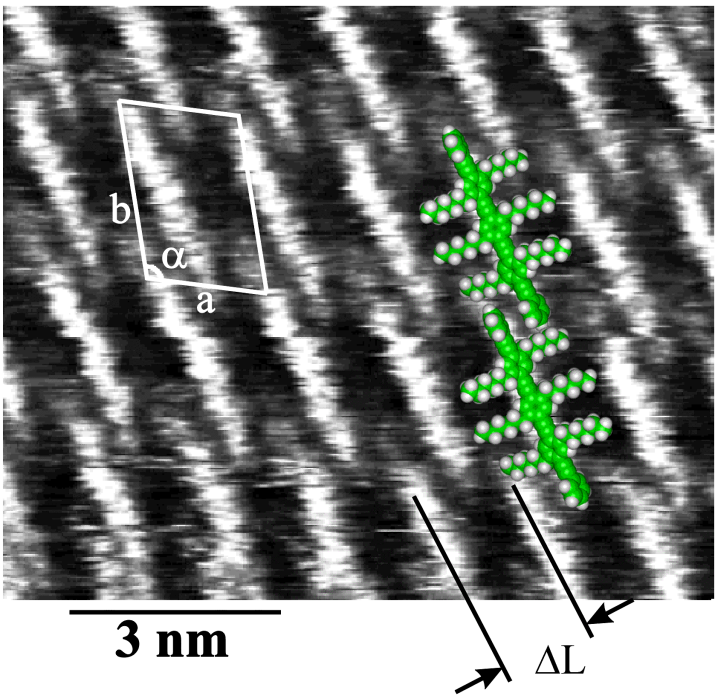

Figure 6.18: STM current image of **2** in 1-phenyloctane imaged at the solid-liquid interface on HOPG (U_t=1.2 V , average I_t= 1.0 nA). 2-D crystal structure with its unit cell, averaged over several images amounts to a=(1.78±0.09) nm, b=(2.90±0.18) nm, α=(113±5)°. The distance between neighboring backbones is in this case ΔL=(1.46±0.11) nn.

The spacing between neighboring parallel backbones, which can be attributed to the width of the molecules, amounts to only ΔL=(1.46±0.11) nm. It is considerably smaller than the 1.9 nm calculated for the case with the alkyl chains extended. This indicates that the side-chains are disordered between adjacent parallel backbones, since an interdigitation of the hexyl groups can be excluded because of steric hindrance. This can be considered a consequence of their high mobility at room temperature. In this case important for the formation of tightly packed crystals epitaxially grown on the basal plane of the substrate seems the remarkable stiffness of the alternating aryl and ethynyl groups in the backbone.

On the other hand, a related trimer has been studied bearing thiol end-groups in the α and ω position which have been protected by carbamoyl functions just in order to increase the stability of the moiety in air environment at room temperature. Its chemical formula and its proper chemical name are given in Fig. 6.19. The crystal structures have been determined

both by means of Scanning Tunneling Microscopy (STM) at the solid-liquid interface and by X-Ray Diffraction (XRD) on the single crystal.

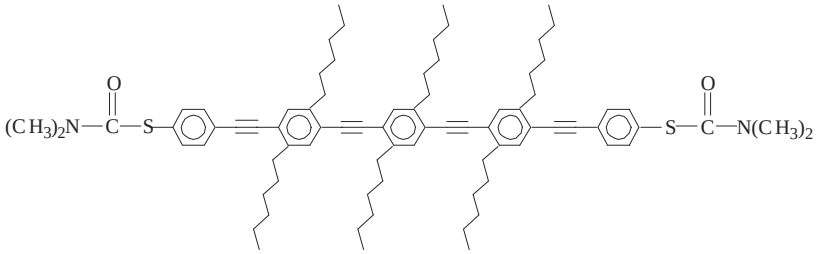

Figure 6.19: 1,4-Bis-[[2,5-dihexyl-4-[[4-[(N,N-dimethylcarbamoyl) thio]phenyl]ethynyl]phenyl]ethynyl]-2,5-dihexylbenzene (**1**).

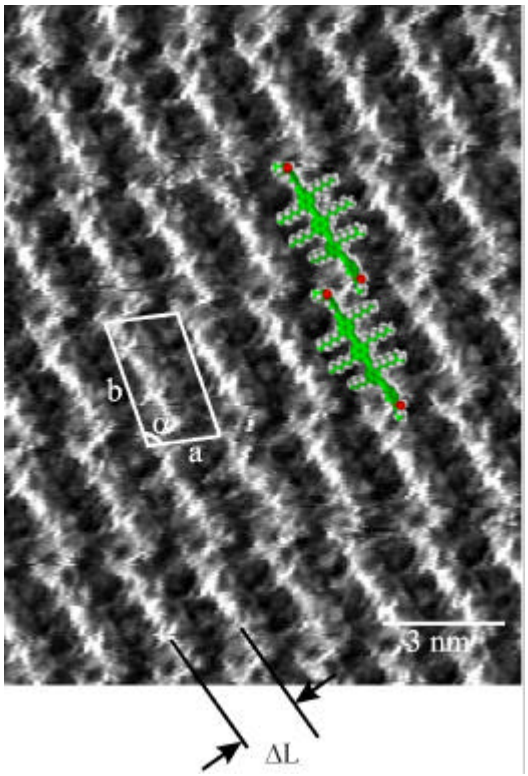

Figure 6.20: STM constant current image of **1** in 1-phenyloctane imaged at the solid-liquid interface on HOPG. U_t = 1.2 V , I_t = 1.0 nA. 2-D crystal structure with its unit cell, averaged on several images: a = (1.83 ± 0.11) nm, b = (3.42 ± 0.12) nm, α= (108 ± 5)°. The distance between parallel backbones is ΔL = (1.52 ± 0.08) nm. The angle between the backbones and the lamella main direction is (67 ± 2)°. Superimposed are two molecular models.

STM investigation of **1** at the solid-liquid interface gave rise to a similar result as for the derivative without the protected thiol end-groups (**2**): the molecules pack in a monocrystalline structure, displayed in Fig. 6.20. A slight interdigitation of the end functionalities in the 2D pattern can be seen. In this case it is likely to be induced by both to hydrogen bonding between adjacent carbamoyl groups and by the steric hindrance of the end-groups that impedes a columnar packing, which was observed for mixtures of alkanes monolayers crystallized on the basal plane of HOPG [Hen92].

On a larger scale the structure is polycrystalline. Single crystallites are characterized by a well-defined molecular orientation with respect to the crystalline substrate. The high resolution imaging made it possible to record defects on the nanometer and the sub-nanometer length scale. The first type of defects are missing molecules within a single molecular crystal; an example of two missing molecules is indicated by an arrow in Fig 6.21. The second type of defects are the domain boundaries that delimitate each crystallite. At these frontiers the molecules are less well packed. This issue will be discussed further in paragraph 6.3.5.

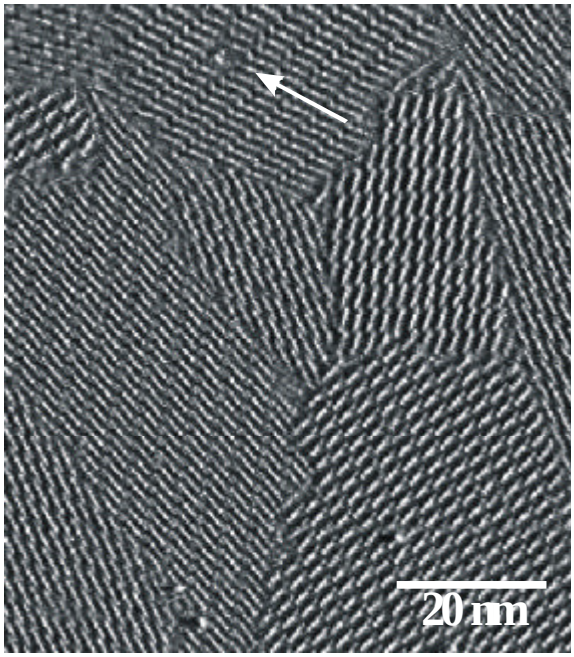

Figure 6.21: STM constant current image of **1** in 1-phenyloctane imaged at the solid-liquid interface on HOPG. U_t = 1.2 V , I_t = 1.0 nA. Polycrystalline structure made of single crystallites with different molecular orientations. The arrow indicates a defect (two missing molecules) in a crystal lattice.

6.3.3 XRD on single crystals

The crystal structures of phenyleneethynylene trimers **1** and **2** has been determined here for the first time by means of XRD. The structure of the related monomer **3** (Fig. 6.22) has been also investigated for comparison.

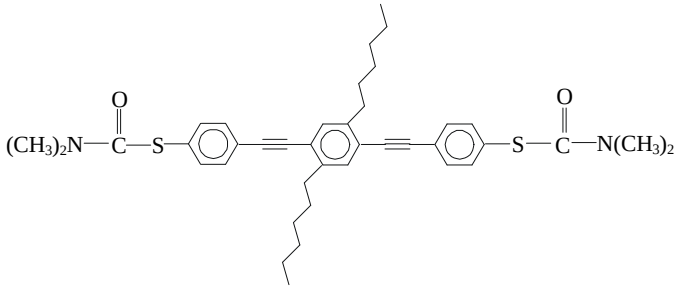

Figure 6.22: Chemical formula of the monomer: 1,4-Bis[2-[4-[(N,N-dimethylcarbamoyl)thio] phenyl]ethynyl-2,5-dihexylbenzene (**3**).

ORTEP plots (fORtran Thermal-Ellipsoid Plot program for Crystal Structure Illustrations) [Joh70, Joh72] of the two crystal structures are shown in Fig. 6.23. Their crystal and refinement data are listed in Table 6.4.

Table 6.4: Crystallographic data and details of the structure refinements of α-[[4-[(N,N-dimethylcarbamoyl)thio]phenyl]ethynyl]-ω-[4-[(N,N-dimethylcarbamoyl)thio]phenyl]-ter[(2,5-dihexylphenylene-1,4)ethynylene)] (**1**) , α-phenylethynyl-ω-phenyl-ter[(2,5-dihexylphenylene-1,4)ethynylene)] (**2**) and 1,4-Bis[2-[4-[(N,N-dimethylcarbamoyl)thio] phenyl]ethynyl-2,5-dihexylbenzene (**3**). The structures were solved by direct methods (SIR92) and refined by full-matrix least squares analysis.

Structure	(**1**)	(**2**)	(**3**)
a (Å)	5.9262(4)	5.6655(6)	8.6807(5)
b (Å)	13.897(1)	11.943(2)	9.1165(5)
c (Å)	22.503(2)	23.154(5)	23.696(2)
α (°)	94.476(3)	84.848(6)	90
β (°)	90.998(6)	86.150(9)	98.095(6)
γ (°)	102.689(6)	80.216(12)	90
V ($Å^3$)	1801.3	1535.5	1856.5
Z	2	2	4
D_x (gcm^{-3})	1.097	1.064	1.167
μ (cm^{-1})	1.133	0.552	15.256
space group	P -1	P -1	P $2_1/n$
number of unique reflections	7427	6061	3863
number of observed reflections	3039	2406	2111
R [a)]	0.084	0.0583	0.0477
R_w [a)]	0.092	0.0775	0.0591
T (K)	210	210	298
λ [b)]	Mo Kα	Mo Kα	Cu Kα
diffractometer [b)]	Nonius KCCD	Nonius KCCD	Nonius CAD4

Technical details:

[a)] R= refinement; R_w=weighted refinement

[b)] Diffractometer used either Nonius Kappa-CCD instrument employing graphite-monochromated Mo Kα radiation, or Enraf Nonius CAD-4 with graphite-monochromated Cu Kα radiation.

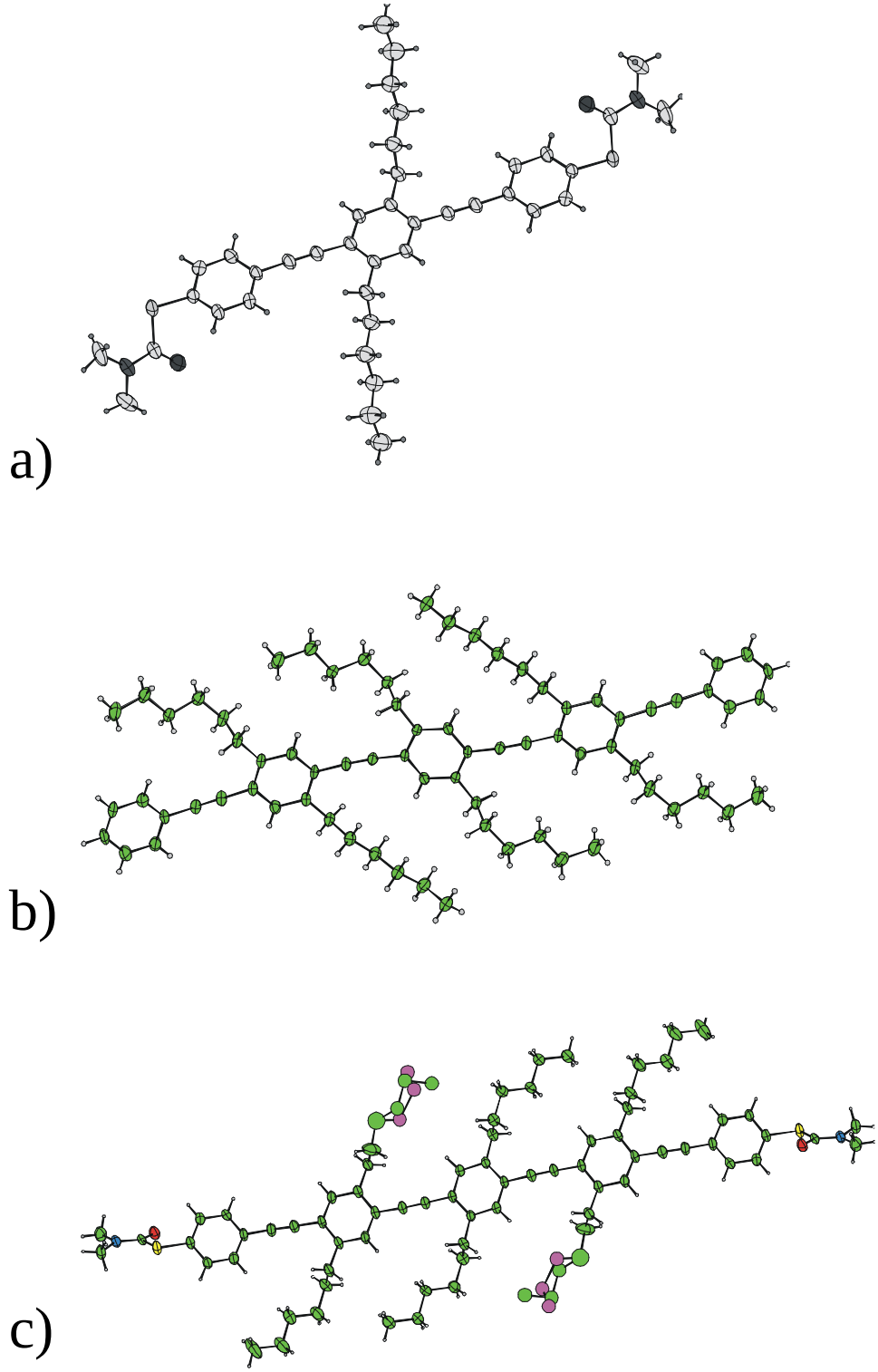

Figure 6.23: Single molecular structure in single crystals of a) (**3**), b) (**2**), c) (**1**).

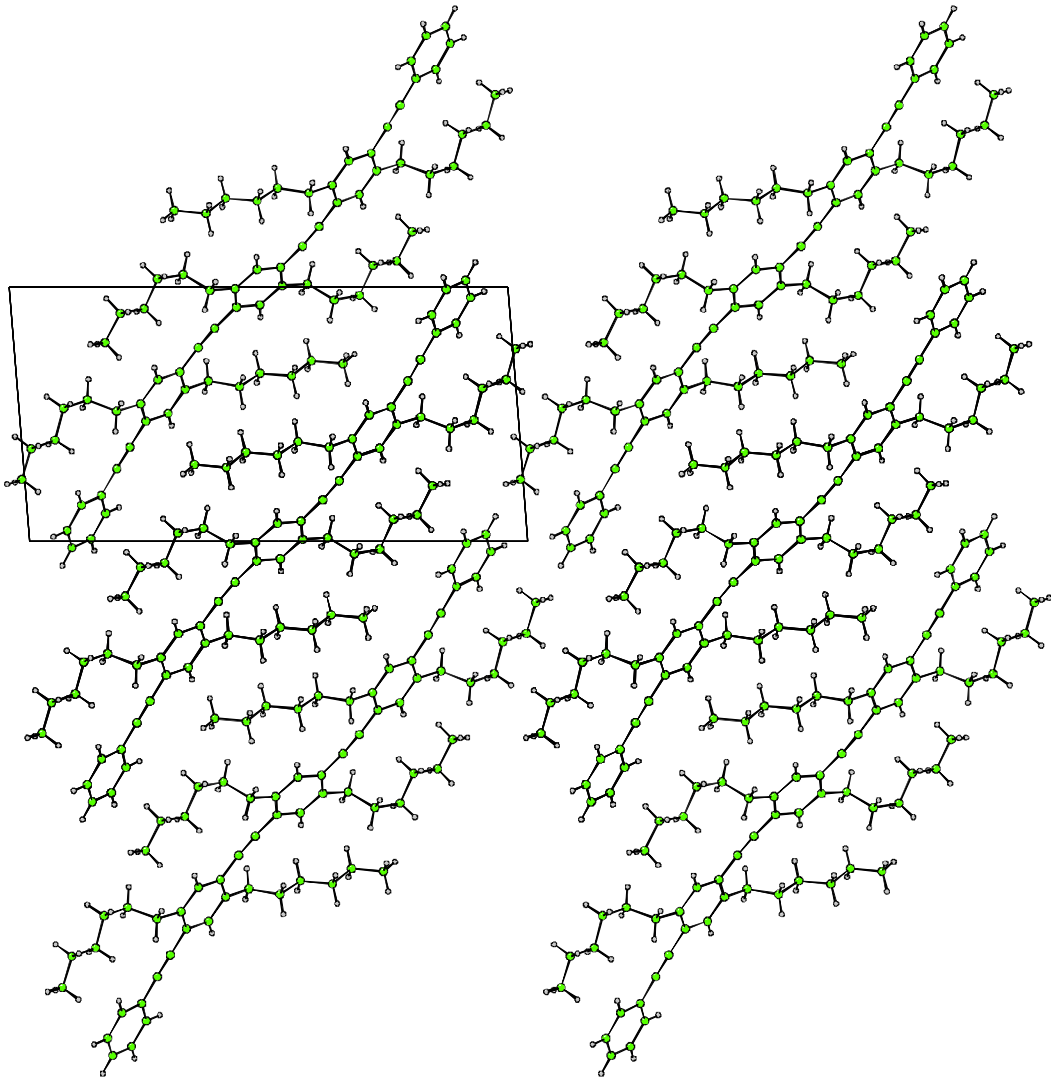

Figure 6.24: Crystallographic structure of α-phenylethynyl-ω-phenyl-ter[(2,5-dihexylphenylene-1,4)ethynylene)] (**2**).

In all three cases the phenyl rings are oriented approximately parallel to each other and the hexyl side chains are coplanar. While in the monomer (**3**) (Fig. 6.23a) the side chains assume a regular all-trans conformation, in the case of the trimers (**1** and **2**) they are bent (Fig. 6.23b-c). The reason for this behavior are intermolecular interactions as shown in Fig. 6.24 and Fig. 6.25: the hexyl side chains do not interdigitate but are bent towards the main chain direction in order to fill the free volume between them. The tilt angle between the main chain and the side chain amounts to 45° for (**2**) and 35° for (**1**); one reason for this difference is likely to be the changed length of the molecule: (**1**) is longer and therefore possesses more free volume to be filled. Consequently in the case of (**1**) the side chains can be more tilted than for (**2**). According to the smaller tilt angles also the distance between the backbones decreases from 9.5 Å to 9.0 Å for (**2**) and (**1**), respectively. An important role for this decreased spacing can

also be ascribed to the stronger interactions between the end-groups in the case of (**1**) than for (**2**).

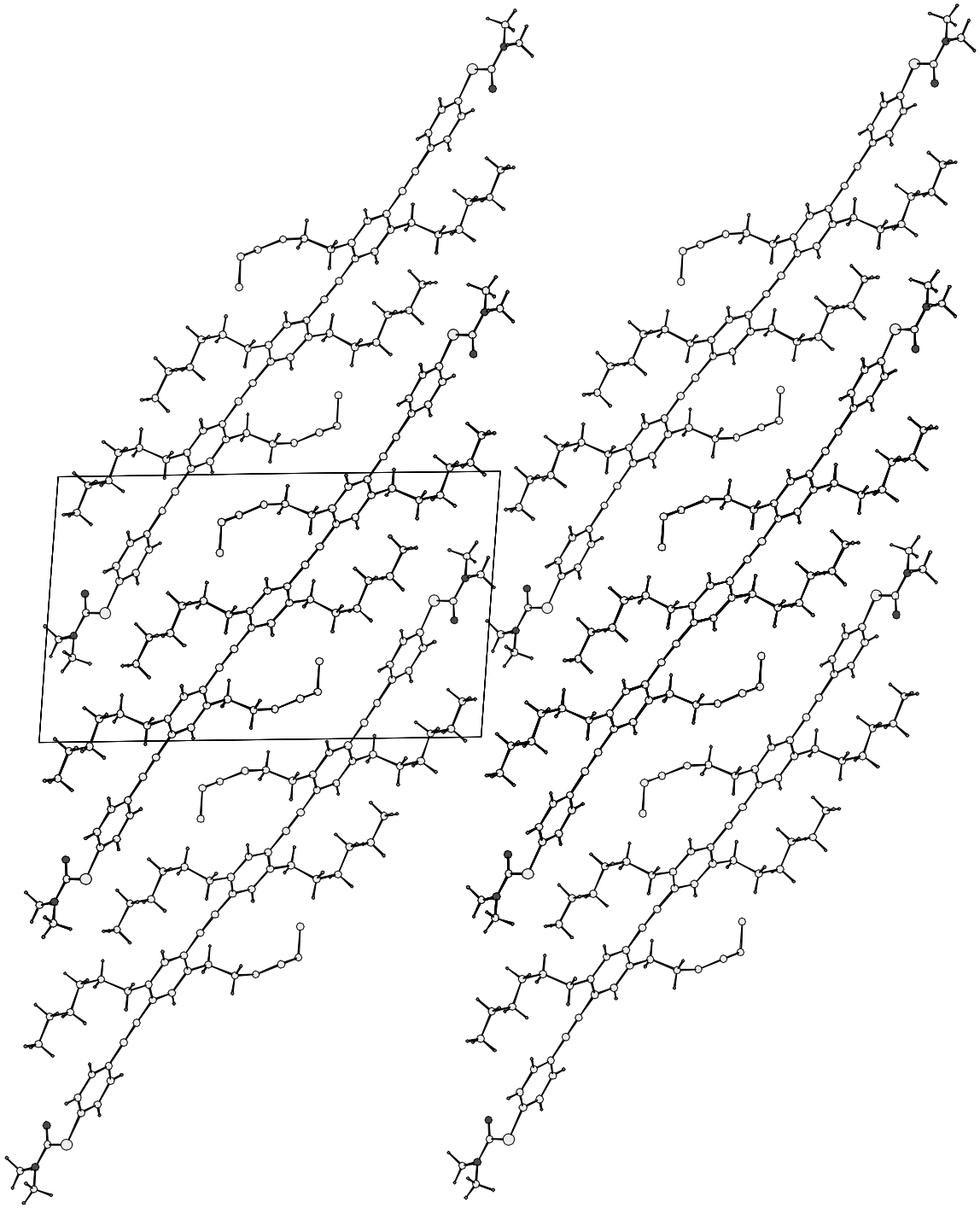

Figure 6.25: Crystallographic structure of Crystallographic intermolecular structure of α-[[4-[(N,N-dimethylcarbamoyl)thio]phenyl]ethynyl]-ω-[4-[(N,N-dimethylcarbamoyl)thio]phenyl]-ter[(2,5-dihexylphenylene-1,4)ethynylene)] (**1**).

Similarly to the 2D case (STM image in Fig. 6.20) the trimer molecules pack regularly parallel to each other forming lamellar structures. Both **2** and **1** exhibit an arrangement which could suggest a high mobility of the side chains at room temperature. Out of 6 hexyl side chains the molecule **2** posseses 4 that are bent and 2 which are rather straight (Fig. 6.23b), while **1** exhibits in these 2 side chains two approximately statistically occupied orientations of the last propyl function (Fig. 6.23c).

6.3.4 Discussion

The spatial organization of molecules in 2D and 3D assemblies depends on intramolecular, intermolecular as well as interfacial forces. This implies that different environments lead to distinct order on the molecular scale. Hence, it is of prime importance to compare and correlate molecular structures in single crystals and in 2D physisorbed monolayers.

The phenyleneethynylene derivatives consist of three essential parts: the conjugated main chain, the aliphatic side groups and the end functions (in α and ω positions). The contribution of each one in the self-assembly can be distinguished. The conjugated backbones exhibit polarizable π electrons that give rise to strong intermolecular interactions. This is the case in the physisorbed monolayers on HOPG where, due to a rehybridization of the π-states of the skeletons with the ones of the conductive substrate, the unsaturated main chains tend to adsorb flat on the basal plane of the support, maximizing in this way the overlap of its electronic states with the ones of the substrate, as suggested from ab-initio calculations [Bis00]. Moreover the remarkable stiffness along this backbone is also important for the packing into lamellae both in 2D and 3D.

On the other hand, the lateral chains play a primary role in conjugated oligomers and macromolecules. They are commonly attached to the backbones to enhance the solubility in organic solvents. In addition they play an important role also in the self-organization and self-assembly of the organic system in 2D and 3D architectures on flat solid substrate [Rod89]. In the present case both XRD and STM results give evidence for the remarkable mobility of the side-groups at room temperature. For the first case indeed two different structural conformations of the terminal propyl functions of the hexyl side chains can be recognized in Fig. 6.23c. In the latter one, even with our home made STM apparatus that allows very fast scanning (200 Hz/line), it was not possible to resolve the single hexyl chains.

This may be attributed to the high conformational mobility of the relatively short alkyl chains. Indeed, the increasing order of solid state aggregates in other PPE derivatives with the length of the side chains can in fact be interpreted in terms of decreasing dynamics of the lateral substituents [Ofe95].

Finally, the end-functions in α and ω position can provide a further stabilization to the molecular arrangement. This is the case of **2** where the carbamoyl end groups interdigitate with the neighboring molecules because of a hydrogen bonding type of interaction.

6.3.5 Dynamics of molecules at the solid-liquid interface

Surfaces grown under non equilibrium conditions are always prone to rearrangement [Bar95,Bisc97]: understanding the mechanisms and kinetics of such a reorganization is necessary to predict the film stability. Subsequent temporal evolution towards the equilibrium state must involve coarsening, i.e., an increase in the characteristic length-scale of the dominant structure. In this context efforts have been mainly devoted to dynamics of metallic or semiconducting thin films [Zin92, Wen96, Mor96, Car97]. On the other hand, physico-chemical phenomena on organic interfaces still need to be understood better at a molecular level [Ulm91], revealing the role of intermolecular interactions in their *ensemble*. In particular little is known on the processes occurring at the liquid-solid interface [Sta95a].

An investigation on a true molecular scale of the coarsening within an organic monolayer can be carried out by means of STM. It allows to characterize the motion of single molecules at the domain boundary between molecular crystals self-assembled at a surface and to discern the thermodynamic and kinetic contributions to the total energies governing this process. Fig. 6.26 shows the Ostwald ripening process of a phenyleneethynylene trimer monolayer of **1** at the solid-liquid interface. The dynamics of the molecular crystallites on a 22 minutes time scale has been recorded. Small domains tend to shrink and disappear while bigger crystals enlarge.

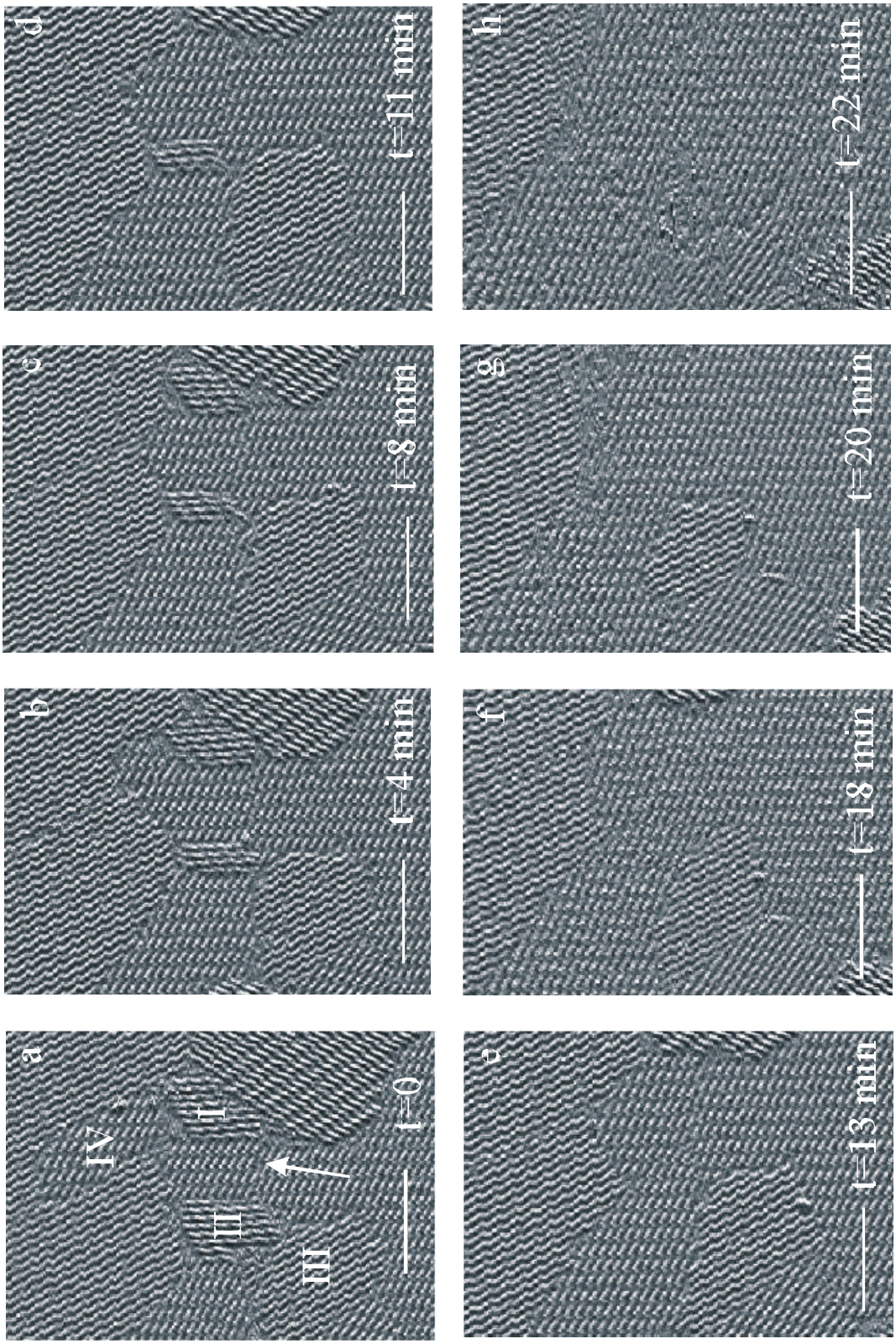

Figure 6.26: STM constant current images. Evolution of the 2-D polycrystal structure of **1** at the solid-liquid interface during 22 minutes: Ostwald ripening phenomena brought about by the reorientation of single molecules in island I, II, III, IV. The white scale bar is 20 nm. Arrow in a) indicates a domain boundary of the type shown in Fig. 6.27a.

Observing carefully the first micrograph in Fig 6.26 one can notice that the different domain boundaries in the polycrystalline structure can be divided into two different classes. The first presents equal orientations of the main molecular axes in the two neighboring islands that differ only by a slight translation of the crystal structures relative to each other (scheme in Fig. 6.27a and indication by the arrow in Fig 6.26a). The second type of domain boundaries is made of molecules oriented differently (Fig. 6.27b); several of these types are visible in Fig. 6.26a. The energies associated with the transitions leading to a large single crystal in these two cases can be discussed for the thermodynamics (energetic gain) or the kinetics (activation energy).

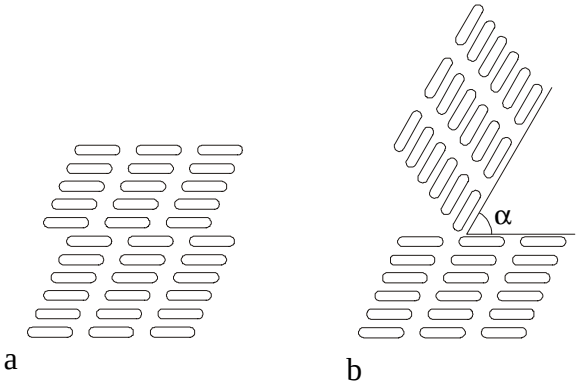

Figure 6.27: Scheme of different types of molecular packing in neighbor domains. Single molecules are represented as a rod. a) translated; b) rotated.

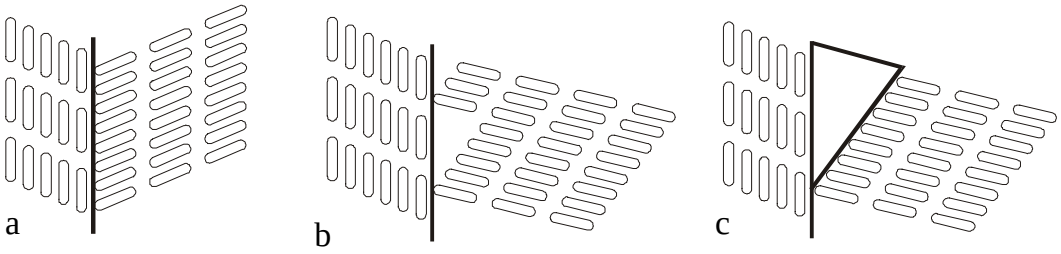

Figure 6.28: Scheme of the molecular packing at the crystallite frontiers.

In the first case (Fig. 6.27a), where the reaction consists of a simple translation, is characterized by a smaller activation energy but the thermodynamic gain is also small. In the

latter case (Fig. 6.27b), the system requires to undergo a rotational motion that needs a larger activation energy to occur, albeit the thermodynamic energy gain is bigger since the new state that is achieved is energetic favorable.

Focusing the attention on the second class of domain boundaries because they are more recurring: at room temperature and atmospheric pressure on the minutes time scale individual molecular rods can change their tilt angle with respect to the underlying substrate without a transition to the supernatant solution. This phenomena, known as Ostwald ripening, is a 2D reaction controlled process that takes place at the boundary between different crystals; it is governed by a minimization of the interfacial energy (or line energy in 2D) [Sta95a]. A strong influence of the STM tip in this process has been ruled out [Sta95a] and confirmed in the present case. In fact simply by stopping the scanning for approximately half hour and restarting the imaging in the same area of the sample revealed that the disappearance of small domains took place irrespective of the scanning of the tip. In addition an evaluation of the kinetics of the process made it possible to reject the hypothesis that this coarsening is governed by diffusion [Sta95a]. The tight molecular structure allowed to monitor this reaction with an increased resolution by following the motion of individual rods in real time.

From the tightness of the molecular packing at the domain frontier, the stability of a front or a predominance of one domain with respect to the other may be predicted. A careful observation of the images in Fig. 6.26 allows to classify domain boundaries according to three types (scheme in Fig. 6.28). The most stable interface, characterized by a remarkable tightness, is made up by two domains packed along one head to head direction oriented parallel to the frontier (case **A**, Fig. 6.28a). A less stable boundary (**B**) consists of a stable domain that is tightly packed to the front and another one that is more loosely packed (Fig. 6.28b). The area between the two crystals that does not exhibit crystallized molecules is characterized by a remarkable dynamics of the molecules: in these zones the trimers are extremely mobile (not immobilized at surface) and there may be also inclusions of the molecules of the solvent. The more loosely packed crystal, after some time, it will reduce its area. A further extension of the limit (free volume) (**C**), which reveals higher dynamics of the molecules in this region, gives rise to an even more unstable interface (Fig. 6.28c).

Using this approach it is possible to classify domains in Fig. 6.26. **IV** is surrounded by three lines of type **B**, and one of **C**. These conditions are characteristic of an unstable region and in fact it dissolves very rapidly. **II** from Fig. 6.26 a to b decreases its area loosing 4 molecules, but acquiring a very stable conformation made by two lateral **A** type frontiers and two **C** type.

The stability of its contour allowed **II** to have a relatively long life, albeit the really small size of the crystal. **I** appears very unstable because limited only by one **A** front, and three **C** ones; indeed it disappears in 9 minutes. The more enduring one turned out to be **III** that is larger than the others and surrounded by four **B** facets. It expires in 22 minutes.

These results suggest that the stability of the domain boundary is related to two factors:

1. geometry of the molecular packing at the domain boundary;
2. size of the crystallite.

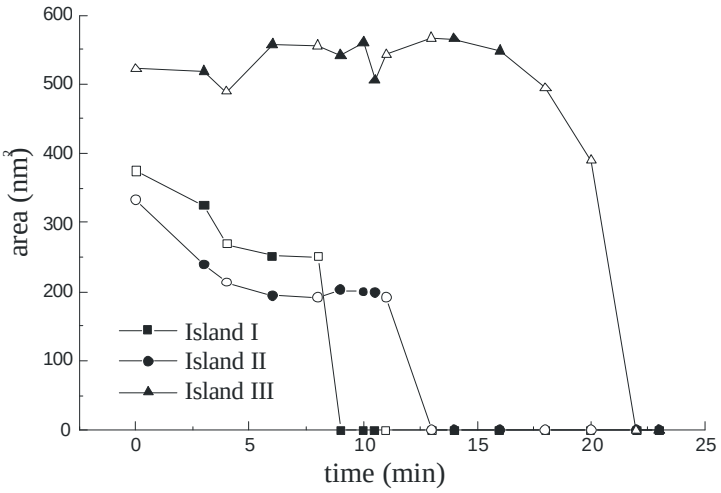

Figure 6.29: Evolution of domain areas with time. Filled symbols correspond to STM images in Fig. 6.26. Open symbols: images not shown.

In addition, an analysis of the kinetics of this process (Fig. 6.29) revealed that first an apparent metastable state exists, where the area of the domains is nearly constant within fluctuations of some nm^2; in this *apéritiv* the domain borders get sharper, along the two head to head directions of the molecular pattern (axes *a* and *b* of the unit cell), at the expense of single molecules that were exceeding the frontier, creating a polygonal shape domain. This plateau can last several minutes (for the less stable domains as shown schematically in Fig 6.28b,c) or for hours (for the more stable crystals, packed as shown in Fig. 6.28a). After this, a slight extension of the domain frontier takes place, which is accompanied by a considerable increase of the dynamics of the molecules. This enables the molecular reorientation reaction to occur emerging as an abrupt decrease of the crystallite sizes and a collapse of the domains in up to 2-4 minutes. This coarsening reminds of a phagocytation process carried out by big

crystallites at the expense of small ones. The molecular motion terminates in the thermodynamic equilibrium regime where only large crystallites extending over the whole substrate crystallites, i.e. over several thousands of nm^2, exists. The velocity of this molecular coarsening, in terms of the disappearance of molecular domains, averaging on several individual crystals, amounts to (160±66) nm^2/min. This rate is 1-2 orders of magnitude slower than for 2-hexadecyl-anthraquinone and tetradodecyl-octathiophene [Sta95a]; the difference is attributed to the ability of **1** to form a more closed packed crystal than the other two compounds. Further support of this explanation is the even slower rate detected for didodecylbenezene [Rab91b] that indeed forms a tightly packed crystalline structure on HOPG.

A secondary role in the STM analysis at the solid-liquid interface, that must not be neglected, is played by the concentration of the supernatant solution. A large activation energy barrier, i.e. the nucleation energy, has to be overcome for diluted solutions to form a crystalline monolayer at surfaces. Moreover, a higher number of defects like missing molecules inside a crystal or a broadening of the domain boundaries have been observed in this case. This is therefore likely to affect the lifetime of the metastable state in the Ostwald ripening process. Another important parameter in these kind of investigations is the density of the solution (that is strongly influenced by the density of the solvent) which if large, can slow down the molecular motion both in the solution and at the interface with the solid substrate.

The comprehensive live view of molecular coarsening at surfaces with a sub-molecular resolution have shown that the Ostwald ripening occurring in monolayers at the solid-liquid interface is a phenomenon mainly ruled by the interplay of intermolecular and interfacial forces on the basal plane of the substrate. The experimental data can be explained in terms of thermodynamics and kinetics of the molecular coarsening. After a metastable regime that have a life-time proportional to the tightness of the molecular structure on the surface, the phenomenon is driven by a minimization of the surface free energy.

6.4 Visualization of single macromolecules in monolayers

The aim of the present study is visualize for the first time a synthetic polydisperse molecular system self-assembled in monolayer at the solid-liquid interface, to gain insights into the conformation of the adsorbed molecule and to monitor with a sub-molecular resolution the macromolecular fractionation at the interface.

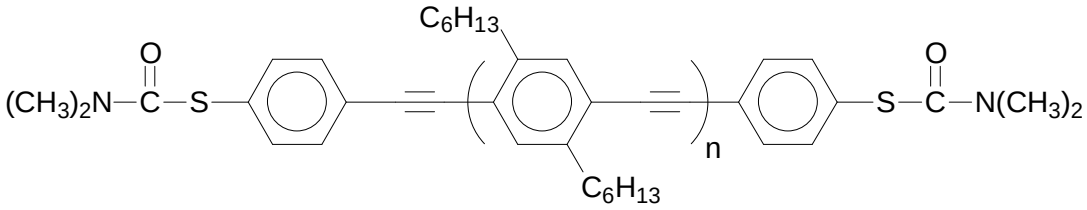

Figure 6.30: Chemical formula of (**4**): α-[[4-[(N,N-dimethylcarbamoyl)thio]phenyl] ethynyl]-ω-[4-[(N,N-dimethylcarbamoyl)thio]phenyl]-poly[(2,5-dihexylphenylene-1,4) ethynylene)].

The STM technique has been employed at the HOPG-solution interface of poly(*para*-phenyleneethynylene) derivatives with various contour lengths along the main chain.

In Fig. 6.31 the first reported molecularly resolved STM images of a synthetic polydisperse polymer at the solid-liquid interface is shown. The self-assembly occurred from an almost saturated solution of PPE (Fig. 6.30) at the interface with a HOPG substrate [Rab91a]. The monolayer exhibits a two dimensional nematic-like molecular order. Both the conjugated skeletons and the hexyl side groups are lying flat on the (0001) plane of the HOPG. The conjugated backbones appear brighter than the aliphatic chains because of a stronger current as previously noted for the case of the trimers (see paragraph 6.3.2). The spacing between neighboring parallel backbones, which can be attributed to the width of the molecules, amounts to $\Delta L=(1.62\pm0.10)$ nm. This is considerably smaller than the 1.9 nm calculated for the case with the alkyl chains extended but it fits well with what has been detected for shorter oligomers, where the side-chains have been found to be disordered between adjacent parallel backbones [Sam99a].

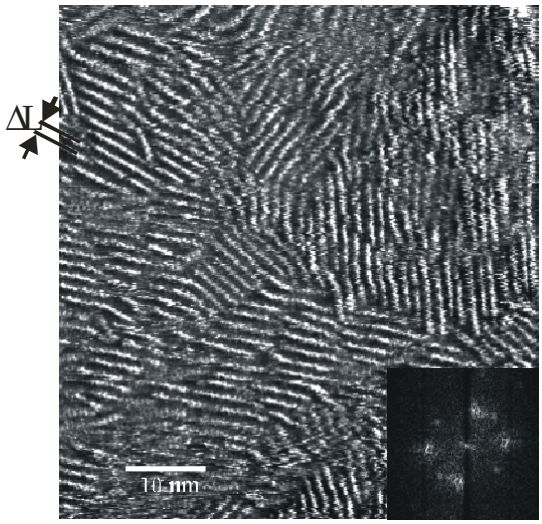

Figure 6.31: STM constant current image of a PPE **4** at the interface between the basal plane of graphite and an organic solution in 1-phenyloctane. U_t=1.2 V , average I_t= 1.0 nA. This PPE, according to ^{1}H-NMR analysis on the end-groups, possesses an average contour length 7.9 nm The molecular backbones exhibit a nematic orientation along preferred directions, as evidenced by the hexagonal pattern in the 2D-Fourier Transform. The distance between the backbones averaged over several images amounts to $\Delta L=(1.62\pm0.10)$ nm.

The 2D molecular arrangement is composed of domains with specific molecular orientations. The conjugated skeletons are aligned along preferred directions, according to the three-fold symmetry of the HOPG lattice, as visualized by the hexagonal spots in the 2D Fourier Transform (Fig. 6.31).

The stiffness of the molecular rods [Mor94, Wau96] and a low polydispersity allowed the molecules to pack in this 2D structure and, therefore, both played a key role for achieving this true molecular resolution imaging of the synthetic macromolecule. Also a finite mobility of the nanorods has been detected, revealing that molecules at the domain boundaries change their tilt angle with respect to the underlying substrate. This molecular dynamics occurs on the time scale of several minutes and can be attributed to a Ostwald ripening process.

Polymeric systems are *ensembles* of molecules with different sizes, that can be expressed in terms of molecular weight or for linear moieties also as molecular contour lengths. This distribution of molecular lengths (polydispersity) hinders the formation of a monocrystal structure in the solid phase. The formation of 2D and 3D crystals of this kind of systems occurs via self-segregation into areas with molecules of similar dimensions [Wan93]. This molecular domains posses a high degree of order, although their extension is small. The

phase segregation process has been observed on a large (micrometer) scale via a different contrast in electron microscopy micrographs [Wan93]. In the present case in fact the difference in the 2D structure of the monodisperse oligomer (see paragraph 6.3.2) and the polydisperse polymer, which on the average is almost three times as long as the trimer, can be is due to the different distribution of molecular lengths, which, for the case of the polydisperse system, does not enable the moieties to assemble into perfect crystals.

The time required for achieving molecular resolution imaging is much longer for the polymer. This is likely to be due to the self-segregation phenomenon and consecutive adsorption that takes place at the molecular level, allowing molecules with different lengths to pack locally well on the substrate.

The true sub-molecular resolution achieved on a synthetic polymer as the one shown in fig. 6.31 opens the possibility to measure for the first time from STM images the true length of the single macromolecules that are self-assembled on the (0001) plane of the HOPG substrate. This allows to study the phase segregation governing the self-assembly of a solid state phase of a polydisperse system. An example of this phenomenon that has been detected on a larger scale with Scanning Force Microscopy will be described later in this chapter in the case of the self-assembly of PPE into dry ribbon-like architectures.

6.4.1 Macromolecular fractionation

Other PPEs with an average contour length of 11.2 nm and 20.3 nm , respectively, (Table 6.5) have been investigated at the solid-liquid interface with STM. Their structures on the nanometer scale are shown in Fig. 6.32 and Fig. 6.33, respectively.

Table 6.5: Samples of PPEs investigated **4** with STM

No. of repeating units	9	14	35
contour length of molecule	7.9 nm	11.2 nm	20.3 nm
U = M_w/M_n	1.92	1.84	10.1

No. of repeating units, contour lengths of molecule (from ^{1}H-NMR analysis on the end-groups) and U=M_w/M_n from Gel Permeation Chromatography (PPP calibrated)

Comparing the three cases listed in Table 6.5, upon self-assembly of the macromolecule in 2D monolayers at the solid-liquid interface, it is possible to observe using STM the following features with increasing polymer length (from Fig. 6.31 – 6.33):

1. the molecules are more mobile. In particular in Fig. 6.32 and Fig. 6.33 the monolayer consists of areas with a stable and tight molecular packing alternated with others possessing a very high molecular dynamics; the structures of these latter ones can not be resolved with a molecular resolution imaging;
2. the average length of the molecules immobilized on the (0001) plane of HOPG increases;
3. the achievement of molecular resolution requires a longer waiting time indicating that the activation energy required for the self-segregation to take place increases;
4. the tunneling parameters that have been used for resolving the molecular structure suggest that with increasing polymer length the molecules tend not to pack flat on the basal plane of the substrate. This feature is likely to be due to the to the self-segregation that hinders the formation of a tightly packed monolayer. In addition the longer molecules possess a higher flexibility, and consequently the system need to loose more entropy for the structural rearrangement, because of the large number of possible states (conformation) which the system can attain.

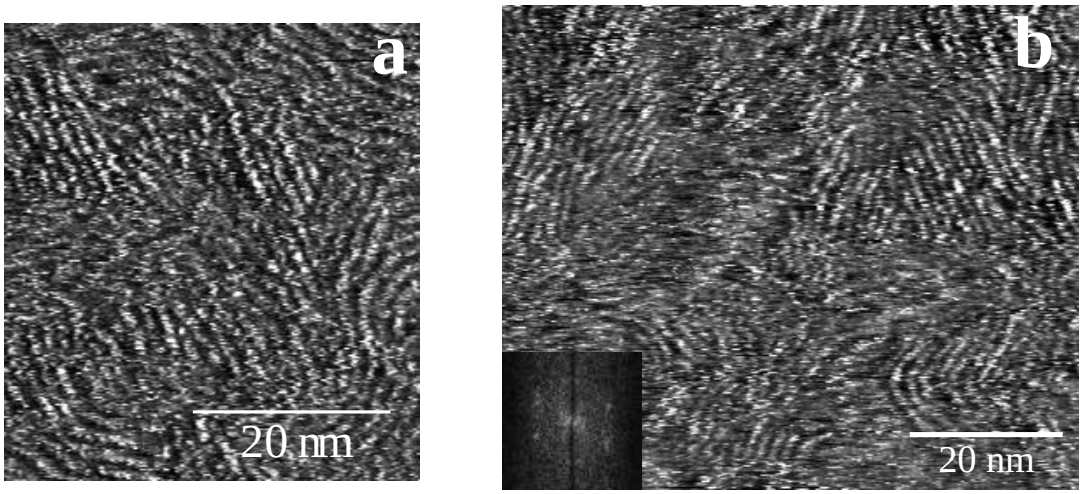

Figure 6.32: STM current images of a PPE **4** at the interface between the basal plane of graphite and an organic solution in 1-phenyloctane. This PPE, according to ^{1}H-NMR analysis on the end-groups, possesses an average contour length of 11.2 nm. The molecular backbones exhibit a nematic orientation along preferred directions, as evidenced by the hexagonal pattern in the 2D-Fourier Transform. a) U_t=1.7 V , average I_t= 0.2 nA; b) 1.35 V, average I_t=0.7 nA.

The macromolecules with an average length of 11.2 nm still organize in a nematic like structure, similar to the one observed for the 7.9 nm moiety with single backbones that are aligned along preferential orientations according to the symmetry of the substrate underneath. This degree of order is lost for the 20.3 nm long polymer.

The histograms in fig. 6.34 describe the distributions of rod lengths obtained from raw data STM current images. Because of the rather high stiffnes of the molecules and their packing that is not characterized by a columnar head to tail alignment, their contour length can be evaluated from STM images. This determination has been executed with an electronic ruler (using the software package Image Tools 1.27 produced by University of Texas - Health Science Center in Saint Antonio). The distributions of the lengths for several hundreds of single rods are plotted together with the Schulz-Zimm distributions, which theoretically describes the molecular weight distribution for a PPE synthesized via a polycondensation route.

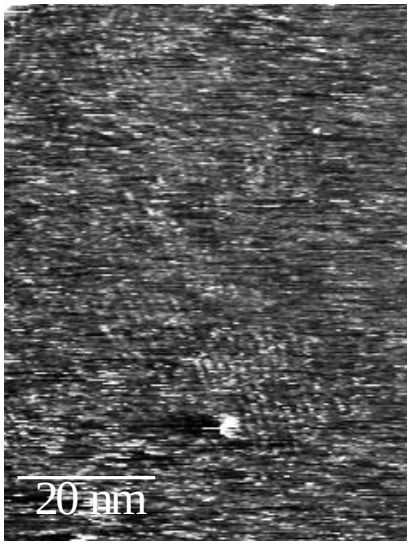

Figure 6.33: STM current images of a PPE **4** at the interface between the basal plane of graphite and an organic solution in 1-phenyloctane. This PPE, according to ^{1}H-NMR analysis on the end-groups, possesses an average contour length 20.3 nm long. U_t=1.4 V , average I_t= 0.55 nA. Besides the molecularly resolved areas there are zones with high molecular dynamics where the molecules are not immobilized at surface.

The curves that refer to the 7.9 nm long PPE (Fig. 6.34a) and to the 11.2 nm long ones (Fig. 6.34b) exhibit three important characteristics:

1. the peak of the distributions moves to higher rod lengths with the increasing polymer length;
2. the peak of the rod lengths is shifted with respect to the mole fraction - Schulz-Zimm plots;
3. the experimental distributions are remarkably narrower than the Schulz-Zimm plots.

In the case of the 20.3 nm long PPE the molecules packed on the HOPG substrate are too few to allow a quantitative investigation and detect a trend on the length of the molecules immobilized at the interface.

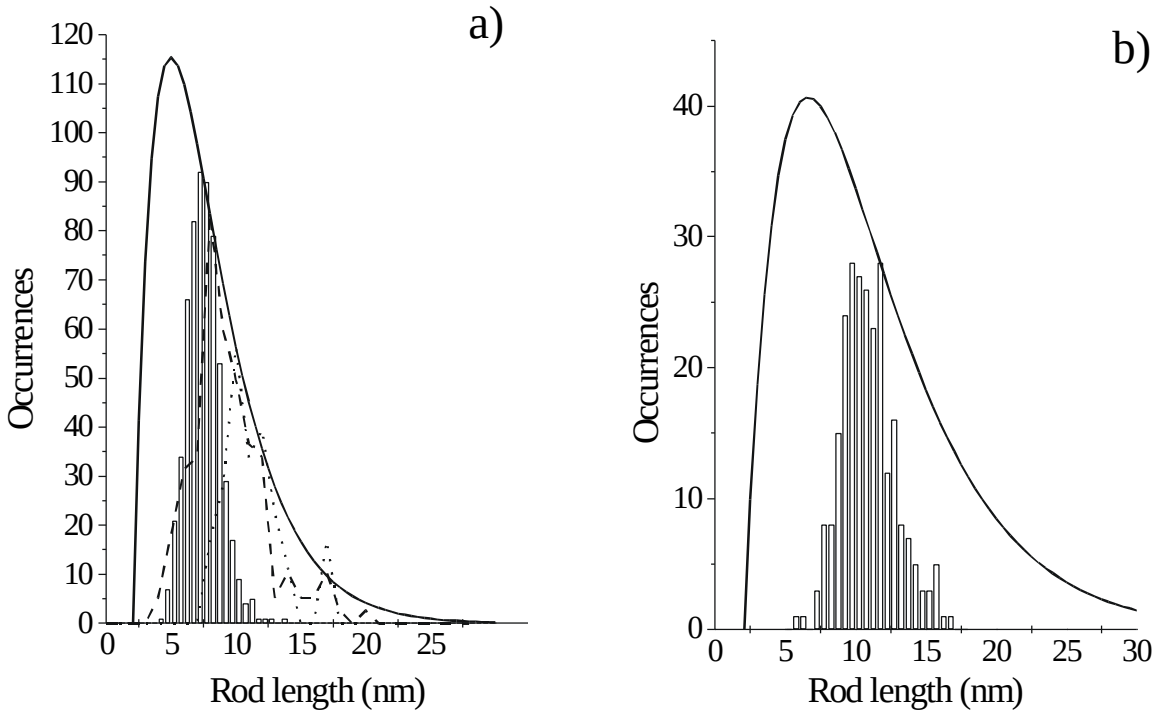

Figure 6.34: Histograms of the distribution of lengths of physisorbed rods. The PPEs posses an average contour length according to ^{1}H-NMR analysis on the end groups, a polydispersity determined by GPC using poly(*para*-phenylene)s for calibration and a number of physisorbed rods as measured: (a) 7.95 nm / 1.92 / 593; (b) 11.2 nm / 1.84 / 253. The mole fraction of the Schulz-Zimm distribution is plotted in solid lines and in (a) Monte Carlo simulation (dashed and dotted lines). Dashed line: ratio of the potential of the interactions molecule-substrate and molecule-molecule = 2; dotted line: interaction molecule-molecule is reduced to zero. The normalization of the curves have been carried out on the tail of the distribution. Simulations have been performed using a repulsive hard core potential and London attractive forces. The model system was designed forming linear rods by overlapping several spheres linearly. The procedure was computed for a distribution of rods according to the Schulz-Zimm distribution. Calculations have been executed varying systematically the ratio between the potential of the interactions molecules-substrate and molecules-molecules in a range that spans from 2 to infinite.

The conformation of the 2,5 dihexyl-*para*-phenyleneethynylene is well-known to be rather straight. Molecular Dynamics (MD) [Bin95] simulations in vacuum revealed (Fig. 6.35) that upon increasing the contour length of a single PPE molecule the end-to-end distance initially increases linearly up to a length of about 20 r.u. (~ 13 nm), while above this length the bending of the chains increases more for bigger molecular lengths and leads to coiling at more than 35 r.u (~ 22.75 nm) (end-to-end distances for coiled regime not given in Fig. 6.35 because a meaningful statistics would require too long simulation times). This suggests that the polymers investigated here (on average 7.95 nm and 11.2 nm long) are well described by elastic rods.

In order to gain a deeper understanding of the physisorption at the solid-liquid interface Monte Carlo simulations [Bin95, Pal98] have been carried out for the adsorption of rigid rods at a surface. An *ensemble* of linear rods with a distribution of lengths according to the Schulz-Zimm mole fraction distribution was constructed. Interactions between molecule-molecule and molecule-substrate were simulated making use of a repulsive hard core potential and London attractive forces.

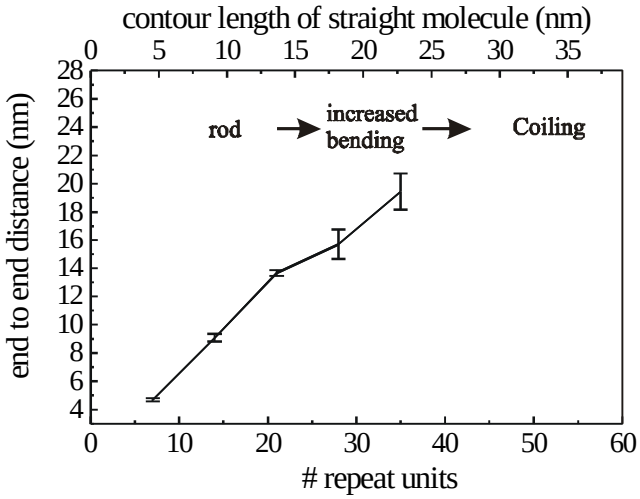

Figure 6.35: Molecular Dynamics simulation of the evolution of the end-to-end distance of a single PPE in vacuum as a function of the increasing polymer length (expressed either in # of repeat units or contour length). The simulations have been computed at room temperature in vacuum applying the pcff force field (Molecular modelling package DISCOVER VERSION 4.0.0, Biosym Technologies Inc., San Diego, CA.) for a time scale of 100 ps for polymer up to 28 r.u., 150 ps for the molecule made of 35 and 42 r.u., and 250 ps for the polymer composed of 49 and 56 r.u.; these turned out to be enough for achieving a constant regime of energy fluctuations. The error bars represents the standard deviation of the end-to-end distance in the final 100 ps calculated.

Using a ratio between the potential of the interactions molecule-substrate and molecule-molecule of 2 (dashed curve in Fig. 6.34a) the distribution is somewhat broader and shifted to even higher rod lengths, approaching the Schulz-Zimm distribution for long chains. Upon increasing the ratio of the potentials the onset of adsorption is shifted to higher molecular lengths, as evidenced by the dotted curve in Fig. 6.34a, for which the potential of interactions molecule-molecule is zero. This fractionation is also accompanied by a notable shift of the peak of the distribution of the adsorbed molecular rod length up to 10 nm (for the 7.9 nm long the polymer).

Figure 6.34a reveals that the Monte Carlo simulation overestimates the adsorption of the very long rods, which needs to be explained. The favored adsorption of long vs. short molecules at the interface can be understood since upon immobilization at the interface they loose translational entropy per particle but they gain potential energy per unit mass. This is in agreement with chromatographic analysis [Fle93] and MD calculations [Xia93]. On the other hand, with the definition of a Kuhn segment (l) [Gro97] one may determine a persistence length ($l/2=R_L^2/2L$). If one considers the R_L (average end-to-end distance) given by the MD calculations, one obtains $l/2=6.85$ nm for a PPE chain of 21 r.u., which is close to the experimental case in our experiment. For longer chains the entropic contribution per unit mass to the overall free energy increases, due to the reduced configurational space of the molecule at the interface. This difference between elastic and fully rigid rods can explain the discrepancy between the experimental and the Monte Carlo results (Fig. 6.34a).

The physisorption of molecules at the solid-liquid interface is characterized by a continuous exchange of the adsorbed molecules with those in the solution. The system evolves towards this equilibrium regime with a rate that depends on several factors including the viscosity of the solution, the energy of adsorption of the molecules on the substrate and the concentration of the solution.

The self-assembly into the monolayer is likely to occur via:

1. stacking of PPE in solution into clusters composed by molecules with similar size;
2. adsorption of these clusters onto graphite along preferential directions induced by the symmetry of the substrate;
3. filling of the missing free space with short molecules;

4. Ostwald ripening at the interface and substitution of short adsorbed molecules with longer ones when sterically permitted.

The segregation phenomenon observed and discussed here on a sub-molecular scale is in good agreement with the one detected on larger scales on dry films of poly(diacetylenes) [Wan93,Hug97]. Since classical methods such as column separation [Rod96], ultracentrifuge [Flo53] and precipitation [Kot67] for π-conjugated polymers are well-known to suffer from uncontrolled cluster formation in solution [Cot96, Hal98] the use of self-assembly at surfaces might be considered an alternative route for achieving fractionation of a macromolecular solution.

In summary, the behavior of rigid (macro)molecules in a physisorbed monolayer has been elucidated on a conductive crystalline substrate. It revealed a macromolecular fractionation at the solid-liquid interface. This phenomenon is governed by the interplay of entropic and enthalpic contributions to the free energy. It indicates that the self-assembly of a polymer on an atomically flat substrate could be a new route for fractionating a polydisperse macromolecular solution. The underlying mechanism may also be operating at solid-liquid interfaces with small inorganic, organic or biological particles exhibiting atomically flat surfaces.

6.5 PPE on insulating substrates

6.5.1 Introduction

In the following paragraph the growth of dry films of PPE from solution will be discussed on different insulating substrates varying systematically several factors:

I. the concentration of the solution [Sam98a];

II. the molecular weight of the PPE [Sam99a];

III. the type of substrate [Sam99c];

IV. the rate of the deposition process [Sam98b];

V. the side chains [Sch99].

The morphologies of these dry films have been investigated by means of Scanning Force Microscopy in Tapping Mode in air environment at room temperature, exploring a range of

scan lengths from 13 µm down to 0.3 µm.

6.5.2 Morphology at different concentrations of the solution

Poly(2,5-dihexyl-1,4-phenyleneethynylene) (PPE), because of its alkyl side chains attached to the aromatic rings, exhibits a good solubility in organic solvents like methanol (MeOH) and tetrahydrofurane (THF). This two solvents have been chosen since they posses a similar boiling point of ca. 65 °C and therefore are likely to evaporate with a similar rate. In this first experiment, therefore, the role of the solvent is not taken into account and will be discussed in paragraph 6.5.5.

The self-assembly of α-[[4-[(N,N-dimethylcarbamoyl)thio]phenyl]ethynyl]-ω-[4-[(N,N-dimethylcarbamoyl)thio]phenyl]-poly[(2,5-dihexylphenylene-1,4)ethynylene)] (**4**) (Fig. 6.30) have been investigated on freshly cleaved muscovite mica as a function of the concentration of the cast solution. This PPE possesses an average contour length along the conjugated backbone of 16.4 nm, according to ^{1}H-NMR analysis on the end-groups. SFM images are displayed in Fig. 6.36.

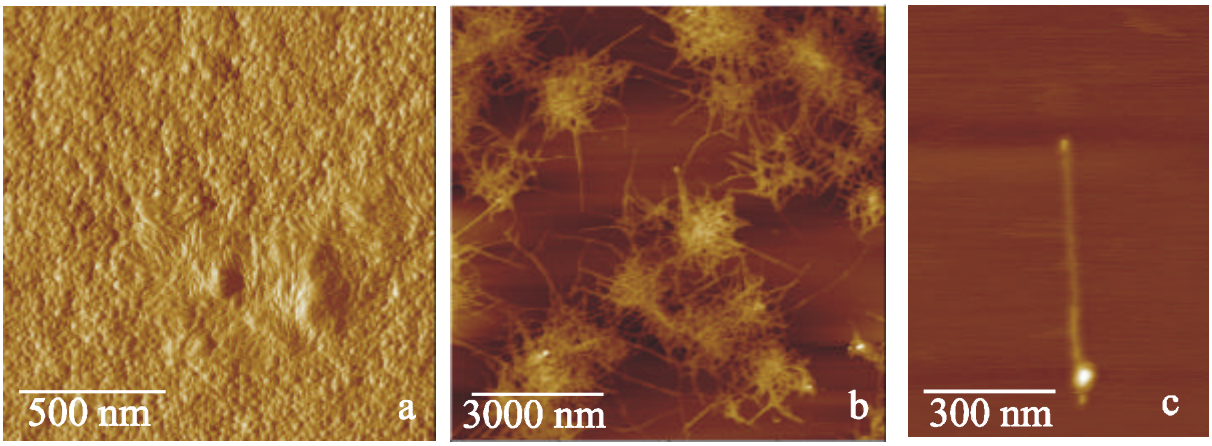

Figure 6.36: TM-SFM images representing the evolution of the morphology of the PPE on mica as a function of the concentration of the polymer. a) 2.0 g/l in MeOH, amplitude image, height range (peak-valley) (h) in the correspondent height image of ~ 70nm; b) 0.14 g/l in THF, height image, h=50 nm; c) 0.07 g/l in THF, height image, h=15 nm.

The structure of a film cast from a concentrated (2.0 g/l) PPE solution in methanol is made up of both areas with grains and areas with more elongated tightly packed architectures that look like ribbons (Fig. 6.36a). Both the diameter of the grains and the width of the ribbons are ca.

25 nm. The mica support is in this case homogeneously coated by a rather thick film. Indeed the height range in the image is ~ 70 nm, which indicates a considerable roughness. The thickness of the film is expected to be some hundreds of nm. At a lower concentration of 0.14 g/l in THF the polymer self-assembles into ribbons with random lengths but with a well defined width and thickness (Fig. 6.36b). Further dilution in THF, down to 0.07 g/l, gives rise to single ribbons lying on the flat mica substrate (Fig. 6.36c).

In both of the last two cases the substrate is only partially covered with the macromolecular moieties. In fact the height ranges are more reduced. In the second case (Fig 6.36b) a medium concentration gives rise to a spider web morphology made of knotty cores where the ribbons are entangled, while the branches are composed of singular ribbons.

It should be pointed out that the same morphologies (grains at high concentrations and ribbons at low concentrations) have been found both in MeOH and in THF. Moreover the ribbons have shown a particularly high stability: upon scanning with SFM in contact mode applying a force of some hundreds of nN on a single assembly it was not possible to deform its shape.

The width of the ribbons is constant for some straight ribbons sections. It is (36±11) nm evaluated on 334 different ribbons from images with 512*512 pixels and a scanlength L ≤ 3μm. The apparent width has to be corrected for the well-known lateral broadening effect in SFM images due to the tip shape [Kel91,But92, Bus97].

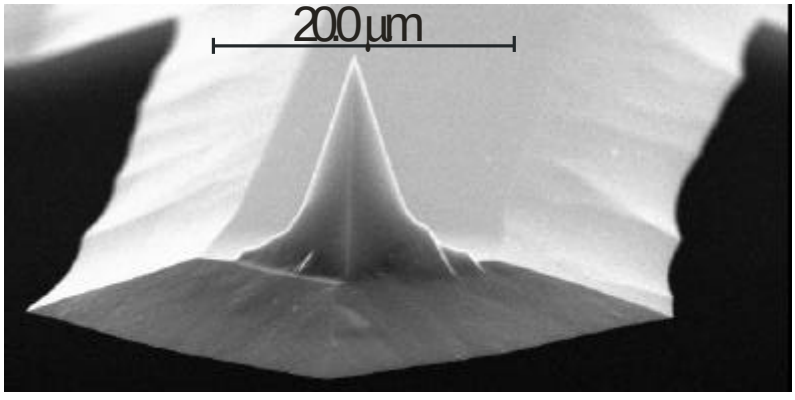

Figure 6.37: Scanning Electron Microscope (SEM) micrograph (courtesy of Dr. Rogaschewski) of commercial Si tip (Digital Instruments). Typical shape of the cantilever with a conical tip attached at its end.

The TM-SFM silicon nano-probe is composed of a stiff cantilever that appears as a parallelepiped diving board with a length of 125 μm and a width of 30 μm, as shown in Fig.

6.37. At its edge a conical tip is attached. These probes are commercially available from Digital Instruments, Santa Barbara, CA. The shape of the tip apex may be approximated by a sphere [But92]. The Scanning Electron Microscopy (SEM) micrograph allowed to recognize its shape on the hundred nanometers scale while, however, the tip apex could not be resolved properly.

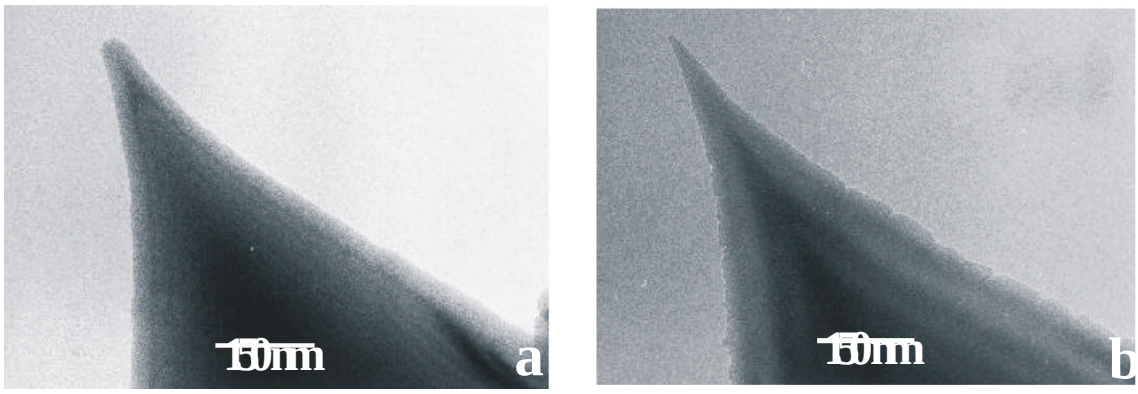

Figure 6.38: Transmission Electron Microscope (TEM) micrograph (courtesy of Dr. C. Böttcher) of commercial Si tips (Digital Instruments). Tips displayed in a) and b) present a different shape. The average of the terminal tip radius of several tips has been evaluated as R = (13±7) nm.

From high resolution TEM imaging on several Si tips, the tip edge and consequently the terminal radius of the spherical end of the probes (Fig. 6.38) could be determined as R=(13±7) nm.

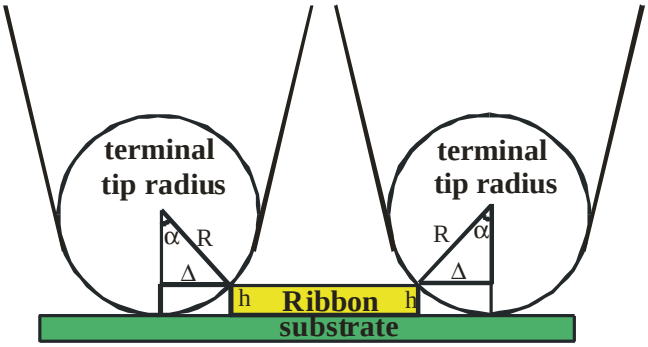

Figure 6.39: Geometrical model for the broadening of the image of a ribbon due to the tip radius. R is the terminal tip radius, h is the mean height of the needles. $\Delta = \sqrt{h(2R-h)}$ = (8±3) nm. The effective broadening results as 2Δ=(16±6) nm.

A simple geometrical model (Fig. 6.39) can be used to calculate the broadening induced by the tip size of the ribbon widths from singular profiles on SFM topographical images. Using this model, computed for a spherical tip and a rectangular cross-section of the ribbon, one obtains for the broadening:

$$2\Delta = 2\sqrt{h(2R-h)} \qquad (6.3)$$

For the present ribbon height, determined as (2.9±0.6) nm from 285 different ribbons profiles, and a mean terminal tip radius of (13±7) nm, 2Δ amounts to (16±6) nm. The effective ribbon width can thus be obtained by subtracting 2Δ from the apparent width. It is comparable to the 16.4 nm average contour length of the molecules as obtained from ^{1}H-NMR analysis on the end-groups. Moreover the mean height of the ribbon of (2.9±0.6) nm is on the order of once or twice the molecular width considering the case where the alkyl side chains are extended, i.e. 1.9 nm.

6.5.3 Morphology at different molecular weight

The role of the molecular weight distribution for the self-assembly of PPE in dry films on mica has been also explored, in this case using two different derivatives of PPE, bearing different end-groups in the α and ω position. The first one (**4**) has been already introduced in Fig. 6.30. The latter one, namely α-iodo-ω-[(2,5-dihexyl-4-ethynyl)phenyl]-poly[(2,5-dihexylphenylene-1,4)ethynylene)] (**5**), is shown in Fig. 6.40.

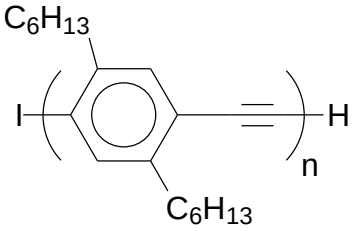

Figure 6.40: Chemical formula of **5**, namely α-iodo-ω -[(2,5-dihexyl-4-ethynyl)phenyl]-poly[(2,5-dihexylphenylene-1,4)ethynylene)].

First of all the average degrees of polymerization, *DP*, namely the average number of repeat units, of the different PPEs obtained with a polycondensation synthesis were determined, also in this case, by ^{1}H-NMR end-group analysis and gel permeation chromatography (GPC). All

data are reported in Table 6.6. ^{1}H-NMR spectroscopy proved complete end-functionalization of the PPEs within the experimental error. It can therefore be used to evaluate *DP*, and consequently the number-average molecular weight, M_n, by integrating the relative signals of the end-groups and those of the main chain. The ^{1}H-NMR spectrum of **5** shows proton signals of the terminal repeating unit carrying the iodine atom at δ = 7.69 and 7.30. Polymer **4** exhibits a signal of the methyl groups in the dimethylthiocarbamoyl function at δ = 3.02 and the aromatic protons at δ = 7.48. The main chain-signal of the aromatic protons for both **5** and **4** appears at δ = 7.36. Nominal contour lengths of the molecules have been calculated from the determined *DP* using literature values for the repeat unit length. GPC was used to estimate the mass-average molecular weight (M_w), M_n , *DP* and the polydispersity of the polymers **5** and **4**. However, this method is very sensitive to the calibration standards. Since poly(styrene) (PS) exhibits a different structure and stiffness from PPE, also a rigid-rod macromolecule, namely a substituted poly(*para*-phenylene) (PPP) with a known molecular weight [Van96], have been used as a calibration standard.

Table 6.6: PPE samples investigated: average number of repeating units and contour lengths according to ^{1}H-NMR results; polydispersity (**Mw / Mn**) from GPC measurements with PPP calibration.

Sample	A	B	C	D	E	F
Average no. of repeating units	9	11	20	22	28	42
Type of PPE	**4**	**4**	**5**	**4**	**4**	**4**
Average contour Length of molecule	7.9 nm	9.2 nm	13.5 nm	16.4 nm	20.3 nm	29.4 nm
Mw / Mn	1.92	3.68	3.82	2.65	2.59	8.23
Morphology at low concentration	Ribbons	Ribbons	ribbons	ribbons	grains	grains

Type of PPE: (4) α-[[4-[(N,N-dimethylcarbamoyl)thio]phenyl]ethynyl]-ω-[4-[(N,N-dimethylcarbamoyl)thio]phenyl]-poly[(2,5-dihexylphenylene-1,4)ethynylene)]

(5) α-iodo-ω -[(2,5-dihexyl-4-ethynyl)phenyl]-poly[(2,5-dihexylphenylene-1,4)ethynylene)]

PPE solutions have been cast onto freshly cleaved mica surfaces. After complete evaporation of the solvent (in this case THF or a mixture of THF/1-phenyloctane have been used), the dry

samples revealed a dependence of the morphology on the molecular weight (Fig. 6.41 and Table 6.6). For polymers A through D with an average of 9, 11, 20 or 22 repeating units and a concentration of the applied solution lower than 0.15 g/l, ribbons were observed (Fig. 6.41a). Higher molecular weight (samples E, F) led to a grainy morphology (Fig. 6.41c). Figs. 6.41a,b exhibit ribbon heights on mica of h=(2.9±0.7) nm, as determined from 422 ribbons on different samples.

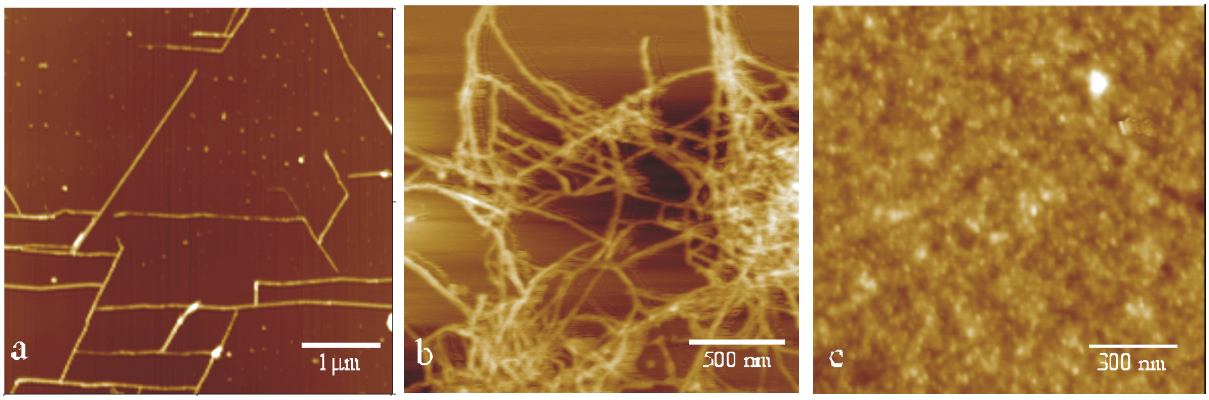

Figure 6.41: SFM Tapping Mode height images representing the evolution of the morphology of the PPE on mica as a function of the polymer length. Average contour length of the molecule according to ^{1}H-NMR results: a) 7.9 nm; b) 16.4; c) 20.3 nm. Height range of images: a) 20 nm; b) 30 nm; c) 20 nm. In case a) a mixture of THF and phenyloctane was used as a solvent while in b and c) pure THF was used.

From the comparison of this value with the spacing between neighboring backbones evaluated from molecularly resolved STM images (Fig. 6.31), it is suggested that the ribbons are typically two monolayers thick with their alkyl chains oriented perpendicular to the substrate (Fig. 6.42). Also some sections with single, triple and even higher multi-layers occur. Moreover the widths of the ribbons are constant for some straight ribbon sections, but not for the whole sample.

In Fig. 6.43 the apparent widths (number counting) determined from SFM images of samples A-D are reported. They need to be corrected for the broadening effect due to a finite radius of the tip. Using the broadening model previously described in Fig. 6.39 , for the present ribbon height of h=(2.9±0.7) nm and a terminal tip radius of the commercial Si tips of R=(13±7) nm, 2Δ amounts to (16±7) nm. The true ribbon width, with a 7 nm error bar, is then obtained by subtracting 2Δ from the apparent width.

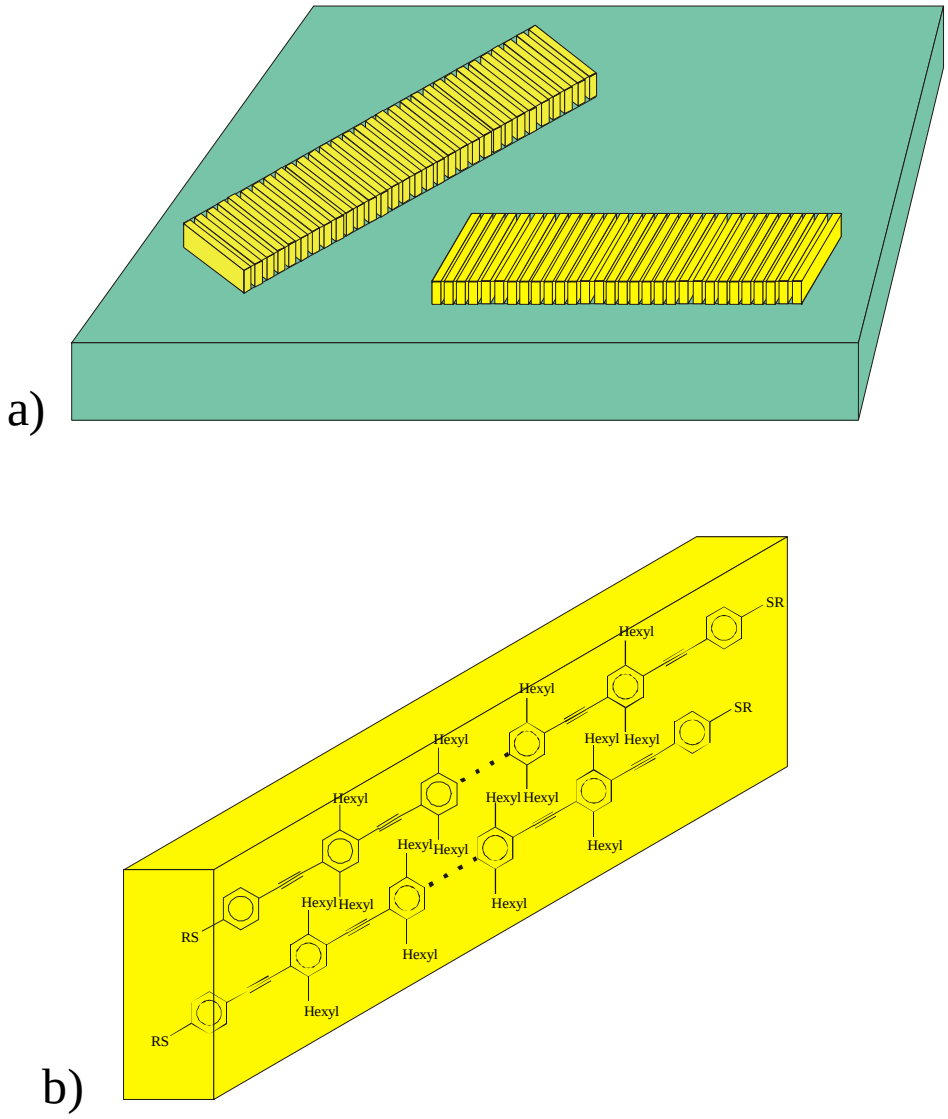

Figure 6.42: Schematic representation of molecular ribbons adsorbed on the mica surface. a) Ribbons are made of several rods packed parallel to each other. b) Each rod is typically made of two PPE molecules packed with the hexyl lateral chains perpendicular to the basal plane of the substrate.

In Fig. 6.43 it is shown that the peaks of the width distributions shift to higher values with increasing polymer length. Since the absolute value of the width is on the order of the length of a single molecule, it is concluded that the extended molecules pack parallel to each other with their long molecular axis perpendicular to the long ribbon axis, as represented in Fig. 6.42. The distribution of the ribbon widths is attributed to the distribution of molecular weights, implying that molecules with similar molecular weights phase segregate into ribbon sections with homogeneous widths. This segregation phenomenon, that governs the ribbons formation, is obviously favored by a small *DP* (Fig. 6.41) and is likely to be also favored by a

low macromolecular polydispersity.

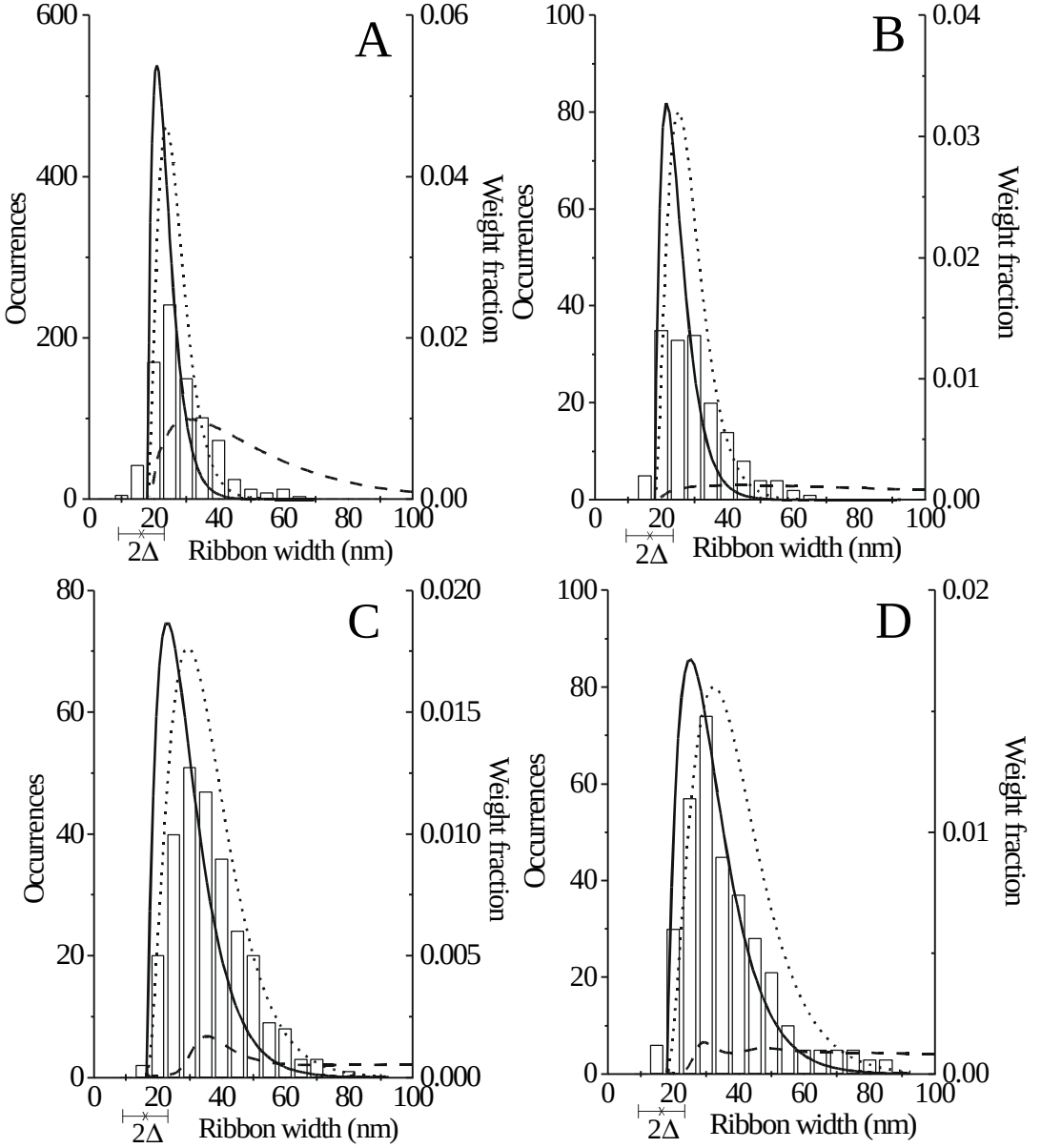

Figure 6.43: Histograms of the distribution of ribbon widths for PPE batches A through D with increasing length. Average contour length of the molecule according to ^{1}H-NMR results (Table 6.6) and number of ribbons measured: (A) 7.9 nm / 846; (B) 9.2 nm / 160; (C) 13.5 nm / 264;(D) 16.4 nm / 334. The Schulz-Zimm distribution is plotted in terms of number counting (solid lines) and weight function (dotted line). $2\Delta=(16\pm7)$ nm is the effective broadening of the tip. Dashed lines are experimental GPC data obtained from PS calibrated measurements.

Attempts to determine the molecular structure directly by electron diffraction were not successful, probably due to the small amount of material in a given ribbon. However, in

continuous films of polydiacetylene [Wan93, Hug97] and poly(*para*-phenyleneethynylene) derivatives [Ofe95] similar molecular architectures have been observed.

The polycondensation reaction used for the PPE synthesis gives a molecular weight distribution, which is theoretically described by the Schulz-Zimm distribution [Ofe95]. This function was computed for samples A-D in terms of molecular contour lengths by assuming the number average degree of polymerization *DP*, according to the number of repeating units estimated by ^{1}H-NMR spectroscopy (Table 6.6).

The mole fraction distribution is expressed as $F(r) = y^k r^{k-1} \frac{e^{-yr}}{\Gamma(k)}$ (see 3.7) and the weight fraction distribution as $W(r) = y^{k+1} r^k \left[\exp(-yr)\right] / \Gamma(k+1)$ (see 3.8). In the present case $y = \frac{k}{DP}$, where *k* is the degree of coupling (in this case *k* =2), *r* is the number of monomers (independent parameter) and *G(k)* is the gamma function. These distributions were plotted on the histograms of Fig. 6.43, after being shifted on the x-axis by the tip broadening effect of 16 nm. This made it possible to relate the estimated molecular lengths to the ribbon widths. Noteworthy, a good fitting between the mole fraction distribution and the distribution of ribbon widths can be recognized.

This match also demonstrates that SFM on these nanostructures may provide a reasonable evaluation of the molecular weight distributions for a rigid rod polymer. Nota bene, due to the commonly observed aggregation of the polymer chains it is difficult to determine correct molecular weight distributions for rigid-rod polymers with standard polymer analytical techniques like, e.g., Gel Permeation Chromatography (GPC). Dashed curves in Fig. 6.43 represent the GPC experimental data (PS calibrated) obtained on the respective polymer. A long tailing of the molecular weight distribution curve to high values is observed in the elugrams of the polymers which drastically increases the polydispersity but has only little effect on M_n. A reasonable agreement between the theoretical Schulz-Zimm plot and the experimental GPC curve has been observed only for the shortest PPE (Fig. 6.43a). In fact with increasing chain length the aggregation of the molecules becomes more intense (Fig. 6.43b-d). Moreover, the values are affected by adsorption of the stiff molecules to the column. Additionally, in the present case, the protected thiol end-groups enhance this phenomenon [Fra98].

A comparison between the different methods used to determine the molecular weight

distributions (^{1}H-NMR, GPC - PS and PPP calibrated) has shown that M_n evaluated with GPC (PPP calibrated) are overestimated on average by 42% with respect to ^{1}H-NMR data. For the case of GPC (PS calibrated) the overestimation is even bigger. The polydispersity (M_w/M_n) measured with GPC is 50% larger for the case of PS calibration if compared to PPP calibration, while M_w is twice as big. This confirms that for investigating *DP* and M_n of a stiff polymer ^{1}H-NMR analysis on the end groups is a suitable technique, while for approximating M_w and polydispersity by GPC at least calibration with a rigid-rod polymeric standard like PPP should be used. [Sam99a]

6.5.4 Morphology on different substrates

In order to understand the phenomena governing the growth of PPE into nanoribbons use has been made of different insulating amorphous supports including glass and carbon-coated copper grids; the resulting molecular arrangements on solid surfaces have been compared to the ones obtained on a crystalline mica substrate. SFM investigations of films processed by casting a very dilute polymer solution on a glass support reveal self-assembled solid nanoribbons (Fig. 6.44a) with a length in the micrometer range, lying flat on the substrate.

The hexyl chains, whose length in an extended conformation spans over 1.9 nm, are more likely to pack similarly to the case on mica, i.e. they are standing perpendicular to the substrate in a disordered conformation [Sam99a] spanning only ~ 1.5 nm. The ribbon heights of (3.9±1.0) nm observed here suggest a packing of 2-3 molecular layers, albeit also multiple layers have been detected.

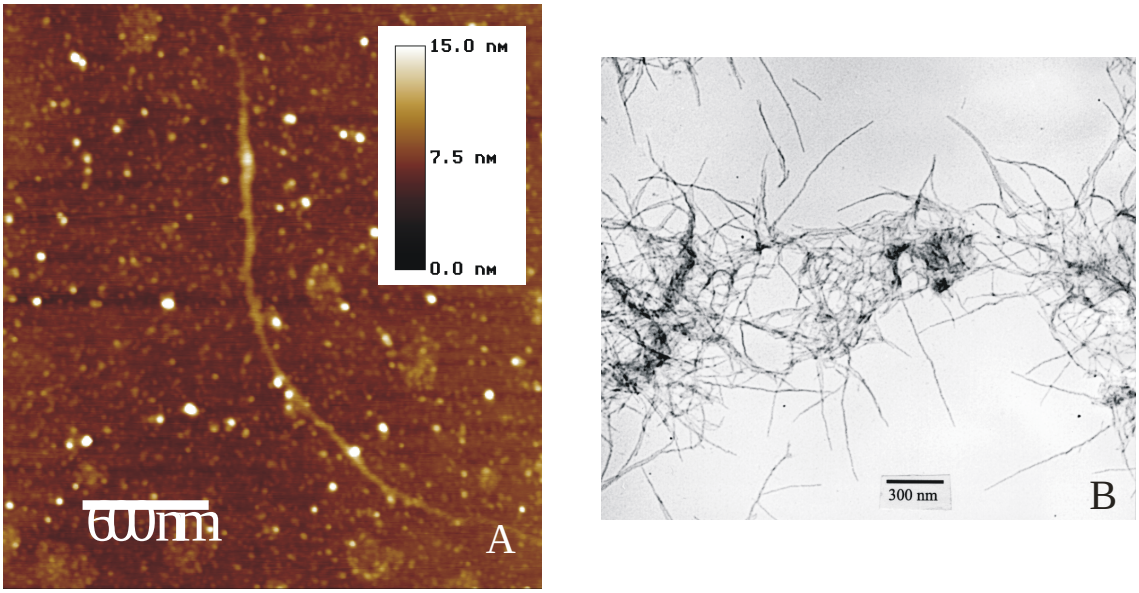

Figure 6.44: A) Tapping Mode SFM height image of an on average 11.2 nm long PPE on glass. Singular nanoribbon assembled on the grainy glass surface. B) TEM micrograph showing webs of ribbons on a carbon copper mesh support made by casting an on average 16.4 nm long PPE from a 0.1 g/l solution in THF.

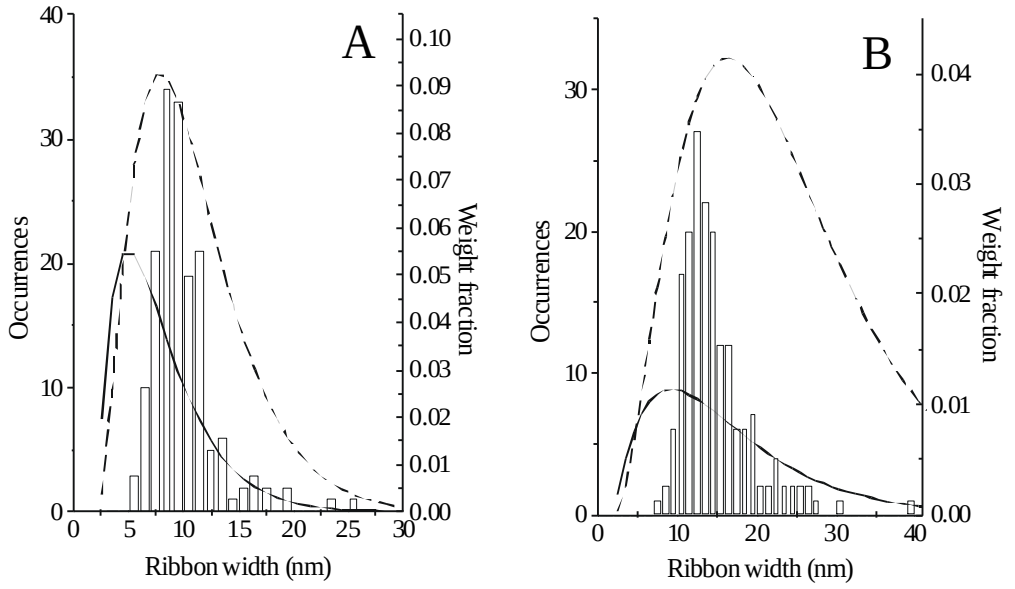

Figure 6.45: Histograms of the distribution of ribbon widths for PPE from profiles on TEM micrographs. Contour length of the molecule according to ^{1}H-NMR results and number of ribbons measured: (A) 7.9 nm / 164; (B) 16.4 nm / 167. Mole fraction (solid line) and weight fraction (dashed line) of the theoretical Schulz-Zimm distribution are in fairly good agreement with the experimental data.

.

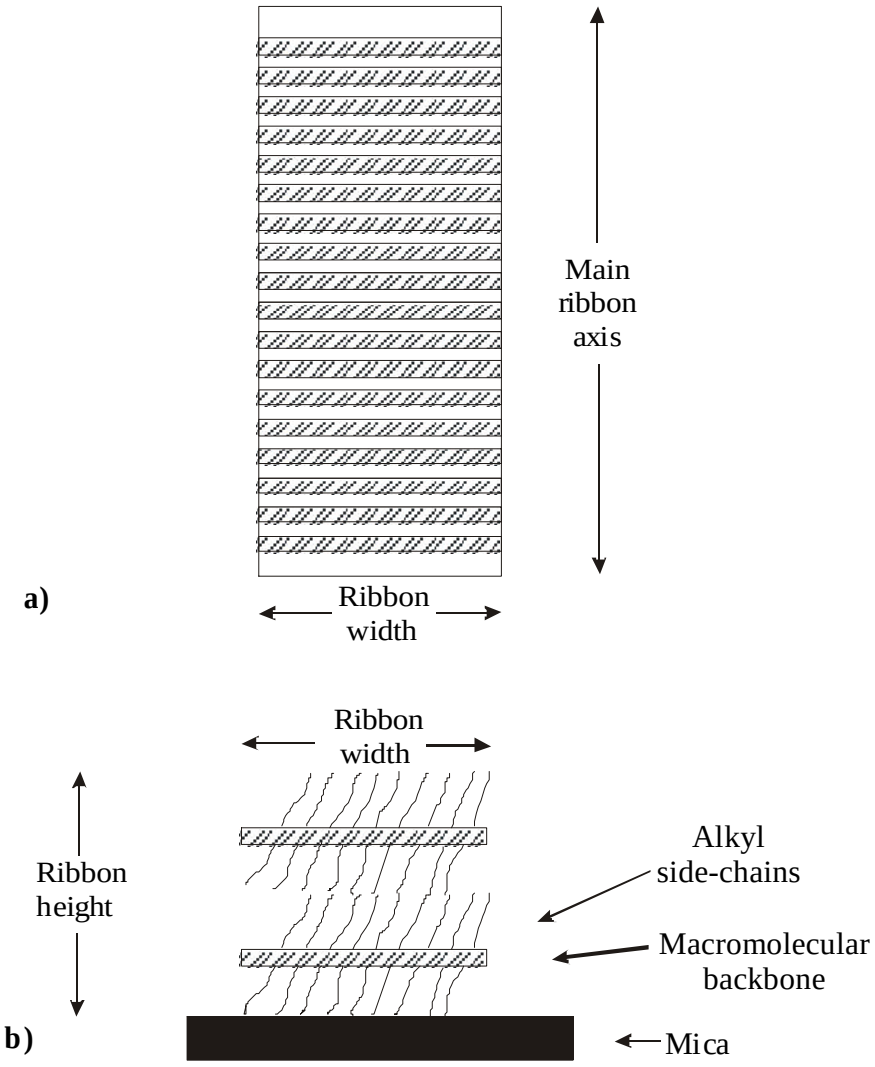

Figure 6.46: Schematic representation of the molecular packing in the nanoribbon: a) Top view: a ribbon is composed by parallel, fully extended backbones, stacked perpendicular to the main ribbon axis; b) Side view: the lateral alkyl chains are disordered between adjacent backbones in a bilayer/trilayer aggregate standing on the substrate.

The apparent width of these assemblies evaluated from individual profiles on SFM micrographs amounts to (41±15) nm. The effective width can be calculated by deducting the broadening 2Δ due to the finite size of the Si tip apex that for a terminal radius of a clean new tip of R=(13±7) nm amounts to (19±6) nm. The true width of the nanoribbon, with a 6 nm error bar, is also in this case in fair agreement with the macromolecular length of 11.2 nm (*U*=2.34) considering that the terminal radius of the tip could get slightly broader after several scans

Moreover, a TEM analysis has been executed on PPE films of different molecular weights cast on a carbon-coated copper grids. Nanoribbons have also been found (Fig. 6.44b), and the distribution of their widths was determined from profiles on TEM micrographs. A polymer with an average contour length of 7.9 nm (sample A in Table 6.6) exhibits a ribbon width of (10±3) nm, while a macromolecule with a length of 16.4 nm (sample D in Table 6.6) forms ribbons with an average width of (15±4) nm. The corresponding two distributions have been plotted in histograms in Fig. 6.45. The nanoribbons are remarkably stable arrays under the electron beam of the electron microscope.

Similarly to what has been observed on mica, with increasing PPE length the peak of the experimental data shifts to higher values and the distribution of ribbon widths gets broader. The ribbon widths correlate well with the theoretical Schulz-Zimm distribution which describe the distribution of molecular weights for a polycondensation synthesis [Bra89]. The peak of the ribbons widths distribution, in terms of spatial units, is in both cases similar to the peak of the histograms of the mole fraction distribution and of the weight fraction distribution, indicating a good agreement between the most frequent ribbon width and the average molecular length obtained from ^{1}H-NMR analysis. In addition, a fairly good agreement between the width of the distribution of ribbon widths and the width of the Schulz-Zimm mole fraction distribution can be recognized. This confirms that measuring the width of these nanostructures is an alternative route to evaluate the molecular weight distribution for this kind of polymer as previously demonstrated using mica as a substrate [Sam99a].

In summary, SFM and TEM applied to samples cast on different substrates, give rise to similar results in terms of the sizes of the nanoribbons in the XY plane while their heights have been only detected by SFM [But92]. Similarly to what has been concluded on mica substrates, the nanoribbons appears to consist of macromolecules oriented with their stiff backbones parallel to the substrate and the hexyl side chains perpendicular to the basal plane of the substrate. The backbones are stacked parallel to each other creating a ribbon of stacked π-conjugated polymers on the substrate (Fig. 6.46).

The demonstrated ability to grow these architectures also on non-crystalline substrates indicates that the main driving force of this self-assembly are intermolecular interactions between the π-conjugated macromolecules. The substrate plays only a secondary role of inducing a particular orientation of these assemblies. Furthermore, the transparency of the glass support opens the possibility to perform spectroscopical investigations like probing the birefringence and fluorescence of single nanoribbons using Scanning Near-Field Optical

Microscopy. This would allow to determine physico-chemical properties of PPE on the nanoscopic level and compare it to single molecular and solid state properties. [Sam99c]

6.5.5 Morphology at different rate of the deposition process

In order to gain further insight into the growth process of these PPE nanoribbons, by solution casting, on crystalline mica substrates different solvents have been used. This allowed to vary the rate of evaporation of the solvent and of crystallization of the organic compound.

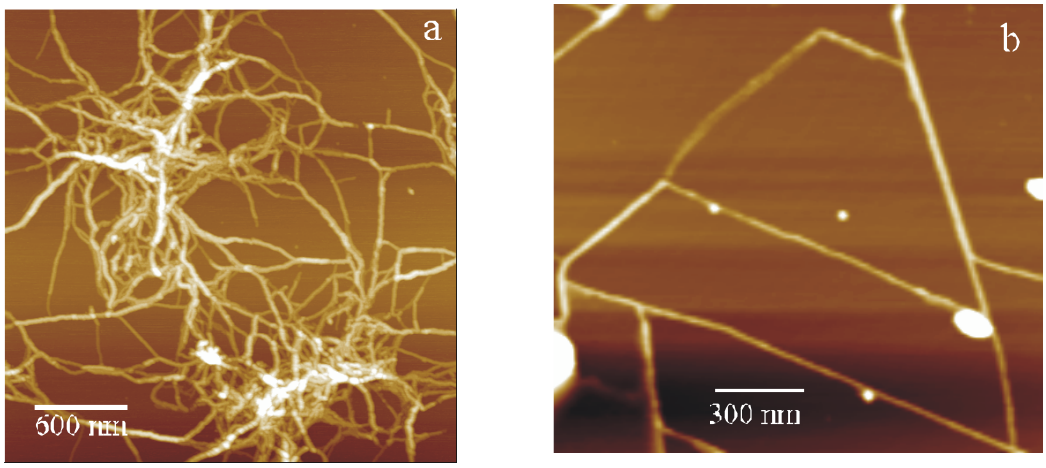

Figure 6.47: Topographical Tapping Mode Scanning Force Microscopy images of PPE cast on freshly cleaved muscovite mica. a) Solvent : THF, height range (peak-valley) h=30 nm; b) Solvent:mixture THF-phenyloctane (5:1), h=20 nm.

The SFM topographical images in Fig. 6.47 show nanoribbons grown on mica from very dilute solutions of a PPE with an average contour length of 7.9 nm (sample A in Table 6.6). These architectures, obtained by solution casting, exhibit a length of up to several micrometers and a two-dimensional cross-section on the molecular scale, confirming once again what has been described in the previous three paragraphs.

The ribbons in Fig. 6.47a were produced from a PPE solution in tetrahydrofurane (THF). These anisotropic nanostructures, whose width of ~11.1 nm (corrected for the lateral broadening tip effect [Sam98a]) fits relatively well with the size of the molecule, hardly shows any favored orientations.

On the other hand, Fig. 6.47b displays highly oriented nanoribbons obtained from the same PPE polycrystalline powder dissolved in a 5:1 mixture of THF and 1-phenyloctane. These anisotropic assemblies exhibit an effective width of ~7.1 nm and are aligned preferentially along directions according to the three-fold symmetry of the underlying mica, with an average angle of (61±7)° between ribbon segments. It is worth to note that it was not possible to grow well-ordered molecular aggregates with a ribbon like shape using a fast deposition method such as spin-coating. The different molecular organization on the basal plane of mica is attributed to the solvent evaporation process that is followed by the self-assembly of the organic compound into the nanoribbons. The ribbon formation, may be divided in two steps:

1. self-segregation of the molecules into straight ribbon segments with homogeneous widths, and
2. self-assembly of long oriented nanoribbons induced by the crystalline substrate.

The first step is governed by intermolecular interactions between the conjugated macromolecules, as previously demonstrated by the ability to grow nanoribbons on amorphous substrates [Sam99c]. The second step takes place on crystalline substrates and is observed only for very slow solvent evaporation rates. In the present case THF has a boiling point (67 °C) which is much smaller than the one of 1-phenyloctane and also of the solvent mixture. Consequently, the time required for the complete evaporation of the solvent was a few hours (2-3) for the first case and a few days (2-3) for the latter. This suggests that in the case of pure THF the solvent evaporation was too fast for step (2) to occur.

The height of the ribbons amounts to (2.9±0.7) nm for the THF deposition, whilst it is (4.7±1.4) nm for the deposition from the solvent mixture. Comparing this value to the width of the molecule of ~1.5 nm [Sam99a] it is suggested that the ribbon is typically made of a molecular bilayer in the first case and of a triple layer in the latter case. The relatively large error bars indicate that the distributions are not sharp but single layers and also higher multiple layers occur. The trend indicates, however, that slowing down the deposition rate leads to thicker nanoribbons. The architecture of these ribbons is as previously described and depicted in Figs. 6.42 and 6.46.

These results demonstrate that it is possible to drive the self-assembly of suitably functionalized PPEs towards nanoribbons. The possibility to align the nanoribbons along the crystallographic axes of the crystalline non conducting substrate by slowing down the evaporation and consequently the crystallization process indicates that the growth of these

nanostructures is a kinetically governed phenomenon. [Sam98b]

6.5.6 Morphology with different side chains

Further PPE derivatives, synthesized in the group of Prof. Dr. W. Heitz (Department of Chemistry, University of Marburg) has been investigated. They posses acid functions (CPPE in Fig. 6.48) or ester side groups (EHPPE in Fig. 6.48) attached to the main conjugated skeleton. These soluble moieties have been also cast on mica and SFM investigation have been carried out. EHPPE crystalline powder has been solubilized and diluted in THF, while CPPE has been solubilized and diluted in KOH+H_20.

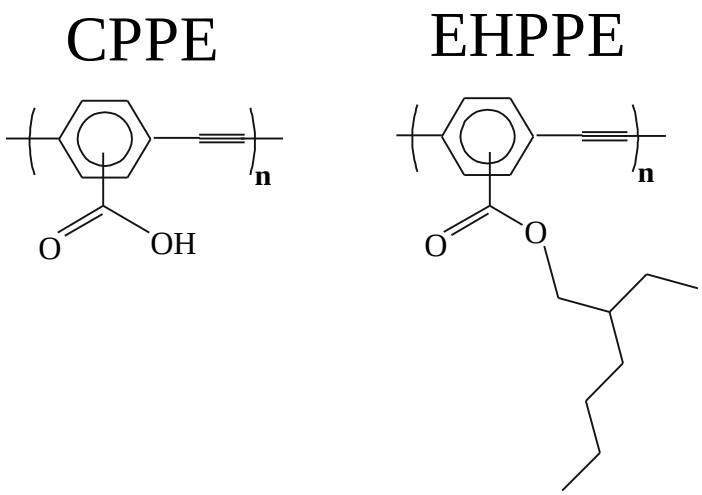

Figure 6.48: Chemical formulae of the CPPE and EHPPE.

Thin films of the conjugated polymer have been prepared by casting the solutions (from 0.065 g/l to 0.00325 g/l) on freshly cleaved muscovite mica discs.

The self-assembly of rigid rod polymers is strongly influenced by its distribution of molecular weights, as previously observed, and by the steric hindrance due to the chains [Wed96].

Films of EHPPE cast from 0.013 g/l show anisotropic features composed of spheroids with a preferential orientation which seems to be induced by the hexagonal crystal lattice of the mica substrate (Fig 6.49a). At higher dilution, a 0.0033 g/l solution of EHPPE in THF cast onto mica gives rise to anisotropic flat domains on the substrate (Fig. 6.49b). These elongated features, similar to wetting foots, are made up of one hump in the middle and a surrounding flat corona, which is a self assembled monolayers with a uniform thickness of 2.9 nm. The calculated width of the polymer with the alkyl chains extended is 1.4 nm; therefore a double

layer packing of the PPE molecules can be expected, as also obtained for PPE with hexyl side chains. Noteworthy, these ellipsoid features have not been visualized with TEM on carbon-copper coated grids indicating the influence of the crystal mica substrate on the self assembling of this PPE derivative.

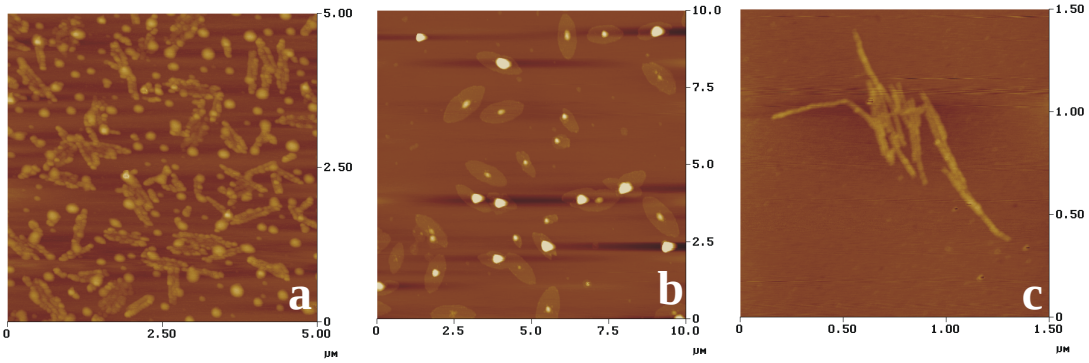

Figure 6.49: Tapping Mode SFM height images of: a) EHPPE from 0.013 g/l in THF, h=40 nm; b) EHPPE from 0.0033 g/l in THF, h=40 nm; c) CPPE from 0.017 g/l in H_20+KOH, h=7 nm.

Besides, films of CPPE, which possess a lower steric hindrance due to the side chains, exhibit more anisotropic structures (ribbon-like) (Fig. 6.49c), from low concentrated (0.017 g/l) solution, with a thickness of 1.4 nm that is just the double of its calculated polymer width of 0.7 nm, confirming once again the double layer packing.

In both of the two derivatives investigated here the polymer self-assembles in well defined structures in one dimension (Z), while the other dimensions (XY) exhibit a low anisotropy, which can be attributed to both the fairly high polydispersity of the synthetic polymer as evaluated by GPC and in particular to the steric hindrance of the side groups on the aromatic rings.

6.5.7 Morphology of thiol free end functionalized PPE

The reactivity of conjugated systems that exhibit free thiol functions at their edges is very high as previously observed for the case of alkenethiols. Indeed they tend to react into disulphide species. In a THF solution an end-functionalized PPE has been deprotected such

that the thiol end groups on the main chains are made to appear. The average contour length of this PPE is 9.2 nm. In order to gain insight into the self-assembly of these deprotected species, thin films have been prepared by solution casting on a SiO_2 wafer.

Unlike previous cases, the morphology is not made of spider webs or long nanoribbons, although short ribbon segments have been occasionally observed (indicated with white arrows in Fig. 6.50). The width of these ribbons is ~30 nm, taking into account the tip broadening effect.

This results confirms that the reactivity of the thiol free PPE is rather high; this renders difficult to drive the self-assembly towards well defined and anisotropic architectures.

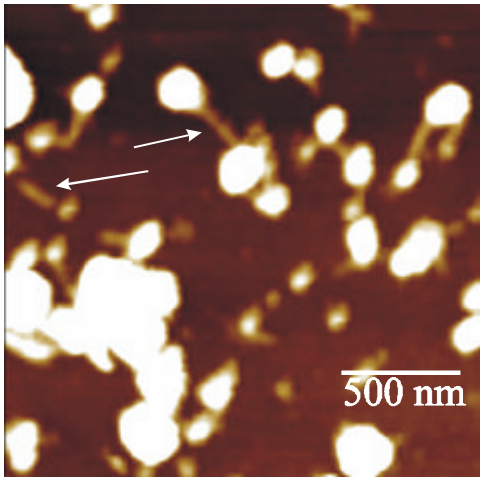

Figure 6.50: Tapping Mode SFM height image of PPE with free thiol end-groups assembled on a SiO_2 wafer. Height of the gray scale h=50nm.
Arrows indicate short ribbon with a molecular cross-section

6.6 Electronic structure of phenyleneethynylene derivatives

6.6.1 Introduction

Photoelectron spectroscopies (PES) can be used to study conjugated polymers at surfaces and their early stages of metal interface formation. They provide information on both chemical and electronic properties and, on the same time, they are extremely surface sensitive and non-destructive to organic systems [Sal96]. The measurements need to be carried out in vacuum; indeed, to determine the kinetic energy of the photoemitted electrons, without significant

collisions with molecules in the background, a pressure in the analysis chamber of $p < 10^{-5}$ mbar is required. In addition, in order to have a non contaminated surface, in particular when working with reactive metals (donors) doping the conjugated species, it is necessary to work in a ultra-high vacuum (UHV) environment, namely at a pressure $< 10^{-9}$ mbar.

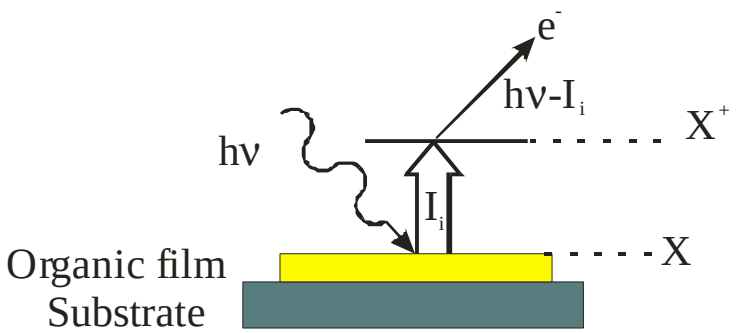

Figure 6.51: Principle of photoelectron spectroscopy of thin organic films on a conductive substrate.

The principle of the technique is represented in Fig. 6.51: a photon (hν) hits and is absorbed by a molecule. This induces an excitation of the electron from its ground state (X in Fig. 6.51) to an excited state (X^+ in Fig. 6.51), where (X^+ – X) corresponds to the ionization energy (I_i). The electrons is then photoemitted from the molecule with a kinetic energy E_K. The binding energy of the electron in the molecule is defined as $E_B = h\nu - E_K = I_i$.

Using soft X-ray photons (namely Xray Photoelectron Spectroscopy, XPS, known also as ESCA), from an excited Mg(K_α) radiation (1254.6 eV) it is possible to investigate both the atomic core-electron energy levels (C_i) and the valence electron energy levels (V_i). With ultraviolet radiation (namely Ultraviolet Photoelectron Spectroscopy, UPS) using a helium discharge source - HeI (21.2 eV) or HeII (40.8 eV) - only the valence electronic states may be studied, but with a resolution higher than the one that is usually achieved by XPS. Noteworthy, PES spectra provide a one-to-one correspondence between the peaks in the photoemitted electron energy distribution and the electron energy states in the molecules as depicted in Fig 6.52. The ideal thickness of the organic adsorbate for these kind of measurements, which arises from the short elastic mean free path for low kinetic energy electrons in solids, is between 5 and 10 nm [Sal96].

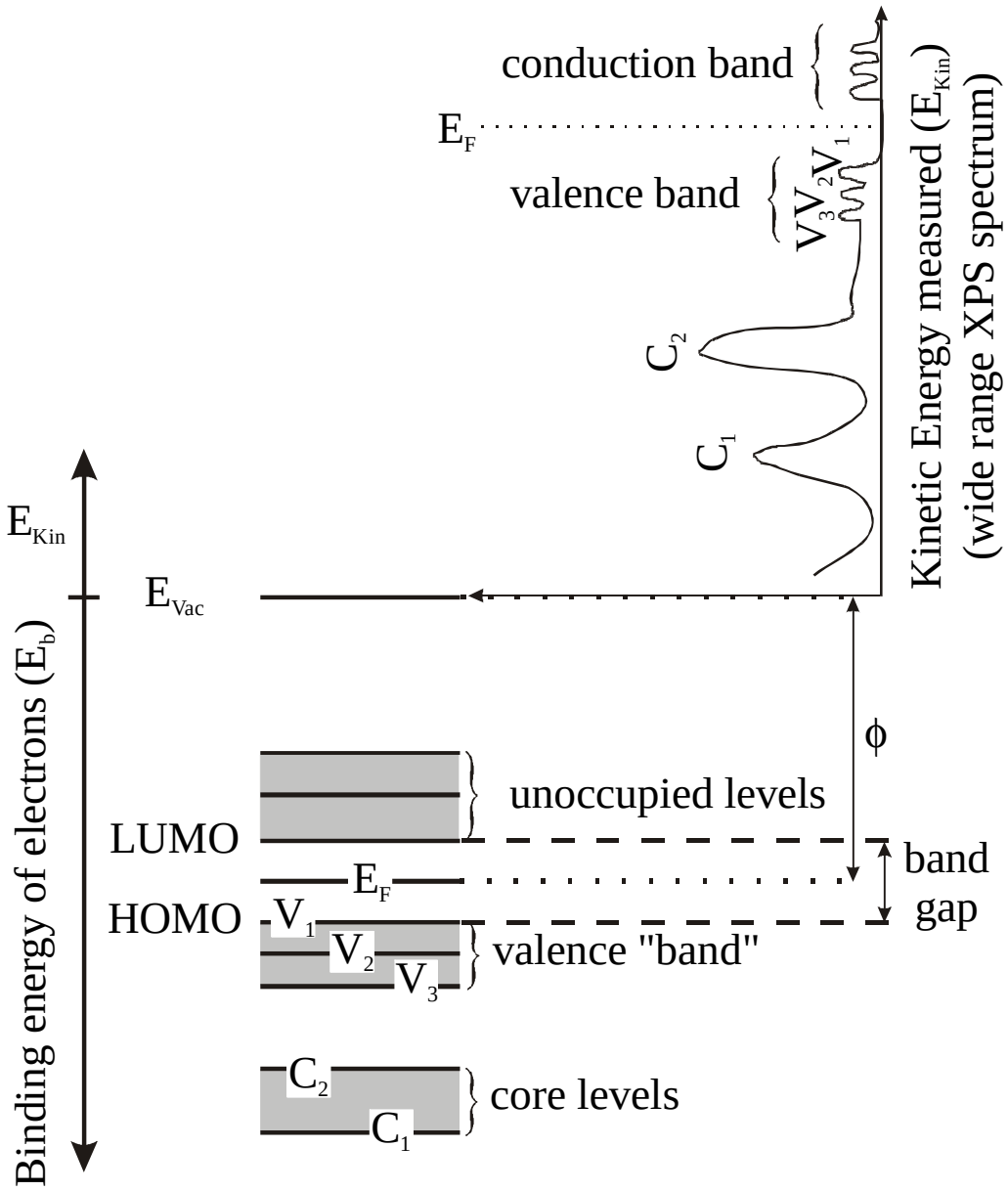

Figure 6.52: Electronic levels in a π-conjugated molecule. E_F=Energy of the Fermi level; E_{Vac}=Energy of the vacuum level; E_{Kin}=Kinetic energy = hν-I_i; ϕ=work function. Bottom of the figure: schematic cartoon of the electronic levels. Top: corresponding PES spectra.

The typical electronic structure in a π-conjugated molecular system is composed of different characteristic features. A core level "band" , a valence "band" whose upper level is the Highest Occupied Molecular Orbital (HOMO), and unoccupied levels that have as the lowest level the Lowest Unoccupied Molecular Orbital (LUMO). In the case of a pristine sample (pure material, non doped) the Fermi level is placed just in the middle of the band gap (energetic gap between HOMO and LUMO). On the other hand the gap between the Fermi level and the vacuum level is known as work function (ϕ).

6.6.2 Work functions of pristine and doped phenylenethynylene trimer and polymer

In this work, the aim was to characterize the electronic structure of oligomeric and polymeric phenyleneethynylene derivatives both of the pristine and of the *n*-doped moiety.

Four different films were investigated: two spin-coated PPE polymer films, one spin-coated and one UHV-sublimed PPE-trimer film.

XPS has been used to determine the stoichiometric composition and purity of the films. Fig. 6.53 shows XPS survey spectra of the four investigated films together with the spectrum of a clean (aceton/iso-propanol cleaned) Au substrate. The spectra confirmed the overall purity of the adsorbate, with the exception of a small quantity of residual oxygen (C to O ratio was between 0.98 and 0.99). The thicknesses of the four films are lying between 3 and 4 nm, estimated from the reduction of the intensity of the Au $4f_{7/2}$ -line due to the organic adsorbate.

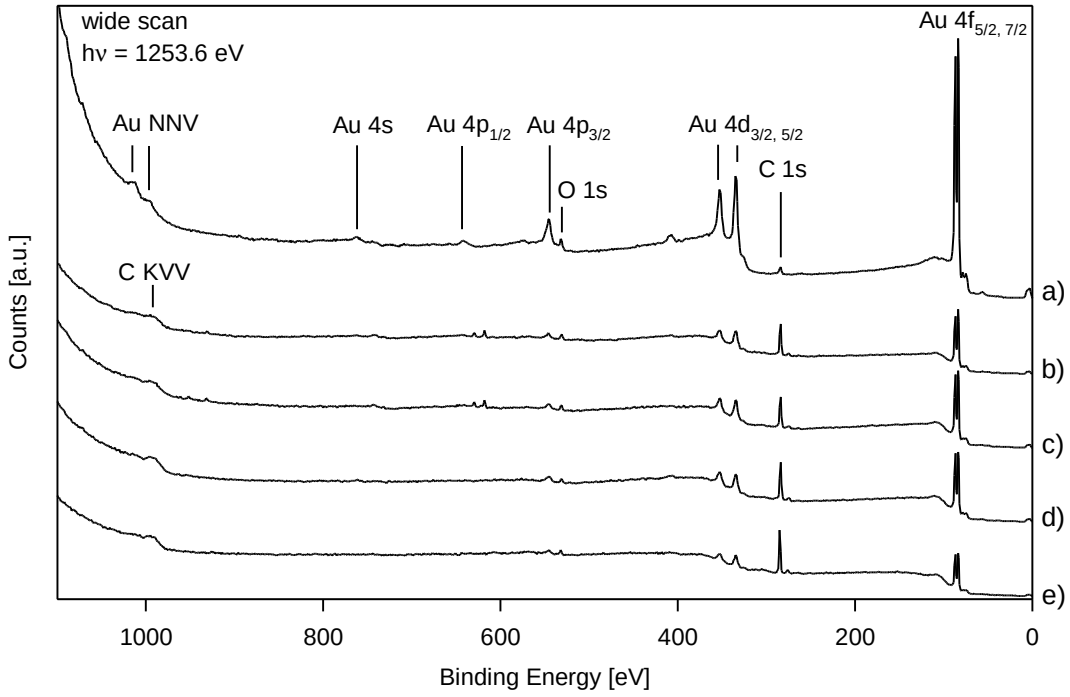

Figure 6.53: XPS survey spectra. a) Au surface cleaned with isopropanol and aceton bath; b) spin coated PPE sample #1 (nominal thickness d=3.1 nm); c) spin coated PPE sample #2 (d= 2.7 nm); d) spin coated PPE trimer (d= 3.0 nm); e) sublimed PPE trimer (d= 4.1 nm).

On the other hand UPS allows to explore the electronic structure near the Fermi level: it allows to localize the HOMO and LUMO and to determine the work function ϕ from the cut-off of the secondary electrons in the HeI spectrum [Sal96]. Fig. 6.54 shows the respective UPS - HeII spectra. The organic films are thick enough to suppress the weakly bound electrons of the gold substrate emitted near the Fermi level. As marked in Fig. 6.54, the UPS spectra of the polymer exhibits in the π-region three features and the spectrum of the spin-coated trimer four features (here, the feature with the lowest binding energy seems to be split) whereas the π-features of the sublimed trimer are barely observable. This latter spectrum is dominated by the σ-bonds of the alkyl chains. In order to increase the π signal the sublimed trimer film has been annealed for 15 minutes in UHV at 100 °C. At this temperature a good part of the adsorbate desorbed. Hence, only the characterization of the spin-coated trimer and polymer films was pursued further.

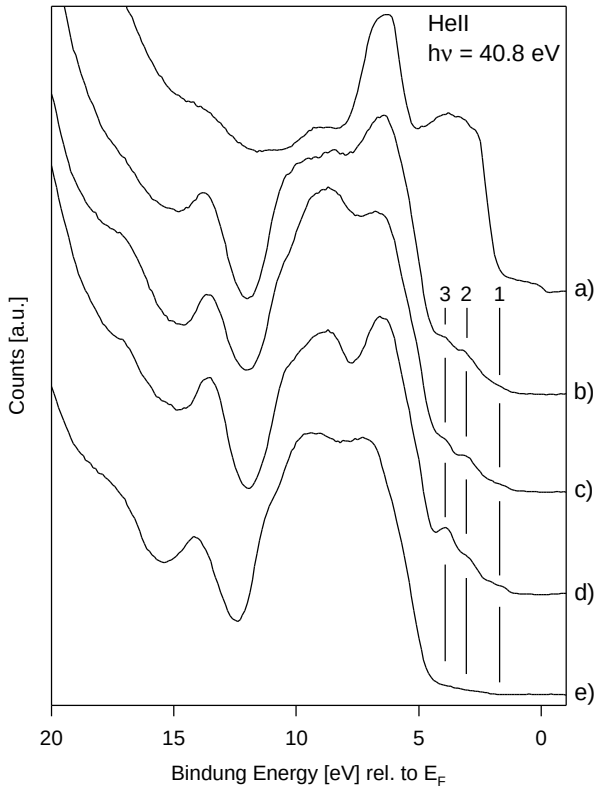

Figure 6.54: UPS HeII spectra of a) Au surface cleaned with isopropanol and aceton bath (work function ϕ=4.1 eV); and pristine samples of: b) spin coated PPE sample #1 (ϕ =4.2 eV); c) spin coated PPE sample #2 (ϕ = 4.3 eV); d) spin coated PPE trimer (ϕ= 4.5 eV); e) sublimed PPE trimer (ϕ = 4.0 eV).

6.6.2.1 Spin coated PPE trimer

The recorded XPS (survey scan, C 1s and Na 1s) and UPS (HeI, HeII spectra at increasing doping are shown in Figs. 6.55 to 6.58. The work functions ϕ are determined from the HeI spectra (not shown here) and the doping levels (number of Na atoms per monomer) are estimated from the ratio of the intensity of the C 1s and the Na 1s peak of the XPS survey spectra (see Fig. 6.55). The evolution of both values is listed in Table 6.7.

Table 6.7: *n*-doping of the PPE trimer: evolution of the work function ϕ with the doping level.

Time of doping (min)	0	1	2	3	5
ϕ (eV)	4,5	3,2	2,8	2,7	2,6
Na-atoms /monomer	0	0.38	0.84	0.98	1.38

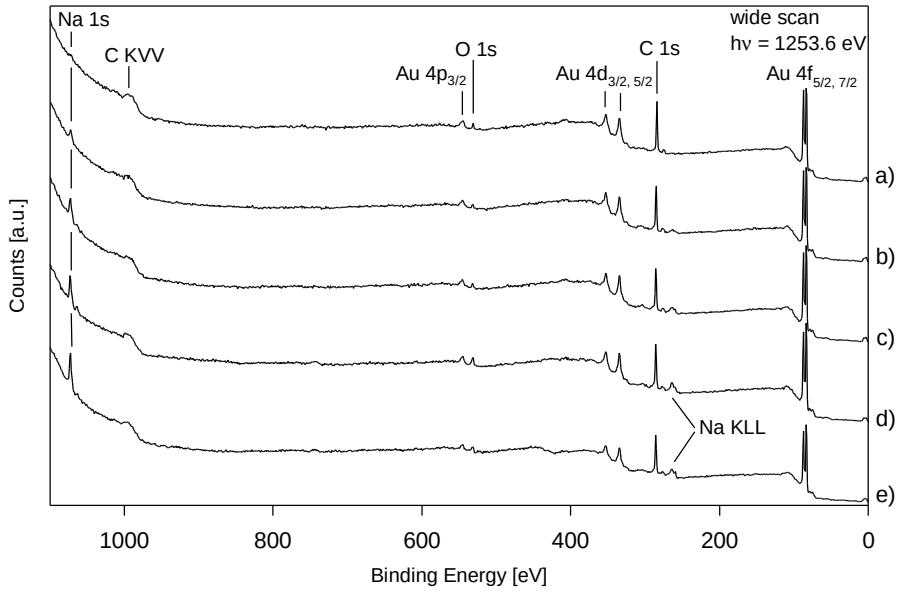

Figure 6.55: XPS survey spectra of spin coated sample of phenyleneethynylene trimer at increasing level of doping. a) Na/C/Au=0/100/17 ; b) 1.9/100/19.6 (0.38 Na-at/mon.); c) 4.2/100/21.2 (0.84 Na-at/mon.); d) 4.9/100/20.1 (0.98 Na-at/mon.); e) 6.9/100/18.5 (1.38 Na- at/mon.).

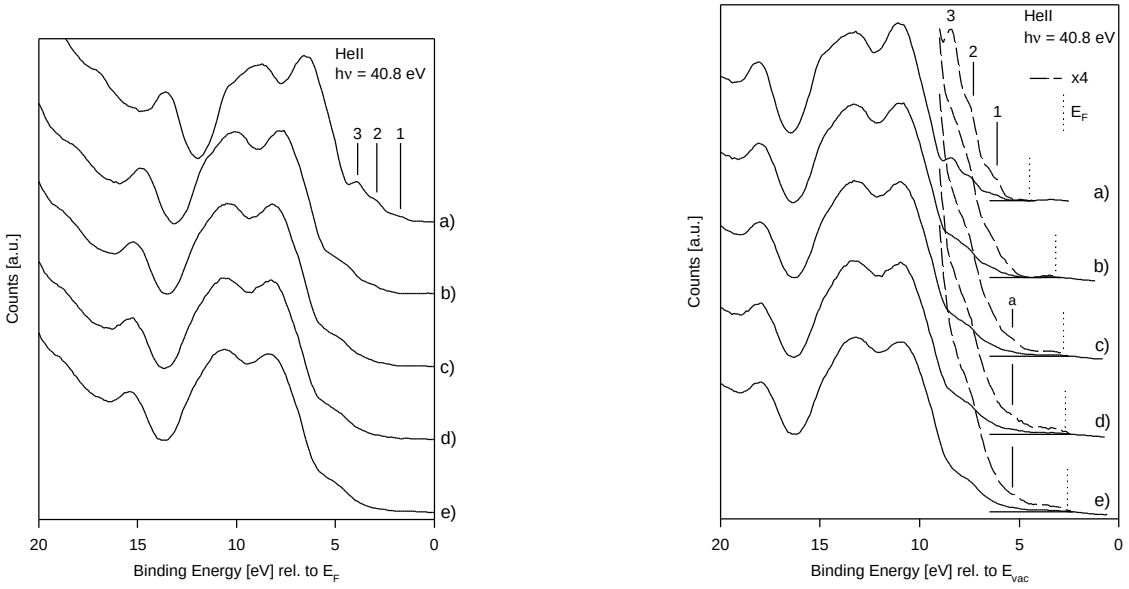

Figure 6.56: UPS HeII spectra of spin coated film of phenyleneethynylene trimer at increasing level of doping. The spectra are plotted relative to the Fermi level (left) and to the vacuum level (right). a) pristine: ϕ=4.5 eV ; b) ϕ= 3.2 eV (0.38 Na-at/mon.); c) ϕ= 2.8 eV (0.84 Na-at/mon.); d) ϕ= 2.7 eV (0.98 Na-at/mon.); e) ϕ= 2.6 eV (1.38 Na-at/mon.).

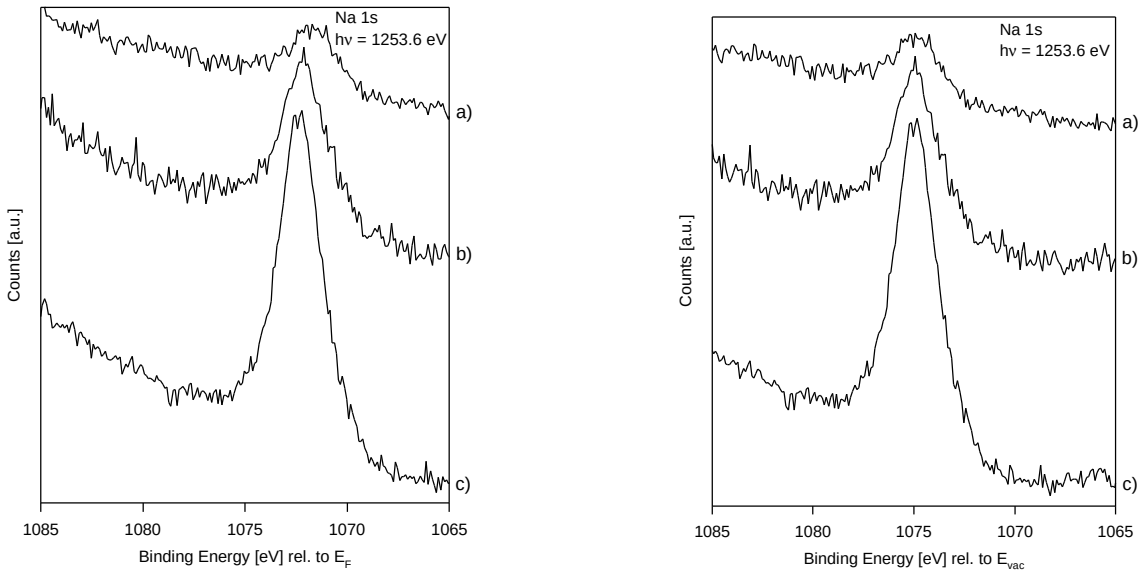

Figure 6.57: XPS spectra zoomed on the Na 1s peak of spin coated sample of phenyleneethynylene trimer at increasing level of doping. The spectra are plotted relative to the Fermi level (left) and to the vacuum level (right). a) ϕ= 3.2 eV (0.38 Na-at/mon.); b) ϕ= 2.8 eV (0.84 Na-at/mon.); c) ϕ= 2.6 eV (1.38 Na-at/mon.).

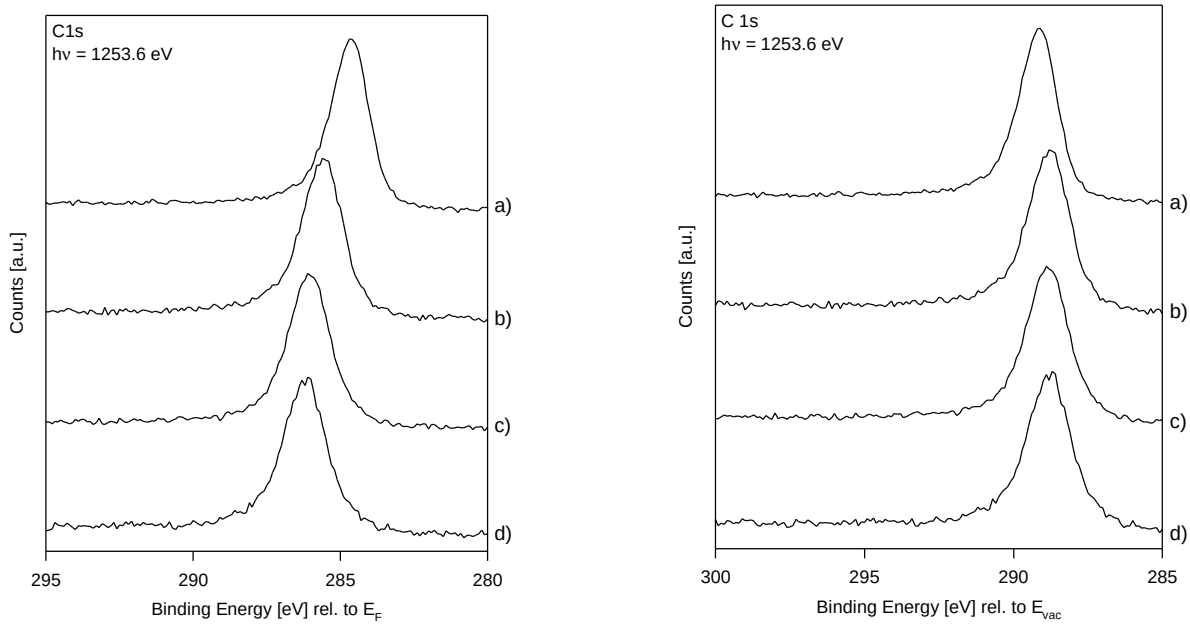

Figure 6.58: XPS spectra zoomed on the C 1s peak for spin coated sample of phenyleneethynylene trimer at increasing level of doping. The spectra are plotted relative to the Fermi level (left) and to the vacuum level (right). a) ϕ= 4.5 eV (pristine); b) ϕ= 3.2 eV (0.38 Na-at/mon.); c) ϕ= 2.8 eV (0.84 Na-at/mon.); d) ϕ= 2.6 eV (1.38 Na-at/mon.).

The sequence of HeII spectra of Fig. 6.56a (the spectra are plotted relative to E_F) shows that the four π peaks are smearing out with increasing Na deposition. Due to an increase of the Fermi level and/or the creation of a surface dipole, the whole spectra are shifted to higher binding energies (Dr. M. Keil, IFM Linköping, Sweden, private communications). An appearance of new peaks directly below the Fermi level is not observed.

In order to take into account the shift of the Fermi level due to Na doping, the HeII spectra of Fig. 6.56b are plotted relative to the vacuum level (the position of E_F is marked as a dotted line). Since no significant shifts of the whole spectra after the respective doping steps can be observed in Fig. 6.56b the changes of the work function from 4.5 eV to 2.6 eV are necessarily due to an increase of the Fermi level (*n*-doping).

Therefore, the Fermi level increases by about 1.9 eV after doping of 1.38 Na-atoms per monomer. At higher doping levels (0.84 - 1.38 Na-atoms / monomer) a new structure appears at ca. 5.5 eV. This feature lies around 2.5 eV below the Fermi level whereas the peak of the highest occupied state before doping lies only 1.5 eV below E_F. At higher doping levels (0.84 - 1.38 Na-atoms / monomer) unstructured features grow up directly below E_F. The shape of these features does not allow to assign them clearly to new levels grown near E_F. Figs. 6.57a

and b show sequences of Na 1s XPS spectra relative to E_F and E_{vac}, respectively. The Na 1s peak of Fig. 6.57a shifts for higher doping levels to higher binding energies (due to a Fermi level shift), whereas no shifts can be observed in Fig. 6.56b. The C 1s spectra of Figs. 6.58a and 6.58b show similar behaviors. Here, the C 1s peak of Fig. 6.59b shifts slightly to a smaller binding energy (relative to E_{vac}) indicating a non-homogeneous distribution of Na in the deeper layers.

6.6.2.2 Spin coated polymer

A polymeric phenyleneethynylene (PPE) solution in THF (1.66 g/l) has been spin-coated on the Au film. Here only the case of the sample # 2 (Fig. 6.53) will be discussed. The recorded XPS and UPS spectra are shown in Figs. 6.59 to 6.60. The following table shows the evolution of the work functions and the doping levels determined from the HeI spectra (not shown here) and the XPS survey spectra (see Fig. 6.59), respectively:

Table 6.8: n-doping of the PPE: evolution of the work function ϕ with the doping level.

Time of doping (min)	0	1	2	3
ϕ (eV)	4,3	3,5	3,0	2,6
Na-atoms /monomer	0	0.42	0.94	1.1

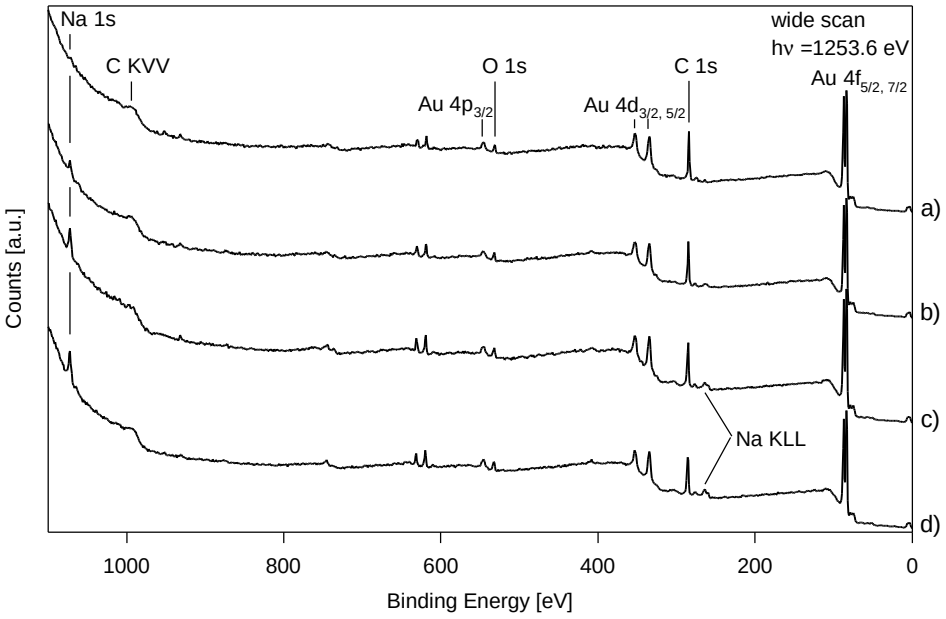

Figure 6.59: XPS survey spectra of spin coated sample of PPE at increasing level of doping. a) Na/C/Au=0/100/23.4 (pristine); b) 2.1/100/24.8 (0.42 Na-at/mon.); c) 4.7/100/28.1 (0.94 Na-at/mon.); d) 5.5/100/29.3 (1.1 Na-at/mon.).

The sequence of HeII spectra of Fig. 6.60a (relative to E_F) shows a smearing of the three π states together with a shift of the whole spectrum to higher binding energies upon successive doping. After aligning the spectra relative to E_{vac} (Fig. 6.60b) it is possible to observe a slight shift of the spectra of about 0.5 eV to lower binding energies due to dipole effects (non-homogeneous Na-distribution, Dr. M. Keil, IFM Linköping, Sweden, private communications). Therefore the increase of E_F after doping of 1.1 Na-atoms / monomer can be estimated as $\phi_{pristine}$-ϕ_{doped}-shift = 4.3 - 2.6 - 0.5 = 1.2 eV. If compared to the trimer film (see Fig. 6.56b) the behavior of HeII spectra of the polymer film (Fig. 6.60b) seems to be different upon doping. After doping of 0.42 Na-atoms per monomer the peak of the highest occupied orbital (at 6 eV) increases in a first step in intensity and then, in a second step at higher doping levels (0.94 - 1.1 Na-atoms per monomer), the peak either shifts to lower binding energies (to 5.5 - 5 eV) or a second peak at 5.5 - 5 eV additionally appears in the forbidden band gap. This new structure lies ca. 2.5 eV below E_F. This value is comparable to the value of the doped trimer film. As seen in the case of the trimer film, the HeII spectra of

the polymer film (Fig. 6.60b) also exhibit unstructured features after doping, which occur directly below E_F.

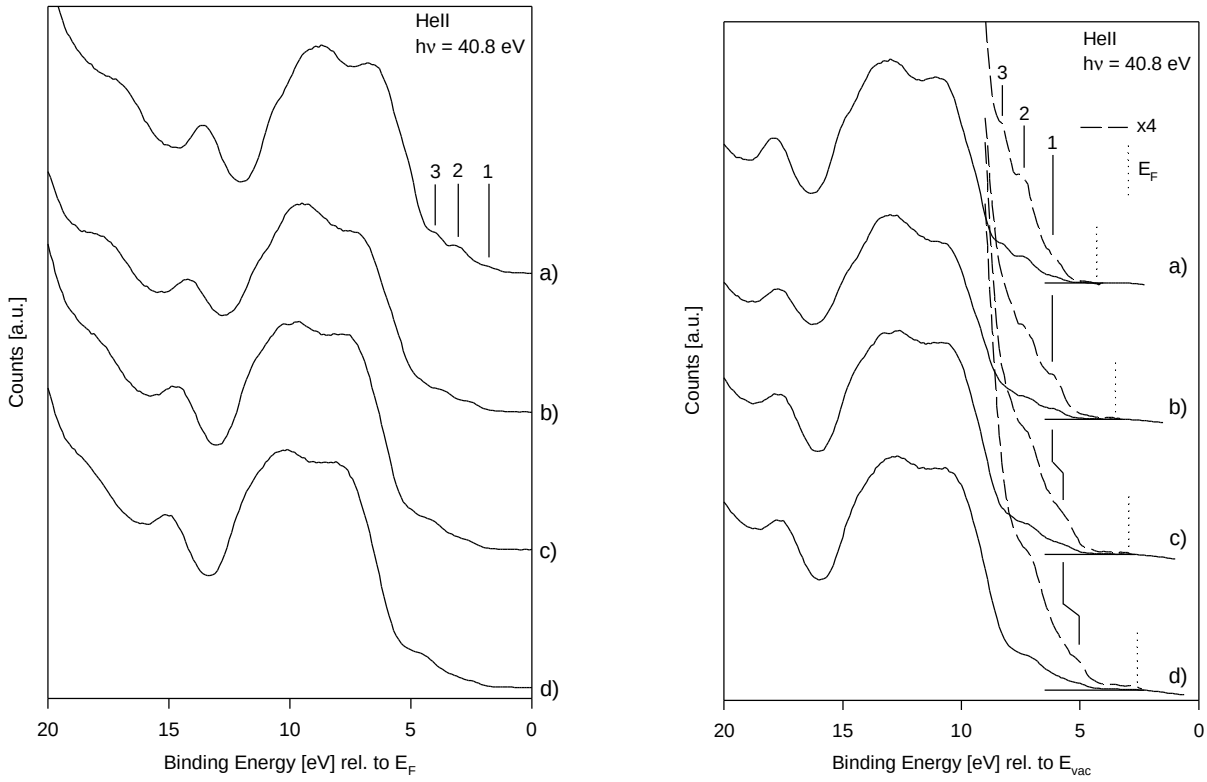

Figure 6.60: UPS HeII spectra of spin coated sample of PPE at increasing level of doping. The spectra are plotted relative to the Fermi level (left) and to the vacuum level (right). a) pristine: ϕ=4.3 eV ; b) ϕ= 3.5 eV (0.42 Na-at/mon.); c) ϕ= 3.0 eV (0.94 Na-at/mon.); d) ϕ= 2.6 eV (1.1 Na-at/mon.).

Focusing on the Na 1s and C 1s peaks (here not shown), results similar to the ones of the trimer were obtained, indicating an inhomogeneity of the Na distribution in the polymer. In addition, an analogous study on the polymer sample #1 (Fig. 6.53) confirmed these results.

In summary, the *n*-doping of the three investigated films with Na was successful. Upon doping, the work functions ϕ of all samples are drastically decreasing and the Fermi levels are increasing. Additionally, due to doping, a new peak appears in the forbidden band gap directly above the valance band edge and unstructured features grow up below the Fermi level. Because of overlapping structures from the background in this energy region, the line shape of these new structures (especially those appearing directly below E_F) can hardly be

determined. This complicates the interpretation of the doping process.

6.6.3 Optical absorption investigation of PPE

The optical absorption of the polymer in the UV-visible range have been investigated in order to gain further insight into the electronic structure and in particular to determine the band gap. Indeed the peak of the absorption spectra can be assigned to the electronic transition between HOMO and LUMO, i.e. band gap.

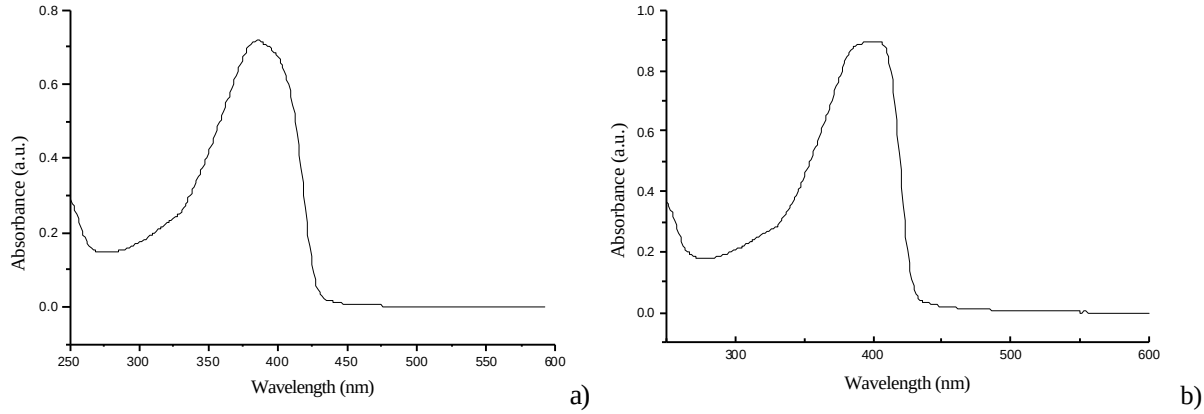

Figure 6.61: UV-Visible optical absorption spectra of PPE. a) Degree of polymerization (*DP*)= 8; b) *DP*=35. (The spectra have been recorded by Dr. V. Francke in MPI for Polymer Research, Mainz, Germany).

The peak of the absorption spectra shifts to higher wavelengths with increasing polymer length (Fig. 6.61). In fact a polymer with a degree of polymerization (*DP*) of 8 shows a maximum at 385 nm while for a *DP*=35 the peak amounts to 402 nm. The band gap amounts to 3.22 eV and 3.09 eV, respectively, i.e. it gets smaller with increasing average length of the macromolecule, as one would expect according to a particle in a box model [Bei69].

6.6.4 Density of valence states calculations

Calculations of the density of valence states (DOVS) were carried out by Dr. Donizetti dos Santos by means of Valence Effective Hamiltonian (VEH) simulations on the basis of an

AM1 optimized geometric structure, which usually provides good estimates of the electronic structure of conjugated polymers. The theoretical ionization potential (I_p) and the electron affinity (E_a) of poly(*para*-phenyleneethynylene) have been determined to I_p = 5.3 eV and E_a = 2.5 eV; as a consequence the band gap amounts to 2.8 eV. This is in fairly good agreement with the experimental results obtained with UV-Visible absorption spectroscopy taking into account that the experiments have been carried out on rather short polymers.

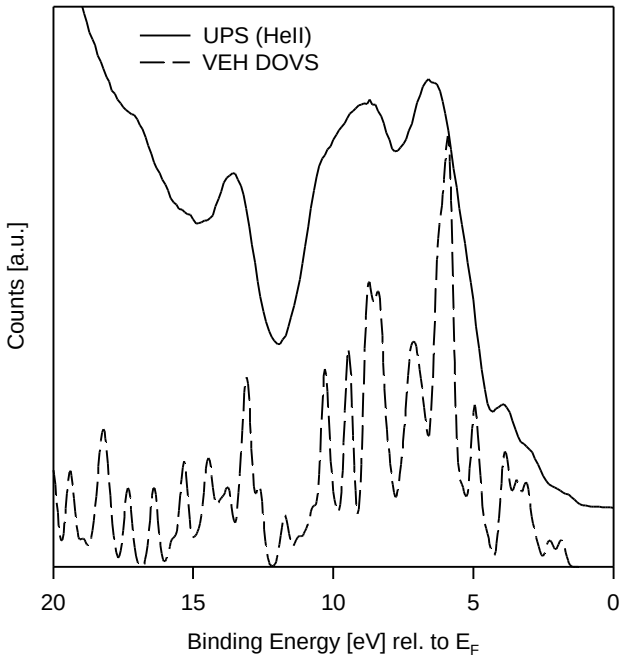

Figure 6.62: Valence Effective Hamiltonian (VEH) of the density of valence states (DOVS) simulated spectra and UPS HeII spectra of a spin coated film of pristine PPE trimer. The spectra are plotted relative to the Fermi level.

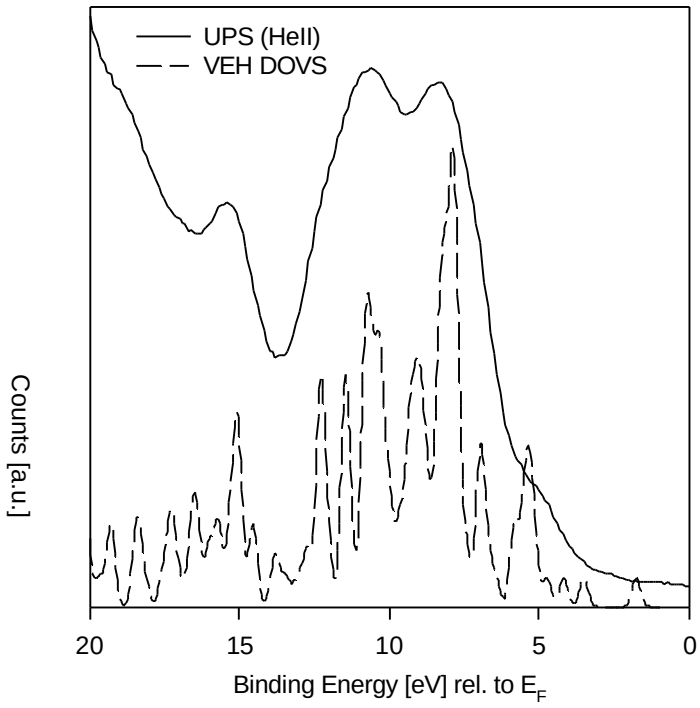

Figure 6.63: Valence Effective Hamiltonian (VEH) of the density of valence states (DOVS) simulated spectra of a doubly charged system and UPS HeII spectra of spin coated film of a doped PPE trimer (1.38 Na at/mon). The spectra are plotted relative to the Fermi level.

Furthermore a simulation of the UPS HeII spectra for the case of the trimer has been computed. The obtained spectra, plotted relative to the Fermi level, are compared to the experimental UPS HeII plot: for the case of the pristine trimer (Fig. 6.62) the theoretical plot fits well with the experimental one. In the latter case shown in Fig. 6.63 the UPS spectra of the 1.38 Na atoms/molecule are reasonably comparable with the doubly negative charged PPE-trimer, although one extra peak near to the Fermi edge can be observed only in the theoretical spectra.

6.7 Current-Voltage (I-V) Measurements

6.7.1 Visualization of the nanoelectrodes

The characterization of the Au electrodes, developed following the recipe discussed in

paragraph 4.3, has been always carried out both performing current-voltage (I-V) type of measurements, in order to proof the existence of a gap, and with Tapping Mode SFM imaging, to visualize the structure and to evaluate the size of the gap. It is fair to note that, due to the finite size of the SFM tip (terminal radius ~ 10 nm), it turns out to be not feasible to visualize of gaps smaller than the diameter of the tip (~ 20 nm). This suggests that SFM is not the ideal technique for this kind of measurements while high resolution TEM seems to be more appropriate.

The Au nanoelectrodes are contacted to macroscopic Au wires using Ag paste. The I-V measurements are performed contacting the macroscopic wires with the voltage source.

Gold nanogaps grown on SiO_2 wafers from three different sources have been used:

1. Dr. S. Rogaschewski (Department of Physics, Humboldt University Berlin);
2. Dr. K. Kragler (Siemens AG, Erlagen);
3. Dr. A. C. F. Hoole (Department of Engineering, University of Cambridge, UK).

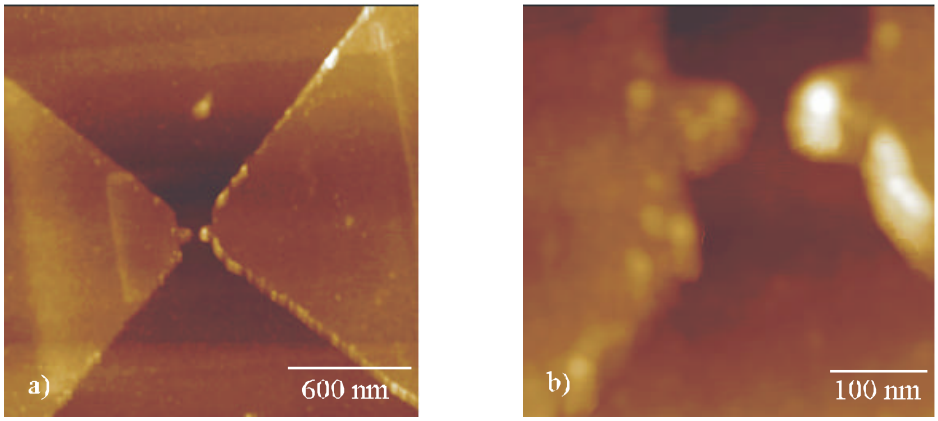

Figure 6.64: Tapping Mode SFM height image of Au nanoelectrodes produced by Dr. S. Rogaschewski. The height of the gray scale (h) is: a) h= 50 nm ; b) h= 40 nm.

The structure of the first type of electrodes has been studied first. The electrodes exhibit a gap usually of about 50 nm (Fig. 6.64) that is unfortunately still rather big. The value has been determined considering the broadening due to the SFM tip during scanning. The model expressed in formula 6.3 can be used also in this case, with a terminal radius of the tip R=(13±7) nm and a height (h) of the Au layer (electrode) that can be evaluated from singular

profiles. For h=10 nm the tip broadening 2Δ ~ 25 nm. Moreover the gap reproducibility is rather poor. Indeed it sometimes has been detected that the lift-off of the gold during the fabrication did not occur completely. In this case the electrodes do not posses any gap (Fig. 6.65).

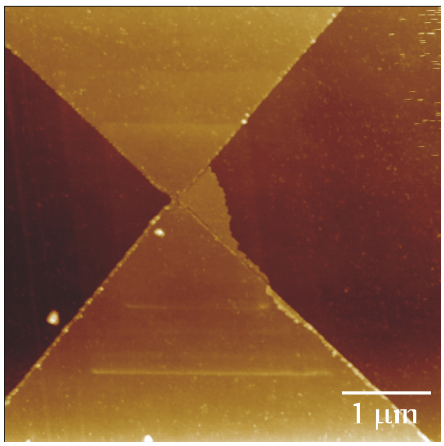

Figure 6.65: Tapping Mode SFM height image of Au nanoelectrodes produced by Dr. S. Rogaschewski. The lift off process was not perfect; therefore there is no gap between the two electrodes. h= 70 nm.

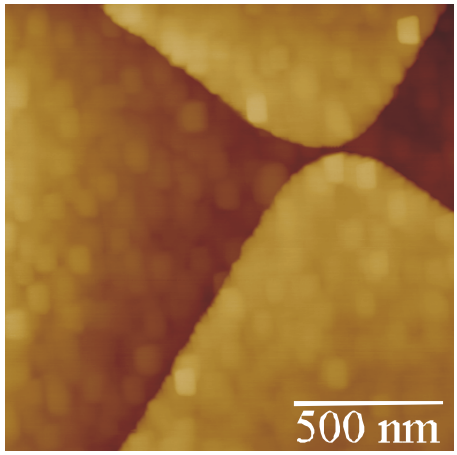

Figure 6.66: Tapping Mode SFM height image of Au nanoelectrodes produced by Dr. K. Kragler. h= 40 nm.

The second type of electrodes are shown in Fig. 6.66. The reproducibility of a gap of 10-20 nm is remarkable.

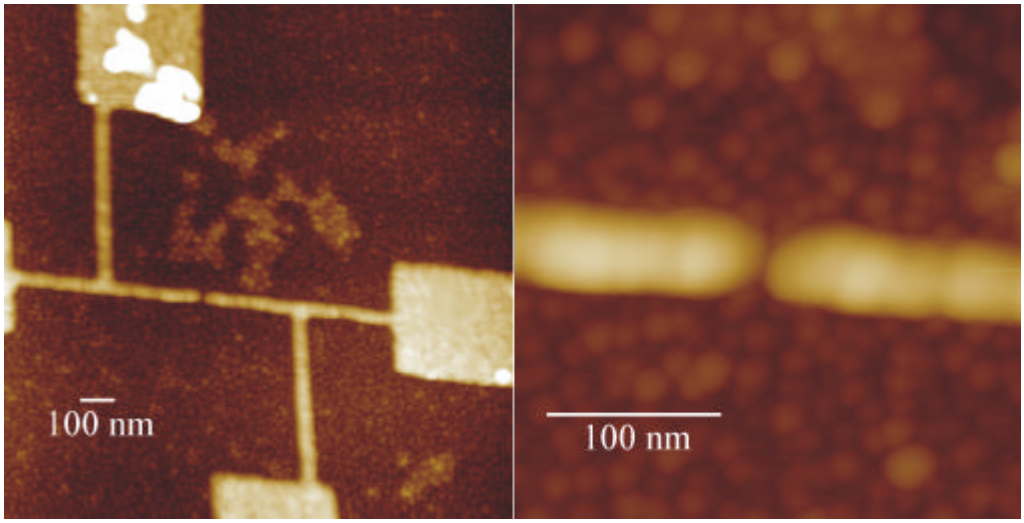

Figure 6.67: Tapping Mode SFM height image of Au nanoelectrodes produced by Dr. A.C.F. Hoole. h= 40 nm.

The third type of electrodes are grown on a 1 μm thick SiO_2 insulating layer on a silicon wafer; the leakage current is about 10^{-13} at a voltage of ± 1V. They are produced by evaporating a 10 nm thick Au layer on the flat substrate. The gap of the nanoelectrodes (Fig. 6.67) determined from topographical profiles on SFM images amounts to ~ 20 - 25 nm, if one considers the SFM tip broadening effect. The reproducibility of this size of the gap is rather high.

The different quality between the three types of electrodes investigated can be due to a variety of factors which can play a role in the electrodes preparation (Fig. 4.3), such as the resolution of the electron beam irradiating the PMMA, the quality of the development, of the metallization and of the lift-off steps.

6.7.2 Bridging metallic nanogaps with molecules

The aim of this experiment is to probe the conductivity of a well defined (macro)molecular architecture by interfacing a PPE nanostructure to the Au nanoelectrodes. The molecules,

when bearing the thiol end-groups in the α and ω position, are expected to chemisorb on the Au nanoelectrodes.

The deprotection reaction of the end groups needs to be performed in situ on the electrodes. Indeed, it is of prime importance to carry out the deprotection reaction of the carbamoyl groups which cap the thiol functions attached to the main chain of the PPE in a free oxygen environment, in order to avoid the aggregation of PPEs through disulphide bridging.

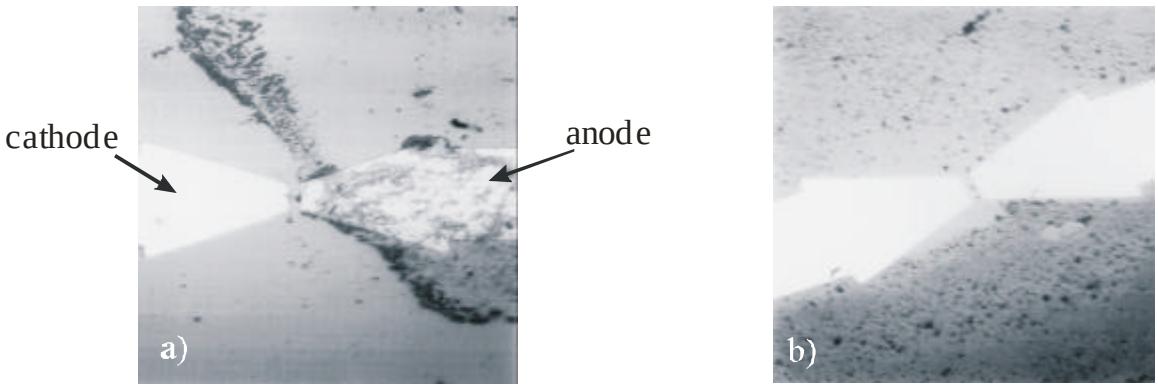

Figure 6.68: Adsorption of sulphur free PPE. a) Electrochemical adsorption induced by the applied voltage between the two electrodes; b) the self-assembly is likely to be governed by the chemisorption of sulphurs on Au nanoelectrodes.

Initially the chemisorption reaction has been tested as a function of the chemical nature of the end groups. A PPE exhibiting sulphur free end-groups on the main chain (Fig 5.10 formula b) have been self-assembled between the two Au nanoelectrodes, and contemporary a voltage of 1V have been applied between the gap: the moieties adsorb (precipitate) onto the anode as shown in an optical microscope snapshot in Fig. 6.68a. In this case the molecule exhibits two negatively charged end groups playing a paramount role in the self-assembly process. The scale length of the image in Fig. 6.68a is some hundreds of micrometers. On the other hand, a more reduced adsorption of the molecules on the electrodes is obtained by casting the same solution without applying voltage between the two electrodes (Fig. 6.68b). In this case the coating appears to be uniform, although different between the Au and the SiO_2 surface; this suggests that in the first example the adsorption was electrochemically driven. In the latter case it is likely that the adsorption of the sulphur end functionalized molecules is governed by the chemisorption of the sulphurs on Au, even though the resolution of the optical microscope does not permit to prove this statement.

The possibility to control the self-assembly of the thiol free PPE on a nanometer scale is rather poor, as discussed in paragraph 6.5.7. Applying a voltage between the electrodes, also in the case of a PPE bearing SH end groups (Fig. 5.10 formula c), the molecular adsorption on the electrodes takes place abruptly (similar to Fig. 6.68a). Because of this reason experiments of the self-assembly of thiol-end PPE have been carried out on the Au nanoelectrodes produced by Dr. K. Kragler, Siemens AG without applying voltage between the gap during the self-assembly.

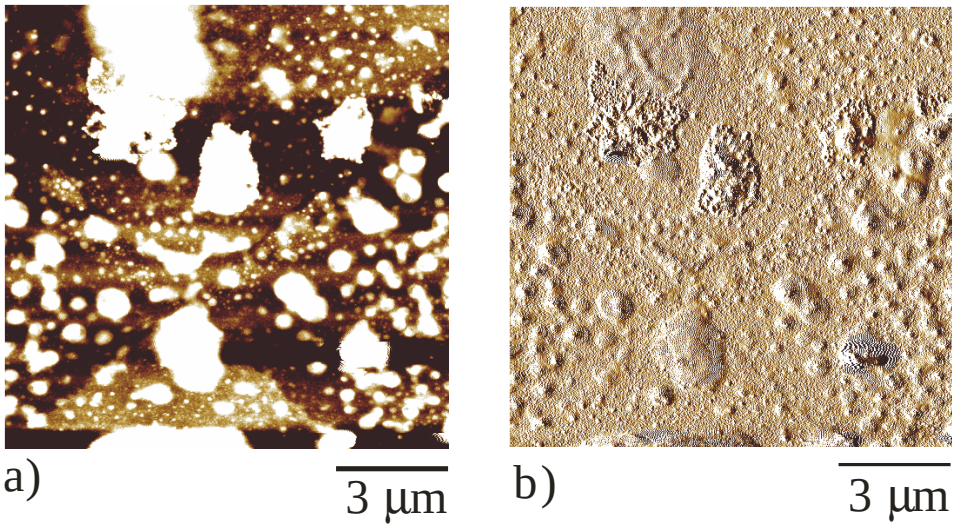

Figure 6.69: Tapping Mode SFM image of a PPE with an average contour length of 14 r.u. . The height image shows electrodes strongly coated. a) Height image: h=70 nm; b) Phase image.

On this molecular scale, even using low concentrations of the solution (~ 0.04 g/l) in a mix THF-phenyloctane it was not possible to produce any ordered architectures. It is worth to note that this is the same range of concentrations that has been used for producing PPE ribbons, such as the ones in Fig. 6.41. In Fig. 6.69 a disordered adsorbate coats the Au nanoelectrodes which are hardly recognizable. The electronic properties of this molecular adsorbate has been characterized. The I-V plots show that the coating gives rise to an enhancement of the current between the two electrodes, although, due to the lack of molecular ordering in the gap, it is not possible to assign this conduction to a well defined *ensemble* of molecules. The conductivity of this non-doped material is still in the range of rather insulating materials (Fig. 6.70). The doping of the PPE, due to the existence of the triple bond in the repeat unit, is chemically feasible only by reducing the polymer with an alkali metal (*n* type doping). This would require to work in a very controlled environment free of oxygen, namely ultra-high vacuum (UHV), which was not done here.

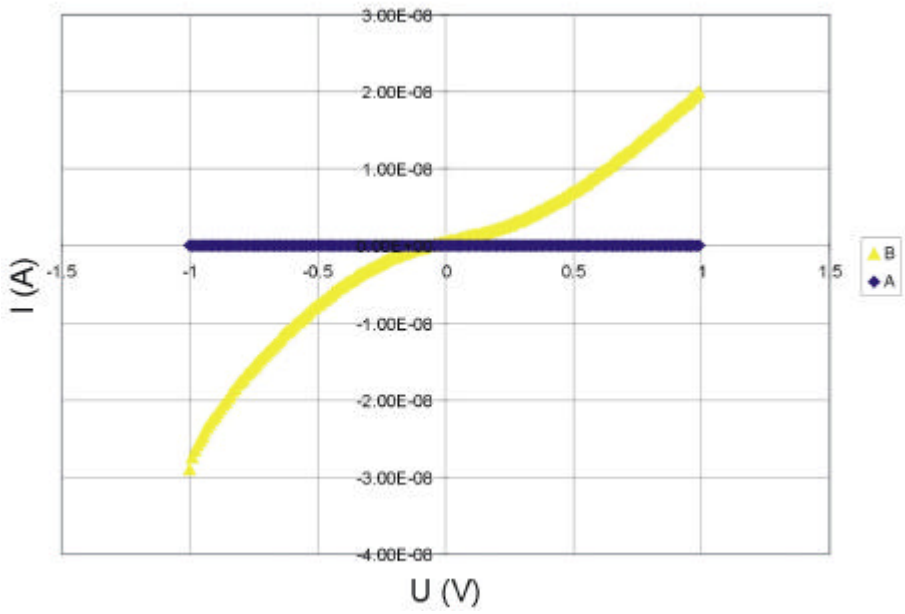

Figure 6.70: Current-voltage curve: A) non coated electrodes; b) coated electrodes. The curve appears to be symmetric and the maximum current is on the order of 10 nA at ± 1V.

6.8 Growth of dry hexakis-dodecyl-hexabenzocoronene films from solutions

By combining chemical sensitive techniques such as photoelectron spectroscopies with the spatial resolution of Scanning Probe Microscopies it is possible to bestow information on both the electronic properties and the molecular arrangements. The aim of the following experiment is to grow and study well defined micrometer size structures of soluble synthetic nanographitic disc like molecules [Mül98c] on conductive substrates, which are atomically flat on the micrometer scale. Physisorbed monolayers at the solid-liquid interface of hexakis-dodecyl-hexabenzocoronene (HBC-C_{12}) [Sta95b] and larger allotropes [Iye98] have been already investigated with STM and a diode-like electrical behaviour of the aromatic part of the molecule in the gap has been probed by means of Scanning Tunneling Spectroscopy (STS) [Sta95b].

HBC-C_{12} (Fig. 6.71) has been self-assembled from solution as dry thin films on HOPG. It has been characterized by Tapping Mode - Scanning Force Microscopy and UPS. XPS was also used to determine the stoichiometric composition and purity of the films.

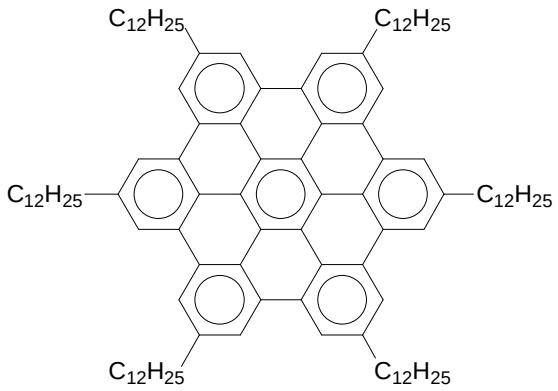

Figure 6.71: hexakis-dodecyl-hexabenzocoronene (HBC-C_{12})

As described in paragraph 5.3.3, the films have been prepared following different procedures in order permit the evaporation of the solvent and molecular assembling to occur at decreasing rate.

The diameter of the HBC-C_{12}, in the case where the alkyl side chains are in their fully extended conformation, amounts to 40 Å while the thickness of the planar molecular disc is 3.55 Å. It is worth to note that this thickness is very similar to the one of a monolayer of HOPG (3.35 Å), due to their alike structure. Because of this reason it is hazardous to assign one interface (domain) to HOPG or HBC-C_{12} just on the base of the thickness detected from SFM topographical profiles. This assignment can be achieved only with a careful observation of the shape of the boundaries and, in cases of uncertainty, by using complementary a chemically sensitive imaging mode such as Phase Imaging SFM [Fin97].

Scanning Force Microscopy images of a HBC-C_{12} spin coated film on HOPG (method A in paragraph 5.3.3) are displayed in Fig. 6.72. They exhibit a flat morphology made of polygonal planes extended on the micrometer scale. The steps in height between these planes amount to 3.5 Å and multiples of it, in good agreement with HOPG steps [Wie92]. Phase imaging (Fig. 6.72b) reveals the existence of only one phase covering the sample surface. In addition Scanning Tunneling Microscopy investigations on these films have demonstrated that the conductive substrate is covered by a non-conductive adlayer. Hence, the graphite

surface appears to be homogeneously coated by the organic semiconducting compound. Albeit the interfacial roughness of this film on the micrometer scale is very little, the degree of molecular order of the organic moiety adsorbed onto the flat substrate may be small on a molecular scale due to the fast rate of physisorption.

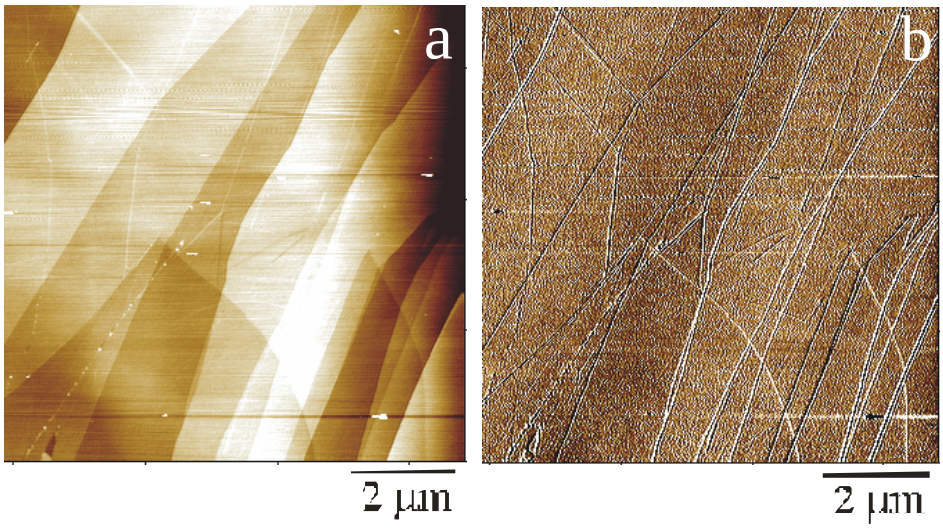

Figure 6.72: Tapping Mode SFM images of HBC-C_{12} film prepared by spin coating the quantity to form ~ 1000 layers coating the HOPG (method A described in paragraph 5.3.3). a) Height image: z-scale (h)=10 nm; b) Phase image: z- scale=7°.

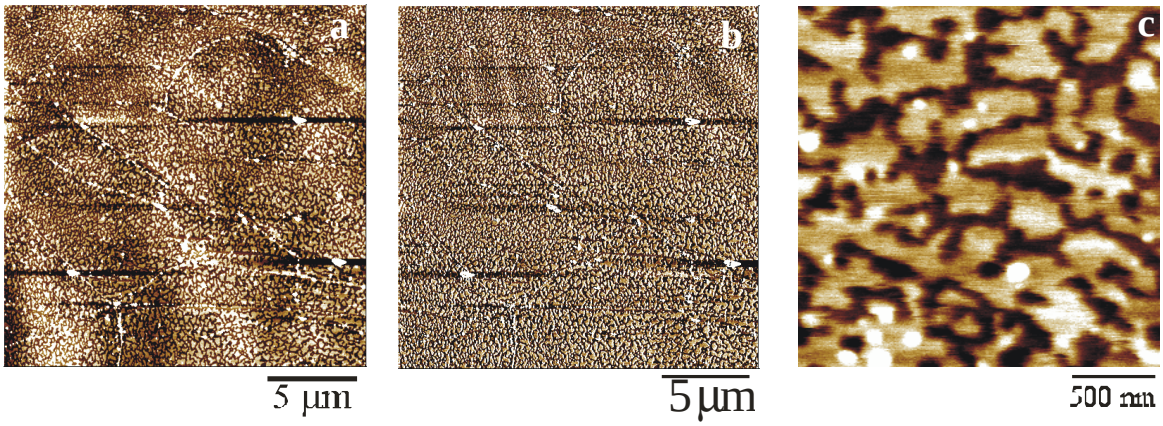

Figure 6.73: Tapping Mode SFM micrographs of HBC-C_{12} grown on HOPG by solution casting (method B in paragraph 5.3.3) a quantity sufficient to coat the HOPG with one layer. a) Height image: h=20 nm; b) Phase image: z- scale=6°; c) Height image: h=20 nm.

On the other hand the morphology of HBC-C_{12} films obtained by fast casting the solution (procedure B) to produce a single layer is shown in Fig. 6.73. In this case, HBC-C_{12} molecules self-assemble into inhomogeneous mono-layers (small islands) with a constant height of 3.5 Å, or multiples thereof, which is consistent with a layer by layer growth of the HBC-C_{12} disk-like molecules oriented flat on the HOPG surface. Thicker domains of higher multiples of 3.5 Å, up to about 25 Å were also observed. The shape of these domains suggests that the stage of the molecular assembly displayed here represents a step towards the formation of more extended clusters occurring via coalescence. The interpretation of the surface composition based on the contrast of the height and phase images, confirmed the existence of different phases on the sample surface that could be due also to a different orientation of the molecules with respect to the basal plane of the substrate.

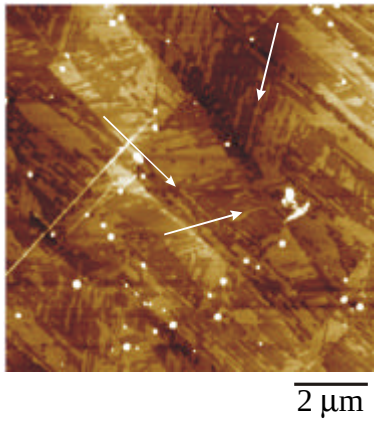

Figure 6.74: Topographical Tapping Mode SFM image of a HBC-C_{12} surface produced by slow solution casting of one layer in controlled environment (route C in paragraph 5.3.3). h=15 nm. The white arrows indicate the preferential directions along which the layers grow anisotropic. The angle between them is 60° in perfect agreement with the three-fold symmetry of the HOPG substrate.

In the third case, thin organic layers prepared by a slow deposition procedure (route C, paragraph 5.3.3) are made of well defined monolayers (Fig. 6.74). Noteworthy, the overlayers exhibit a texture with orientation along preferential directions with an angle between them of 60°, according to the three-fold symmetry of the crystalline HOPG substrate, as indicated by the arrows in Fig. 6.74.

Applying relatively high shear forces in the tens of nN range with Scanning Force Microscopy in contact mode it was not easily possible to scratch all the films by moving the upper layers. Nevertheless the first layers in contact with the substrate are relatively strongly bound by van der Waals interactions, and therefore hardly removable [Bis00].

It is likely that in this first layer both the aliphatic part the molecule and the aromatic one are lying flat on the basal plane of the substrate [Bis00] due to hybridization of the electronic states of the organic molecules with the "metallic band" of the graphite. Then overlayers are grown on the first layer in contact with the substrate. These upper layers exhibit an increasing degree of order with a decreasing rate of the solvent evaporation. The mechanism governing the formation of these layers may be divided in three steps:

1. homogeneous coating of the substrate with the first layer, which dependent on the rate of formation exhibits more or less order;
2. creation of overlayers in a layer by layer growth;
3. ordering of the overlayers along preferential directions induced by the crystalline substrate.

The first step takes place for every type of film preparation discussed above, (A) through (C). The second step, where the molecules are oriented parallel to the (0001) plane of the HOPG, occurs certainly for films prepared by solution casting (B and C). The third step takes place only using a slow casting (C). Note that in both methods (B) and (C), the molecular coverage obtained, due to the dewetting process, is not homogeneous over the macroscopic size (mm^2) of the sample. It turned out that these variations over large distances may be controlled to a certain extent by using the slow deposition procedure (C).

The surface compositions of the films have been checked routinely making use of X-ray photoelectron spectroscopy which revealed an overall purity of the adsorbate with the exception of a quantity of residual oxygen limited to a few percents.

UPS allowed to obtain information concerning the order of the adsorbate on a molecular scale. Focusing on the region of the spectra with a binding energy lower then 5 eV, namely the peaks that have been assigned to the π states of the HBC-C_{12} [Kei00], it is possible to gain insight into the orientation of the molecules with respect to the substrate.

From the graphs in Fig. 6.75 it is evident that the π-peaks are growing with decreasing deposition rates (moving from Fig. 6.75a to Fig. 6.75c). The increasing of the thickness of the adsorbate from Fig. 6.75a to Fig. 6.75b is also accompanied by a growth of the π-peaks due to the higher number of conjugated discs that get irradiated by the photon beam. In addition for the case of Figs. 6.75b and 6.75c thermal annealing carried out for 1 hour at 150 °C led to an increase of the π peak. Furthermore a preliminary experiment of angle resolved - UPS on slowly coated (C) HBC-C_{12} have been carried out both with the irradiating light

normal to the substrate and at 45° from it (Fig. 6.76). From the intensity of the π peaks, it is

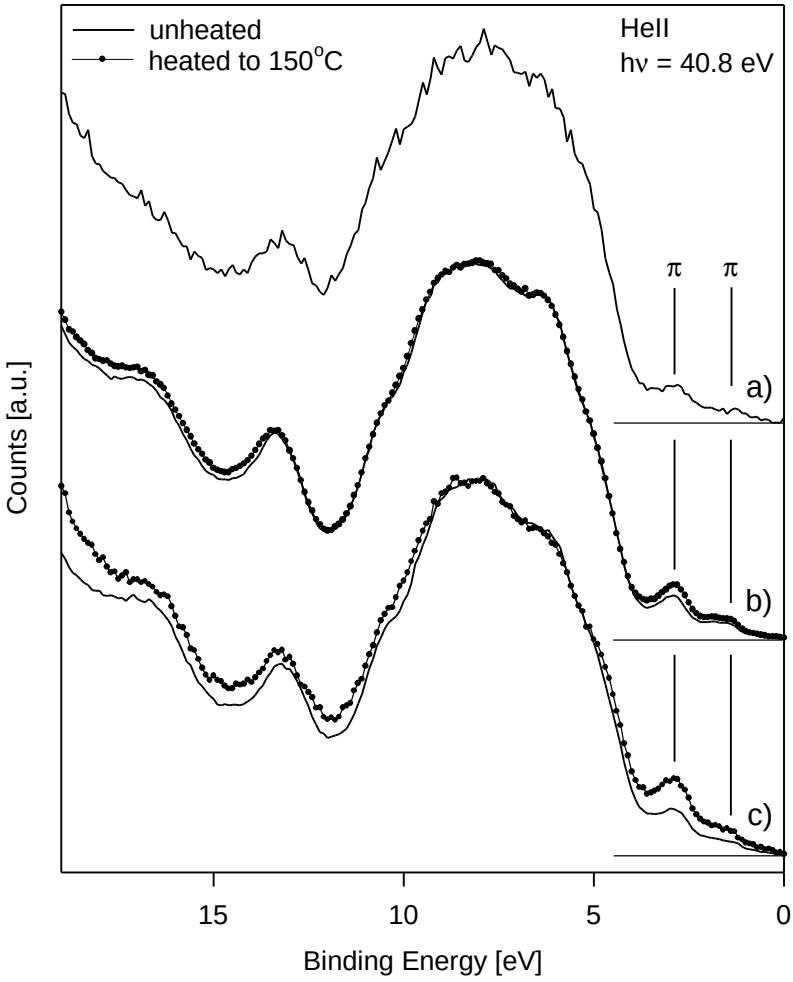

possible to establish that the molecular discs tend to lie flat on HOPG.

Figure 6.75: UPS HeII spectra of HBC-C_{12} plotted relative to the Fermi level of samples prepared at decreasing rates of physisorption: a) casting 1 layer; b) casting ~ 1000 layers; c) slow casting of 1 layer.

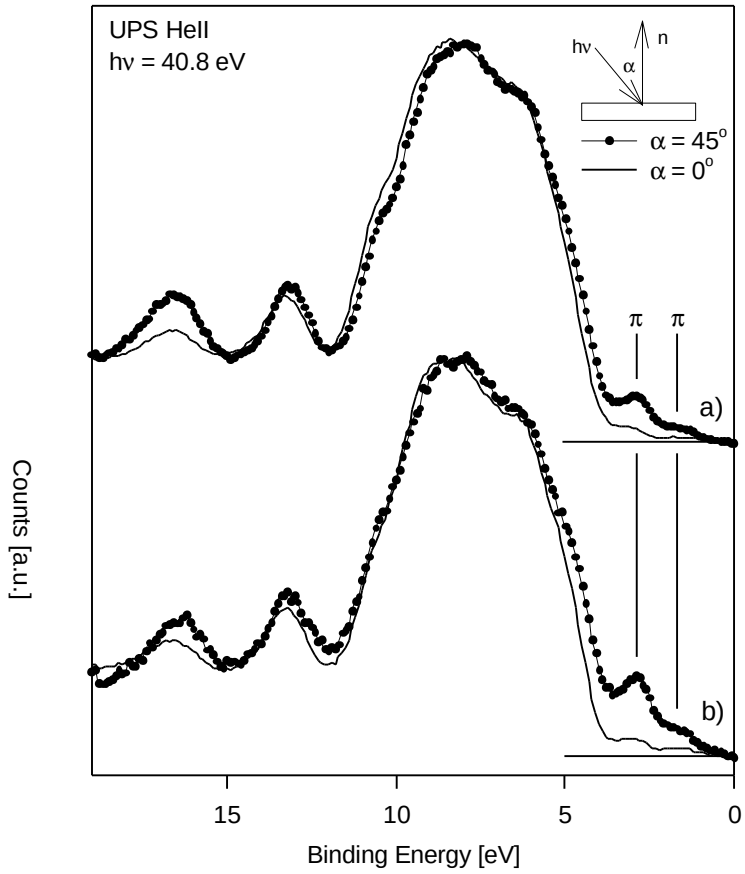

Figure 6.76: Angle Resolved UPS He(II) spectra of HBC-C_{12} plotted relative to the Fermi level of sample prepared by slow casting 1 layer. a) sample as prepared; b) thermally annealed sample at 200°C for 2 hours.

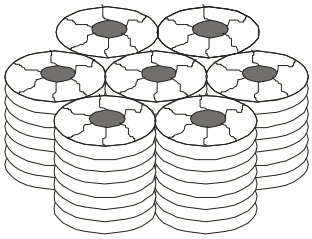

Figure 6.77: Scheme of the packing of HBC-C_{12} into columnar arrays (from [Her96]).

The stacking of several layers is likely to give rise to a columnar structure as the one shown in Fig. 6.77. This order can be further increased by making use of thermal annealing for 2 hours

at 200 °C, as shown in Fig. 6.76. This result is in good agreement with the mesophase detected between 60 and 399 °C where the molecules tend to stack in columnar aggregates like in Fig. 6.77 [Her96].

In summary, by changing the rate of the self-assembly from solution of the HBC-C_{12} it was possible to produce well defined and epitaxially oriented layers. Both SFM and Angle resolved UPS spectroscopy suggest that HBC-C_{12} are lying flat on the HOPG substrates. These results strongly suggest that the growth into layered architectures is a kinetically governed phenomenon which leads to an hetero-epitaxial ordering of the organic interface.

7 Conclusions

Chemisorption and physisorption have been used alternatively to design reproducible (macro)molecular architectures from π-conjugated systems. In the first case Self-Assembled Monolayers of thiol-end functionalized alk*a*nes and alk*e*nes have been grown both on Au and on Ag surfaces. The role of the substrate in the self-assembly has been discussed; for this purpose a novel ultra flat Au surface (Template Stripped Gold) has been developed. Different thicknesses of the organic layer (length of the alkyl chain) and different compositions of the adsorbate (saturated or unsaturated chain) have shown distinct electronic properties of the molecular adlayer.

In the latter case, making use of intramolecular, intermolecular and interfacial forces highly ordered 2D and 3D polymolecular micro- and nano-scopic architectures have been produced.

Scanning Tunneling Microscopy (STM) investigations at the interface between an almost saturated solution and a solid substrate (HOPG) allowed to characterize both the structure and the dynamics of these systems. Phenyleneethynylene trimers pack in an oriented 2D polycrystalline structure. The dynamics of the single molecular nanorods on a several minutes time scale has been recorded. This Ostwald ripening phenomenon is driven by a minimization of the line energies. Such a high resolution imaging allowed to gain insight into the kinetics of this process and to draw conclusions on thermodynamic and kinetic contributions to the total energy governing this grain coarsening. In addition defects within epitaxial crystals like missing molecules have been monitored. The corresponding polydisperse system is the first polymeric system which has been viewed with a sub-molecular resolution allowing to determine phase segregations in polydisperse polymers on the molecular scale. These macromolecules exhibit a nematic-like molecular order at the interface with HOPG. Single rods are oriented along preferential directions according to the threefold symmetry of the substrate. The true molecular lengths for several hundreds of molecules have been determined from STM images. The key result is a narrow macromolecular fractionation at the interface with the solid substrate: only macromolecules with a rod length around the peak of the distribution of molecular weights segregate at the interface with HOPG.

On the other hand, dried macromolecular films of PPE prepared by solution casting have been

studied with Scanning Force Microscopy (SFM) in Tapping Mode. Varying several parameters during the self-assembly, like the substrate, the solvent, the concentration of the solution and the average length of the macromolecule along the conjugated backbone, allowed to understand and drive the growth of these architectures towards epitaxially oriented micrometer long nanoribbons. These nanostructures are typically two to three monolayers thick with their alkyl chains oriented perpendicular to the substrate. The distribution of ribbon widths is in good agreement with the molecular weight distribution according to the Schulz-Zimm distribution, taking into account a broadening effect due to the SFM tip. This result indicates that SFM offers an valuable alternative route to determine molecular weight distributions for a rigid rod polymer. These nanoribbons are molecular architectures which upon thiol functionalization at their edges are nanostructures ready to bridge Au nanoelectrodes in a molecular nanowire device. Results on the electric properties of PPE molecular aggregates between the two Au nanoelectrodes have been presented. Moreover the electronic structures of phenyleneethynylene derivatives both for the case of a pristine and n-doped thin films have been investigated by means of photoelectron spectroscopies corroborated by theoretical calculations.

Furthermore highly ordered layer architectures of hexakis-dodecyl-hexabenzocoronene have been grown from solutions. Complementary insight into the molecular order in organic dry thin films have been gained with Tapping Mode - Scanning Force Microscopy and angle-resolved photoemission measurements. It is found that this disc-like molecule on a conductive solid flat substrate like highly oriented pyrolitic graphite (HOPG) can self-assemble into monolayers with the π-conjugated disc like system lying preferentially parallel to the basal plane of the substrate. Varying the procedures of the film preparation from solution it was possible to tune the rate of the molecular self-assembly. At very slow deposition speeds it was possible to produce layers aligned preferentially along the crystallographic axes of the HOPG substrate. This suggests that the growth of this molecular system is a kinetically governed phenomenon which on the crystalline support in equilibrium leads to a hetero-epitaxial type of growth.

8 Zusammenfassung

Sowohl Chemisorption als auch Physisorption wurden verwendet, um reproduzierbare (makro)molekulare Architekturen aus π-konjugierten Systemen herzustellen.

Im ersten Fall sind selbstorganisierte Monolagen aus thiol-endfunktionalisierten Alkanen und Alkenen auf Au- und Ag-Oberflächen erzeugt worden. Die Rolle des Substrats in der Selbstorganisation ist diskutiert worden; dazu wurde eine neue, ultraglatte Au-Oberfläche entwickelt (Template Stripped Gold). Unterschiedliche Dicken der organischen Schicht (Länge der Alkylkette) und unterschiedliche Zusammensetzungen des Adsorbats (gesättigte oder ungesättigte Kette) haben zu deutlich unterschiedlichen elektronischen Eigenschaften der molekularen Schicht geführt.

Im zweiten Fall wurden hochgeordnete zweidimensionale und dreidimensionale polymolekulare mikro- und nanoskopische Architekturen hergestellt, indem intra- und inter-molekulare, sowie Grenzflächen-Kräfte ausgenutzt wurden. Mit tunnelmikroskopischen Untersuchungen an der Grenzfläche zwischen einer fast gesättigten Lösung und einem festen Träger (HOPG) konnten sowohl die Struktur als auch die Dynamik dieser Systeme charakterisiert werden. Phenyleneethinylen-Trimere packen in einer orientierten zweidimensionale polykristallinen Struktur. Die Dynamik der einzelnen molekularen Nanostäbchen ist über mehrere Minuten aufgenommen worden. Die treibende Kraft dieses Phänomens (Ostwald Reifung) ist die Minimierung der Grenzlinienenergien. Die hohe Auflösung erlaubte es, Aussagen über die Kinetik dieses Prozesses zu gewinnen und Schlüsse über die thermodynamischen und kinetischen Beiträge zum Domänenwachstum zu ziehen. Ausserdem sind Defekte in epitaktischen Kristallen wie etwa fehlende Moleküle abgebildet worden. Das entsprechende polydisperse System ist das erste polymere System, das mit einer submolekularen Auflösung beobachtet worden ist. Die Makromoleküle zeigen eine nematische Ordnung an der Grenzfläche mit HOPG. Einzelne Stäbchen sind entlang bevorzugter Richtungen entsprechend der dreizähligen Symmetrie dieses Substrats orientiert. Die tatsächliche molekulare Länge ist aus tunnel-mikroskopischen Bildern für mehrere hundert Moleküle bestimmt worden. Das Hauptresultat ist eine starke Fraktionierung der Makromoleküle an der Grenzfläche mit dem festen Träger: nur Makromoleküle mit einer Länge nahe dem Maximum der Verteilung der Molekulargewichte ordnen sich auf HOPG.

Andererseits sind trockene, aus Lösung abgeschiedene Filme aus Poly-*para*-phenyleneethinylen (PPE) mit Hilfe der Raster kraft mikroskopie im Tapping Modus untersucht worden. Das Wachstum dieser Architekturen lieβ sich verstehen und es gelang epitaktisch orientierte, mikrometerlange Nanobänder herzustellen, indem verschiedene Parameter wie das Substrat, das Lösungsmittel, die Zusammensetzung der Lösung und die durchschnittliche Länge der Makromoleküle entlang der konjugierten Hauptkette variiert wurden. Die erhaltenen Nanostrukturen sind typischerweise zwei oder drei Monolagen dick, wobei die Alkylketten senkrecht zum Substrat orientiert sind. Unter Berücksichtigung des Verbreitungseffekts der kraftmikroskopischen Spitze stimmt die Breite der Molekulargewichtverteilung gut mit der Schulz-Zimm Verteilung überrein. Dieses Ergebnis zeigt, daß die Kraftmikroskopie eine gute Alternative darstellt, um Molekulargewichtsverteilungen für steife polymere Stäbchen zu bestimmen. Die Nanobänder sind molekulare Architekturen, die nach Thiolfunktionalisierung an ihren Enden Brücken zwischen Au-Elektroden in einer molekularen Nanofadenanordnung bilden könnten. Ergebnisse über elektrische Eigenschaften von PPE Molekularaggregaten zwischen zwei Au-Elektroden sind vorgestellt worden. Ausserdem sind die elektronischen Strukturen der PPE-Derivate sowohl für den Fall einer undotierten als auch n-dotierter Dünnschicht mit Photoelektronenspektroskopie und theoretischen Berechnungen untersucht worden

Darüber hinaus wurden hochgeordnete Lagen aus Hexakis-dodekyl-hexabenzocoronen aus Lösung abgeschieden. Kraftmikroskopie im Tapping Modus und winkelaufgelöste Photoemissionsmessungen haben ergänzende Aussagen über die molekulare Ordnung in trockenen organischen Dünnschichten geliefert.

Dabei wurde gefunden, daß das scheibenförmige Molekül auf einem leitenden glatten Substrat wie hoch orientiertem „pyrolytische“ Graphit (HOPG) in Monolagen selbstorganisieren kann, wobei die π-konjugierte Scheibe bevorzugt parallel zur Substratebene liegt. Die Geschwindigkeit der molekularen Selbstorganisation wurde variiert, indem das Verfahren der Schichtpräparation aus der Lösung variiert wurde. Bei sehr niedrigen Ablagerungsgeschwindigkeiten ist es gelungen, bevorzugt zu den kristallographischen Achsen vom HOPG-Träger ausgerichtete Lagen herzustellen. Dieses deutet darauf, daß das Wachstum dieses Molekularsystems auf festen Trägern ein kinetisch dominiertes Phänomen ist, das auf kristallinen Substraten im Gleichgewicht zu einem hetero-epitaktischen Wachstum führt.

9 Bibliographic references

[Alv92] C.A Alves, E.L. Smith, M.D. Porter, *J. Am. Chem. Soc.*, **114**, 1222 (1992).

[Atk94] P.W. Atkins, "Physical Chemistry", Oxford University Press, 5fth edition (1994).

[Bai89a] C.D. Bain, H.A. Biebuyck, G.M. Whitesides, *Langmuir*, **5**, 723 (1989).

[Bai89b] C.D. Bain, E.B. Troughton, Y.T. Tao, J. Evall, G.M. Whitesides, *J. Am. Chem. Soc.*, **111**, 321 (1989).

[Ban90] A. Banerjea, J. R. Smith, J. Ferrante, *J. Phys. Condens. Matt.*, **2**, 8841 (1990).

[Bäu93] P. Bäuerle, *Adv Mater*., **5**, 879 (1993).

[Bäu95] P. Bäuerle, T. Fischer, B. Bidlingmeier, A. Stabel, J.P. Rabe, *Angew. Chem. Int. Ed. Engl.*, **34**, 303 (1995).

[Bar95] A.-L. Barbarási, H.E. Stanley, Fractal Concept in Surface Growth (Cambridge University Press, Cambridge, U.K., 1995).

[Bei69] A. Beiser, Perspectives of modern physics (Mc-Graw Hill Kogikusha LTD. 1969).

[Bes87] K. Besocke, *Surf. Sci.*, **181**, 145-153 (1987).

[Bes88] K. H. Besocke, M. Teske, J. Frohn, *J. Vac. Sci. Technol. A*, **6**, 408-411 (1988).

[Bez97a] A. Bezryadin, C. Dekker, *J. Vac. Sci. Technol. B*, **15**, 793 (1997).

[Bez97b] A. Bezryadin, C. Dekker, G. Schmid, *Appl. Phys. Lett*, **71**, 1273 (1997).

[Bin82a] G. Binnig, H. Rohrer, C. Gerber, E. Weibel, *Helv. Phys. Acta*, **55**, 726 (1982).

[Bin82b] G. Binnig, H. Rohrer, C. Gerber, E. Weibel, *Appl. Phys. Lett*, **40**. 178 (1982).

[Bin83a] G. Binnig, H. Rohrer, C. Gerber, E. Weibel, *Surf. Sci. Lett.*, **131**, L379 (1983).

[Bin83b] G. Binnig, H. Rohrer, Ch. Gerber, E. Weibel, *Phys. Rev. Lett.*, **50**, 120 (1983).

[Bin86] G. Binnig, C.F. Quate, C. Gerber, *Phys. Rev. Lett.*, **56**, 930 (1986).

[Bin87] G. Binnig, C. Gerber, E. Stoll, T. R. Albrecht, C. F. Quate, *Europhys. Lett.*, **3**, 1281 (1987).

[Bin95] K. Binder, *Montecarlo and Molecular Dynamics simulations in polymer science*.

(Oxford Univ. Press - Oxford 1995).

[Bis95] F. Biscarini, R. Zamboni, P. Samorí, P. Ostoja, C. Taliani, *Phys. Rev. B,* **52**, 14868 (1995).

[Bis97] F. Biscarini, P. Samorí, O. Greco, R. Zamboni, *Phys. Rev. Lett.*, **78**, 2389 (1997).

[Bis00] F. Biscarini, private communications (2000).

[Bou93] L. Bourdieu, O. Rosin, D. Chatenay, *Science*, **259**, 798 (1993).

[Bra89] J. Brandrup, E.H. Immergut, Polymer Handbook, 3rd ed., Wiley Interscience 1989, pp. 275-296.

[Buc91] M. Buck, F. Eisert, M. Grunze, F. Träger, *J. Appl. Phys A,* **53**, 551 (1991).

[Bum96] L.A. Bumm, J.J. Arnold, M.T. Cygan, T.D. Dunbar, T.P. Burgin, L. Jones II, D.L. Allara, J.M. Tour, P.S. Weiss, *Science*, **271**, 1705 (1996).

[Bun00] U. H. F. Bunz, *Chem. Rev.*, **100**, 1605-1644 (2000).

[Buo96] M. Buongiorno Nardelli, D. Cvetko, V. De Renzi, L. Floreano, R. Gotter, A. Morgante, M. Peloi, F. Tommasini, R., Danieli, S. Rossini, C. Taliani, R. Zamboni, *Phys. Rev. B*, **53**, 1095 (1996).

[Bur90] J.H. Burroughes, D.D.C. Bradley, A.R. Brown, R.N. Marks, K. Mackay, R.H. Friend, P.L. Burns, A.B. Holmes, *Nature*, **347**, 539 (1990).

[Bus95] C. Bustamante, D. Keller, *Physics Today*, 32-38, December (1995).

[But92] H.-J. Butt, R. Guckenberger, J.P. Rabe, *Ultramicroscopy*, **46**, 375 (1992).

[Cam93a] N. Camillone, C.E.D. Chidsey, P. Eisenberger, P. Fenter, J. Li, K. Liang, G.-Y. Liu, G. Scoles, *J. Chem Phys.*, **99**, 744 (1993).

[Cam93b] N. Camillone, C.E.D. Chidsey, G.-Y Liu, G. Scoles, *J. Chem Phys.*, **98**, 3503 (1993).

[Car97] G.R. Carlow, M. Zinke-Allmang, *Phys. Rev. Lett.*, **78**, 4601 (1997).

[Chi77] C. K. Chiang, C. R. Fincher, Y. W. Park, A. J. Heeger, H. Shirakawa, E. J. Louis, S. C. Gau, A. G McDiarmid, *Phys. Rev. Lett.*, **39**, 1098 (1977).

[Chi88] C. E. D. Chidsey, D. N. Loiacono, T. Sleater, S. Nakahara, *Surf. Sci.,* **200**, 45-66

(1988).

[Chi89] C.E.D. Chidsey, G.-Y. Liu, P. Rowntree, G. Scoles, *J. Chem Phys.*, **91**, 4421 (1989).

[Chi90] C.E.D. Chidsey, D.N. Loiacono, *Langmuir*, **6**, 682 (1990).

[Chi93] L. F. Chi, M. Anders, H. Fuchs, R. R. Johnston, H. Ringsdorf, *Science*, **259**, 213 (1993).

[Cin93] S. Cincotti, J.P. Rabe, *Appl. Phys. Lett.*, **62**, 3531 (1993).

[Coo88] J. H. Coombs, J. K. Gimzewski, B. Reihl, J. K. Saas, R. R. Schlittler, *J. Microsc.* **152**, 325 (1988).

[Cot96] P.M. Cotts, T.M. Swager, Q. Zhou, *Macromolecules* **29**, 7323-7328 (1996).

[Dee65] W.A. Deer, R.A. Howie, J. Zussman, "Rock forming Minerals", vol.3, Longmans London (1965), pp.1-30.

[Del96] E. Delamarche, B. Michel, H.A. Biebuyck, C. Gerber, *Adv. Mater.*, **8**, 719 (1996).

[Die75] H. A. Dieck, R. F. Heck, *J. Organomet. Chem.*, **93**, 259 (1975).

[Dhi97] A. Dhirani, P.-H. Lin, P. Guyot-Sionnest, R. W. Zehner, L. R. Sita, *J. Chem. Phys.*, **106**, 5249 (1997).

[Eic96] K. Eichhorst-Gerner, A. Stabel, G. Moessner, D. Declerq, S. Valiyaveettil,V. Enkelmann, K. Müllen, J.P. Rabe, *Angew. Chem. Int. Ed. Engl.*, **35**, 1492 (1996).

[Eri94] D. A. Erie, G. L. Yang, H. C. Schultz, C. Bustamante, *Science*, **266**, 1562 (1994).

[Fee94] R. M. Feenstra, *Surf. Sci.*, **299-300**, 965 (1994).

[Fee87] R. M. Feenstra, J. A. Stroscio, J. Tersoff, A. P. Fein, *Phys. Rev. Lett.*, **58**, 1192 (1987).

[Fin97] M. O. Finot, M. T. Mc Dermot, *J. Am. Chem. Soc.*, **119**, 8564 (1997).

[Fle93] G.J. Fleer, M.A. Cohen Stuart, J.M.H.M. Schentjens, T. Cosgrove, B. Vincent, Polymers at interfaces (Chapman & Hill – London, 1993), p. 272.

[Flo53] P. J. Flory "Principles of Polymer Chemistry", Cornell Univ. Press (Ithaca) 1953.

[Fos88] J. S. Foster, J. E. Frommer, *Nature*, **333**, 542 (1988).

[Fra98] V. Francke, T. Mangel, K. Müllen, *Macromolecules*, **31**, 2447 (1998).

[Fri94] C. D. Frisbie, L. F. Rozsnyai, A. Noy, M. S. Wrighton, C. M. Lieber, *Science*, **245**, 2071 (1994).

[Fro89] J. Frohn, J. F. Wolf, K. H. Besocke, M. Teske, *Rev. Sci. Instr.*, **60**, 1200-1201 (1989).

[Gar90] F. Garnier, G. Horowith, X. Peng, D. Fichou, *Adv. Mater.*, **2**, 592 (1990).

[Gie96] R. Giesa, *J. Macromol. Sci. Rev. Chem. Phys.*, **C36**, 631 (1996).

[Gim87] J. K. Gimzewski, R. Möller, *Phys. Rev. B*, **36**, 1284 (1987).

[Gra99] M. Grandbois, M. Beyer, M. Rief, H. Clausen-Schaumann, H.E. Gaub, *Science*, **283**, 1727 (1999).

[Gri97] P.C.M. Grim, S. De Feyter, A. Gesquière, P. Vanoppen, M. Rücker, S. Valiyaveettil, C. Moessner, K. Müllen, F.C. De Schryver, *Angew. Chem. Int. Ed. Engl.*, **36**, 2601 (1997).

[Gro97] A.Y. Grosberg, A.R. Khokhlov, Giant molecules here, there everywhere ... (Academic Press – London, 1997) p. 73.

[Guc94] R. Guckenberger, M. Heim, G. Cevc, H.F. Knapp, W. Wiegräbe, A. Hillebrand, *Science*, **266**, 1539 (1994)

[Häh93] G. Hähner, Ch. Wöll, M. Buck, M.Grunze, *Langmuir*, **9**, 1955 (1993).

[Hal91] V. M. Hallmark, S. Chiang, J. K. Brown, C. Wöll, *Phys. Rev. Lett.* **66**, 48 (1991).

[Hal95] J.M. Halls, C.A. Walsh, N.C. Greenham, E.A. Marseglia, R.H. Friend, S.C. Moratti, A.B. Holmes, *Nature*, **376**, 498 (1995).

[Hal98] C. E. Halkyard, M. E. Rampey, L. Kloppenburg, S. L. Studer-Martinez, U. H. F. Bunz, *Macromolecules*, **31**, 8655 (1998).

[Ham95] B. Hammer, J.K. Norskov, *Nature*, **376**, 238 (1995).

[Han87] P. K. Hansma, J. Tersoff, *J. Appl. Phys.*, **61**, R1 (1987).

[Har90] U. Hartmann, *Phys. Rev. B*, **42**, 1541 (1990).

[Heg93] M. Hegner, P. Wagner, G. Semenza, .*Surface Science*, **291**, 39 (1993).

[Hei92] H. Heinzelmann, E. Meyer, D. Brodbeck, G. Overney, H.-J. Güntherodt, *Z. Phys. B - Cond. Matt.*, **88**, 321 (1992).

[Hei94] R. Heinz, A. Stabel, J. P. Rabe, G. Wegner, F. C. De Schryver, D. Corens, W. Dehaen, C. Süling, *Angew. Chem. Int. Ed. Engl.*, **33**, 2080 (1994).

[Hei95] R. Heinz, J.P. Rabe, *Langmuir*, **11**, 506-511 & 2857 (1995).

[Hen92] R. Hentschke, L. Askadskaya, J.P. Rabe, *J. Chem. Phys.* **97**, 6901 (1992).

[Hen93] R. Hentschke, B.L. Schürmann, J.P. Rabe, *J. Chem. Phys.*, **96**, 6213 (1992) and **98**, 1756 (1993).

[Her96] P. Herwig, C.W. Kayser, K. Müllen, H-W- Spiess, *Adv. Mater.*, **8**, 510 (1996)

[Her98] M.C. Hersam, A.C.F. Hoole, S.J. O'Shea, M.E. Welland, *Appl. Phys. Lett.*, **72**, 915 (1998).

[Hot93] S. Hotta, K. Waragai, *Adv. Mat.*, **5**, 896 (1993).

[Hug97] K.E. Huggins, S. Son, S.I. Stupp, *Macromolecules*, **30**, 5305 (1997).

[Isr92] J. Israelchvili, *Intermolecular and Surface Forces*, (Academic Press, San Diego 1992).

[Iss91] N. Isshiki, K. Kobayashi, M. Tsukada, *J. Vac. Sci. Technol. B*, **9**, 475 (1991).

[Iye98] V.S. Iyer, K. Yoshimura, V. Enkelmann, R. Epsch, J.P. Rabe, K. Müllen, *Angew. Chem. Int. Ed.* **37**, 2696 (1998).

[Joh70] C.K. Johnson, *ORTEP: A FORTRAN Thermal-Ellipsoid Plot Program for Crystal Structure Illustrations*., Report ORNL-3794, 135 pages (1970).

[Joh72] C.K. Johnson, J.F. Guerdon, P. Richard, S. Whitlow, S.R. Hall, ORTEP. The X-RAY system of Crystallographic Programs. TR-192, 283 (1972).

[Jun96] T. A. Jung, R. R. Schlitter, J. K. Gimzewski, H. Tang, C. Joachim, *Science* **271**, 181 (1996).

[Jun97] T. A. Jung, R. R. Schlittler, J. K. Gimzewski, *Nature*, **386**, 696 (1997).

[Kas97] S. Kasas, N. H. Thomson, B. L. Smith, H. G. Hansma, X. S. Zhu, M. Guthold, C. Bustamante, E. T. Kool, M. Kashlev, P. K. Hansma, *Biochemistry*, **36**, 461 (1997).

[Kei00] M. Keil, P. Samorí, D.A. dos Santos, T. Kugler, J.D. Brand, K. Müllen, J.L. Brédas, J.P. Rabe, W.R. Salaneck, *J. Phys. Chem. B* **104**, 3967 (2000).

[Kel91] D. J. Keller, *Surf. Sci.*, **253**, 353 (1991).

[Kel94] S. P. Kelty, A. F. Ruppert, R. R. Chianelli, J. Ren, M. H. Whangbo, *J. Am. Chem. Soc.*, **116**, 7857 (1994).

[Kim91] Y. Kim, J.-L. Huang, C. M. Lieber, *Appl. Phys. Lett.*, **59**, 3404 (1991).

[Kim92] Y.-T. Kim, A.J. Bard, *Langmuir*, **8**, 1096 (1992).

[Kim96] T. Kim, Q. Ye, L. Sun, K.C. Chan, R.M. Crooks, *Langmuir*, **12**, 6065 (1996).

[Kot67] A. Kothera, in M.J. Cantow, Polymer Fractionation (Academic Press, New York 1967).

[Kra98] A. Kraft, A. C. Grimsdale, A. B. Holmes, *Angew. Chem. Int. Ed. Eng.*, **37**, 402 (1998).

[Lan85] N. D. Lang, *Phys. Rev. Lett.*, **55**, 230 (1985).

[Laz97] R. Lazzaroni, A. Calderone, J.L. Brédas, J.P. Rabe, *J. Chem. Phys.*, **107**, 99 (1997).

[Lec96] P. Leclere, R. Lazzaroni, J. L. Brédas, J. M. Yu, P. Dubois, R. Jerome, *Langmuir*, **12**, 4317 (1996).

[Leh93] J.-M. Lehn, *Science*, **260**, 1762 (1993).

[Lie91] C. M. Lieber, Y. Kim, *Thin Solid Films*, **206**, 355 (1991).

[Lip89] P. H. Lippel, R. J. Wilson, M.D. Miller, C. Wöll, S. Chiang, *Phys. Rev. Lett.*, **62**, 171, (1989).

[Liu86] H.- Y. Liu, F. F. Fan, C. W. Lin, A. J. Bard, *J. Am. Chem. Soc.* **108**, 2824 (1986).

[Lud94] C. Ludwig, B. Gompf, J. Petersen, R. Strohmaier, W. Eisenmenger, *Z. Phys. B*, **93**, 365 (1994) .

[Mar87] Y. Martin, H. K. Wickramasinghe, *Appl. Phys. Lett*, **50**. 1455 (1987).

[Mar99] R. E. Martin, F. Diederich, *Angew. Chem. Int. Ed. Eng.*, **38**, 1350 (1999).

[Mat92] C. M. Mate, *Phys. Rev. Lett.*, **68**, 3323 (1992).

[Mat87] C. M. Mate, G. M. McClelland, R. Erlandsson, S. Chiang, *Phys. Rev. Lett.*, **59**, 1942 (1987).

[Mel91] A. J. Melmed, *J. Vac. Sci. Technol. B*, **9**, 601-608 (1991).

[Moi88] Y.N. Moiseev , V. M. Mostepanenko, V. I. Panov, I Y. Sokolov, *Phys. Lett. A*, **132**,

354 (1988).

[Mor94] M. Moroni, J. Le Moigne, S. Luzzati, *Macromolecules*, **27**, 562 (1994).

[Mor96] K. Morgenstern, G. Rosenfeld, G. Comsa, *Phys. Rev. Lett.,* **76**, 2113 (1996).

[Mül98a] K. Müllen, G. Wegner "Electronic Materials: the oligomer approach", Wiley-VCH (Weinheim) 1998.

[Mül98b] K. Müllen, J. P. Rabe in Molecular Electronics: Science and Technology, **852**, 205-218 Eds: A. Aviram, M. Ratner, Annals of the New York Academy of Sciences (1998).

[Mül98c] M. Müller, C. Kübel, K. Müllen, *Chem. Eur. J.*, **4**, 2099 (1998).

[Nis94] S. Nishimura, S. Biggs, P. J. Scales, T. W. Healy, K. Tsunematsu, T. Tateyama, *Langmuir* **10**, 4554 (1994).

[Nis95] S. Nishimura, P. J. Scales, H. Tateyama, K. Tsunematsu, T. W. Healy, *Langmuir* **11**, 291 (1995).

[Nuz87] R.G. Nuzzo, B.R. Zegarski, L.H. Dubois, *J. Am. Chem. Soc.*, **109**, 733 (1987).

[Nuz90] R.G. Nuzzo, L.H. Dubois, D.L. Allara, *J. Am. Chem. Soc.*, **112**, 558 (1990).

[Ofe95] D. Ofer, T.M. Swager, M.S. Wrighton, *Chem. Mater.*, **7**, 418 (1995).

[Ohn93] F. Ohnesorge, G. Binnig, *Science*, **260**, 1451 (1993).

[Ove91] R. M. Overney, L. Howald, J. Frommer, E. Mayer, H.-J.Güntherodt, *J. Chem. Phys.*, **94**, 8441 (1991).

[Pal98] V. Palermo, F. Biscarini, C. Zannoni, *Phys. Rev. E.* **57**, R2519 (1998).

[Par87] S.I. Park, C.F. Quate, *Rev. Sci. Instrum.,* **58**, 2004 (1987).

[Pei95] Q. Pei, G.. Yu, C.Zhang, Y. Yang, A.J. Heeger, *Science*, **270**, 1789 (1995).

[Poh94] D. W. Pohl, W. Denk, M. Lanz, *Appl. Phys. Lett*, **44**. 651 (1984).

[Poi96] G.E. Poirer, E.D. Pylant, *Science*, **272**, 1145 (1996).

[Poi97] G. E. Poirer, *Chem. Rev.,* **97**, 1117 (1997).

[Por87] M.D. Porter, T.B. Bright, D.L. Allara, C.E.D. Chidsey, *J. Am. Chem. Soc.,* **109**, 3559 (1987).

[Rab91a] J. P. Rabe, S. Buchholz, *Science*, **253**, 424 (1991).

[Rab91b] J. P. Rabe, S. Buchholz, *Phys. Rev. Lett.*, **66**, 2096 (1991).

[Rab93] J. P. Rabe, S. Buchholz, L. Askadskaya, *Synth. Met.*, **54**, 339 (1993).

[Ree97] M. A. Reed, C. Zhou, C. J. Muller, T. P. Burgin, J. M. Tour, *Science*, **278**, 252 (1997).

[Reh89] M. Rehan, A.-D. Schlüter, G. Wegner, *Polymer*, **30**, 1060 (1989).

[Rod89] J. M. Rodriquez-Prada, R. Duran, G. Wegner, *Macromolecules*, **22**, 2507 (1989).

[Rod96] F. Rodriguez, Principles of Polymer Systems. (Taylor & Francis London, 1996) p.200.

[Rug90] D. Rugar, P.K. Hansma, *Physics Today*, 23-30, October (1990).

[Sal96] W. R. Salaneck, S. Stafström, and J. L. Brédas, Conjugated polymer surfaces and interfaces: Electronic and chemical structure of interfaces for polymer light emitting devices (Cambridge University Press, Cambridge, 1996).

[Sam96] B. Samorí, I. Muzzalupo, G. Zuccheri, *Scanning Microscopy*, **10**, 953 (1996).

[Sam98a] P. Samorí, V.Francke, T. Mangel, K.Müllen; J.P. Rabe, *Optical Materials*, **9**, 390 (1998).

[Sam98b] P. Samorí, V.Francke, K.Müllen; J.P. Rabe, *Thin Solid Films*, **336**, 13 (1998).

[Sam99a] P. Samorí, V. Francke, K. Müllen, J.P. Rabe, *Chem. Eur. J.*, **5** , 2312 (1999).

[Sam99b] P. Samorí, J. Diebel, H. Löwe, J. P. Rabe, *Langmuir*, **15**, 2592-2594 (1999).

[Sam99c] P. Samorí, I. Sikharulidze, V. Francke, K. Müllen, J.P. Rabe, *Nanotechnology*, **10**, 77 (1999).

[Sch99] H. Schnablegger, M. Antonietti, C. Göltner, J. Hartmann, H. Cölfen, P. Samorí, J.P. Rabe, H. Häger, W. Heitz, *Journal of Colloid and Interface Science*, **212**, 24 (1999).

[Sei93] C. Seidel, Ph.D thesis, Univ. Stuttgart (1993).

[Ser93] B. Servet, S. Ries, M. Trotel, P. Alnot, G. Horowitz, F. Garnier, *Adv. Mat.*, **5**, 461 (1993).

[Sha93] T. G. Sharp, P. I. Oden, P. R. Buseck, *Surf. Sci. Lett.*, **284**, L405 (1993).

[Smi89] D. P. E. Smith, H. Hörber, C. Gerber, G. Binnig, *Science*, **245**, 43 (1989).

[Son75] K. Sonogashira, Y. Tohda, N. Hagihara, *Tetrahedron Lett.*, **50**, 4467 (1975).

[Sou96] A. Soukopp, K. Glöckler, P. Bäuerle, M. Sokolowski, E. Umbach, *Adv. Mat.*, **8**, 902 (1996).

[Spo89] J. K. Spong, H. A. Mizes, L. J. LaComb Jr., M. M. Dovek, J. E. Frommer, J. S. Foster, *Nature*, **338**, 137 (1989).

[Sta95a] A. Stabel, R. Heinz, F. C. De Schryver, J. P. Rabe, *J. Phys. Chem.*, **99**, 505 (1995).

[Sta95b] A. Stabel, P. Herwig, K. Müllen, J. P. Rabe, *Angew. Chem. Int. Ed. Engl*, **34**, 1609 (1995).

[Sta95c] A. Stabel, R. Heinz, J. P. Rabe, G. Wegner, F. C. De Schryver, D. Corens, W. Dehaen, C. Süling, *J. Phys. Chem.*, **99**, 8690 (1995).

[Sta97] D. Stamou, D. Gourdon, M. Liley, N.A. Burnham, A. Kulik, H. Vogel, C. Duschl, *Langmuir*, **13**, 2425 (1997).

[Sto98a] W. Stocker, B. Karakaya, B. L. Schürmann, J. P. Rabe, A.-D. Schlüter, *J. Am. Chem. Soc.*, **120**, 7691 (1998).

[Sto98b] W. Stocker, B. L. Schürmann, J. P. Rabe, S. Förster, P. Lindner, I. Neubert, A.-D. Schlüter, *Adv. Mater.*, **10**, 793 (1998).

[Str88] L. Strong, G.M. Whitesides, *Langmuir*, **4**, 546 (1988).

[Tad96] K. Tada, M. Onoda, M. Hirohata, T. Kawai, K. Yoshino, *Jpn. J. Appl. Phys.*, **35**, L251 (1996).

[Tam96] J. Tamayo, R. Garcia, *Langmuir*, **12**, 4430 (1996).

[Ter83] J. Tersoff, D. R.Hamann, *Phys. Rev. Lett.*, **50**,1988 (1983).

[Thu93] T. Thundat, X. Y. Zheng, G. Y. Chen, R. J. Warmack, *Surf. Sci. Lett.*, **294**, L939 (1993).

[Tou96] J.M. Tour, *Chem. Rev.*, **96**, 537 (1996).

[Ulm91] A. Ulmann, a. *An introduction to Ultrathin Organic Thin Films: from Langmuir Blodgett to Self-Assembly*; Academic: Boston, MA, 1991.

[Van96] S. Vanhee, R. Rulkens, U. Kehmann, C. Rosenauer, M. Schulze, W. Köhler, G. Wegner, *Macromolecules*, **29**, 5136 (1996).

[VdC98] A. M. van der Craats, J.M. Warman, K. Müllen, Y. Geerts, J. D. Brand, *Adv. Mater.*, **10**, 36 (1998).

[Vix98] A. Vix, W. Stocker, M. Stamm, G. Wilbert, R. Zentel, J. P. Rabe, *Macromolecules*, **31**, 9154 (1998).

[Wag95] P. Wagner, M. Hegner, H.J. Güntherodt, G. Semenza, *Langmuir*, **10**, 3867 (1995).

[Wan93] W. Wang, G. Lieser, G. Wegner, *Liquid Crystals*, **15**, 1 (1993).

[Wau96] P. Wautelet, M. Moroni, L. Oswald, J. Le Moigne, A. Pham, J.-Y. Bigot, S. Luzzati, *Macromolecules*, **29**, 446 (1996).

[Wed96] C. Weder, M.S. Wrighton, *Macromolecules*, **29**, 5157 (1996).

[Wed98] C. Weder, C. Sarwa, A. Montali, C. Bastiaansen, P. Smith, *Science*, **279**, 835 (1998).

[Wei92] A. L. Weisenhorn, P. Maivald, H.-J. Butt, P. K. Hansma, *Phys. Rev. B* **45**, 11226 (1992).

[Wei95] V. Weinstein, M. Slutzky, A. Arenshtam, E. Ben-Jacob, *Rev. Sci. Instrum.*, **66,** 3075-3076 (1995).

[Wen96] J.-M. Wen, J.W. Evans, M.C. Bartekt, J.W. Burnett, P.A. Thiel, *Phys. Rev. Lett.*, **76** 652 (1996).

[Wid91] C.A Widrig, C.A. Alves, M.D. Porter, *J. Am. Chem. Soc.*, **113**, 2805 (1991).

[Wie92] R. Wiesendanger and H.-J. Güntherodt eds., Scanning Tunneling Microscopy I and II, (Springer, Berlin 1992).

[Wie98] R. Wiesendanger ed., Scanning probe microscopy and spectroscopy, methods and applications, (Cambridge University Press, Cambridge 1998).

[Wil69] J.A. Wilson, A.D. Yoffe, *Advances in Physics*, 192 (1969).

[Wil86] C. C. Williams, H. K. Wickramasinghe, *Appl. Phys. Lett*, **49**. 1587 (1986).

[Xia93] T. K. Xia, U.Landman, *Science*, **261**, 1310 (1993).

[Zin92] M. Zinke-Allmang, L.C. Feldman, M.H. Grabow, *Surf. Sci. Rep.,* **16**, 377 (1992).

[Zho93] Q. Zhong, D. Inniss, V. Elings, *Surf. Sci.,* **290**, 688 (1993).

10 Acknowledgments

It is a great pleasure for me to express my deep gratitude to Prof. Dr. Jürgen P. Rabe for giving me the opportunity to work in his group. He has provided exceptional scientific guidance and a lively, informal yet stimulating atmosphere. I would like to also emphasize the importance of all the members of the group. In particular: Dr. J. Francis Wolf's helpful and constructive inspiring discussions and suggestions have played a key role; Dr. Wolfgang Stocker who has shown me several important experimental tricks of polymer science; Dr. Paul Hillner and Katherin Eichhorst-Gerner introduced me to the use of home made Scanning Tunneling Microscopes. Dr. Nikolai Severin, Thilo Böhme and Dr. Britta Schürmann have kindly supplied Montecarlo, molecular mechanics and dynamics simulations on PPE. Patrick Kölsch has created an exciting atmosphere in the group. He has been for me more than a colleague, a great friend; Evi Poblenz and Lothar Geyer provided an invaluable excellent technical support. Sincere thanks are also extended to Dr. Armelle Vix, Dr. Rebekka Epsch, Jörg Barner, Irakli Sikharulidze, Sabine Schönherr and Roger Bilewicz.

I owe much to Prof. Dr. Klaus Müllen and Dr. Viola Francke for their superb spirit of collaboration. I am deeply indebted to them for their ever lasting provision of high quality

synthetic materials and for being always ready to discuss results and future projects. I also gratefully acknowledge Johann D. Brand and Dr. Timo Magel for the synthesis of the molecules. In addition I would like to thank Dr. Volker Enkelmann for performing the XRD measurements on the oligomers of PPE.

I also offer my gratitude to Dr. Matthias Keil, Dr. Thomas Kugler and Prof. Dr. William R. Salaneck whose contribution in the photoelectron spectroscopies and doping of HBC and PPE have been remarkable. Also notable was the direct input to this work from Dr. Donizetti dos Santos, Prof. Dr. Roberto Lazzaroni and Prof. Dr. Jean Luc Brédas who furnished calculations important for interpreting the electronic structure of PPE and HBC. I am grateful for their help.

I am thankful to Dr. Alexandre Wei and Prof. Dr. Jean-Marie Lehn for their contribution to the challenging project of designing prototypes of molecular rectifier with alkenethiols.

The imaging of Scanning Force Microcopy tips by SEM and TEM have been carried out by Dr. Siegfried Rogaschewski and Dr. Christoph Böttcher respectively, while Dr. Petr Thiele

prepared the metallic substrates. The gold nanogaps have been produced by Dr. Andrew C.F. Hoole and Dr. Karl Kragler. I really appreciated their help.

I wish to thank Dr. Heimo Schnabblegger, Dr. Christine Göltner and Prof. Dr. Markus Antonietti for the fruitful collaboration that helped me to gain a better understanding of the self-assembly of PPE in thin films.

I would like to point out the importance of financial support from the European Union, especially for providing me a personal TMR grant "Nanowires from conjugated rigid-rod molecules". The research was also financed by the ESPRIT Long Term Research Project PRONANO (8523), TMR network SISITOMAS and BMBF Projekt "Molekulare Elektronik".

I desire moreover to thank all the friends that have made these four years in Berlin an unforgettable and terrific time. Last but not least, I want to truly acknowledge my family, Claudia, Bruno and Marco, who gave me the right *force* to tackle this experience and whose

love always meant light at the end of the *tunnel*.

11 Lebenslauf

Vorname und Name:	Paolo Samorí
Geburtsdatum:	3 Mai 1971
Geburtsort:	Imola (Bologna, It

September 1977 – Juli 1982	Grundschule (Scuola Elementare)
	Cremonini Ongaro, Bologna, Italy
September 198 2- Juli 1985	Secondary School (Scuola Media)
	Carducci, Bologna, Italy
September 1985-Juli 1990	Wissenschaftliches Lyceum mit Abschluß Abitur (Maturità Scientifica)
	High School “Copernico” , Bologna, Italy
October 1990 - November 1995	Laurea in Industrial Chemistry (Master in Science)
	Institut für "Chimica Fisica ed Inorganica" – Universtität zu Bologna, Italy, und
	Institut für “Spettroscopia Molecolare” – C.N.R. Bologna, Italy
	Betreuer: Prof. G. Calestani and Dr. F. Biscarini
	Titel: ” Analysis of organic thin films studied with Scanning Force Microscopy and Scanning Tunneling Microscopy ”
April 1996-	Promotionsstudent am Insitut für Physik – Humboldt Unversität zu Berlin
	Betreuer: Prof. Dr. J. P. Rabe
	Titel: “ Self-assembly of conjugated (macro)molecules: nanostructures for molecular electronics“

12 List of publications, awards and conferences presentations

Publication in international journals:

1. F. Biscarini, R. Zamboni, P. Samorí, P. Ostoja, C. Taliani, "Growth of conjugated oligomer thin films studied by atomic force microscopy", *Physical Review B*, **52**, 14868 (1995).

2. F. Biscarini, O. Greco, A. Lauria, P. Samorí, C. Taliani, R. Zamboni, "Growth of high vacuum sublimed oligomer thin films", *ACS Polymer Preprints*, **37**, 2, 618 (1996).

3. F. Biscarini, P. Samorí, A. Lauria, P. Ostoja, R. Zamboni, C. Taliani, P. Viville, R. Lazzaroni, J.L. Brédas, "Morphology and roughness of high-vacuum sublimed Oligomer Thin Films", *Thin Solid Films* **284-285**, 439 (1996).

4. F. Biscarini, P. Samorí, O. Greco, R. Zamboni, "Scaling behavior of anisotropic organic thin films grown in high-vacuum", *Physical Review Letters*, **78**, 12, 2389 (1997).

5. P. Samorí,V. Francke, T. Mangel, K. Müllen and J. P. Rabe, "Poly-*para*-phenylene-ethynylene assemblies for a potential molecular nanowire: an SFM study", *Optical Materials* **9**, 1-2, 390 (1998).

6. P. Viville, R. Lazzaroni, J.L. Brédas, P. Moretti, P. Samorí, F. Biscarini, "Influence of thermal annealing on the morphology of sexithienyl thin films", *Advanced Materials*,**10**, 57 (1998).

7. P. Samorí, V. Francke, K. Müllen, J. P. Rabe, "Growth of solution cast macromolecular π-conjugated nanoribbons on mica", *Thin Solid Films*, **336**, 13 (1998).

8. H. Schnablegger, M. Antonietti, C. Göltner, J. Hartmann, H. Cölfen, P. Samorí, J. P. Rabe, H. Häger, W. Heitz,"Morphological characterization of the molecular superstructure of polyphenylene ethynylene derivatives", *Journal of Colloid and Interface Science*, **212**, 24 (1999).

9. P. Samorí, I. Sikharulidze, V. Francke, K. Müllen, J. P. Rabe, "Nanoribbons from conjugated macromolecules on amorphous substrates observed by SFM and TEM", *Nanotechnology*, **10**, 77 (1999).

10. P. Samorí, J. Diebel, H. Löwe, J. P. Rabe, "Template Stripped Gold supported on Ni as a substrate for SAMs", *Langmuir*, **15**, 2592 (1999).

11. P. Samorí, V. Francke, K. Müllen, J. P. Rabe, "Self-Assembly of a Conjugated Polymer: From Molecular Rods to a Nanoribbon Architecture with Molecular Dimensions", *Chemistry - A European Journal*, **5**, 2312 (1999).

12. P. Samorí, N. Severin, K. Müllen, J. P. Rabe, " Macromolecular fractionation of rod-like polymers at atomically flat solid-liquid interfaces", *Advanced Materials*, **12**, 579 (2000).

13. M. Keil, P. Samorí, D. A. dos Santos, T. Kugler, S. Stafström, J. D. Brand, K. Müllen, J. L. Brédas, J. P. Rabe, W. R. Salaneck, "Influence of the morphology on the electronic structure of hexa-*peri*-hexabenzocoronene thin films", *Journal of Physical Chemistry B*, **104**, 3967 (2000).

14. T. Yatabe, M. A. Harbison, J. D. Brand, M. Wagner, K. Müllen, P. Samorí, J. P. Rabe, "Extended Triphenylenes: Synthesis, Mesomorphic Properties and STM of Hexakis(dialkoxyphenyl)-triphenylenes and Dodecaalkyloxy[tris(triphenylenylene)]s" *Journal of Materials Chemistry* **10**, 1519 (2000).

15. G. Gottarelli, S. Masiero, E. Mezzina, S. Pieraccini, J. P. Rabe, P. Samorí, and G. P. Spada " The Self-assembly of Lipophilic Guanosine Derivatives in Solution and on Solid Surfaces ", *Chemistry - a European Journal* **6** (17), 3242-3248 (2000).

16. P. Samorì, S. Pieraccini, S. Masiero, G.P. Spada, G. Gottarelli, J.P. Rabe, " Controlling the self-assembly of a deoxiguaninosine on mica ", accepted for publication on *Colloids and Surfaces B: Biointerfaces* (Sept. 2000)

17. P. Samorí, M. Keil, R. Friedlein, J. Birgerson, M. Watson, K. Müllen, W. R. Salaneck, J. P. Rabe " Growth of ordered hexakis-dodecyl-hexabenzocoronene layers from solution: a SFM and ARUPS study ", submitted to *Journal of Physical Chemistry B* (Oct. 2000)

18. P. Samorí, F. Jäckel, A. Godt, J.P Rabe, " Self-assembly of a [2]catenane into ordered nanostructures at surfaces - a sub-molecularly resolved STM study ", submitted to *Angew. Chem. Int. Ed.* (Oct. 2000)

19. P. Samorí, H. Engelkamp, P. de Witte, A. E. Rowan, R. J. M. Nolte, J.P Rabe, " Shape persistent phthalocyanine disks and cylinders at surfaces: self-assembly and manipulation ", (2000) to be submitted to *Angew. Chem. Int. Ed.*

20. P. Samorí, V.Francke, K.Müllen and J.P. Rabe, “ Mechanism, thermodynamic and kinetic aspects of dynamics of molecules at surfaces”, (2000) to be submitted.

21. P. Samorí, V.Francke, V. Enkelmann, K.Müllen, J.P. Rabe, “ Structural Characterization of a novel conjugated trimer”, (2000) to be submitted.

22.F. Biscarini, P. Samorí, R. Zamboni, C. Taliani, "Roughness analysis on vacuum growth organic thin films", (2000) in preparation.

23. H. Engelkamp, P. Samorí, A. E. Rowan, J. P Rabe, R. J. M. Nolte," Synthesis and characterization of polymeric phthalocyanines ", (2000) in preparation.

24. P. Samorí, A. Fechtenkötter, F. Jäckel, K. Müllen, J. P. Rabe, “ Supramolecular staircase through the self-assembly of disc-like molecules at the solid-liquid interface”, (2000) in preparation.

25. P. Samorí, C. Simpson, K. Müllen, J. P. Rabe, “Self-assembly of large hexabenzocoronene layers through dehydrogenation at surfaces”, (2000) in preparation.

26. P. Samorí, M. Keil, D.A. dos Santos, V.Francke, K. Müllen, T. Kugler, J.L. Brédas, J.P. Rabe, W.R. Salaneck, “Na doping of phenyleneethynylene derivatives”, (2000) in preparation.

27. U. Hubler, H. P. Lang, B. A. Hermann, H.-J. Güntherodt, P. Samorí, J.P Rabe, G. Greiveldinger, P. B. Rheiner, P. Murer, T. Sifferlen, D. Seebach, "Macromolecular structure of an oligo-dendrimer at surfaces", (2000) in preparation.

Awards:

1. Graduate Student Award: E-MRS '98 Spring Meeting (Strasbourg, France, June 1998).

2. Graduate Student Award - Silver Medal: MRS '00 Spring Meeting (San Francisco, CA, US, April 2000).

3. Finalist at Semerano Award 2000- Division of Physical Chemistry - Societa' Chimica Italiana.

Invited seminars:

1. Mons (Belgium), Service de Chemie des Materiaux Noveaux, 22 February 1996.

2. Berlin (Germany), Institüt fur Physik von Makromolekülen, Hümboldt University, 14 March 1996.

3. Montelibretti - Rome (Italy), Istituto di Chimica dei Materiali - C.N.R., 4 November 1998.

4. Rome (Italy), Istituto di Elettronica dello Stato Solido - C.N.R., 5 November 1998.

5. Pisa (Italy), Department of Chemistry and Industrial Chemistry, University of Pisa, 31 May 1999.

6. Berkeley (California, US), Department of Chemistry, University of Berkeley, 21 April 2000.

Proceedings of conferences:

Oral communications:

1."SFM study of conjugated molecular rods"

P. Samorí, J. P Rabe

Corso Teorico-Pratico di Microscopia a Sonda (SIME); Bologna, Italy, 23-25 October 1996.

2."STM and SFM investigations of the self-assembly of a conjugated system: a candidate for a molecular nanowire"

P. Samorí, J. P. Rabe

Raster - Sonden - Mikroskopien und Organische Materialien VI; Tuebingen, Germany, 8-10 October 1997.

3."Dry layers and ribbons from functionalised HBC and PPE"

P. Samorí

TMR-SISITOMAS Meeting; Mainz, Germany, 3-4 June, 1998.

4."Self-assembled nanostructures from π-conjugated polymers at surfaces"

P. Samorí, V. Francke, K. Müllen, J. P Rabe

European Materials Research Society '98 Spring Meeting; Strasbourg, France, 16-19 June 1998.

5."Nanostructures of a conjugated polymer at surfaces"

P. Samorí, V. Francke, K. Müllen, J. P Rabe

Europhysic Conference on Macromolecular Physics: Electrooptical Properties of Polymers and related phenomena Conference; Varenna, Italy, 13-17 September 1998.

6."Macromolecular conjugated nanostructures for molecular electronics"

P. Samorí, V. Francke, K. Müllen, J. P Rabe

International Bunsen Discussion Meeting: Conduction and Transport Mechanisms in Organic Materials:Preparation-Characterisation-Applications; Heidelberg, Germany, 27-30 September 1998.

7."STM and SFM as a tool for evaluating molecular weight distributions from polymeric nanostructures at surfaces"

P. Samorí, J. P. Rabe

Raster - Sonden - Mikroskopien und Organische Materialien VII; Berlin, Germany, 7-9 October 1998.

8."Self-assembly and doping of π-conjugated thin films"

P. Samorí

TMR-SISITOMAS Meeting; Bruges, Belgium, 27-28 January, 1999.

9."Controlling the self-assembly from solution of a conjugated macromolecule at surfaces"

P. Samorí, V. Francke, K. Müllen, J. P Rabe

Proceedings of the Frühjahrstagung der Deutschen Physikalische Gesellschaft; Muenster, Germany, 22-26 March 1999 .

10."SFM and UPS investigations of dry alkylated hexabenzocoronene layers on HOPG"

P. Samorí, J. P Rabe

Sonderforschungsbereich 448 "Mesoskopisch strukturierte Verbundsysteme" workshop ;

Caputh, Germany, 23-24 April 1999.

11."Self-assembly of a conjugated polymer: From the structure and dynamics of single molecular rods to supramolecular architectures with molecular dimensions"

P. Samorí, V. Francke, K. Müllen, J. P Rabe

Europolymer Conference 1999; Gargnano (BS), Italy, 23-28 May 1999.

12."Epitaxial growth of hexabenzocoronene from solution"

P. Samorí, M. Keil, Th. Kugler, W. R. Salaneck, J. D. Brand, K. Müllen, J. P. Rabe

European Conference of Molecular Electronics 1999; Linkoeping, Sweden, 8-11 September 1999.

13."Use of π–π interactions to tailor supramolecular architectures at surfaces"

P. Samorí, V. Francke, K. Müllen, J. P Rabe

3rd Workshop für Konjugierte Polymere und Oligomere Von der Synthese zur elektronischen Funktion (KOPO'99); Ulm, Germany, 22-25 September 1999.

14."Self-assembly of π–conjugated (macro)molecules at interfaces"

P. Samorí, V. Francke, K. Müllen, J. P Rabe

European Physical Society Conference on Macromolecular Physics:Molecular Orientation in Polymers; Potsdam, Germany, 30 September-2 October 1999.

15."Nanoscopic organization of interfaces and materials"

P. Samorí

Graduate Meeting 1999 of the "Gerhard M. J. Schmidt -Minerva Center of Supramolecular Materials"; Caputh, Germany, 4-5 October 1999.

16. " Use of non-covalent bonds to tailor (macro)molecular nanostructures at surfaces "

P. Samorí

TMR-SISITOMAS Meeting; Nijmegen, The Netherlands, 21-23 November, 1999.

17. "π-conjugated macromolecules at interface: supramolecular architectures and molecular dynamics"

P. Samorí

Workshop "Biophysik und weiche Materie"; celebrating the 65ft birthday of Prof. Dr. E. Sackmann ; München, Germany, 26-27 November 1999.

18. " Self-assembly of π-conjugated macromolecules at surfaces"

P. Samorí, K. Müllen, J. P Rabe

MRS - Spring 2000 Meeting; San Francisco, California, USA, 24-28 April, 2000.

19."Controlling the self-assembly of a rigid-rod polymer at surfaces "

P. Samorí, K. Müllen, J. P Rabe

MRS - Spring 2000 Meeting; San Francisco, California, USA, 24-28 April, 2000.

20."Thermodynamics of the macromolecular physisorption at the solid-liquid interface "

P. Samorí, K. Müllen, J. P Rabe

MRS - Spring 2000 Meeting; San Francisco, California, USA, 24-28 April, 2000.

21. "Self-assembly of lipophilic deoxyguanosine derivatives into planar hydrogen bonded ribbon-like architectures in solution and on solid surfaces"

G. Gottarelli, S. Masiero, E. Mezzina, S. Pieraccini, P. Samorí, J. P. Rabe, G. P. Spada

SELOA Spring School on Conjugated Polymers; Bologna, Italy, 21-25 May 2000.

22. "Conjugated disks at surfaces: self-assembly, manipulation and electronic properties "

P. Samorí, Th. Boehme

TMR-SISITOMAS Meeting; Leuven, Belgium, 8-9 June, 2000.

23. " Directing self-assembly of lipophilic guanosines hydrogen bonded architectures"

G. Gottarelli, S. Masiero, E. Mezzina, S. Pieraccini, P. Samorí, J. P. Rabe, G. P. Spada

LB9-Potsdam 2000 "The Ninth International Conference on Organised Molecular Films"; Potsdam, Germany, 28 August - 1 September 2000.

24. " Nanoengineering of hydrogen bonded architectures of lipophilic guanosines"

G. Gottarelli, S. Masiero, E. Mezzina, S. Pieraccini, P. Samorí, J. P. Rabe, G. P. Spada

2nd International Conference on Supramolecular Science & Technology; Leuven, Belgium, 10-15 September 2000

25. " Shape persistent phthalocyanine disks and cylinders at surfaces "

P. Samorí, H. Engelkamp, P. de Witte, A. E. Rowan, R. J. M. Nolte, J. P. Rabe

Berliner Polymerentage; Berlin, Germany, 9-11 October 2000.

Poster presentations:

1. F. Biscarini, P. Samorí, P. Ostoja, R. Zamboni and C. Taliani

Convegno Scientifico del Consorzio Interuniversitario per la Chimica dei Materiali; Firenze, Italy, May 1995.

2."SFM study of conjugated molecular rods"

P. Samorí, J. P Rabe

Raster - Sonden - Mikroskopien und Organische Materialien V; Muenster, Germany, 7-9 October 1996.

3."Self-assembly of a conjugated polymer: needles with molecular dimensions for molecular electronics"

P. Samorí, V. Francke, K. Müllen, J. P Rabe

Proceedings of the Frühjahrstagung der Deutschen Physikalische Gesellschaft; Muenster, Germany, 17-21 March 1997.

4."Self-assembly of a conjugated polymer: needles with molecular dimensions for molecular electronics"

P. Samorí, V. Francke, K. Müllen, J. P Rabe

SELOA Spring School on Conjugated Polymers; Siena, Italy, 11-16 May 1997.

5."Conjugated molecular rods self-assembled into needles with molecular cross-sections"

P. Samorí, V. Francke, K. Müllen, J. P Rabe

European Materials Research Society '97 Spring Meeting; Strasbourg, France, 16-20 June 1997.

6."Molecular nanowires made from conjugated macromolecules"

P. Samorí, V. Francke, K. Müllen, J. P Rabe

STM'97 9th International Conference on Scanning Tunneling Microscopy/Spectroscopy; Hamburg, Germany, 20-25 July 1997.

7."Self-assembly of phenyleneethynylene derivatives at surfaces: an STM and SFM study"

P. Samorí, V. Francke, K. Müllen, J. P Rabe

Berliner Polymerentage; Berlin, Germany, 9-11 October 1997.

8."Molecular Weight Distribution of rigid rod polymers in Self-Assembled Nanostructures Evaluated by Scanning Probe Microscopies"

P. Samorí, V. Francke, K. Müllen, J. P Rabe

"Nanoscience and Nanotechnology" UE-TMR Euroconference: Hindsgavl Slot, Denmark, 16-19 May 1998.

9."Molecular nanostructures for molecular electronics"

P. Samorí, V. Francke, K. Müllen, J. P. Rabe

ICCC'98 Meeting; Firenze, Italy, 30 Agust-4 September 1998.

10."Growth of hexabenzocoronene monolayers from solution"

P. Samorí, M. Keil, W. R. Salaneck, J. P. Rabe

Raster - Sonden - Mikroskopien und Organische Materialien VII; Berlin, Germany, 7-9 October 1998.

11."Polymeric phenyleneethynylene nanoassemblies at surfaces for molecular electronics"

P. Samorí, V. Francke, K. Müllen, J. P Rabe

VIII Wolfgang-Ostwald-Kolloquium; Berlin, Germany, 19-21 November 1998 .

12."Solution grown hexabenzocoronene layers"

P. Samorí, M. Keil, Th. Kugler, W. R. Salaneck, J. D. Brand, K. Müllen, J. P. Rabe

SMARTON-ESF Workshop; Bruges, Belgium, 28-31 January, 1999.

13."STM investigations of dendrimers"

U. Hubler, H. P. Lang, B. A. Hermann, H.-J. Güntherodt, P. Samorí, J. P Rabe, G.. Greiveldinger, P. B. Rheiner, P. Murer, T. Sifferlen, D. Seebach

Proceedings of the Frühjahrstagung der Deutschen Physikalische Gesellschaft; Muenster, Germany, 22-26 March 1999 .

14."Epitaxial ordering of hexabenzocoronene layers from solution"

P. Samorí, M. Keil, Th. Kugler, W. R. Salaneck, J. D. Brand, K. Müllen, J. P. Rabe

EL.B.A. - Foresight Conference on Nanotechnology, Rome, Italy, 14-16. April 1999.

15."Nanostructuring in 2D and 3D: from the structure and dynamics of single (macro)molecules to supramolecular architectures"

P. Samorí, V. Francke, K. Müllen and J. P. Rabe

EL.B.A. - Foresight Conference on Nanotechnology, Rome, Italy, 14-16. April 1999.

16."Hexabenzocoronene epitaxial layers grown from solution"

P. Samorí, M. Keil, Th. Kugler, W. R. Salaneck, J. D. Brand, K. Müllen, J. P. Rabe

Europolymer Conference 1999 Gargnano (BS), Italy, 23-28 May 1999.

17."Epitaxial growth of hexabenzocoronene ultrathin films from solution"

P. Samorí, M. Keil, W. R. Salaneck, K. Müllen, J. P. Rabe

MRS - Spring 2000 Meeting; San Francisco, California, USA, 24-28 April, 2000.

18. "Phthalocyanine disks and cylinders nanostructures at surfaces "

P. Samorí, H. Engelkamp, P. de Witte, A. E. Rowan, R. J. M. Nolte, J. P. Rabe

2nd International Conference on Supramolecular Science & Technology; Leuven, Belgium, 10-15 September 2000

19. “ Self-assembled hydrogen bonded architectures of lipophilic guanosines"

G. Gottarelli, S. Masiero, E. Mezzina, S. Pieraccini, P. Samorí, J. P. Rabe, G. P. Spada

Berliner Polymerentage; Berlin, Germany, 9-11 October 2000.

Coauthor of communications:

1. F. Biscarini, P. Samorí, P. Ostoja, R. Zamboni, C. Taliani

STM'95 Eight International Conference on Scanning Tunneling Microscopy/Spectroscopy; Snowmass Village, CO, USA, 1995.

2."Sexithiophene film growth: an atomic force microscopy study"

F. Biscarini, P. Samorí, P. Ostoja, R. Zamboni, C. Taliani

The 7th Conference on Organized Molecular Films; Numana (Ancona), Italy, 1995.

3. F. Biscarini, P. Samorí, P. Ostoja, R. Zamboni, C. Taliani

XX Congresso di Microscopia Elettronica (SIME); Rimini, Italy, 1995.

4."Growth of high-vacuum sublimed thin films"

F. Biscarini, O. Greco, A. Lauria, P. Samorí, C. Taliani, R. Zamboni

212th ACS National Meeting; Orlando, Florida – USA, 25-29 Agust 1996.

5."Roughness scaling behaviour and mechanism of growth in high-vacuum of conjugated anisotropic thin films"

F. Biscarini, P. Moretti, P. Samorí

STM'97-9th International Conference on Scanning Tunneling Microscopy/Spectroscopy; Hamburg, Germany, 20-25 July 1997.

6."Self-assembled nanostructures of macromolecular rods"

J. P. Rabe, W. Stocker, P. Samorí

Proceedings of European Conference on Molecular Electronics (ECME); Cambridge, United Kingdom, 7-10 September 1997.

7."Synthesis of α,ω thiol-functionalised oligo- and poly-*para*-(phenyleneethynylene)"

V. Francke, T. Mangel, P. Samorí, J. P. Rabe, K. Müllen

Berliner Polymerentage; Berlin, Germany, 9-11 October 1997.

8."Macromolecular nanostructures observed by scanning probe microscopies"

J. P. Rabe, W. Stocker, P. Samorí

6th SPSJ International Polymer Conference - Polymer Science and technology focused the 21st century; Kusatsu, Japan, 20-24 November 1997.

9."Self-assembly of macromolecular rods at solid-liquid interfaces"

J. P. Rabe, W. Stocker, P. Samorí

2nd International Workshop on Wetting and Self-Organization in Thin Liquid Films, Muenchen, Germany, 2-6 March 1998.

10."Photoelectron spectroscopy investigations of thin films of disk-like and rod-like molecules - the influence on the electronic structure upon *n*-doping"

M. Keil, P. Samorí , Th. Kugler, S. Stafström, W. R. Salaneck, J. P. Rabe

TMR-SISITOMAS Meeting; Bruges, Belgium, 27-28 January, 1999.

11."Electronic structure and morphology of pristine and *n*-doped films of hexa-*peri*-benzocoronene on different substrates"

M. Keil, P. Samorí, T. Kugler, D.A. dos Santos, J. L. Brédas, S. Stafström, J. D. Brand, K. Müllen, J. P. Rabe

European Conference of Molecular Electronics 1999; Linkoeping, Sweden, 8-11 September 1999.

Selbständigkeitserklärung

Hiermit versichere ich, die vorliegende Arbeit selbständig angefertigt zu haben und keine weiteren als die Hilfsmittel verwendet zu haben.

Paolo Samorí

Berlin, 14 Juli 2000.